

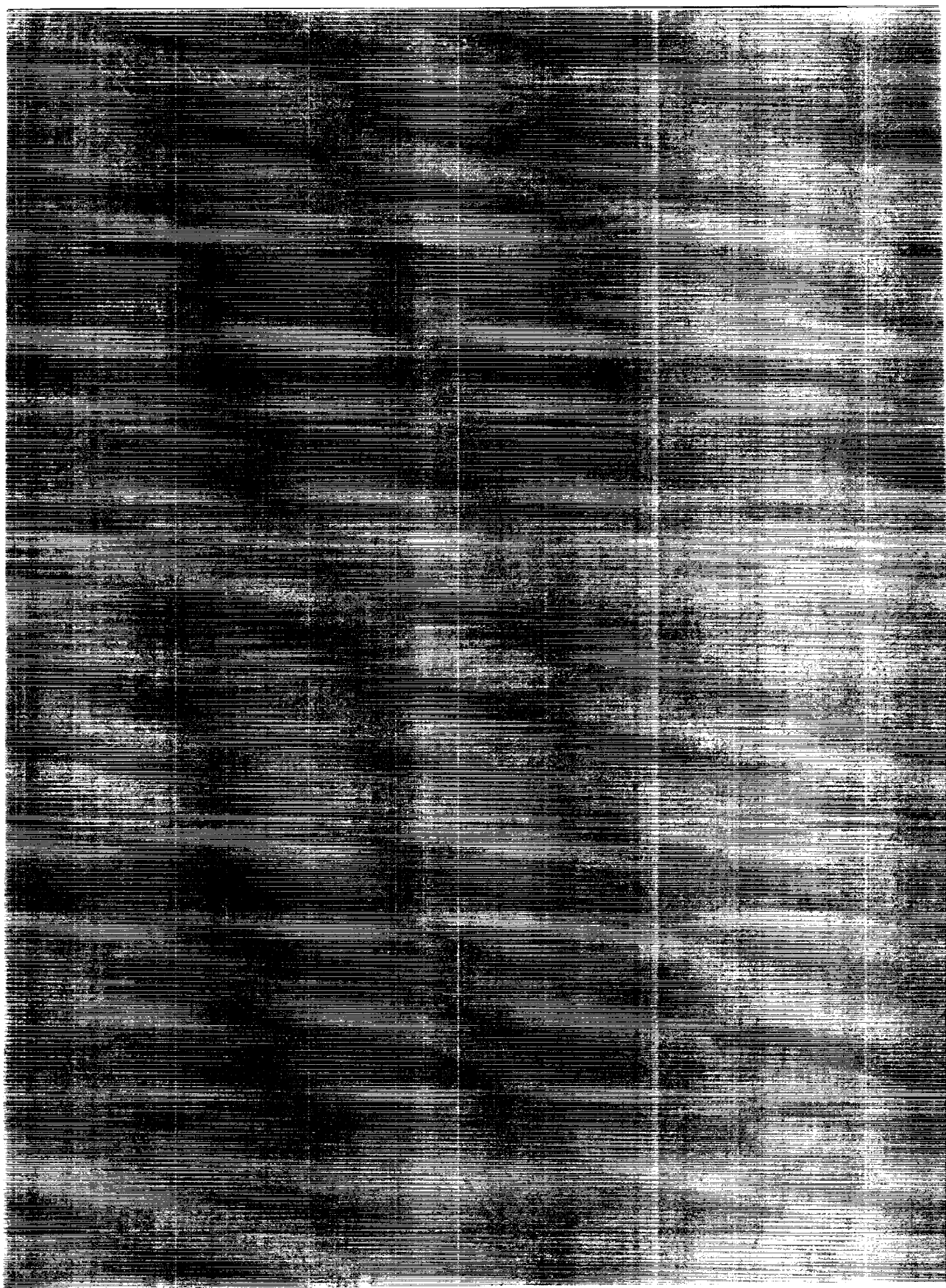
(NAPS-01-9506-Vol-1) EFFECTS OF ROTATION ON  
OIL AND FANLAD: HEAT TRANSFER. VOLUME 1:  
OIL AND FANLAD WITH OIL IN WALLS (OWA)  
1962

CSCL 200

NP1-00489

Unclas

H1/34 0050591



NASA Contractor Report 4396, Vol. I

# Effects of Rotation on Coolant Passage Heat Transfer

## *Volume I—Coolant Passages With Smooth Walls*

T. J. Hajek, J. H. Wagner, B. V. Johnson,  
A. W. Higgins, and G. D. Steuber  
*Pratt & Whitney*  
*East Hartford, Connecticut*

Prepared for  
Lewis Research Center  
under Contract NAS3-23691



National Aeronautics and  
Space Administration

Office of Management

Scientific and Technical  
Information Program

1991



## FOREWORD

This report covers work performed under NASA Contract NAS3-23691 to investigate heat transfer characteristics of rotating multipass passages for configurations and dimensions typical of modern gas turbine blades under the Hot Section Technology (HOST) program. The NASA Program Manager is Mr. Frederick Yeh, Hot Section Technology (HOST), NASA Lewis Research Center. Mr. Seyf Tanrikut served as Program Manager at Pratt & Whitney. Acknowledgements are given to L. D. Aceto, R. A. Graziani, F. C. Kopper, I. Linask, S. Orr and the assistance of their colleagues at Pratt & Whitney and UTRC for their contributions to the program.



## TABLE OF CONTENTS

<u>Section</u>	<u>Page</u>
1.0 Summary	1
2.0 Introduction	2
3.0 Experimental Apparatus and Procedures	7
3.1 Heat Transfer Model	7
3.1.1 Model Design	7
3.1.2 Model Instrumentation	10
3.2 Rotating Heat Transfer Facility	13
3.2.1 Data Acquisition System	16
3.2.2 Heat Power Source	16
3.2.3 Flow Monitoring System	16
3.3 Experimental Procedures	16
4.0 Experimental Parameters and Test Matrix	18
5.0 Stationary Heat Transfer Results	26
5.1 Baseline Flow Condition	26
5.2 Effect of Density Ratio	29
5.3 Effect of Reynolds Number	29
5.4 Conclusions	29
6.0 Rotating Heat Transfer Results	32
6.1 Baseline Flow Conditions	32
6.2 Effect of Rotation Number	35
6.2.1 High Pressure Surfaces	35
6.2.2 Low Pressure Surfaces	37
6.2.3 Side Walls	37
6.2.4 Turns	37
6.3 Effect of Density Ratio	38
6.3.1 Straight Sections	38
6.3.2 Turns	40
6.4 Effect of Reynolds Number	40
6.5 Effect of Model Radius	40
6.6 Effect of Model Angular Orientation	43
6.7 Conclusions	47
7.0 Discussion of Combined Effects on Heat Transfer	48
7.1 Effect of Density Ratio	48
7.2 Effect of Rotation Number	51
7.2.1 High Pressure Surfaces	51
7.2.2 Low Pressure Surfaces	54
7.3 Effect of Buoyancy Parameter	54
7.4 Effect of Flow Direction	58
7.5 Conclusions	61

## TABLE OF CONTENTS (Continued)

<u>Section</u>	<u>Page</u>
8.0 Correlation of Heat Transfer Results	62
8.1 Physical Effects of Rotation	62
8.2 Rotation Heat Transfer Correlations	67
8.2.1 Side Wall Heat Transfer	67
8.2.2 High Pressure Wall Heat Transfer	72
8.2.3 Turn Heat Transfer	76
8.2.4 Low Pressure Wall Heat Transfer	79
8.3 Comparison of Results with Other Experiments	86
8.3.1 Comparison With Results of Iskakov	88
8.3.2 Comparison With Results of Morris	91
8.3.3 Comparison With Results of Eckert	91
9.0 Conclusions	96
10.0 Appendix	98
10.1 Analysis of Equations of Motion	98
10.2 Model Inlet Flow Characterization	100
10.3 Error Analysis and Repeatability	106
10.3.1 Repeatability	107
10.3.2 Low Rotation	107
10.3.3 Effect of Rotation Direction	107
10.4 Pressure Loss Measurements	113
10.4.1 Instrumentation	113
10.4.2 Estimate of Pressure Measurement Accuracy	113
10.4.3 Data Analysis	113
10.4.4 Results for $\Omega = 0$ and Low Pressure	114
10.4.5 Results for Nonrotating Tests	114
10.4.6 Results for Rotating Tests	115
10.5 Model Geometry Information	116
List of Symbols	119
References	124



## LIST OF TABLES

<u>Table</u>		<u>Page</u>
<u>Section 4.0 Experimental Parameters and Test Matrix</u>		
I	Test Conditions for Rotating Heat Transfer Experiments with Smooth Wall Model	19
II	Supplementary Test Conditions for Rotating Heat Transfer Experiments with Smooth Wall Model	20
III	Test Conditions for Heat Transfer Experiments with Smooth Wall Model	22
<u>Section 10.0 Appendix</u>		
IV	Symmetry of Model and Repeatability of Heat Transfer Results. Rotating Heat Transfer Experiments with Smooth Wall Model	108
V	Model Heat Transfer Geometry Information	117
VI	Model Pressure Tap Geometry Information	118

## LIST OF FIGURES

<u>Figure</u>	<u>Page</u>
<u>Section 2.0 Introduction</u>	
1. Cooling Concept of a Modern Multipass Turbine Blade.	3
2. Typical Secondary Flow Pattern for Isothermal Laminar Developed flow with Orthogonal-Mode Pattern Rotation (Barua, 1955).	4
3. Local Mass Transfer Result in Laminar Region. (Ito and Nanbu, 1970)	4
4. Local Analogous Nusselt Number in Laminar Regions (rotation). (Ito and Nanbu, 1970)	5
<u>Section 3.0 Experimental Apparatus and Procedures</u>	
5. Cross Sectional View of Coolant Passage Heat Transfer Model Assembly. Streamwise Location of Test Sections Identified by A to R. All Four Test Section Surfaces for Streamwise Locations A Through R are Heated.	8
6. Details of Test Section Elements.	9
7. Photograph of Uninstrumented Coolant Passage Heat Transfer Model With Leading Edge ( $+\Omega$ ) Plane Test Sections Removed.	10
8. Instrumentation Plan for Coolant Passage Heat Transfer Model.	11
9. Test Surface Identification Plan for Coolant Passage Heat Transfer Model (View from the axis of rotation looking radially outward to the model).	12
10. Photograph of Instrumented Coolant Passage Heat Transfer Model With Trailing Edge ( $+\Omega$ ) Plane Test Section Removed. (Two thermocouples and thin film heaters mounted on each test section).	14
11. Photograph of Assembled Model Mounted on Base With Pressure Shell Removed.	14
12. Photograph of Model Mounted in Rotating Heat Transfer Facility. (Rotating heat transfer facility with cover removed).	15
13. Rotating Heat Transfer Facility.	15

## LIST OF FIGURES (Continued)

<u>Figure</u>	<u>Page</u>
<u>Section 4.0 Experimental Parameters and Test Matrix</u>	
14. Test Conditions for Parametric Rotating Heat Transfer Study.	24
<u>Section 5.0 Stationary Heat Transfer Results</u>	
15. Heat Transfer Results for Stationary Baseline Flow Conditions.	27
16. Comparison of Heat Transfer in Straight Segments for Test Condition Number 1A With Previous Heat Transfer Results for Entrance Regions.	28
17. Effect of Wall Temperature on Heat Transfer Ratio for Non-rotating Flow Conditions.	30
18. Effect of Reynolds Number on Heat Transfer Ratio for Stationary Condition.	31
<u>Section 6.0 Rotating Heat Transfer Results</u>	
19. Comparison of Heat Transfer Ratio for Rotating and Stationary Baseline Flow Conditions.	33
20. Effects of Rotation Rate on Heat Transfer Ratio.	36
21. Effects of Density (Temperature) Ratio on Heat Transfer Ratio.	39
22. Effects of Reynolds Number on Heat Transfer Ratio.	41
23. Effects of Model Radius on Heat Transfer Ratio.	42
24. Effects of Model Orientation on Heat Transfer Ratio.	44
25. Variation of Heat Transfer Ratio Around Test Section with Streamwise Location, Rotation Number and Model Orientation in First Leg of Model.	45
26. Comparison of Heat Transfer Ratio Around Test Section From Passages With Inward and Outward Flow.	46
<u>Section 7.0 Discussion of Combined Effects on Heat Transfer</u>	
27. Variation of Heat Transfer Ratio with Density Ratio for Selected Rotation Numbers.	49
28. Variation of Heat Transfer Ratio with Density Ratio for Selected Rotation Numbers.	50

## LIST OF FIGURES (Continued)

<u>Figure</u>	<u>Page</u>
29. Variation of Heat Transfer Ratio with Rotation Number for Selected Inlet Density Ratios.	52
30. Variation of Heat Transfer Ratio with Rotation Number for Selected Inlet Density Ratios.	53
31. Variation of Heat Transfer Ratio with Buoyancy Parameter.	56
32. Variation of Heat Transfer Ratio with Buoyancy Parameter.	57
33. Comparison of Heat Transfer Ratios from Passages with Inward and Outward Flow.	59
34. Comparison of Heat Transfer Ratios from Passages with Inward and Outward Flow.	60
 <u>Section 8.0 Correlation of Heat Transfer Results</u>	
35. General Effects of Rotation on Radially Outward Flow in a Square Channel.	63
36. Schematic of Moore's Test Section (Moore, 1967).	63
37. Moore's Rotating Square Duct Centerline Velocity Profile (Moore, 1967).	64
38. Rotational Passage of Moon's Experiment (Moon, 1964).	64
39. Moon's Centerline Velocity Profiles with Boundary Layer and Displacement Thickness (Moon, 1964).	65
40. Moore's Skin Friction Variation with Aspect Ratio (Moore, 1967).	66
41. Mainstream Flow Direction and Buoyancy Force Direction in Radially Inward and Radially Outward Flowing Passages.	67
42. Sidewall Heat Transfer at $Re = 25,000$ for the First Straight Passage.	68
43. Effect of Reynolds Number for Low Rotation ( $Ro \leq 0.20$ ) on Sidewall Heat Transfer.	70
44. Effect of Radius Variation on Sidewall Heat Transfer for High Rotation ( $Ro > 0.20$ ).	71

# LIST OF FIGURES (Continued)

<u>Figure</u>	<u>Page</u>
45. High Pressure Surface Heat Transfer for Radially Outward Flow $Re = 25,000$ .	73
46. Effect of Reynolds Number for Low Rotation ( $Ro < 0.20$ ) on High Pressure Surface Heat Transfer.	74
47. Effect of Radius Variation on High Pressure Surface Heat Transfer for High Rotation Regime ( $Ro > 0.20$ ).	75
48. Tip Turn Heat Transfer: Outer Sidewalls, $Re = 25,000$ .	77
49. Leading and Trailing Surface Heat Transfer in Tip Turn (Solid Symbols = Trailing Surface).	78
50. Root Turn Heat Transfer: Outer Sidewalls, $Re = 25,000$	80
51. Leading and Trailing Surface Heat Transfer in Root Turn (Solid Symbols = Trailing Surface).	81
52. Effect of Rotation Number on Heat Transfer Ratio for Low Pressure Surface; $Re = 25,000$ , $(\rho/\rho)_{in} = 0.13$ , $\bar{R}/d = 49$ .	82
53. Leading Side Heat Transfer for First Passage: Radially Outward Flow (Test section elements 34, 35, 36).	83
54. Leading Side Heat Transfer $Ro \geq 0.25$ : $Re = 25,000$ (Test section elements 34, 35, 36).	84
55. Leading Side Heat Transfer with Rotation Compared to Kays (1966) Laminar Heat Transfer: ( $Re = 25,000$ , $\bar{R}/d = 49$ , $\alpha = 0$ ).	85
56. Flow Visualization of Rotating Channel Flow (Johnston, 1970).	85
57. Leading Side Heat Transfer with Rotation Compared to Kays (1966) Laminar Heat Transfer: ( $Re = 12,500$ , $\bar{R}/d = 49$ , $\alpha = 0$ )	87
58. Leading Side Heat Transfer with Rotation Compared to Kays (1966) Laminar Heat Transfer: ( $Re = 50,000$ , $\bar{R}/d = 49$ , $\alpha = 0$ )	87
59. Present Data and Johnston's Flow Map (Johnston 1970) Showing Laminarization on the Low Pressure Surface.	88

## LIST OF FIGURES

<u>Figure</u>	<u>Page</u>
60. Effects of Rotation on the Coefficient of Change in Heat Transfer with Centrifugal Flow of Air on the (a) Trailing Side and (b) on the Leading Side (Iskakov and Trushin, 1985).	89
61. Comparison of Iskakov's Correlation with Averaged Heat Transfer Data of this Experiment: $Re = 25,000$ (Iskakov and Trushin, 1985).	90
62. Comparisons of Leading Surface Rotating Heat Transfer Results for $X/d = 12.4$ with (Morris 1981).	92
63. Circumferentially Averaged Heat Transfer Coefficients for Outflow Passage Compared with Eckert's Counterflow Results (Eckert and Diaguilla, 1954).	93
64. Circumferentially Averaged Heat Transfer Coefficients for Inflow Passage Compared with Eckert's Parallel flow Results (Eckert and Diaguilla, 1954).	93
 <u>Section 10.0 Appendix</u>	
65. Rotating Pipe Coordinates.	98
66. Nozzle Probe Traverse Locations and Nomenclature.	101
67. Nozzle Exit Flow Profiles in Z and Y Directions.	102
68. Variation in Velocity Surfaces and Contours for Nozzle Exit Flow.	103
69. Channel Exit Flow Profiles in Z and Y Directions.	104
70. Variation in Velocity Surfaces and Contours for Channel Exit Flow.	105
71. Repeatability of Heat Transfer Data.	110
72. Effect of Low Rotation on Heat Transfer.	111
73. Effect of Rotation Direction on Heat Transfer	112
74. Pressure Distribution in Nonrotating Model at the Low Model Pressure Condition.	114
75. Effect of Reynolds Number on Pressure Distribution in Nonrotating Model.	115
76. Effect of Rotation on Pressure Distribution in Model.	116

## 1.0 SUMMARY

An experimental program was conducted to investigate heat transfer characteristics of rotating multipass passages for configurations and flow parameters typical of modern gas turbine blades. The experiments were conducted with a smooth wall, large scale heat transfer model. The objective was to obtain the heat transfer data base required to develop heat transfer correlations and to assess computational fluid dynamic techniques for rotating coolant passages. An analysis of the governing equations showed that four parameters influence the heat transfer in rotating passages (coolant density ratio, rotation number, Reynolds number and radius ratio). These four parameters were varied over ranges which exceed the ranges of current open literature results, but which are typical of current and advanced gas turbine engine operating conditions. Rotation affected the heat transfer coefficients differently for different locations in the coolant passage. For example, heat transfer at some locations increased with rotation, but decreased and then increased again at other locations. Heat transfer coefficients varied by as much as a factor of 5 between the leading and trailing surfaces for the same test condition and streamwise location. Comparisons with previous results are also presented.

This work was supported by the NASA/Lewis Research Center under the Hot Section Technology (HOST) initiative, Contract No. NAS3-23691 to Pratt & Whitney, Commercial Engineering. The work was performed under the direction of Mr. F. Yeh, NASA Project Manager, and Mr. S. Tanrikut, Pratt & Whitney Program Manager. Additional experiments were conducted under United Technologies Corporation independent research sponsorship in order to enhance the benchmark data base. These data are also included in this report.

## 2.0 INTRODUCTION

Current high performance gas turbine engines exploit internal convection cooling schemes to maintain acceptable airfoil metal temperatures. This approach requires complex coolant passage configurations within the rotating blades as illustrated in Figure 1. Most coolant passage designs enhance heat transfer coefficients above smooth channel levels by utilizing turbulence promoters. Summaries of the technical problems and needs of the current gas turbine blade designer are presented by Suo (1978) and Taylor (1980).

A review of general heat transfer literature by Bergles and Webb (1970), contains significant references for turbine airfoil cooling passage design. Webb et.al. (1971) has reported measurements and correlations for flow in nonrotating tubes with repeated rib roughness. Burggraf (1970) and Han et.al. (1978) conducted experimental heat transfer studies with rib roughened geometries typical of gas turbine engines. Buoyancy effects in vertical stationary ducts were reported by Eckert et.al. (1953), Metais and Eckert (1964) and Brundrett and Burroughs (1967). There are limited amounts of rotating passage heat transfer data, with the bulk of this work done with circular tubes. The effects of rotation on secondary flow and stability have been investigated by Moore (1967), Hart (1971), Wagner and Velkoff (1972), Johnston et.al. (1972) and Rothe and Johnston (1979). Heat transfer in rotating, smooth wall models has been investigated by Mori et.al. (1971), Johnson (1978), Morris and Ayhan (1979), Lokai and Gunchenko (1979), Morris (1981), Iskakov and Trushin (1983) and more recently, Guidez (1988). Some of the results contained in this report have been previously reported in Wagner et. al. (1989, 1991) and Wagner et. al. (1990).

Large increases and decreases in local heat transfer were found to occur by some investigators under certain conditons of rotation while others showed lesser effects. Analysis of these results does not produce consistent trends in the effects of rotation on heat transfer. The disparity in the results is indicative of differences in the measurement techniques and models used in the experiments as well as the nonuniformity of the test conditions.

Initial work to investigate rotating bound shear flows examined unheated circular and rectangular duct flows. For radially outward flow, rotation was shown to generate secondary flows perpendicular to the mainstream flow direction in ducts orthogonal to the axis of rotation. Much of the early work was conducted for laminar flow since rig limitations in an unpressurized duct allow only low Reynolds number flows at appropriate rotation or Rossby numbers. The secondary flow patterns of Barua (1954-1955), shown in Figure 2, illustrate the effect of rotation on isothermal laminar flow in a circular duct. Ito and Nanbu (1970) conducted one of the first heat and mass transfer experiments in a rotating circular tube. These results, shown in Figures 3 and 4, compare the non-rotating and rotating values of local heat transfer. The small dashed inner circle in Figure 4 represents the level of non-rotating heat transfer. Notice the strong shift in heat transfer in the rotating duct. Plotted on a polar plot, most of the tube exhibits significant increases in local Nusselt number up to six times the non-rotating level. Only precisely on the centerline of the leading surface is a decrease in heat transfer evident.



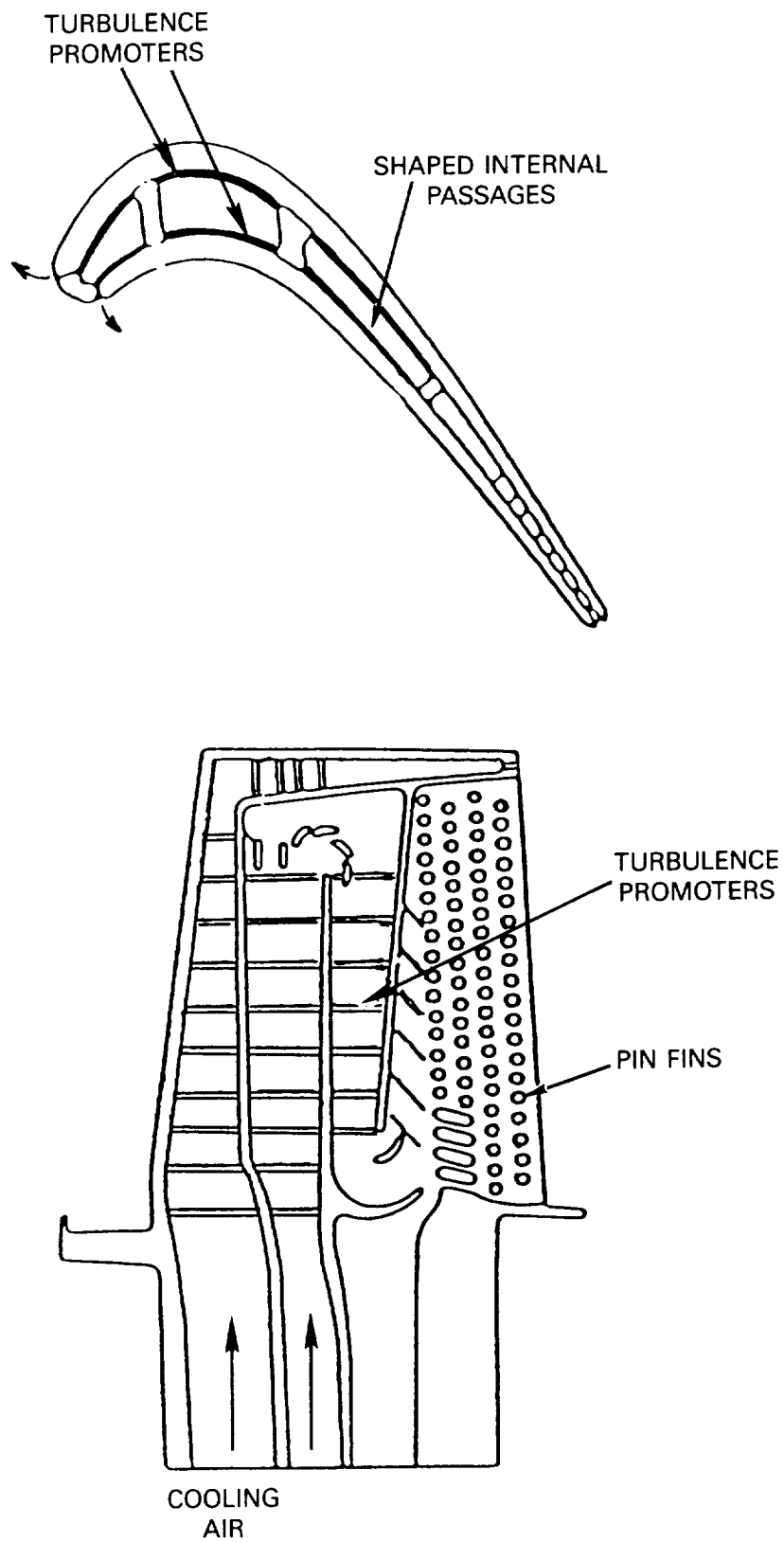


Figure 1.- Cooling Concept of a Modern Multipass Turbine Blade.

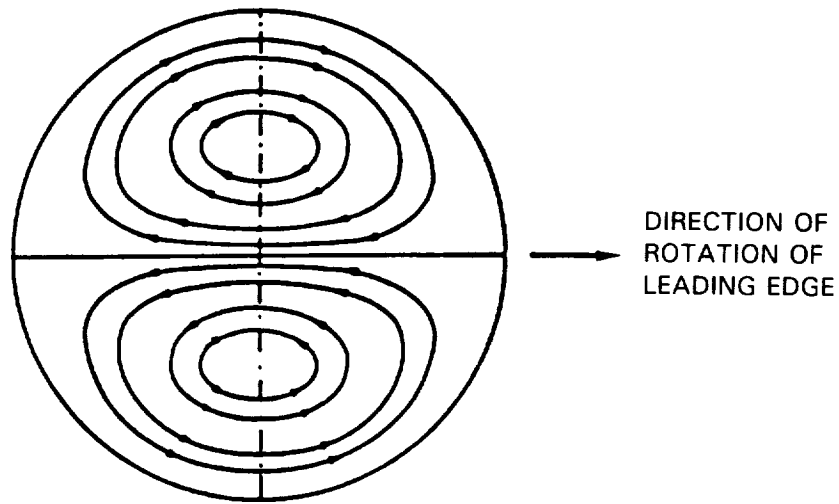


Figure 2.- Typical Secondary Flow Pattern For Isothermal Laminar Developed Flow With Orthogonal-Mode Pattern Rotation (Barua, 1955).

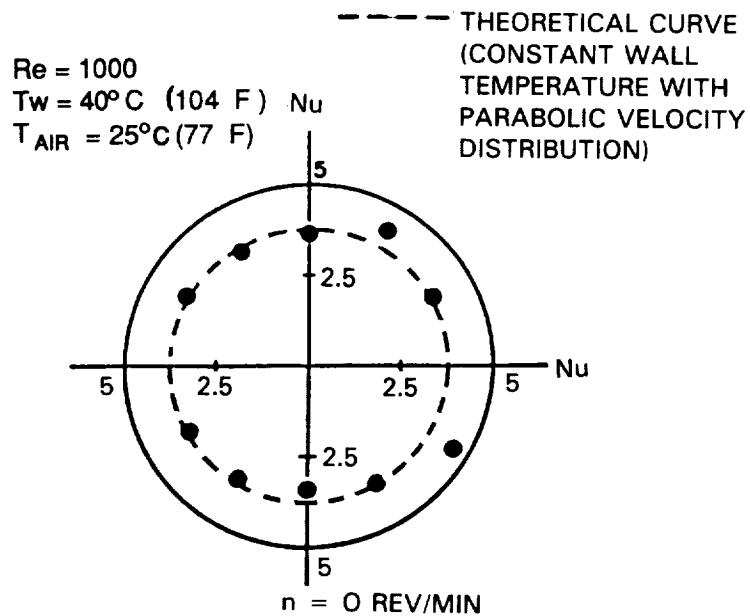


Figure 3.- Local Mass Transfer Result in Laminar Region (Ito and Nanbu, 1970).

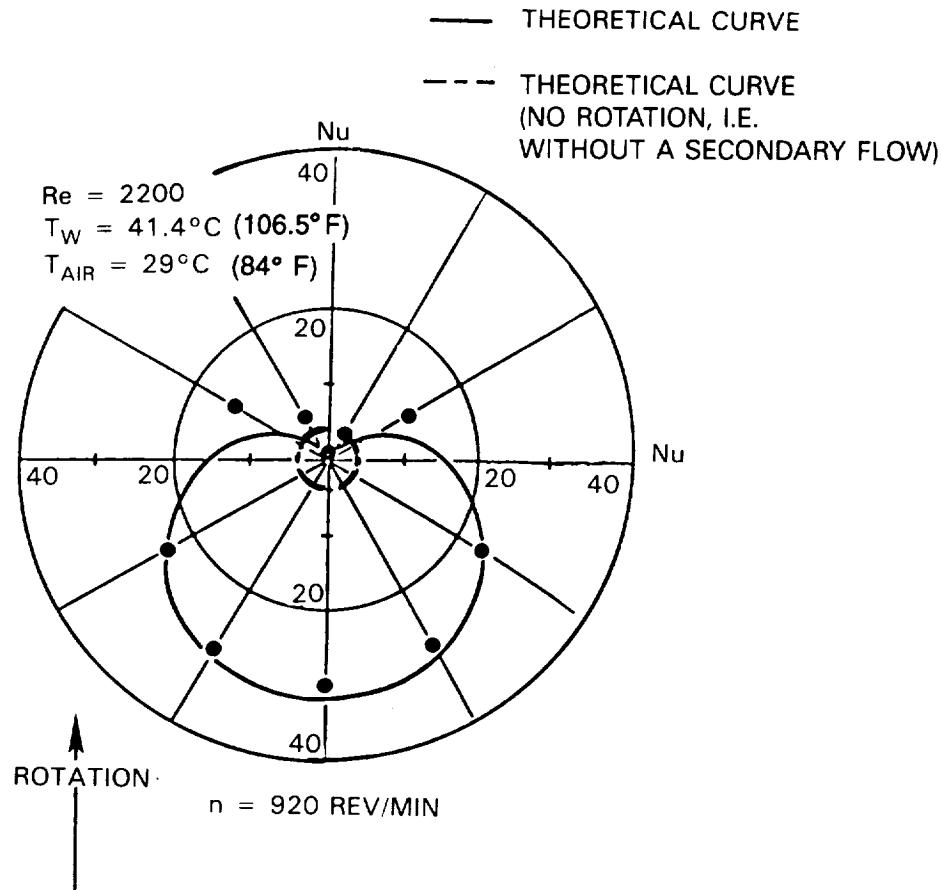


Figure 4.- Local Analogous Nusselt Number in Laminar Regions (rotation)  
(Ito and Nanbu, 1970).

The generation of secondary flows by Coriolis forces produces a complicated three-dimensional flow that greatly alters the circumferential heat transfer distribution in rotating duct flows. The secondary flows produced in these configurations will influence the distribution of heat transfer according to the movement or migration of fluid from one surface to another and the mixing of the near-wall fluid with the mainstream or core flow. Thus, the circumferential distribution of heat transfer will be vastly different in each of these geometries, as it will be in the wide variety of cooling channel geometries found in advanced aircraft gas turbine blades.

Most of the published work on rotating duct flows has been on experiments conducted with long straight ducts with flow traveling either radially outward or radially inward with respect to the axis of rotation. As depicted in Figure 1, modern gas turbine airfoils employ complicated serpentine shaped coolant passages that utilize coolant flowing both radially inward and radially outward. During the rotation of blades, the centrifugal forces of rotation will influence the heat transfer in each of these cases differently. Also, the upstream and downstream influence of the turns will affect the heat transfer in these passages and becomes very complicated during rotation. A further discussion of the physical effects of rotation on heat transfer including the work of other experimenters is presented in Sections 8.1 and 8.3.

Currently, the analysis of airfoil internal passage heat transfer and pressure loss relies mainly on correlations derived from testing models in a static (nonrotating) environment. Executing tests with rotation is difficult and costly. As a consequence, there is limited data that can be used to account for the effects of rotation on internal heat transfer and pressure loss in typical turbine blade designs. Some data are available for smooth tubes over a limited range of relevant parameters, but application of these data to complicated flow passages of a turbine airfoil would not be appropriate. Presently, adjustment factors are applied to the static test derived correlations to bring them into nominal correspondence with engine experience. This, in practice, accounts for rotation effects.

The objective of this phase of the program was to acquire heat transfer and pressure drop data and to develop correlations for multipass rotating, smooth-surface coolant passages under conditions similar to those expected in the first stages of advanced aircraft gas turbines. Local heat transfer was measured along the smooth wall coolant passage and around its periphery for radial outflow and inflow conditions. Local heat transfer was also measured in the three turns, two at the model tip and one at the model root. Incremental pressure drop was measured along the passages. All data were obtained for a range of rotational, flow, and heat flux conditions representative of engine operation.

The information generated with the smooth model was evaluated and compared with the results from the following two test phases utilizing turbulators in the same model to enhance local heat transfer. Upon completion of the entire program, detailed information will be available on the effects of rotation on internal flow and heat transfer in rotating, heated passages with and without turbulators. A complete set of data files from all three phases of this experimental program can be obtained through Mr. F. Yeh, NASA Project Manager at the NASA Lewis Research Center.

### 3.0 EXPERIMENTAL APPARATUS AND PROCEDURES

#### 3.1 Heat Transfer Model

A four legged heat transfer model, used for the NASA-sponsored heat transfer and pressure drop experiments, was designed, fabricated and instrumentated under UTC sponsorship. The model consists of three heated straight sections, one unheated straight section, and three turn sections as shown in Figure 5. The streamwise location of each test surface is identified by a letter A to R. The orientations of the test surface at each streamwise location are denoted "leading" and "trailing" for the surfaces in the plane of Figure 5 and "side walls" for the surfaces (crosshatched) perpendicular to the plane of Figure 5. Cross sections of the straight sections are shown in Figure 6. The model was designed for constant temperature, steady-state heat balance measurements and for wall static pressure measurements. A photograph of the uninstrumented coolant passage heat transfer model is shown in Figure 7.

##### 3.1.1 Model Design

Each streamwise location in the straight heated sections has the cross-sectional shape and features shown in Figure 6. All four copper walls were heated on the side opposite the test surface with thin film electric resistance heaters. The heaters were designed to produce a maximum heat flux of 4.6 to 6.2 watts per square centimeter (30 to 40 watts per square inch). The heaters were fastened to the copper test surfaces using standard strain gage adhesives useable for 177°C (350°F) operation. The temperatures of the copper test surfaces were measured with two chromel-alumel thermocouples inserted into drilled holes of each test surface and fastened with epoxy. The copper test surfaces were separated from each other in both the streamwise direction and around the coolant passage cross section with 1.52mm (0.060 in.) thick sections of G-10 or G-11 laminated fiberglass material. Details on the heat balance and the calculation of the effective heat transfer area for each test section will be discussed in a subsequent section.

The turn sections had three sides of the turn cross section heated and the fourth side unheated. The unheated surface was the inner-radius, curved surface shown in Figure 5. One heated test surface (leading and trailing wall surfaces) covers the coolant passage in the plane shown in Figure 5 for streamwise locations E, F, J, K, P and R. Two heated test surfaces cover the outer radius curved surfaces (side walls surfaces).

TEST SECTION ELEMENT IDENTIFICATION  
SIDE WALL TEST SECTION SURFACES. 1-32 ARE IN  
PLANE PERPENDICULAR TO VIEW SHOWN

TEST SECTION SURFACES 33-48 ARE ON "+  $\Omega$ " LEADING PLANE

TEST SECTION SURFACES (49)-(64) ARE ON "+  $\Omega$ " TRAILING PLANE

PRESSURE MEASUREMENT LOCATIONS 1 - 16

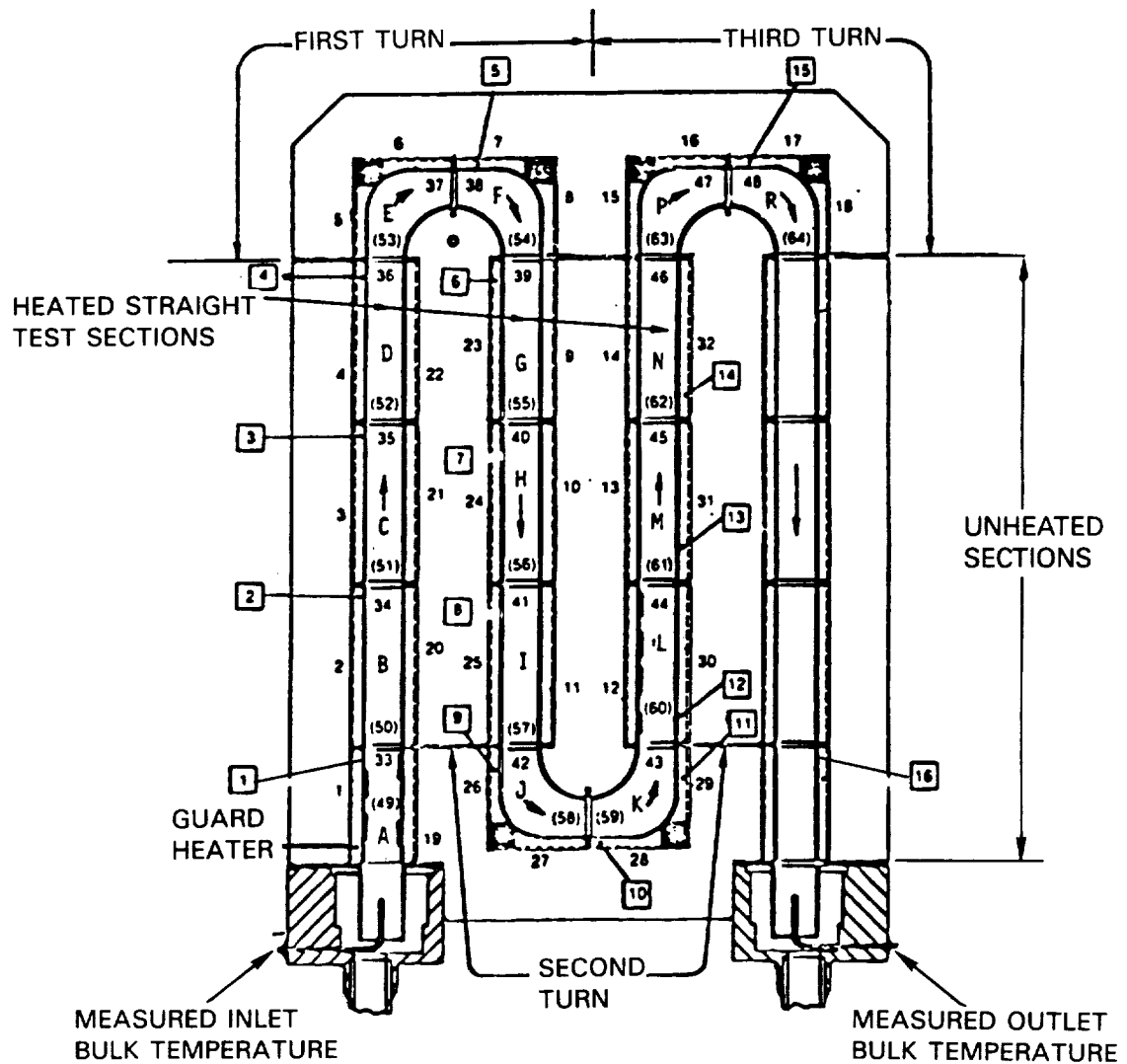


Figure 5.- Cross Sectional View of Coolant Passage Heat Transfer Model Assembly. Streamwise Location of Test Sections Identified by A to R. All Four Test Section Surfaces for Streamwise Locations A Through R are Heated.

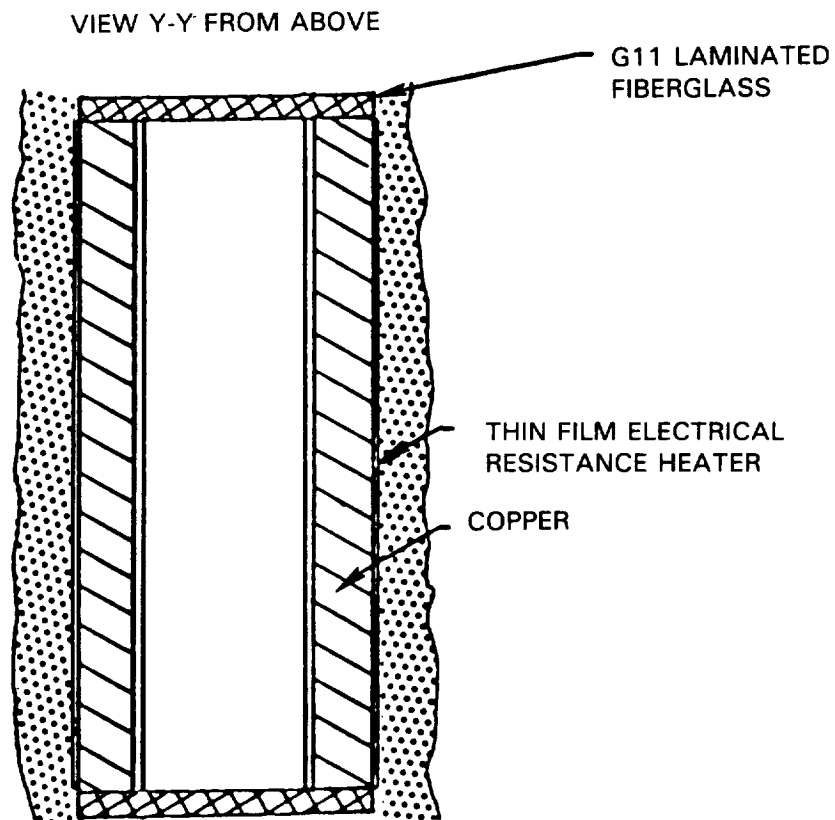
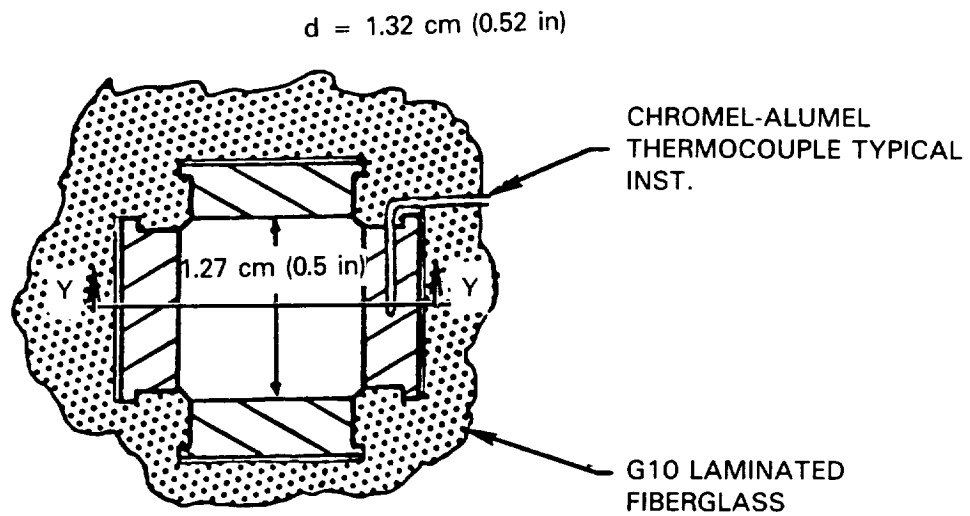


Figure 6.- Details of Test Section Elements.

ORIGINAL PAGE  
BLACK AND WHITE PHOTOGRAPH

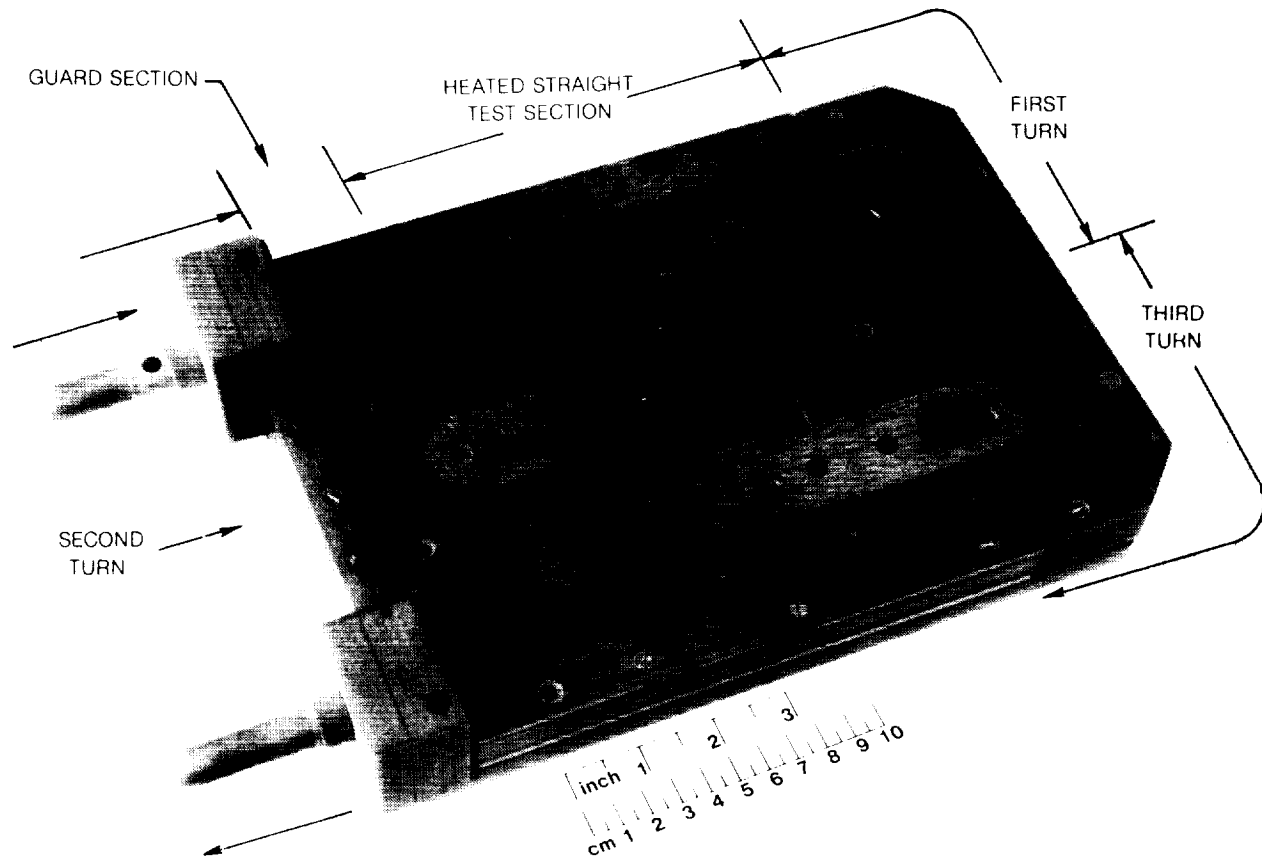


Figure 7.- Photograph of Uninstrumented Coolant Passage Heat Transfer Model With Leading Edge (+ $\Omega$ ) Plane Test Sections Removed.

### 3.1.2 Model Instrumentation

The instrumentation plan and the test surface instrumentation plan for the coolant passage heat transfer model are shown in Figures 8 and 9, respectively. The streamwise locations (A through R) previously shown in Figure 5 are repeated in Figure 8. In addition each heat transfer test surface is identified by a number (1 through 64). Note that test surfaces 2, 20, 34 and 50 are located at streamwise location B (Figure 8). Test surfaces 34 and 50 are the leading and trailing surfaces respectively when the model is in the  $\alpha = 0^\circ$  orientation (Figure 9). Test surfaces 2 and 20 are at sidewall locations for  $\alpha = 0^\circ$ .

Pressure measurement locations are shown at 16 places on Figure 8. The locations are on the side walls as shown and were chosen to separate the turn pressure losses from the straight section losses. The pressure tap is a 0.51 mm (0.020 in.) diameter hole drilled perpendicular to the test section surface midway across the passage.



TEST SECTION ELEMENT IDENTIFICATION  
SIDE WALL TEST SECTION SURFACES. 1-32 ARE IN  
PLANE PERPENDICULAR TO VIEW SHOWN

TEST SECTION SURFACES 33-48 ARE ON "+  $\Omega$ " LEADING PLANE

TEST SECTION SURFACES (49)-(64) ARE ON "+  $\Omega$ " TRAILING PLANE

PRESSURE MEASUREMENT LOCATIONS 1 - 16

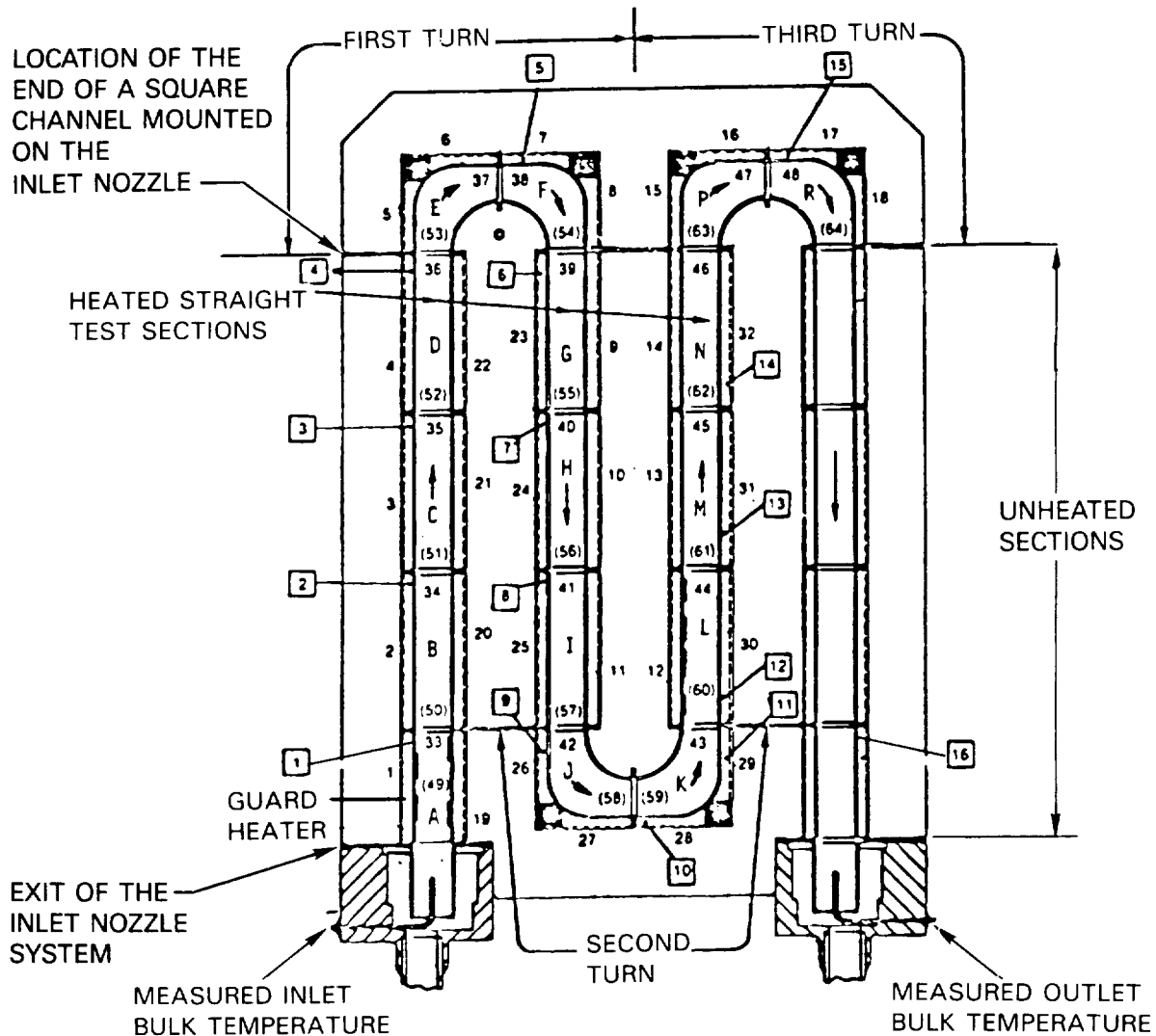


Figure 8.- Instrumentation Plan for Coolant Passage Heat Transfer Model.

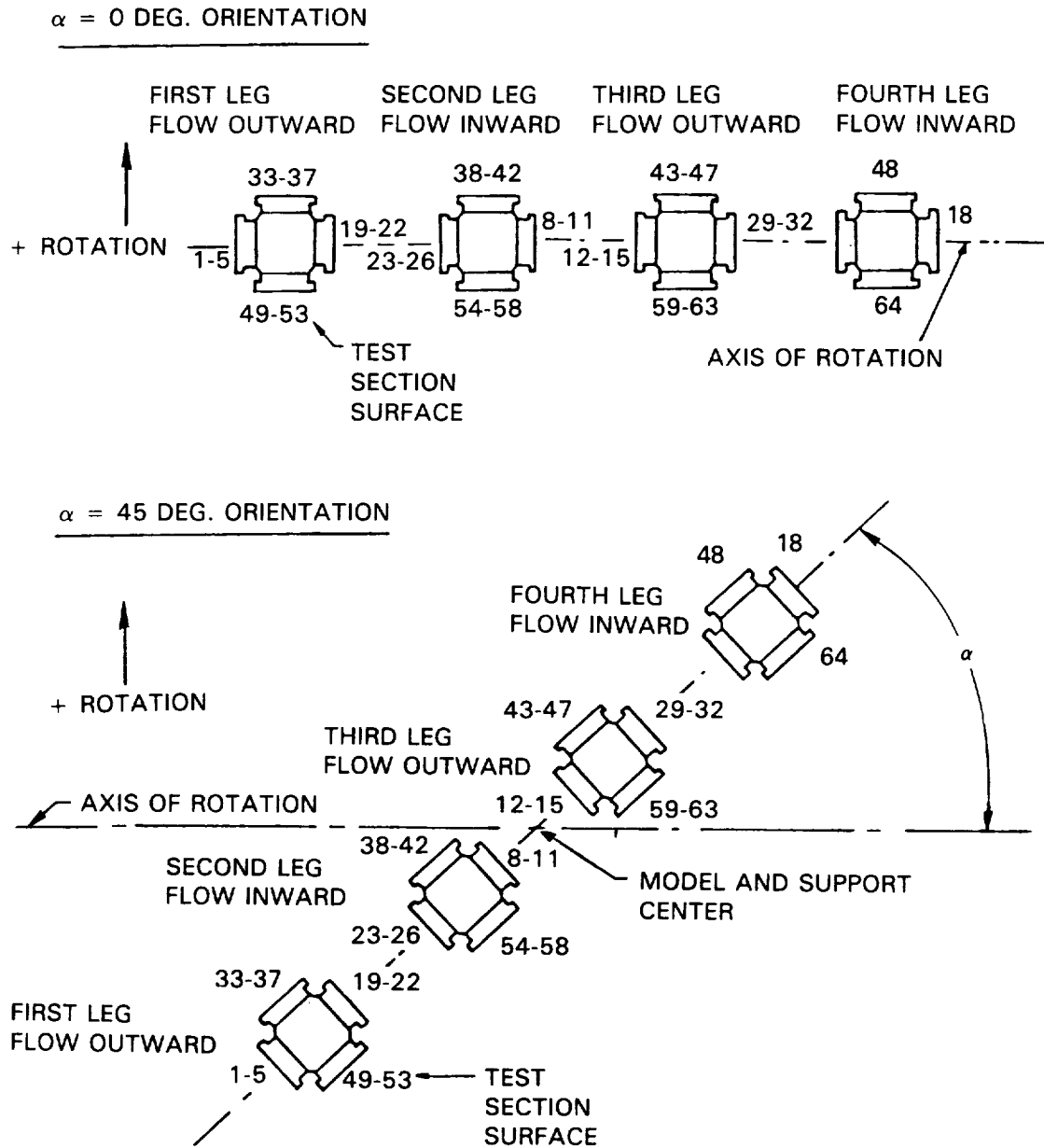


Figure 9.- Test Surface Identification Plan for Coolant Passage Heat Transfer Model (View from the axis of rotation looking radially outward to the model).

The test section surface locations for the  $\alpha = 0^\circ$  and the  $\alpha = 45^\circ$  orientations are shown in Figure 9. Note that for  $\alpha = 0^\circ$ , the centerlines of all four straight test sections pass through the axis of rotation and the straight sections are also radial sections. For  $\alpha = 45^\circ$ , the centers of the test sections are offset from radial as shown in Figure 9. The radial positions of several locations are shown on Figure 5 for reference.

A photograph of the partially-assembled, instrumentated, coolant passage heat transfer model is shown in Figure 10. Each of the 64 test surfaces has two chromel-alumel thermocouples imbedded and has a thin film heater attached. The six leads from each test surface multiplied by sixty four test surfaces result in 384 leads for this portion of the model. Additional thermocouples are positioned at the air inlet and exhaust locations and on the steel backing plates. A photograph of the assembled model mounted on the base is shown in Figure 11. A photograph of the model mounted in the Rotating Heat Transfer Facility is shown in Figure 12.

### 3.2 Rotating Heat Transfer Facility

The Rotating Heat Transfer Facility (RHTF) (Figure 13) consists of the containment vessel with the integral arm assembly and motor with associated controller. The containment vessel is 1.83 m (6.0 ft.) in diameter and was designed to withstand a destructive failure of the rotating assembly. The vessel was designed for operation at pressure of 5 to 13 mm of Hg absolute to reduce the power required to rotate the arm. The rotating arm assembly is driven by a 11KW (15 Hp) DC motor via a toothed belt. Shaft rpm is controlled by an adjustable feedback electronic controller. Maximum shaft speed is approximately 3,500 rpm producing body forces on the model of approximately 14,000 g's at the tip of the model and approximately 10,000 g's at the root. The maximum shaft speed for the present program was 1100 rpm. A safety shutdown interlock circuit is used to turn off the drive motor and model heater power supplies, turn on a magnetic brake and open the containment vessel vacuum chamber vent. The safety shutdown system prevents damage to the model or the facility in the event of a leak in the model or an imbalance in the rotating assembly.

The shaft assembly comprises a main outer shaft with two shorter inner shafts. This shaft arrangement was designed for dual fluid paths from each rotary union mounted on the ends of the shaft to the rotating assembly. Grooves located on the exterior surface of the outer shaft allow instrumentation and power leads to extend from the rotating arm to the rotating portion of the instrumentation slipring. Two slipring assemblies (a 40 channel unit located on the upper end of the shaft and a 200 channel unit located on the lower end of the shaft) are used to transfer heater power and instrumentation leads between the stationary and rotating frames of reference.

ORIGINAL PAGE  
BLACK AND WHITE PHOTOGRAPH



Figure 10.- Photograph of Instrumented Coolant Passage Heat Transfer Model With Trailing Edge (+Ω) Plane Test Section Removed (Two thermocouples and thin film heaters mounted on each test section).

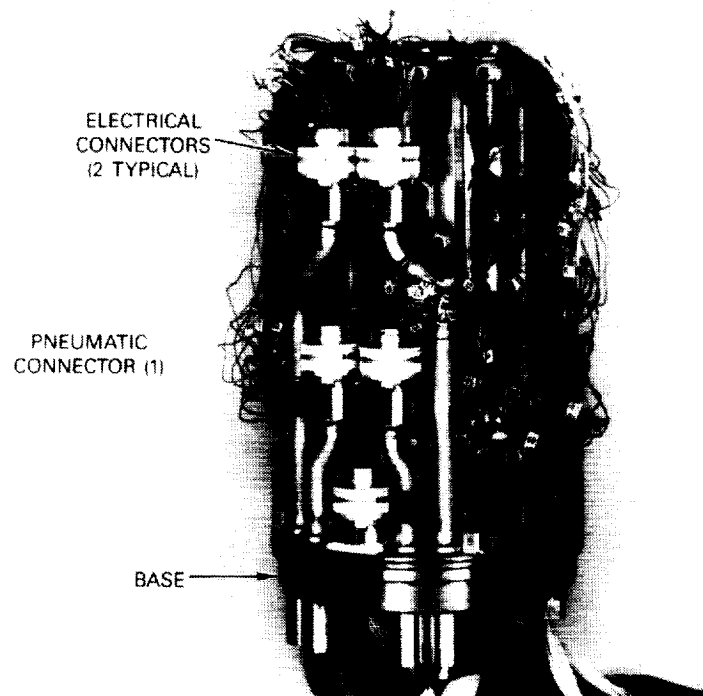


Figure 11.- Photograph of Assembled Model Mounted on Base With Pressure Shell Removed.

ORIGINAL PAGE  
BLACK AND WHITE PHOTOGRAPH

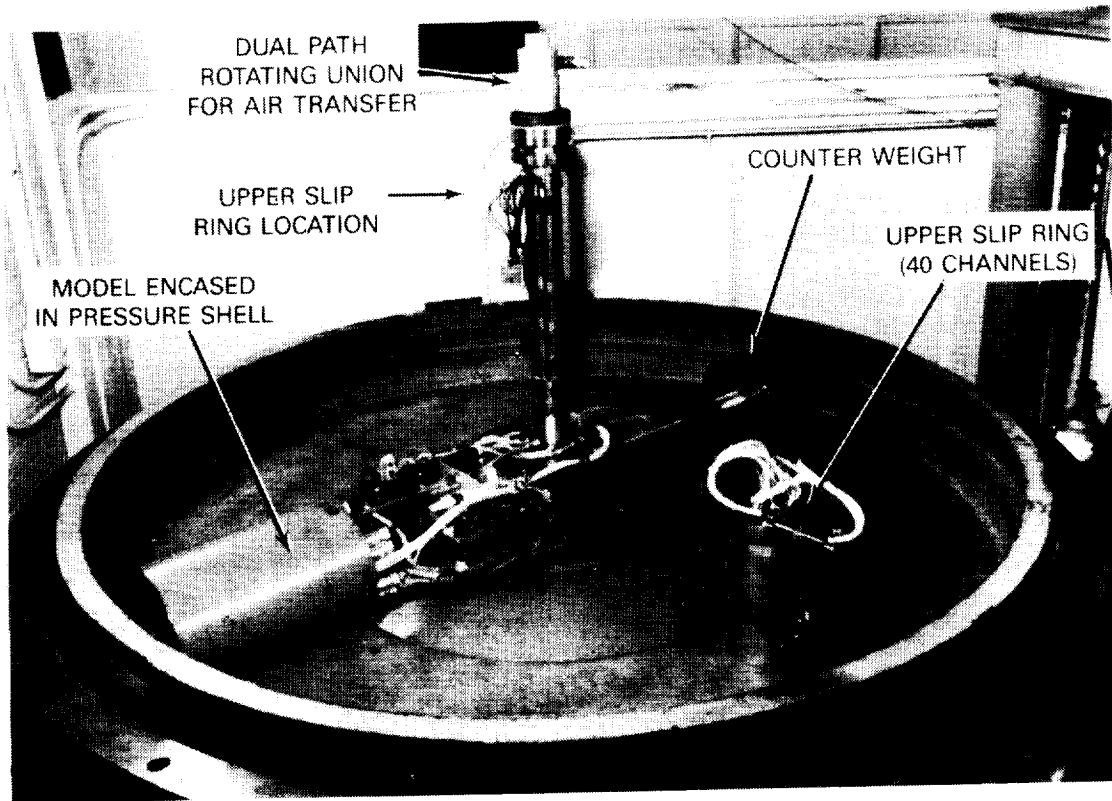


Figure 12.- Photograph of Model Mounted in Rotating Heat Transfer Facility.  
(Rotating heat transfer facility with cover removed).

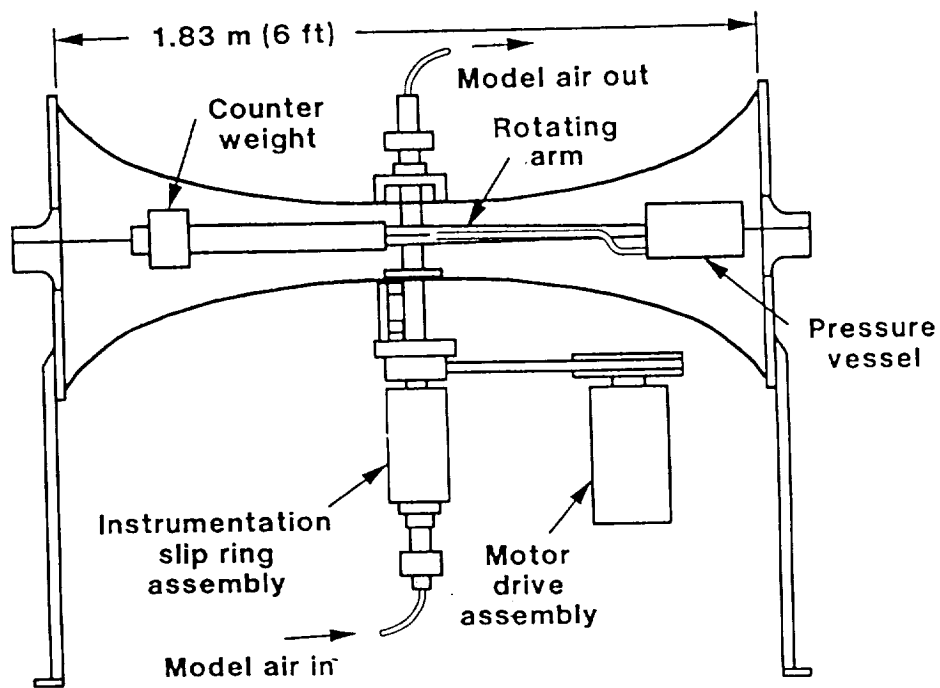


Figure 13.- Rotating Heat Transfer Facility.

### 3.2.1 Data Acquisition System

The data acquisition system contains two major components; the computer and the data acquisition control unit. The computer consists of a DEC PDP 11/03 processor unit with 128k memory, two 20cm (8 in.) floppy disk drives and a DECWRITER III terminal. The Hewlett Packard 3497A data acquisition system can be controlled from the front panel or through the interface connected to the computer. The model heater voltages are set manually and adjusted until the required wall surface temperatures are obtained. Upon completion of the acquisition of voltage data, results are calculated and printed in engineering units. Flow parameter and raw data are stored on disk for future reduction.

### 3.2.2 Heater Power Source

The power supply system provides DC power for the thin film foil resistance heaters used to heat the model test section elements. There are 72 individually controlled power supplies which are rated for 50 watts of power with a maximum current draw of one amp. Individual units can be arranged in parallel as needed to supply additional power. Heater supply voltage and the voltage across precision current measurement resistors are measured by the data acquisition unit.

### 3.2.3 Flow Monitoring System

Model coolant air is supplied by the UTRC 27 atm (400 psig) air system which is regulated to approximately 10 atm (150 psig) at the RHTF. The air flow rate is measured with variable area flow meters. The model coolant return air flows through an additional flow meter to determine a mass flow balance on the system. Model pressure is controlled by back pressuring the model air flow system with the return air control valve. The maximum mass flow rate available is dependent on the model operating pressure and the total pressure loss of the system including the heat transfer model. For typical models the maximum air flow rate is approximately 0.02 kg/sec. (0.044 lbm/sec)

## 3.3 Experimental Procedures

Heat transfer characteristics was determined from a heat balance on each heated test surface. The heat added to the coolant by convection was determined from the electrical power used to heat each test surface and the heat conducted from the test surface to the support structure. Heater supply power for individual model segments was determined by multiplying the calculated voltage across each of the microfoil heater leads and the current determined from the voltage measured across precision 0.1 ohm resistors. The voltage across the microfoil heater leads was determined by accounting for the voltage drop across the heater supply leads. The net heat flux (convected heat flux), assuming negligible radiation energy transfer, was determined by subtracting the conducted backloss from the heater power input.

The conduction loss parameter for each heated segment was determined by uniformly heating the model segments with no coolant flow to a steady state condition and measuring the voltage and current required to calculate heater power and all the model temperatures. For this condition, the convected heat flux is zero and the total heater power is backloss. The conduction backloss parameter is calculated by dividing this heater power by the temperature difference of the heated segments and the support frame. The bulk temperature used to calculate heat transfer coefficients was determined with a thermodynamic energy balance through each discrete system of heated segments. Rotating heat transfer results were normalized with the nonrotating values.

Electronic noise in the data signals of the RHTF was present only when the shaft was rotating. The probable sources for this electronic noise were (1) rotating instrumentation leads through magnetic flux lines generated by the DC motor, (2) motor power controller noise and (3) induced alternating currents through the lead and slipring instrumentation system generating fluctuating voltages. The voltage data used in the data reduction program was obtained by averaging ten successive voltage measurements of each data channel. Repeatability of the measurements indicated the calculated mean temperature was consistently within  $0.2^{\circ}\text{C}$  ( $0.36^{\circ}\text{F}$ ) of the mean temperature. An error analysis of the data reduction equations showed that approximately  $3/4$  of the estimated error in calculating heat transfer coefficient was due to the error in the temperature measurement. Estimates in the error in calculating heat transfer coefficient typically varied from approximately  $\pm 2\%$  at the inlet to  $\pm 10\%$  at the exit of the heat transfer model.

#### 4.0 EXPERIMENTAL PARAMETERS AND TEST MATRIX

The present study of heat transfer from a serpentine, square-passage, smooth wall model for a variety of stationary and rotating flow conditions provided results that can be used to model a variety of geometric locations in the internal cooling passages of a gas turbine blade. This study comprised (i) experiments originally proposed under the present contract (Tests Nos. 1-13), (ii) supplementary experiments performed under United Technologies Corporation (P&W and UTRC) independent research program (Test Nos. 101 - 117) and (iii) supplementary experiments performed under redirected effort on the present contract (Test Nos. 118-126). The test conditions for these experiments are shown on Tables I, II, and III.

A dimensional analysis study performed at UTRC prior to the onset of the present study (Suo, 1980), similar to that of Guidez (1988), showed that the flow patterns and hence convective heat transfer would be influenced by four nondimensional flow parameters and several geometric parameters. The nondimensional flow parameters are as follows:

Reynold number -  $\rho V d / \mu$   
Rotation Number -  $\Omega d / V$   
Density ratio -  $(\rho_b - \rho_w) / \rho_b = (T_w - T_b) / T_w$   
Buoyancy Parameter  $[(\rho_b - \rho_w) / \rho_b](\Omega R / V)[\Omega d / V]$

For flow in rotating radial coolant passages, Coriolis forces, represented by the nondimensional parameter,  $\Omega d / V$ , and the nondimensional streamwise velocity gradients, produce secondary flows in the plane perpendicular to the radial direction. These secondary flows are produced by the viscous force/Coriolis force interaction. Buoyancy also produces secondary flows in the radial direction. For flow in rotating radial coolant passages with walls hotter than the bulk fluid, the buoyancy effects always tend to drive the heated flow inward. Thus the buoyancy flow direction is opposite the mean velocity direction for flow radially outward and is in the same direction for flow radially inward. From previous studies, both the Coriolis and buoyancy forces can be expected to produce significant changes to the coolant passage flow field and hence heat transfer. Rotating constant-temperature flow studies by Johnston et al, (1972) have shown that the Coriolis forces can dampen turbulent fluctuations and laminarize flow in portions of a channel. Combined free and forced convection studies in stationary systems have shown that the turbulent shear structure and heat transfer is significantly altered with co-flowing or counter-flowing buoyancy effects (Eckert et al, 1953 and Metais and Eckert, 1964). The results from the present experimental study show regions where the viscous, Coriolis or buoyancy forces dominate the flow field and regions where the interactions between the forces are strong. The geometric parameters are as follows:

Axial location -  $X/d$   
Radial location -  $R/d$   
Flow direction - inward, outward  
Passage orientation -  $\alpha$



TABLE I  
TEST CONDITIONS FOR ROTATING HEAT TRANSFER EXPERIMENTS WITH SMOOTH WALL MODEL  
Contract NAS3-23691

Test UTRC No. Run		Dimensional Parameters			Basic Dimensionless Parameters				Secondary Dimensionless Parameters			Comments		
		$\frac{P}{N/m^2 \times 10^{-6}}$ (psi)	$\Omega$ rpm	$\dot{m}$ Kg/sec (lb/sec)	$\Delta T$ °C (°F)	$\bar{R}$ cm (in)	$\alpha$ deg.	Re	$Ro$ $\left(\frac{\Delta T}{T_{in}}\right)$	$\frac{\bar{R}}{d}$	$\left(\frac{\Delta \rho}{\rho}\right)$	$\left(\frac{\Omega R}{v}\right) Gr/Re^2$	$Gr \times 10^{-8}$	
1	49.9	1.017 (147.5)	0	0.0059 (0.013)	44.4 (80)	63.5 (25)	0	25,092	0	0.13	49	0	0	Nonrotating
2	14.10	1.010 (146.5)	0	0.0032 (0.007)	42.8 (77)	63.5 (25)	0	12,490	0	0.13	49	0	0	
3	15.11	1.010 (146.5)	0	0.018 (0.026)	43.3 (78)	63.5 (25)	0	49,985	0	0.13	49	0	0	
4	22.12	1.024 (148.5)	550	0.0059 (0.13)	44.4 (80)	63.5 (25)	0	25,221	0.238	0.13	49	1.29	0.22	1.96 Baseline
5	20.13	1.015 (147.2)	275	0.0032 (0.0007)	45.0 (81)	63.5 (25)	0	12,591	0.227	0.13	49	1.18	0.19	0.43 Re Varied
6	37.8	1.014 (147.0)	1100	0.0118 (0.026)	45.0 (81)	63.5 (25)	0	49,627	0.253	0.13	49	1.41	0.25	8.81
7	33.7	1.026 (148.8)	1100	0.0059 (0.013)	44.4 (80)	63.5 (25)	0	24,475	0.475	0.13	49	2.46	0.82	7.33 Ro Varied
8	19.12	1.013 (146.9)	275	0.0059 (0.013)	45.0 (81)	63.5 (25)	0	24,812	0.118	0.13	49	0.64	0.05	0.46
9	23.10	1.026 (148.8)	550	0.0059 (0.013)	22.2 (40)	63.5 (25)	0	25,299	0.244	0.07	49	0.72	0.72	1.13 $\Delta T/T$ Varied
10	24.9	1.025 (148.7)	550	0.0059 (0.013)	67.2 (121)	63.5 (25)	0	25,117	0.237	0.18	49	1.82	0.30	2.73

NOTES:  $Re = \bar{\rho} v d / \mu$   $Gr/Re^2 = (\Delta \rho / \rho) (\Omega R / v) (\Omega d / v)$   
 $Ro = \Omega d / v$   $Gr = (\Delta \rho / \rho) (\Omega R / v) (\Omega d / v) (\rho v d / \mu)^2$

TABLE II  
SUPPLEMENTARY TEST CONDITIONS FOR ROTATING HEAT TRANSFER EXPERIMENTS WITH SMOOTH WALL MODEL  
PW/UTRC - Internal Research

Test No	UTRC Run No.	Dimensional Parameters				Basic Dimensionless Parameters				Secondary Dimensionless Parameters			Comments
		P N/m <sup>2</sup> x 10 <sup>-6</sup> (psi)	$\Omega$ rpm	$\dot{m}$ Kg/sec (lb/sec)	$\Delta T$ °C (°F)	$\bar{R}$ cm (in)	$\alpha$ deg.	Re	Ro $\left(\frac{\Delta T}{T}\right)_{in}$	$\frac{\bar{R}}{d} \left(\frac{\Delta P}{P}\right) \left(\frac{\Omega R}{v}\right)$	Gr/Re <sup>2</sup>	Gr x 10 <sup>-8</sup>	
101	17.9	1.023 (148.3)	15	0.0059 (0.013)	44.4 (80)	63.5 (25)	0	25,035	0.006	0.13	0.04	0.00	Low Ro effects on leading wall
102	24.15	1.025 (148.7)	550	0.0059 (0.013)	88.9 (160)	63.5 (25)	0	24,242	0.233	0.22	2.22	0.36	Additional point at max $\Delta T$
103	44.8	0.998 (144.7)	825	0.181 (0.040)	45.0 (81)	63.5 (25)	0	75,295	0.116	0.13	0.64	0.05	Effect of Re at Ro = 0.12
104	39.6	1.007 (146.1)	550	0.0118 (0.026)	44.4 (80)	63.5 (25)	0	50,033	0.119	0.13	0.66	0.06	1.98
105	41.8	1.023 (148.3)	825	0.0059 (0.013)	22.2 (40)	63.5 (25)	0	25,166	0.362	0.07	1.04	0.28	Effect of $\Delta T$ at Ro = 0.35
106	42.10	1.019 (147.8)	825	0.0059 (0.013)	45.0 (81)	63.5 (25)	0	24,730	0.350	0.13	1.84	0.45	4.22
107	43.8	1.025 (148.7)	825	0.0059 (0.013)	67.2 (121)	63.5 (25)	0	24,914	0.350	0.18	2.61	0.64	5.70
108	45.7	1.022 (148.2)	-15	0.0059 (0.013)	44.4 (80)	63.5 (25)	0	25,039	-0.006	0.13	-0.04	0.0	Symmetry check
109	46.7	1.021 (148.1)	-550	0.0059 (0.013)	44.4 (80)	63.5 (25)	0	24,955	-0.233	0.13	-1.23	0.20	1.79
110	50.8	1.018 (147.6)	0	0.0059 (0.013)	22.2 (40)	63.5 (25)	0	25,098	0.000	0.07	0.00	0.00	Effect of $\Delta T$ at Ro = 0.0

NOTES:  $Re = \rho V d / \mu$   $Gr/Re^2 = (\Delta P / \rho) (\Omega R / V) (\Omega d / V)$   
 $Ro = \Omega d / V$   $Gr = (\Delta P / \rho) (\Omega R / V) (\Omega d / V) (\rho V d / \mu)^2$

TABLE II - (Continued)  
SUPPLEMENTARY TEST CONDITIONS FOR ROTATING HEAT TRANSFER EXPERIMENTS WITH SMOOTH WALL MODEL  
PW/UTRC - Internal Research

Test No	UTRC Run No.	Dimensional Parameters				Basic Dimensionless Parameters			Secondary Dimensionless Parameters			Comments		
		P N/m <sup>2</sup> x10 <sup>-6</sup> (psi)	Ω rpm	$\dot{m}$ Kg/sec (lb/sec)	ΔT °C (°F)	$\bar{R}$ cm (in)	α deg.	Re	Ro	$\left(\frac{\Delta T}{T}\right)_{in}$	$\frac{\bar{R}}{d}\left(\frac{\Delta P}{\rho}\right)\left(\frac{\Omega R}{v}\right)$		Gr/Re <sup>2</sup>	Grx10 <sup>-8</sup>
111	51.8	1.015 (147.2)	0	0.0059 (0.013)	66.7 (120)	63.5 (25)	0	25,098	0.000	0.18	49	0.00	0.00	
112	52.6	1.015 (147.2)	0	0.0059 (0.013)	88.9 (160)	63.5 (25)	0	25,082	0.000	0.23	49	0.00	0.00	
113	59.8	1.017 (147.5)	412	0.0059 (0.013)	86.7 (120)	63.5 (25)	0	25,076	0.178	0.18	49	1.38	0.17	1.55 Effect of ΔT at Ro = 0.18
114	58.8	1.017 (147.5)	412	0.0059 (0.013)	45.0 (81)	63.5 (25)	0	24,840	0.178	0.13	49	0.97	0.12	1.06
115	57.6	1.020 (148.0)	412	0.0059 (0.013)	22.8 (41)	63.5 (25)	0	25,131	0.183	0.07	49	0.54	0.07	0.63
116	60.7	1.017 (147.5)	412	0.0059 (0.013)	89.4 (161)	63.5 (25)	0	25,021	0.171	0.23	49	1.66	0.20	0.18 Effect of Ro
117	54.8	1.016 (147.3)	145	0.0059 (0.013)	44.4 (80)	63.5 (25)	0	25,018	0.062	0.13	49	0.34	0.01	0.13

NOTES:  $Re = \rho V d / \mu$   $Gr/Re^2 = (\Delta P / \rho) (\Omega R / V) (\Omega d / V)$   
 $Ro = \Omega d / V$   $Gr = (\Delta P / \rho) (\Omega R / V) (\Omega d / V) (\rho V d / \mu)^2$

TABLE III  
TEST CONDITIONS FOR HEAT TRANSFER EXPERIMENTS WITH SMOOTH WALL MODEL  
Contract NAS3-23691 AND PW/UTRC INTERNAL RESEARCH

Test No.	UTRC Run No.	Dimensional Parameters				Basic Dimensionless Parameters			Secondary Dimensionless Parameters			Comments			
		$P$ $N/m^2 \times 10^{-6}$ (psi)	$\Omega$ rpm	$\dot{m}$ Kg/sec (lb/sec)	$\Delta T$ °C (°F)	$R$ cm (in)	$\alpha$ deg.	Re	$Ro \left( \frac{\Delta I}{T} \right)_{in}$	$\frac{R}{d} \left( \frac{\Delta P}{\rho} \right) \left( \frac{\Omega R}{v} \right) Gr/Re^2$	$Gr \times 10^{-8}$				
12	67.8	1.015 (147.2)	550	0.0059 (0.013)	44.4 (80)	63.5 (25)	45	24,805	0.243	0.13	49	1.32	0.22	1.98	Effect of $\alpha$ varying $\Delta T$ and Ro at Re = 25,000
118	68.5	1.016 (147.4)	550	0.0059 (0.013)	66.7 (120)	63.5 (25)	45	24,627	0.234	0.18	49	1.77	0.29	2.52	
119	71.9	1.016 (147.4)	825	0.0059 (0.013)	44.4 (80)	63.5 (25)	45	24,670	0.341	0.12	49	1.76	0.42	3.66	
120	72.72	1.016 (147.4)	825	0.0063 (0.014)	66.7 (120)	63.5 (25)	45	24,606	0.323	0.17	49	2.28	0.51	4.48	
121	64.10	1.016 (147.4)	412	0.0059 (0.013)	44.4 (80)	63.5 (25)	45	24,778	0.176	0.13	49	0.94	0.12	1.02	
122	65.6	1.016 (147.4)	412	0.0063 (0.014)	66.7 (120)	63.5 (25)	45	24,745	0.169	0.18	49	1.26	0.15	1.30	
13	73.9	1.016 (147.4)	-550	0.0059 (0.013)	44.4 (80)	63.5 (25)	45	24,818	-0.230	0.13	49	-1.20	0.19	1.71	Reversal of Rotation Direction for $\alpha$ Change
123	74.7	1.016 (147.4)	-550	0.0063 (0.014)	66.7 (120)	63.5 (25)	45	24,907	-0.219	0.17	49	-1.60	0.24	2.18	
11	76.9	1.014 (147.1)	550	0.0059 (0.013)	44.4 (80)	43.2 (17)	0	24,863	0.24	0.13	33	0.87	0.15	1.31	Radius Change Effects on Centrifugal Buoyancy Parameter $Gr/Re^2$
124	77.6	1.015 (147.2)	550	0.0063 (0.014)	91.1 (164)	43.2 (17)	0	24,858	0.22	0.23	33	1.42	0.24	1.99	
125	82.9	1.016 (147.3)	825	0.0059 (0.013)	45.0 (81)	43.2 (17)	0	24,774	0.35	0.12	33	1.19	0.31	2.57	
126	83.8	1.016 (147.3)	825	0.0063 (0.014)	88.9 (160)	43.2 (17)	0	24,886	0.33	0.22	33	2.02	0.47	4.18	

NOTES:  $Re = \rho v d / \mu$      $Gr/Re^2 = (\Delta \rho / \rho) (\Omega R / v) (\Omega d / v)$   
 $Ro = \Omega d / v$      $Gr = (\Delta \rho / \rho) (\Omega R / v) (\Omega d / v) (\rho v d / \mu)^2$

Entrance effects ( $X/d$ ) are expected to be significant in each of the three legs as the flow develops downstream of the inlet and downstream of the turns. The radial location ( $R/d$ ) of the model was varied to isolate the effects of the rotation and the buoyancy rotation parameters. The passage orientation was varied to determine effects of coolant passage orientation at the leading and trailing regions of the blade, as well as the effects of the secondary flow interactions caused by the turns.

The variation of Reynolds number, rotation number and inlet wall to bulk temperature difference which produced the parametric study is shown in Figure 14. The standard flow condition used in the study was that for test No. 4:  $Re = 25,000$ ,  $Ro = \Omega d/V = 0.24$ ,  $\Delta T_{in} = 44.4^\circ C$  ( $80^\circ F$ ),  $R/d = 49$  and  $\alpha = 0$ . The original plan was to vary parameters only about the standard flow condition, varying only one parameter at a time. However at the completion of the original test plan, it became apparent that the heat transfer relationships were complex and that the viscous, Coriolis and buoyancy forces each dominated the flow field for various combinations of the test conditions.

The results obtained show first order effects for the following parameters:

1. Streamwise location - The range of  $X/d$  in each straight passage varies from 0 up to 12.4 and for most of the passage length, the results are in the developing flow region for constant wall temperature conditions. However, for the nonrotating test conditions the results approach fully developed flow levels at the end of each passage.
2. Reynolds number - The Reynolds number was varied from 12,500 to 50,000 for the stationary experiments and from 12,500 to 75,000 for the rotating experiments.
3. Rotation Number - The rotation number  $\Omega d/V$ , (the inverse of the Rossby number) and the streamwise velocity gradients are the primary nondimensional factors governing secondary flow in the plane perpendicular to the centerline of rotating radial ducts.
4. Density ratio - The density ratio,  $(\rho_b - \rho_w)/\rho_b$ , is one of the basic nondimensional parameters obtained from several previous dimensional analysis of flow in a rotating radial duct. The product of the density ratio  $(\rho_b - \rho_w)/\rho_b$  and a gravitational parameter,  $(\Omega d/V)^2(R/d)$ , cause secondary flow in the radial direction. For this study with heated walls and for the gas turbine blades, the buoyancy effect is always radially inward whether the flow direction is radially inward or outward. Note:  $(\rho_b - \rho_w)/\rho_b = (T_w - T_b)/T_w$ ,  $(\Delta\rho/\rho)_{in} = (\Delta T/T)_{in}$ .
5. Radius ratio - The ratio,  $R/d$ , was also obtained from several dimensional analysis and is related to buoyancy effects. An alternative nondimensional parameter could be used as the fifth basic parameter, as discussed in a subsequent paragraph. However, the  $R/d$  parameter is readily recognized by the designer and researcher alike.

$$\alpha = 0 \text{ (STD)}$$

$$\bar{R}/d = 49 \text{ (STD)}$$

NOTE: STD. BASELINE FLOW CONDITIONS

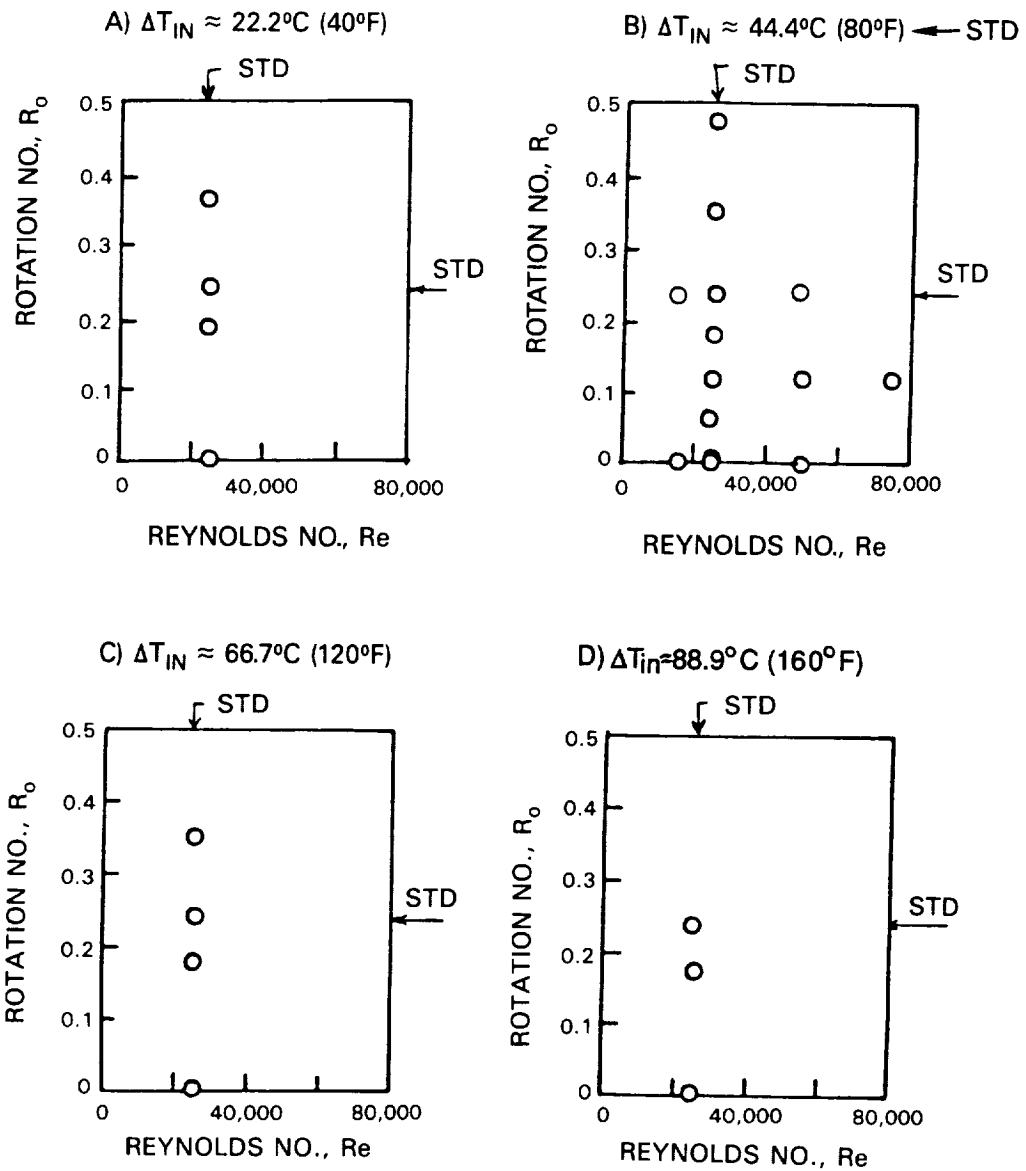


Figure 14.- Test Conditions for Parametric Rotating Heat Transfer Study.

6. Passage orientation - The serpentine model was constructed such that the plane, which contains the centerlines of all four passages, could be rotated about a radial axis through the geometric centerline of all four evenly-spaced passages. For  $\alpha = 0^\circ$ , extensions of the centerlines of all four passages would pass through the axis of rotation as shown in Figure 9. One side of the square passage becomes the leading side, i.e.  $\square \uparrow$ . For  $\alpha = 45^\circ$ , each test section passage has two leading and two trailing sides, i.e.  $\diamond \uparrow$ .
7. Flow Direction - The direction of the flow causes the buoyancy, viscous and Coriolis forces to interact in a complex manner. Previous investigators conducting free and forced convection experiments in stationary tests have attributed the differences in heat transfer between flow upward and downward to changes in the turbulent structure of the flow.

A total of thirty-nine tests were conducted with the smooth wall model as shown in Tables I, II, and III (Repeat runs were also obtained under the same test number). In order to make the presentation of the principle results for this program tractable and discernible to the reader, the heat transfer data is presented in several stages.

- 1) The heat transfer results are presented as a variation of the basic parameters about a standard flow condition for selected streamwise locations. The stationary heat transfer results is presented in Section 5.0 with the variation of Reynolds number and density ratio about the standard stationary flow condition (Test 1). The rotating heat transfer results will be presented in Section 6 with the variation of rotation parameter, density ratio, Reynolds number, model radius and model orientation angle about the standard rotating flow conditions (Test 4).
- 2) The results in Section 7.0 is presented as a function of two basic or secondary nondimensional parameters for all the data with  $\alpha = 0^\circ$ . This presentation will be used to discern the complex heat transfer relationships that occurs for various geometrical locations over a wide range of flow conditions. The range of nondimensional flow conditions for which data was obtained in this study with one model geometry encompasses the range of nondimensional flow conditions in present and future small and large aircraft gas turbines.
- 3) Heat transfer correlations based on the results of this experimental program and suitable for use by gas turbine designers are presented in Section 8.0.
- 4) The results from the present program are compared in Section 8.3 with results from previously published rotating heat transfer experiments and with results from stationary combined free and forced convection heat transfer experiments.

## 5.0 STATIONARY HEAT TRANSFER RESULTS

### 5.1 Baseline Flow Condition

The baseline flow condition for the stationary heat transfer experiments is test number 1A. Test 1A was conducted after two-thirds of the rotating test program was conducted and after the heat transfer segments had "set" due to rotation. Examination of the smooth wall model after the conclusion of all the heat transfer experiments showed no perceivable changes from the "before" condition. Test 1A was used as the basis for comparison for all the rotating tests as well as the stationary tests.

The variation of Nusselt number,  $Nu = hd/k$ , with streamwise location for test 1A is shown in Figure 15. The Nusselt number for a fully developed flow in a constant-wall-temperature, square duct is shown for comparison. Note that the heat transfer rate on all four walls decreases by a factor of 1.5 from the first to the third heat transfer segment in each straight segment. Nusselt numbers for most of the third segments in each straight passage i.e., Segments D, I & N, approach the Nusselt number for fully developed flow previously obtained in square ducts.

The heat transfer increases significantly in the turn sections, as expected. The heat transfer on the leading and trailing turn surfaces increases a factor of approximately two greater than the smooth duct value. The heat transfer rate is approximately 10% greater in the second half of the turn compared to the first half. The heat transfer on the side wall surfaces is more complex. The first half of side walls E, J and P are continuations of the straight section side walls. The second half of side walls E, J and P and the first half of side walls F, K and R are perpendicular to the straight segments. The turbulence level of the flow adjacent to these surfaces and the heat transfer rate are both expected to be higher than the fully developed flow. The second half of segments F, K and R are extensions of the straight passage walls. The heat transfer on these segments is high but somewhat inconsistent from turn to turn.

The conclusion from the results of Test 1A is that the heat transfer characteristic for this smooth wall model are reasonably well behaved. The heat transfer rates on each of the four walls at each location in the straight segments are generally within 10 percent of the average. The exception is for streamwise location D, where the outside sidewall (test surface 4) increases, possibly due to acceleration effects from the turn and/or separation of the flow from adjacent surfaces.

The heat transfer results for the first two straight sections are represented in Figure 16 as the ratio of local Nusselt number to the Nusselt number for fully developed flow in a square duct with the same hydraulic diameter and the same level Reynolds Number. This heat transfer ratio,  $Nu/Nu_{fd}$  will be used in all succeeding comparisons. Present data are compared with previous results from entrance region heat transfer analysis and experiments in Bergles and Webb (1970). The results from the present experiment lie in the range of previous results. Note that the results for the first straight passage lie in the top range of the previous results, whereas, those from the second straight passage lie in the center to lower range of previous results. The conclusion from this comparison of the present results with limited results from previous experiments is that the present data generally falls in the expected range.



# TEST 1A

$$Re \approx 25,000 \quad \left(\frac{\Delta T}{T}\right)_{in} = 0.13$$

$$Ro = 0 \quad \bar{R}/d = 49$$

$$RPM = 0 \quad \alpha = 0$$

$$\Delta T = 44.4^\circ C (80^\circ F)$$

SYMBOL	□	△	◇	×
LOCATION, + Ω	SIDE	SIDE	LEADING	TRAILING
SURFACE NOS.	1-18	19-32	33-48	49-64

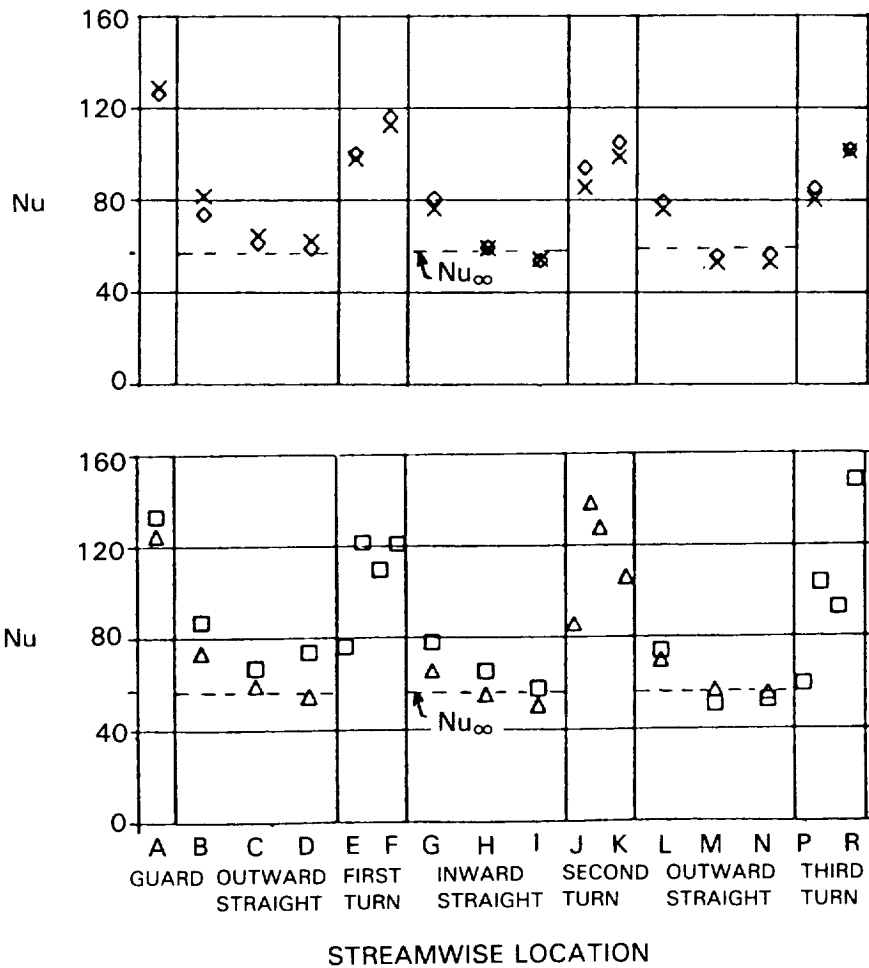


Figure 15.- Heat Transfer Results for Stationary Baseline Flow Conditions.

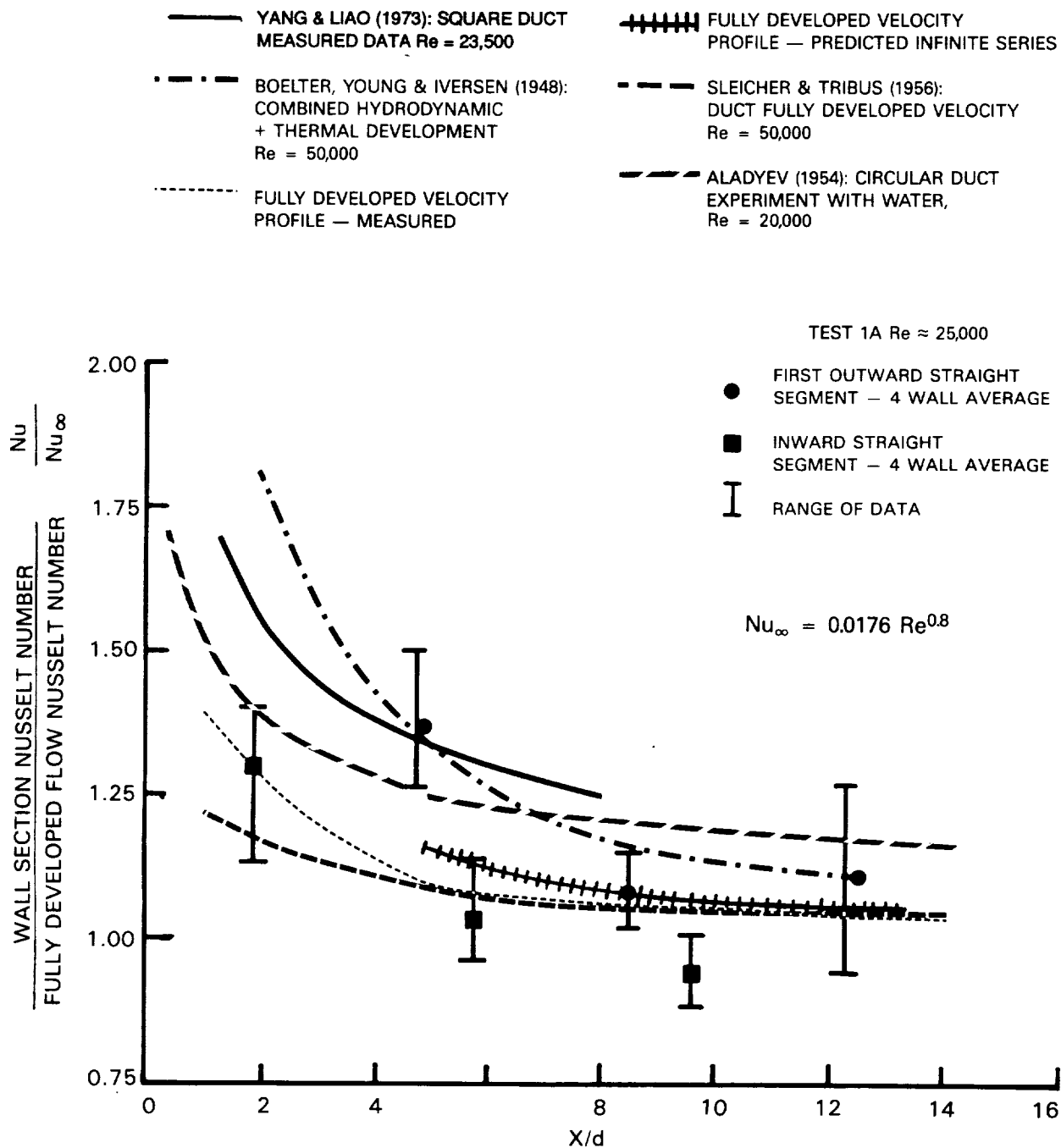


Figure 16.— Comparison of Heat Transfer in Straight Segments for Test Condition Number 1A With Previous Heat Transfer Results for Entrance Regions.

## 5.2 Effect of Density Ratio

The effect of density differences between the wall and bulk temperature on the heat transfer ratio is shown in Figure 17. Results are presented for the baseline flow condition (Test 1A) with a wall to inlet bulk temperature difference of 43.9°C (79°F) and for temperature differences of 22.2°C, 66.7°C, and 88.8°C (40°F, 120°F and 160°F). The heat transfer ratios are essentially the same for all four temperature differences at each heat transfer segment. The fully developed Nusselt number used for comparison was calculated at each segment using the local film temperature, i.e. the average of the bulk and wall temperature for the determination of the transport properties ( $\mu$  and  $k$ ) used in the correlation. The major conclusion from these experiments with various wall to bulk temperature differences is that the use of the film temperature for the determination of transport property values causes the heat transfer ratio results to be independent of temperature differences for this range. This conclusion is compatible with general heat transfer practice when the heat transfer is dominated by forced convection.

## 5.3 Effect of Reynolds Number

The heat transfer ratio distribution for three Reynolds numbers is shown in Figure 18. The heat transfer ratio at each streamwise location in the straight sections is generally independent of Reynolds number. The small variations with Reynolds number at streamwise locations A and B may be due to weak variations in the entrance region length with Reynolds number. However, the variations are of the same order as the experimental uncertainty. The heat transfer in the turns shows generally higher heat transfer ratios at the lowest Reynolds number and may indicate that the exponent "N" for a  $Nu \propto Re^N$  relationship in the turns is less than the value 0.8 used for the Nu correlation. The conclusion from these experiments with Reynolds numbers equal, above and below the stationary baseline flow condition is that the heat transfer ratio for stationary conditions is generally independent of Reynolds number and primarily a function of geometric location.

## 5.4 Concluding Remarks

The heat transfer characteristics of the smooth wall, serpentine heat transfer model are generally well behaved and in agreement with previous experiments and heat transfer practice. The heat transfer results in each straight passage show entrance region effects and are approximately equal on all four sides. The heat transfer ratio distribution is independent of bulk-to-wall temperature differences when the film temperature is used to determine the transport properties. The heat transfer ratio for each segment is a weak function of Reynolds number. Most of the differences between the results at various Reynolds numbers was within the expected accuracy for these heat transfer experiments.

$Re \approx 25000$

$Ro = 0$

$RPM = 0$

$R/d = 49$

$\alpha = 0$

SYMBOL	TEST NO.	$\Delta T$ °C (°F)	$\left(\frac{\Delta T}{T}\right)_{in}$
□	110	22.2 (40)	.07
●	1A	43.9 (79)	.13
△	111	66.7 (120)	.18
◇	112	88.9 (160)	.23

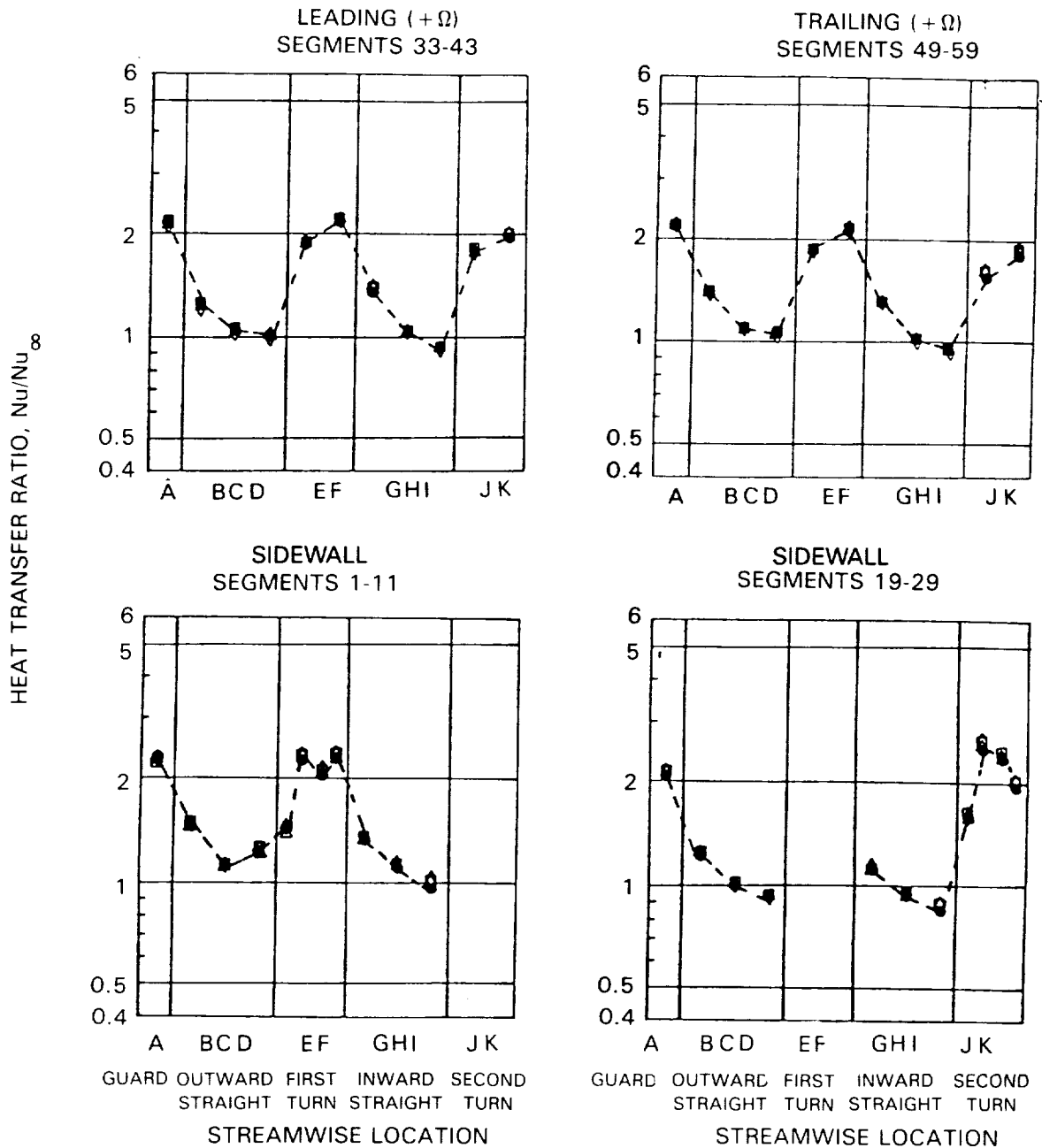


Figure 17.- Effect of Wall Temperature on Heat Transfer Ratio for Nonrotating Flow Conditions.

$$Ro = 0 \quad \Delta T \approx 44.4^\circ\text{C} (80^\circ\text{F})$$

$$\text{RPM} = 0 \quad \bar{R}/d = 49$$

$$\left(\frac{\Delta T}{T}\right)_{\text{in}} = 0.13 \quad \alpha = 0$$

SYMBOL	TEST NO.	Re
●	1	25,000
△	2	12,500
□	3	50,000

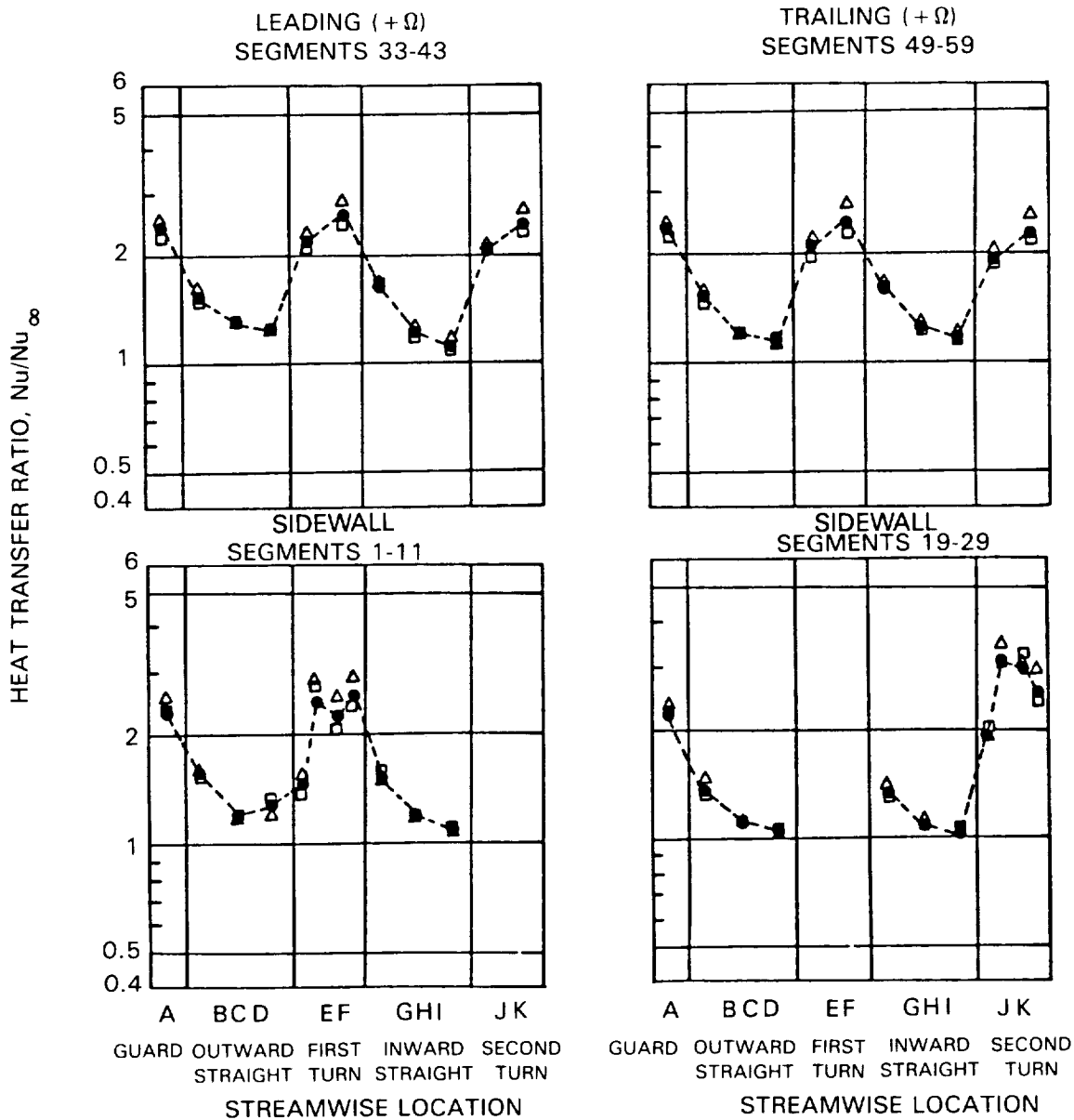


Figure 18.- Effect of Reynolds Number on Heat Transfer Ratio for Stationary Condition.

## 6.0 ROTATING HEAT TRANSFER RESULTS

### 6.1 Baseline Flow Condition

The baseline flow condition for the rotating experiments is test number 4. Test number 4 has a rotation number,  $\Omega d/V$ , equal 0.24, a temperature ratio,  $(\Delta T/T)_{in}$  equal to 0.13, and a Reynolds number equal to 25,000. The Reynolds number and the density ratio are the same as those for the stationary baseline flow condition. The rotation number and the ratio of buoyancy forces to viscous forces are in ranges where previous constant-temperature, rotating experiments (Moon, 1964 and Johnston, et al, 1972) and stationary combined free and forced convection experiments (Eckert, et al, 1953) have shown strong and moderate effects, respectively. These nondimensional test flow conditions are also in the central region of the nondimensional operating flow condition range for advanced aircraft gas turbines. In addition, the rotating baseline flow condition is in a region where the extrapolation of heat transfer correlations from previous rotating heat transfer experiments would predict large decreases in the heat transfer coefficient below fully developed turbulent rates (Morris, 1981). Therefore, at least modest variations in the heat transfer rate are expected to occur because of rotation.

The results for the Rotating Baseline Flow Condition will first be presented and compared with the results for the Stationary Baseline Flow Condition. In the following paragraphs, the effects of rotation and buoyancy will be related to previous rotating flow experiments with constant density fluids, and to stationary heat transfer experiments with free and forced convection effects. The author's conjectures will be identified as appropriate. The probable cause and effect relationships for the flow and heat transfer will be further discussed as the experimental results for variations in the rotation rate, density ratio, and radius ratio are presented.

The variations of heat transfer ratio with streamwise location are shown in Figure 19 for the rotating and stationary baseline flow conditions. The heat transfer ratio on the leading and trailing segments shows the largest variation from the stationary heat transfer values. In the outward straight passage (streamwise locations A to D), the heat transfer ratio decreases to about 40% of the stationary value on the leading segment at streamwise location C. For the same passage, the heat transfer ratio increases to more than 2.3 times the stationary value on the trailing segment at streamwise location D. On both sidewalls in the first outward straight passage, the heat transfer ratio increases with rotation, compared to the stationary heat transfer ratios.

The difference in heat transfer between the rotating and nonrotating flow conditions on the trailing and sidewall surfaces of the first radially outward flowing passage is attributed to both the increasing strength of the secondary flow cells associated with the Coriolis force and the buoyancy. The decrease in heat transfer near the inlet of the passage on the leading surfaces is attributed to the stabilizing of the near-wall flow, as observed by Johnston (1972). The subsequent increase in heat transfer near the end of the passage is postulated to occur when the secondary flow cells become more developed and interact with the buoyant, stabilized near-wall flow on the leading side of the passage. Further discussion of this interaction will be presented in subsequent sections.

$$Re \approx 25,000$$

$$\Delta T \approx 44.4^\circ\text{C} (80^\circ\text{F})$$

$$\left(\frac{\Delta T}{T}\right)_{in} = 0.13$$

$$\bar{R}/d = 49$$

$$\alpha = 0$$

SYMBOL	TEST NO.	Ro	$\Omega$ RPM
●	1A	0.000	0
■	4	0.238	550

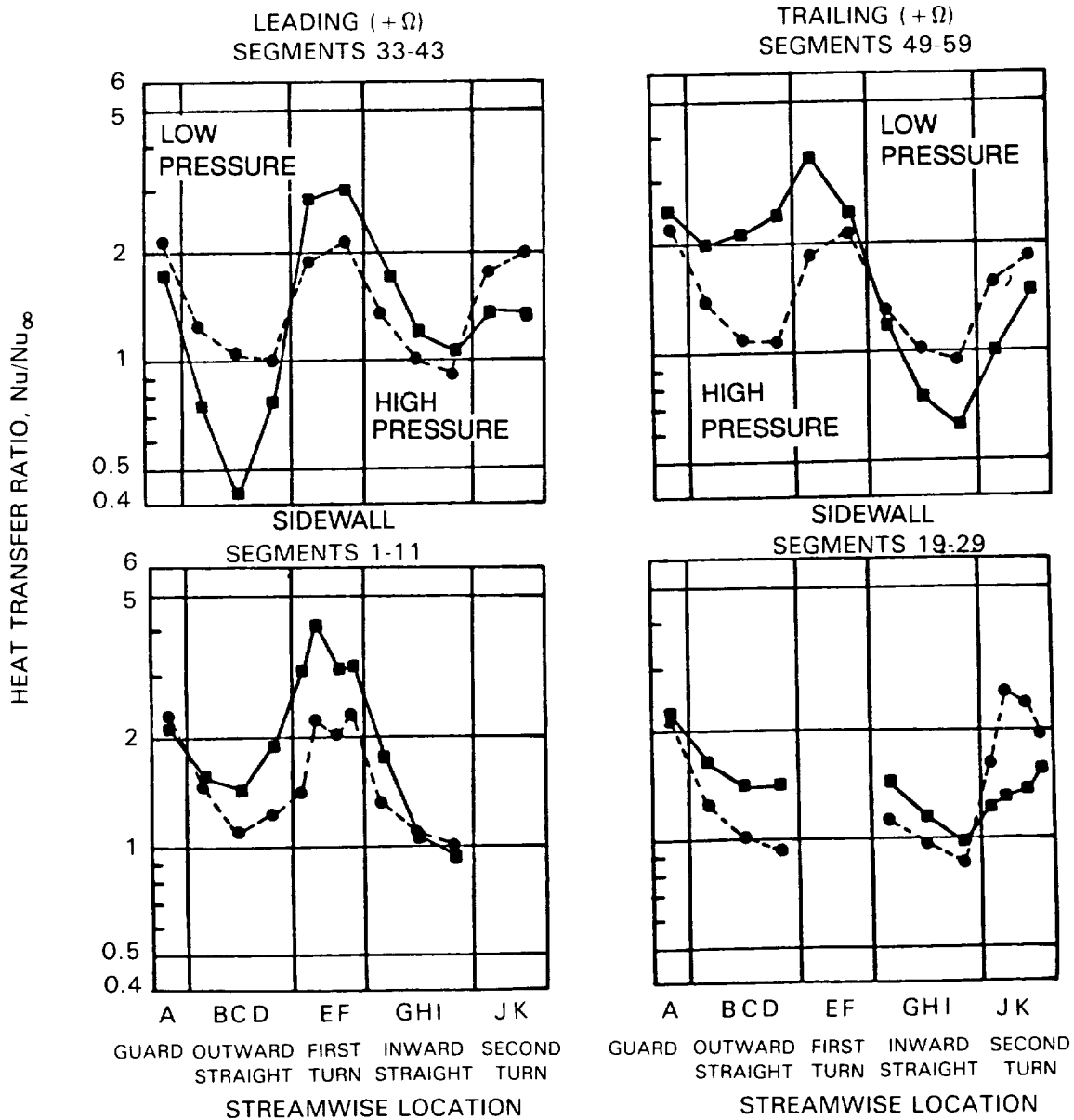


Figure 19.- Comparison of Heat Transfer Ratio for Rotating and Stationary Baseline Flow Conditions.

The effect of rotation on heat transfer in the inward straight passage (streamwise locations G to I), are also significant but less dramatic. The heat transfer ratio increases about 20% on the leading segments compared to the stationary results. The heat transfer on the trailing segments decreases from 5 to 30% of their stationary heat transfer rates. The heat transfer on the side walls for the inward straight passage is generally greater with rotation than for the stationary flow condition. The exception occurred for segments 10 and 11 at streamwise locations H and I where the heat transfer rates are 5 percent less than the stationary values.

The difference in heat transfer on the high pressure sides of the coolant passage (i.e. trailing surfaces of the first, outward flowing passage and leading surfaces of the second, inward flowing passage) is believed to be a result of the combined effects of the secondary flow induced by Coriolis forces and buoyancy driven secondary flow. When a counterflow situation exists (i.e. buoyancy driven flow in a direction opposite the mean flow direction as occurs for outward flow and heated walls), the combined effects of buoyant and Coriolis-driven secondary flows cause significant increases in the heat transfer coefficients. When a parallel flow situation exists (i.e. buoyancy driven flow in the same direction as the mean flow direction), the combined effects of rotation and buoyancy appear to counteract each other and only a modest (10 percent) increase in heat transfer occurs, compared to the stationary results. Further discussion of these effects will be presented in subsequent sections.

The heat transfer in the turn regions is also significantly increased and decreased by rotation. Note that the heat transfer ratios for the first outside turn (streamwise locations E and F) increases by 50% on all segments compared to the nonrotating values. The heat transfer rates for the second inside turn (streamwise locations J and K) decreases by an amount equal to 15 to 50% of the stationary value. Because the increased heat transfer on the outside turn and decreased heat transfer on the inside turn occurs on both the leading and trailing surfaces, these changes are more likely to be caused by buoyancy effects rather than by the conservation of vorticity through the turn. Note, however, that the heat transfer for the outside turn at streamwise location F is considerably greater for the leading segment than the trailing segment. These asymmetric differences in the heat transfer ratio are likely to be caused by the convection of the secondary flow (produced in the straight passages by Coriolis forces) around the 180° turn.

The conclusion from this comparison of the heat transfer ratios for the rotating and stationary flow conditions is that the effects of rotation on heat transfer in a radial passage are significant. The heat transfer rate decreased to less than half the stationary value on a leading wall segment, increased by a factor of two on a trailing wall segment, increased by as much as a factor of two on the outside turn and decreased by as much as 50% in the inside turn. The presentation of results at other rotating flow conditions, obtained by varying one of the four basic dimensionless parameters, will isolate the effects of each parameter. The effects of the rotation numbers, density ratio, Reynolds numbers and radius ratio will be discussed in the aforementioned order which is also the order of decreasing importance to heat transfer.



## 6.2 Effect of Rotation Number

The effect of rotation number,  $\Omega d/V$ , on heat transfer ratio is shown in Figure 20. All other flow conditions i.e.,  $\Delta T$ ,  $R/d$ ,  $Re$  and  $\alpha$ , are held constant at their baseline values. illustrative results are presented for 5 rotation rates including the stationary and rotating baseline flow conditions. Additional data are available at 15, 137 and 380 rpm. The effects of rotation on the heat transfer ratio are complex for some geometric regions and are monotonic in others.

### 6.2.1 High Pressure Surfaces

The most straightforward effect of rotation is observed on the trailing segments of the first outward straight passage (streamwise locations A to D). On these segments, the heat transfer ratio increases monotonically with rotation at all streamwise locations. Note that the largest relative increases occur at streamwise locations C and D for a rotation number change from 0 to 0.12. The largest absolute increase occurs at streamwise location B and C for a rotation number change from 0.24 to 0.35. Note that the heat transfer ratio increases by more than a factor of 3.5 at streamwise location C for rotation number of 0.48 compared to the zero rotation value. Smaller increases in the heat transfer ratio on the leading segments occurred for the inward flow straight passage (streamwise locations G, H and I).

The effects on heat transfer due to Coriolis generated secondary flows might be expected to be approximately the same for the trailing segments of the first passage and the leading segments of the second passage. The differences in heat transfer between the outward and inward flowing passages are therefore attributed to the different effects of buoyancy in the counter-flowing first passage (radially outward flow) and the co-flowing second passage (radially inward flow).

The lesser increases in the heat transfer ratio on the high pressure side of the second passage are attributed to the counteracting effects of rotation and parallel-flow, combined-free-and-forced convection in the passage. Previous authors have attributed the decreased heat transfer in stationary parallel-flow free-and-forced-convection experiments to a reduction in the generation of near-wall turbulence. In the first passage, the near-wall buoyancy driven flow was inward toward the axis of rotation and the coolant flow was outward. This counter flow situation generated additional near-wall turbulence due to the strong shear gradient. This increase in the shear forces combined with the cross stream secondary flows generated by Coriolis forces cause large increases in heat transfer in the first passage. However, when the flow and the buoyancy driven near-wall flows are coincident, as in the second passage, the generation of near-wall turbulence may be decreased because of the changes in the velocity profile. Therefore, the combined effects of the buoyant and the cross stream secondary flows in the second passage on the heat transfer are less. The magnitude of the buoyancy effect on the heat transfer is unclear in that the buoyancy effect in the second passage may be zero (which implies a modest Coriolis dominated heat transfer increase) or negative (which implies a larger Coriolis dominated heat transfer increase which is offset by a reduction due to buoyancy). The cause and effect relationships presented in this paragraph are the author's speculations, and will require further experimentation or calculations by direct numerical simulation in order to be substantiated or rejected.

# BASELINE TEMPERATURE RATIO, REYNOLDS NUMBER AND GEOMETRY

$Re \approx 25,000$      $\Delta T \approx 44.4^\circ C$  ( $80^\circ F$ )

$$\left(\frac{\Delta T}{T}\right)_{in} = 0.13 \quad \bar{R}/d = 49$$

$$\alpha = 0$$

SYMBOL	TEST NO	$\frac{\Omega d}{V}$	$\Omega$ (rpm)
●	1A	0.000	0
△	8	0.118	275
■	4	0.238	550
◇	106	0.350	825
▽	7	0.475	1100

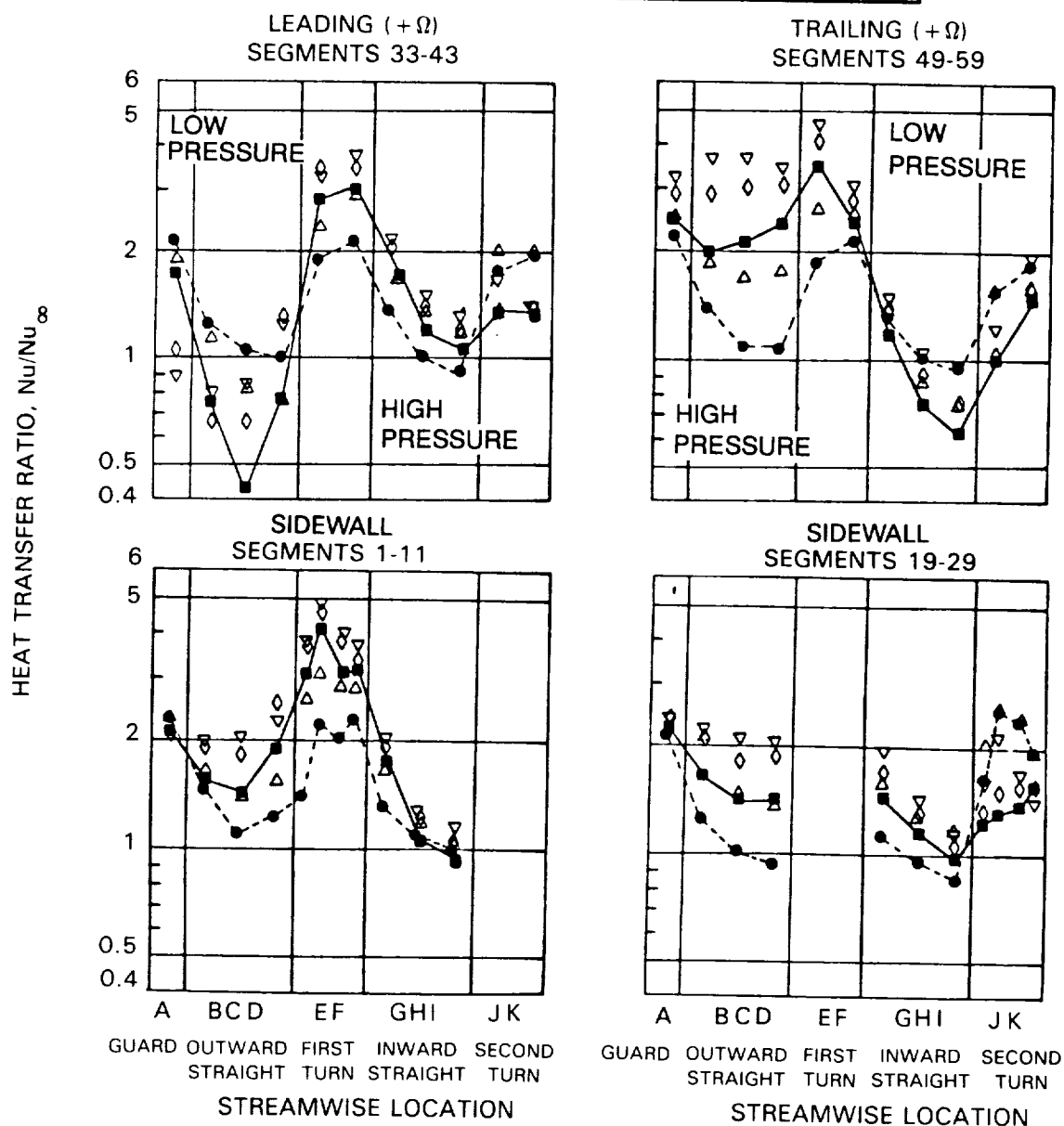


Figure 20.- Effects of Rotation Rate on Heat Transfer Ratio.

### 6.2.2 Low Pressure Surfaces

In contrast to the continual increase in heat transfer with increasing rotation number on the trailing side of the first passage, the heat transfer ratio decreases with increasing rotation number on the leading side of the passage near the inlet. For all of the remaining locations on the leading side of the passage, the heat transfer ratio decreases and then increases again with increasing rotation number. Heat transfer from the trailing, low pressure surfaces of the second passage also had large decreases in heat transfer. Heat transfer in the second passage decreased to almost 60% of the stationary heat transfer levels compared to 40% in the first passage. In the second passage, the heat transfer decreased and then subsequently increased again as the rotation rate was increased.

The decreases in the heat transfer ratio are attributed, for the most part, to the Coriolis generated cross stream flow patterns as well as the stabilization of the near-wall flow on the leading side of the first passage (Johnston et al., 1972). The cross stream flows cause heated, near-wall fluid from the trailing and sidewall surfaces to accumulate near the leading side of the coolant passage resulting in reduced heat transfer. In addition, the rotation stabilizes the shear layers along this wall and further reduces the turbulent transport of heat. The increase in the heat transfer ratio in the latter half of the coolant passage for the larger rotation numbers is attributed to increases in the buoyancy effects. These could include the formation of radial recirculation cells. Similar effects of rotation are noted for the low pressure surfaces in both the first and second passages, irrespective of flow direction. These results suggest that the heat transfer on low pressure surfaces is dominated by Coriolis generated cross stream flows which cause a stabilization of the near-wall flows and that the heat transfer on the high pressure surfaces is affected by a combination of Coriolis and buoyant effects. Therefore, it can be expected that the correlations of local heat transfer data may be substantially different depending on local flow conditions (i.e. due to differing near-wall shear gradients).

### 6.2.3 Side Walls

The effects of rotation on the heat transfer from the side walls in the straight passage are less than the leading and trailing segments. The general effect is that the side wall heat transfer increases with rotation. The increases in heat transfer ratio on the side wall segments (1-4 and 19-22) in the first passage with outward flow are approximately one-third the increases on the trailing segments (49-52). The increases on the side wall segments (9-11 and 23-25) in the second straight section with inward flow are equal or less than the increases on the leading segments (39-41).

### 6.2.4 Turns

The effect of rotation number on heat transfer from the outside turn (streamwise locations E and F) is monotonic for almost all points; the heat transfer ratio increases with rotation rate. The effect of rotation number on heat transfer ratio from the inside turn (streamwise locations J and K) is more complex. For the inside turn, the heat transfer decreases on the trailing

segments (58, 59) and side walls (26-29) as the rotation number is increased from 0 to 0.24 and then increases slightly as  $Ro$  is increased to 0.48. The heat transfer on the leading segments (42, 43) decreases from 0 to 20% as  $Ro$  is increased to 0.24 and then increases 30% as  $Ro$  is increased from 0.24 to 0.48.

Although the rotation number is a basic dimensionless parameter governing the flow in rotating passages, the variations of the rotation number in these heat transfer experiments also causes buoyancy effects. Therefore, no conclusions regarding the effects of rotation number alone can be deduced without the analysis of further experiments where the buoyancy effects are also fixed. The effects of rotation number are isolated in the analysis of results from a more complete set of flow conditions in Section 7.

### 6.3 Effect of Density Ratio

#### 6.3.1 Straight Sections

The effects of varying the density ratio (wall temperature) on the heat transfer ratio are shown in Figure 21. All flow conditions were held at the rotating baseline flow condition except the inlet density ratio ( $\Delta\rho/\rho$ ) in which was varied from 0.07 to 0.22. These sets of data were obtained at a constant rotation number and therefore conclusions can be obtained regarding the effects of buoyancy for flow conditions near the rotating baseline flow conditions.

For the trailing and side wall segments in both the outward and inward flow straight passages, increasing the density ratio (and hence buoyancy) increases the heat transfer ratio. This increase ranges from 10 to 50%, depending upon location.

Increasing the inlet density ratio (i.e. the wall-to-coolant temperature difference) from 0.07 to 0.22 causes the heat transfer ratio in the first passage to increase on the trailing surfaces by as much as 50% and on the leading surfaces by as much as 100%. The exception to the general increase in heat transfer with increasing density ratio occurred near the inlet of the first passage on the leading side, where the heat transfer ratio is observed to decrease slightly.

Heat transfer in the second, inward flowing passage also increases with increasing density ratio. In general, the increases in heat transfer in the second passage were approximately half of those in the first passage (on the order 10 to 50% compared to maximum relative increase of 100% in the first passage).

The differences in heat transfer behavior due to changes in the density ratio between the first and second passages are attributed to the differing mechanisms of Coriolis and buoyancy interaction. If the effect of Coriolis generated secondary flow on heat transfer is similar (regardless of flow direction) and the effect of increasing density ratio for fixed rotation number generally causes heat transfer to increase, then the interaction of the two effects is significant and also counteracting. The counteraction of the two effects was evident in the relatively small increases in heat transfer on the high pressure side of the second passage. The reason for this behavior is not known at this time.

BASELINE ROTATION NUMBER, REYNOLDS  
NUMBER AND GEOMETRY

$Re \approx 25,000$

$\bar{R}/d = 49$

$Ro \approx .24$

$\alpha = 0$

RPM = 550

SYMBOL	TEST NO.	$\Delta T$ °C (°F)	$(\Delta p / p)_{in}$
○	9	22.4 (40.4)	.07
■	4	44.7 (80.4)	.13
△	10	67.1 (120.7)	.18
◇	102	89.1 (160.4)	.22

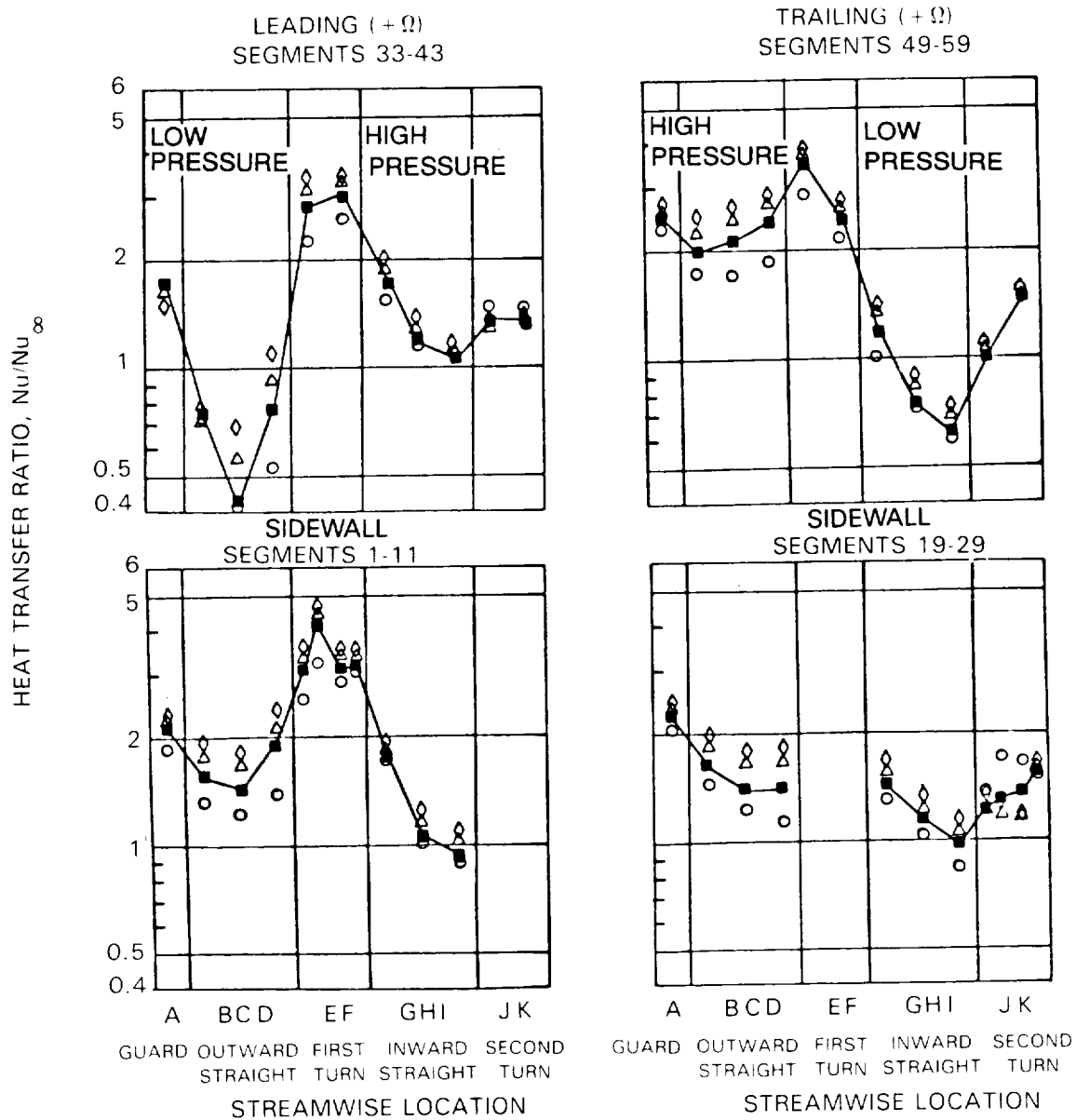


Figure 21.— Effects of Density (Temperature) Ratio on Heat Transfer Ratio.

### 6.3.2 Turns

The variation of the heat transfer ratio with increasing density ratio was monotonic in both the outside and inside turns. Increasing the density ratio (wall-to-bulk temperature difference) causes the heat transfer from all surfaces on the outside turn (locations E and F) walls to increase. However, increasing the density ratio causes the heat transfer from all surfaces on the inside turn (locations J and K) to decrease. Because the heat transfer on the leading and trailing sides of the turns (for both the first and second turns) is not equal, and because increasing the density ratio does not significantly reduce the differences, it is plausible that the transport of the secondary flow vorticity from the upstream straight sections has an important effect on heat transfer ratio near the rotating baseline flow condition.

The conclusion from this discussion is that increasing the density ratio (wall to bulk temperature difference) generally causes the heat transfer in both the inward and outward flow straight passages to increase. Heat transfer in the turns increases on the outside turn and decreases on the inside turn as the density ratio increases.

### 6.4 Effect of Reynolds Number

The effect of varying the Reynolds number above and below the baseline value while maintaining all other basic dimensionless parameters at the rotating baseline flow conditions value is shown in Figure 22. In the first passage (location A to D), the heat transfer ratio increases modestly (10%) on most segments for both an increase and decrease in Reynolds number. In the second passage (location G, H and I), the increase was somewhat greater (up to 25%).

The variation of heat transfer ratio with Reynolds number at the rotating flow conditions is considerably greater than observed for the same variation at their stationary flow conditions. Although the basic dimensionless parameters are constant and thus the ratio of Grashoff/Reynolds<sup>2</sup>, a parameter judged to influence the relative effects of free and forced convection, is constant for these experiments, the absolute value of the Grashoff number varies by a factor of 16 for a variation of the Reynolds number by a factor of 4 (from 12,500 to 50,000). The conclusion from these tests are that the Reynolds number effects are generally contained in the  $Nu_{\infty} \propto Re^{0.8}$  parameter used in the denominator of the heat transfer ratio and that the use of the heat transfer ratio is an acceptable method of normalizing the test results for these rotating heat transfer experiments. The effects of Reynolds number variation are also discussed in Section 8.0 - Correlation of Heat Transfer Results.

### 6.5 Effect of Model Radius

The effects of buoyancy are coupled as the product of three of the four basic flow parameters into a combined buoyancy parameter:  $(\Omega d/V)^2 (R/d)(\Delta\rho/\rho)$ . In order to isolate the effects of  $R/d$  and obtain heat transfer data at several conditions with the same product of  $(R/d)(\Delta\rho/\rho)$ , the model radius was decreased to about two-thirds of its baseline value. The effects of this decrease in model radius on the heat transfer ratio are shown in Figure 23. The overall impression is that decreasing the radius did not significantly change the heat

ROTATING BASELINE ROTATION NUMBER,  
TEMPERATURE RATIO AND GEOMETRY

$$Ro \approx .24 \quad \Delta T \approx 44.4^\circ\text{C} (80^\circ\text{F})$$

$$\left(\frac{\Delta T}{T}\right)_{in} = 0.13 \quad \bar{R}/d = 49$$

$$\alpha = 0$$

SYMBOL	TEST NO.	Re	RPM
○	5	12,592	275
■	4	25,221	550
△	6	49,626	1100

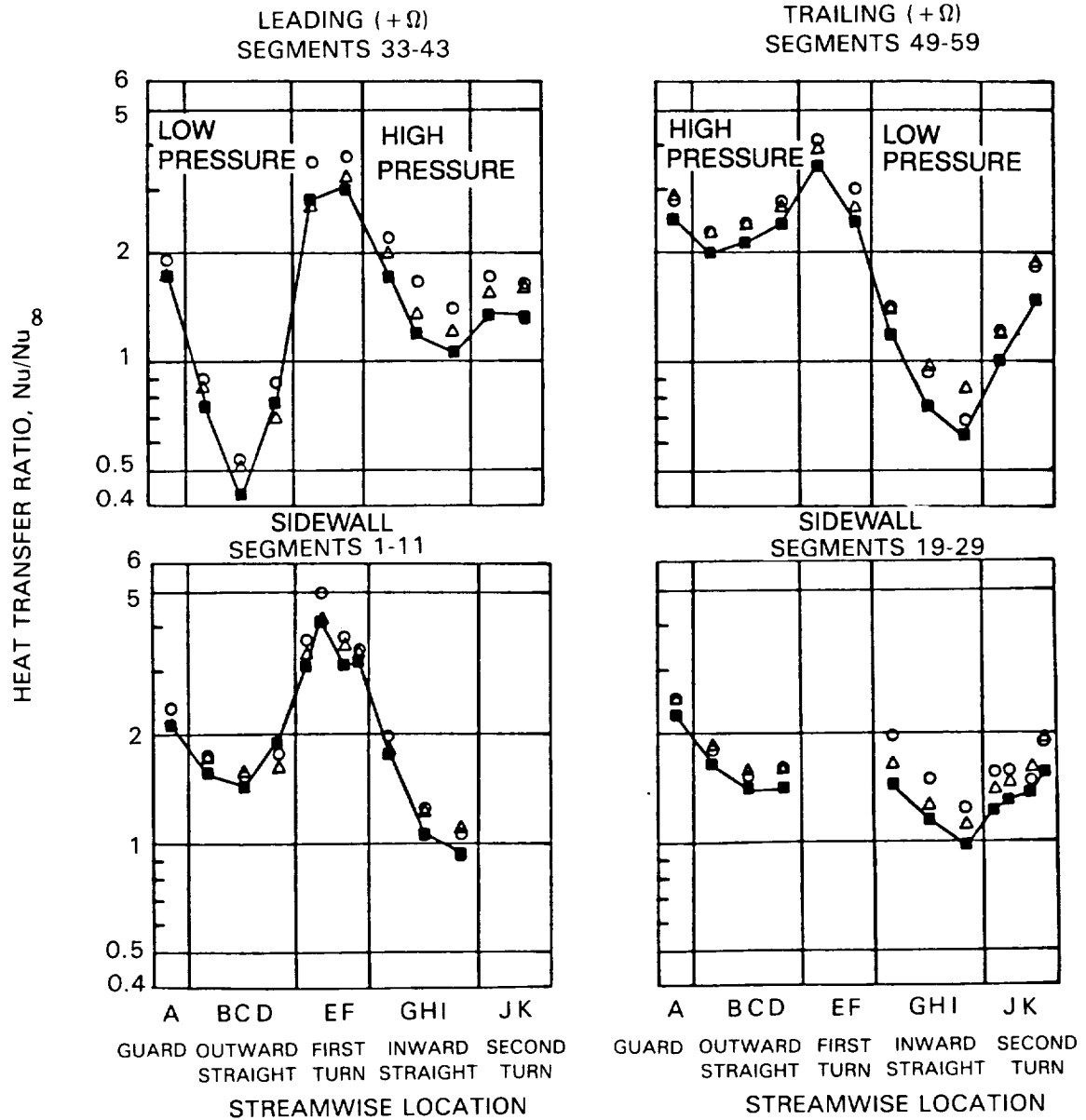


Figure 22.- Effects of Reynolds Number on Heat Transfer Ratio.

ROTATING BASELINE ROTATION NUMBER,  
TEMPERATURE RATIO AND REYNOLDS NUMBER

$Re \approx 25,000$

$\left(\frac{\Delta T}{T}\right)_{in} = 0.13$

$Ro \approx .24$

$\Delta T = 44.4^\circ\text{C} (80^\circ\text{F})$

RPM = 550

$\alpha = 0$

SYMBOL	TEST NO.	MODEL RADIUS (IN.)	$\bar{R}/d$
■	4	25	49
△	11	17	33

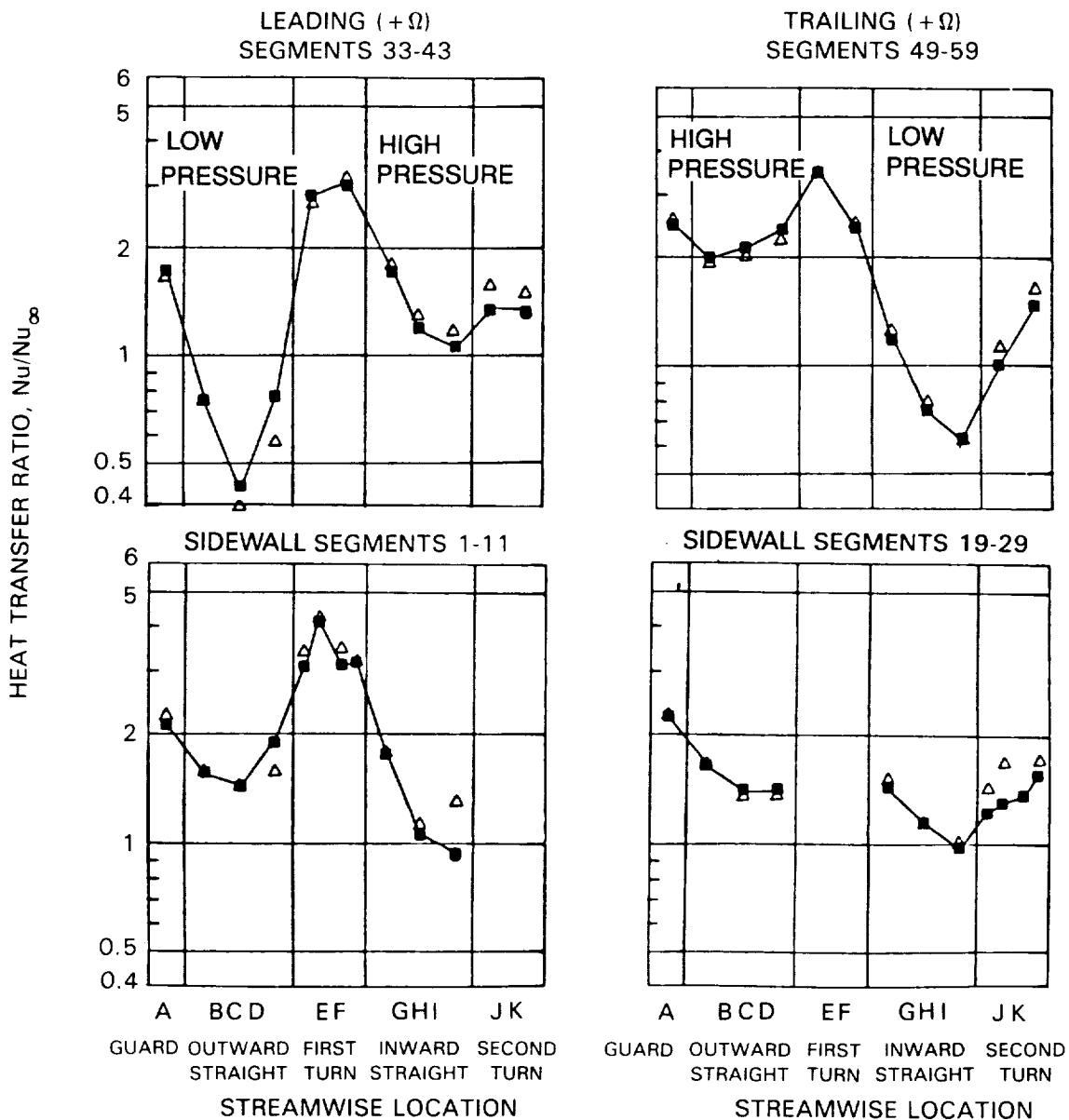


Figure 23.- Effects of Model Radius on Heat Transfer Ratio.



transfer distribution. However, there are several effects which are consistent with previously described results. The heat transfer ratios,  $Nu/Nu_{\infty}$ , on both the leading and trailing segments at location C and D are slightly less (0.1 to 0.2  $Nu/Nu_{\infty}$ ) than the rotating baseline values. These results are similar to those discussed in section 6.3 where density ratio was decreased from the baseline value of 0.13 to 0.07. Because the effects of buoyancy are coupled as the product of two flow parameters and one geometric parameter into a combined buoyancy parameter  $(\Delta\rho/\rho)(R/d)(\Omega d/V)^2$ , varying the density ratio or the radius ratio by similar amounts should cause similar variations in the heat transfer distributions.

## 6.6 Effect of Model Angular Orientation

The baseline rotating flow condition has the test model oriented such that the centerlines of all four straight passages pass through the axis of rotation. However, coolant passages are typically oriented at various angles to the axis of rotation, and therefore, it is desirable to determine these effects. The model was rotated  $45^\circ$  on the support arm as shown in Figure 9. The result is that segments 33 to 36 and 19 to 22 are co-leading segments in the first passage and segments 1 to 4 and 49 to 52 are the co-trailing segments. The effect of model orientation on the heat transfer ratio is shown in Figure 24. All the flow conditions for test no. 12 are nearly identical to those for test no. 4 (the rotating baseline flow conditions), except for the model orientation angle  $\alpha$ . Note that for the first outward passage of test no. 12, the heat transfer from the co-trailing segments 49-52 and segments 1-4 for streamwise locations A, B, C and D are approximately equal. Likewise, the heat transfer from the co-leading segments 33-36 and segments 19-22 are approximately equal. A similar trend is shown in the first inward passage. Thus, the heat transfer is symmetric about a diagonal in the direction of rotation across the passage. The heat transfer on both the co-leading and co-trailing segments ( $\alpha = 45^\circ$ ) is greater than or equal the heat transfer from the leading and trailing segments ( $\alpha = 0^\circ$ ) for the baseline flow condition, with the exception of Segments 19-29 which show lower heat transfer for  $\alpha = 45^\circ$  than for  $\alpha = 0^\circ$ .

The effects of model orientation on the heat transfer ratio shown in Figure 24 are also shown in Figures 25 and 26 as the variation of heat transfer around the test section at selected streamwise locations. The results from all four streamwise locations in the first outward sections are presented in Figure 25; the results for two streamwise locations in all three legs are compared in Figure 26. The symmetry of the heat transfer ratio for  $\Omega d/V = 0.24$  noted for the first leg is apparent in these presentations. Small asymmetries occur in the second and third leg with  $\Omega d/V = 0.24$ .

The combined effects of model orientation and rotation number on the heat transfer ratio in the first leg are also shown in Figure 25 (For  $\Omega d/V = 0$ , heat transfer data obtained for  $\alpha = 0^\circ$  is also replotted at the same segment location for  $\alpha = 45^\circ$ ). Note the change of shape of the heat transfer ratio distributions as the flow progresses from the guard (streamwise location A) to the third section (streamwise location D) in Figure 25. A key result is that the decrease in heat transfer ratio on the leading surfaces due to rotation is less for  $\alpha = 45^\circ$  than for  $\alpha = 0^\circ$ . The minimum heat transfer ratio in the first leg for  $\alpha = 45^\circ$  was approximately 0.9, whereas, the minimum value of the heat transfer ratio for  $\alpha = 0^\circ$  was 0.45.

ROTATING BASELINE ROTATION NUMBER, TEMPERATURE  
RATIO, REYNOLDS NUMBER AND RADIUS

$Re \approx 25,000$

$$\left(\frac{\Delta T}{T}\right)_{in} = 0.13$$

$Ro \approx .24$

$\Delta T = 44.4^\circ\text{C} (80^\circ\text{F})$

RPM = 550

$\bar{R}/d = 49$

SYMBOL	TEST NO.	$\alpha$ DEG.
■	4	0
△	12	45

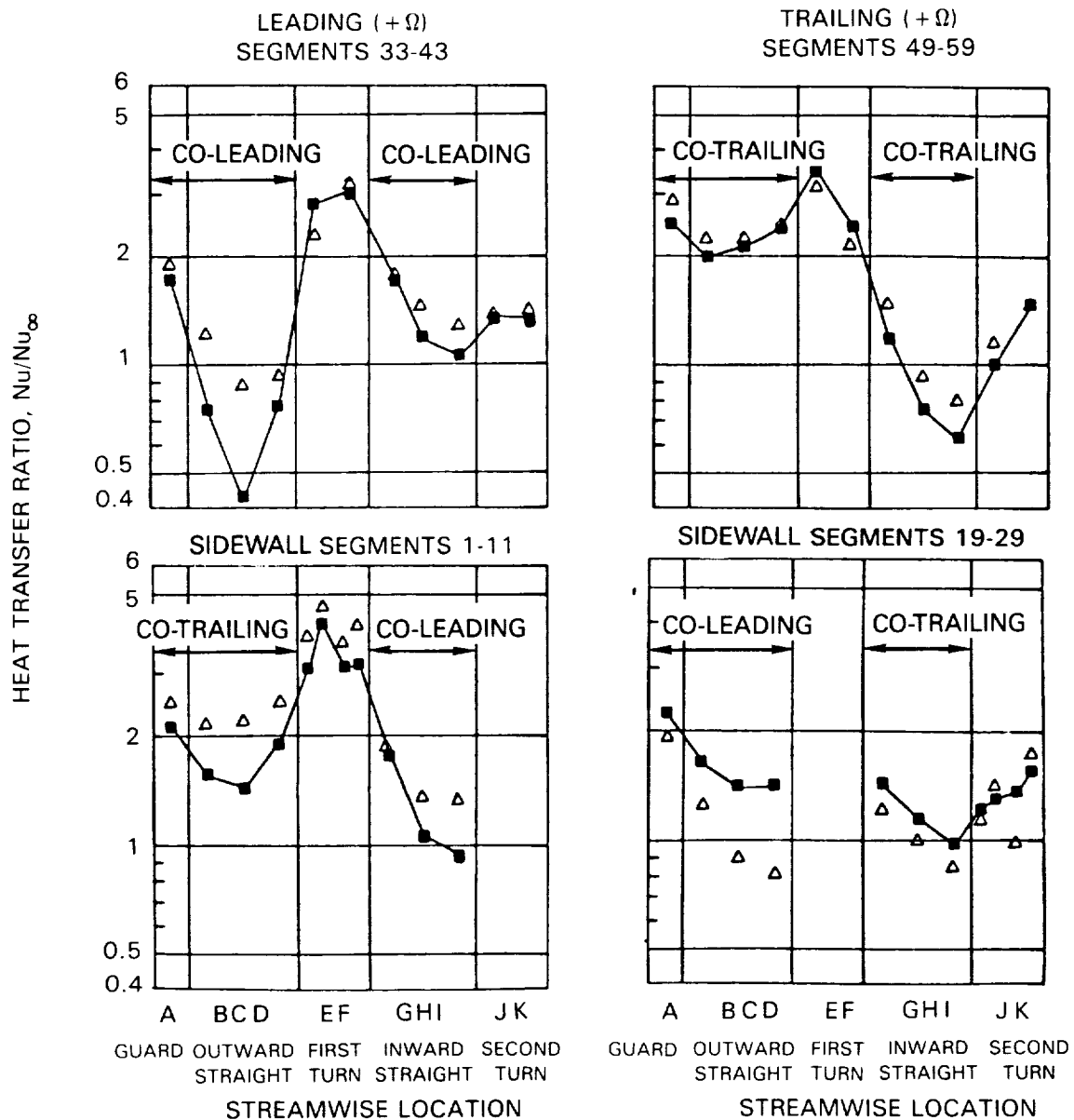


Figure 24.- Effects of Model Orientation on Heat Transfer Ratio.

ALL TEST CONDITIONS STANDARD EXCEPT FOR  $\alpha$  AND  $\Omega d/V$

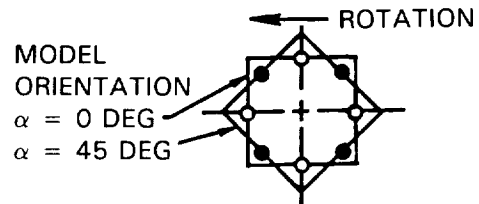
$$Re \approx 25,000$$

$$\left(\frac{\Delta T}{T}\right)_{in} = 0.13$$

$$\Delta T \approx 44.4^\circ\text{C} (80^\circ\text{F})$$

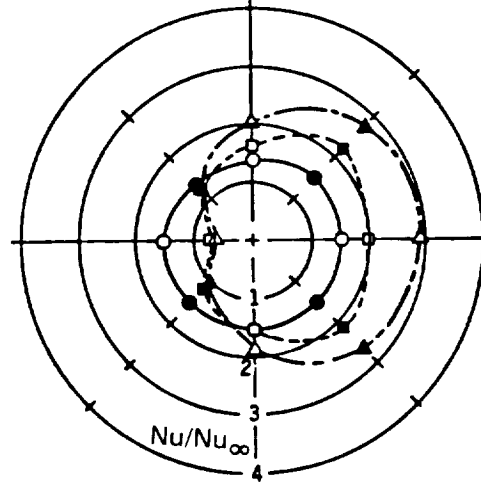
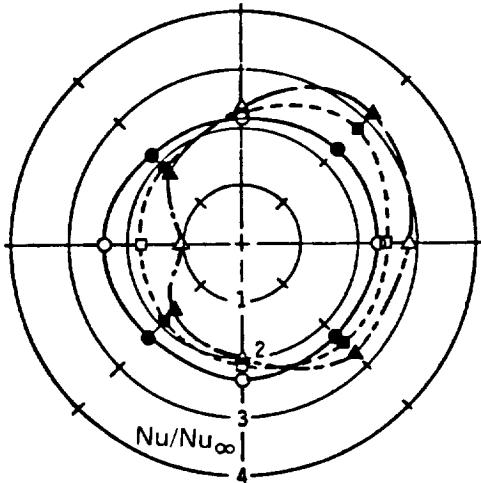
$$\bar{R}/d = 49$$

SYMBOL	TEST NO.	$\alpha$ DEG.	$Ro$	RPM
○	1A	0	0	0
●	1A	0	0	0
□	4	0	0.24	550
■	12	45	0.24	550
△	106	0	0.35	825
▲	119	45	0.34	825



GUARD (A)

FIRST SECTION (B)



SECOND SECTION (C)

THIRD SECTION (D)

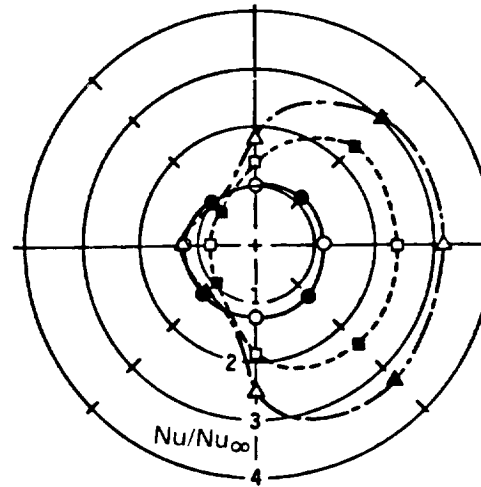
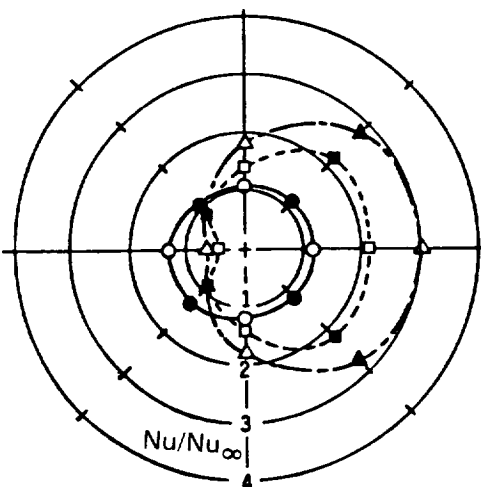


Figure 25.- Variation of Heat Transfer Ratio Around Test Section With Streamwise Location, Rotation Number and Model Orientation in First Leg of Model.

ALL TEST CONDITIONS STANDARD EXCEPT FOR  $\alpha$  AND  $\Omega d/V$

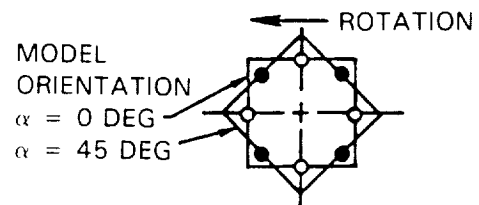
$$Re \approx 25,000$$

$$\left(\frac{\Delta T}{T}\right)_{in} = 0.13$$

$$\Delta T \approx 44.4^\circ\text{C} (80^\circ\text{F})$$

$$\bar{R}/d = 49$$

SYMBOL	TEST NO.	$\alpha$ DEG.	$Ro$	RPM
○	1A	0	0	0
●	1A	0	0	0
□	4	0	0.24	550
■	12	45	0.24	550
△	106	0	0.35	825
▲	119	45	0.34	825



FIRST LEG  
FLOW OUTWARD

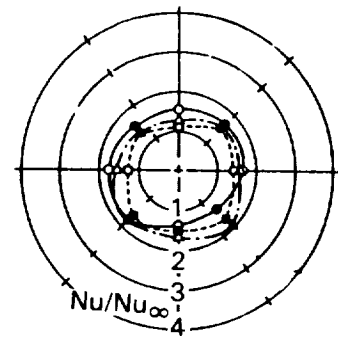
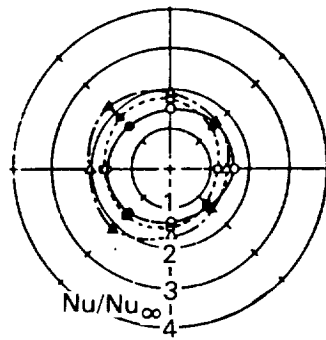
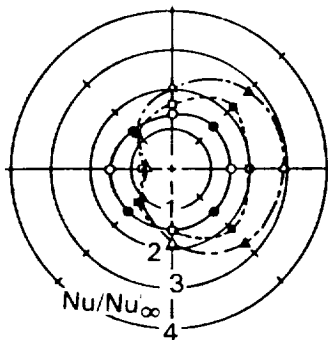
SECOND LEG  
FLOW INWARD

THIRD LEG  
FLOW OUTWARD

TEST SECTION B

TEST SECTION G

TEST SECTION L



ROTATION

ROTATION

TEST SECTION D

TEST SECTION I

TEST SECTION N

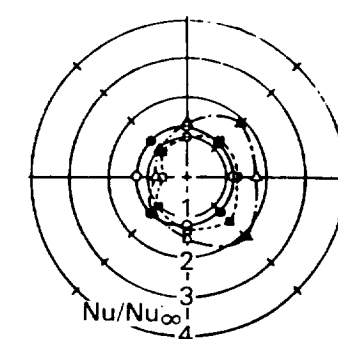
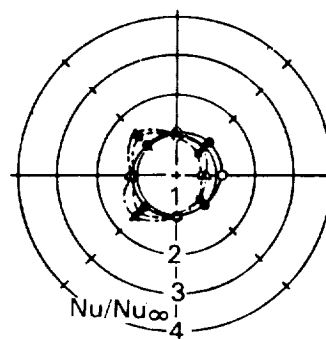
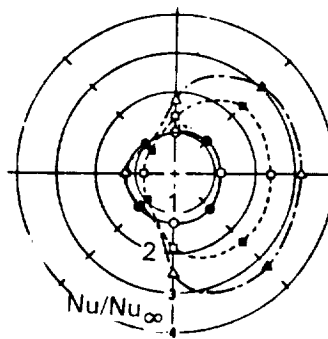


Figure 26.- Comparison of Heat Transfer Ratio Around Test Section From Passages With Inward and Outward Flow.

The combined effects of model orientation and rotation number on the heat transfer ratio in all three legs are shown in Figure 26. The heat transfer ratio distributions for the second and third legs are somewhat less symmetrical than the distributions for the first leg. The heat transfer ratio distribution for streamwise location I appears anomalous. Note that at this location, the heat transfer ratios on the co-leading surfaces for  $\alpha = 45^\circ$  are greater than the ratios for on the leading surface for  $\alpha = 0^\circ$ . This phenomena occurred only at this streamwise location where the flow was inward.

The results from the experiments with  $\alpha = 45^\circ$  were well behaved in the first leg of the model and more complex in the second and third leg. The heat transfer ratio distributions in the second and third leg are less well behaved, probably due to the more complex interactions as the flow passes through the turns and becomes reestablished in the straight sections. Although the amount of data available from the  $\alpha = 45^\circ$  was limited, the results do show the general effects of model orientation.

## 6.7 Conclusions

The heat transfer characteristics of the smooth wall serpentine heat transfer model with rotation are considerably more complex than without rotation. The results showed large effects of rotation number on the heat transfer ratio for the leading and trailing surfaces. In the first leg of the model, the heat transfer ratio decreased to as much as 40% of the stationary value on the leading surfaces and increased to as much as 300% of the stationary value on the trailing surfaces. This resulted in a factor of 7.5 difference in the heat transfer coefficients on opposite sides of the coolant passage. The effects of density ratio were also significant although less than the effects of rotation number. In all of the straight sections, increasing the density ratio caused the heat transfer ratio to increase. (The sole exception was for the guard heater on the leading segment in the first leg.) The increase in the heat transfer ratio was as much as 100% for an increase in the inlet wall-to-bulk temperature difference from  $22.2^\circ\text{C}$  to  $88.9^\circ\text{C}$  ( $40^\circ\text{F}$  to  $160^\circ\text{F}$ ). This corresponds to an increase in the inlet density ratio from 0.07 to 0.22. The effects of Reynolds number were less than those of rotation number and density ratio. The effects of model radius location were also moderate and will be discussed further in the next section. The effect of model orientation was also complex. One beneficial result of model orientation ( $\alpha = 45^\circ$ ) was that the very low heat transfer ratios measured on the leading surface in the first leg were ameliorated.

## 7.0 DISCUSSION OF COMBINED EFFECTS ON HEAT TRANSFER

A dimensional analysis of flow in radial rotating ducts, conducted prior to the onset of this study (Appendix 10.1), showed that two combinations of dimensional parameters cause changes in a flow field within a rotating heated duct, compared to the stationary duct. There are:

$$(\Omega d/V)(1 + (\Delta\rho/\rho))/(2 \vec{k} \times \vec{V}) \quad (7.1)$$

Coriolis forces causing secondary flow in the plane perpendicular to the flow direction, and

$$(\Omega d/V)(\Delta\rho/\rho)(\Omega R/V)\vec{i} \quad (7.2)$$

buoyancy forces causing secondary flow in the radial direction.

In the limit as  $\Delta\rho/\rho \rightarrow 0$ , only the Coriolis forces are present. For this case, the Reynolds number  $(\rho V d/\mu)$  and the rotation number  $(\Omega d/V)$  should correlate results for a given geometry. As the parameter  $(\Delta\rho/\rho)(\Omega R/V)$  approaches the value of 1, Coriolis forces and buoyancy forces are of equal magnitude and will begin to interact in a complex manner. When the parameter  $(\Delta\rho/\rho)(\Omega R/V)$  becomes order of 10, buoyancy forces will tend to dominate the flow field.

Early rotating heat transfer studies, e.g. Morris et al, (1979) used relationships of the type:  $Nu = A (Gr/Re^2)^{B_{Pr}} B_{Ro}^C$  to correlate their results. (The parameter  $Gr/Re^2$  is equivalent to  $(\Omega d/V)(\Omega R/V)(\Delta\rho/\rho)$  or  $(\Omega d/V)^2 (R/d)(\Delta\rho/\rho)$ , the aforementioned buoyancy parameter. From the previous paragraph, it can be discerned that Coriolis and buoyancy forces are closely coupled through the presence of the rotation number. In order to understand the complex cause/effect relationships between forced convection, Coriolis and buoyancy forces, the results from the experiments will first be presented as functions of the basic parameters,  $\Omega d/V$  and  $(\Delta\rho/\rho)_{in}$ , and then be presented as functions of the buoyancy parameter with the rotation parameter noted. In this manner, the flow regimes where viscous, Coriolis and buoyancy forces dominate and interact will be identified.

### 7.1 Effects of Density Ratio

The variations of heat transfer ratio with inlet density ratio  $(\Delta\rho/\rho)_{in}$  for the test surfaces on the leading and trailing sides of the first leg are shown in Figures 27 and 28 for  $Re = 25,000$  and selected rotation numbers,  $\Omega d/V$ . Curves have been drawn through sets of data at the same rotation number and extrapolated to  $(\Delta\rho/\rho)_{in} = 0$  to determine the effects of Coriolis forces without buoyancy effects. The extrapolations for the trailing side of the model, (Figure 28 - Heaters 50, 51 and 52) are fairly linear. Note that, for  $\Omega d/V = 0$ , the heat transfer ratio is independent of  $(\Delta\rho/\rho)_{in}$  as expected when  $Nu/Nu_{\infty}$  is determined using film properties (see Section 5.2).

LEG 1 - FLOW OUTWARD  $Re \approx 25,000$ ,  $\bar{R}/d = 49$ ,  $\alpha = 0$   
LEADING TEST SECTION SURFACES

SYMBOL	○	◇	☆	△	D	□	▴	▽	SYMBOL FLAGS
ROTATION NUMBER	0.0	0.006	0.06	0.12	0.18	0.25	0.35	0.50	
TEST NO. AT $\Delta T = 22.2^\circ\text{C}$ ( $40^\circ\text{F}$ )	110	—	—	—	115	9	105	—	○
$\Delta T = 44.4^\circ\text{C}$ ( $80^\circ\text{F}$ )	1	101	117	8	114	4	106	7	○
$\Delta T = 66.7^\circ\text{C}$ ( $120^\circ\text{F}$ )	111	—	—	—	113	10	107	—	○
$\Delta T = 88.9^\circ\text{C}$ ( $160^\circ\text{F}$ )	112	—	—	—	116	102	—	—	○

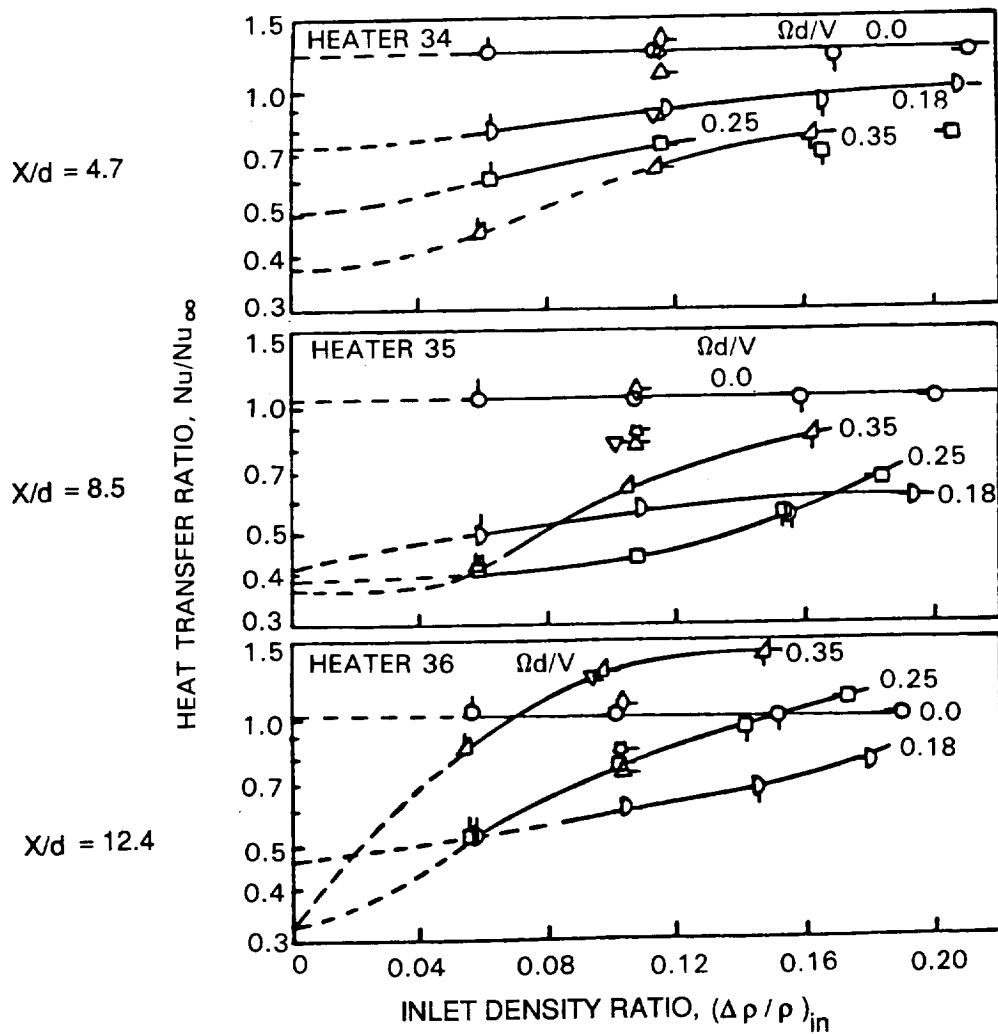


Figure 27.- Variation of Heat Transfer Ratio with Density Ratio for Selected Rotation Numbers.

LEG 1 — FLOW OUTWARD  $Re \approx 25,000$ ,  $\bar{R}/d = 49$ ,  $\alpha = 0$   
TRAILING TEST SECTION SURFACES

	○	◇	☆	△	D	□	▵	▽	SYMBOL FLAGS
ROTATION NUMBER	0.0	0.006	0.06	0.12	0.18	0.25	0.35	0.50	
TEST NO. AT $\Delta T = 22.2^\circ\text{C}$ (40°F)	110	—	—	—	115	9	105	—	○
$\Delta T = 44.4^\circ\text{C}$ (80°F)	1	101	117	8	114	4	106	7	○
$\Delta T = 66.7^\circ\text{C}$ (120°F)	111	—	—	—	113	10	107	—	○
$\Delta T = 88.9^\circ\text{C}$ (160°F)	112	—	—	—	116	102	—	—	○

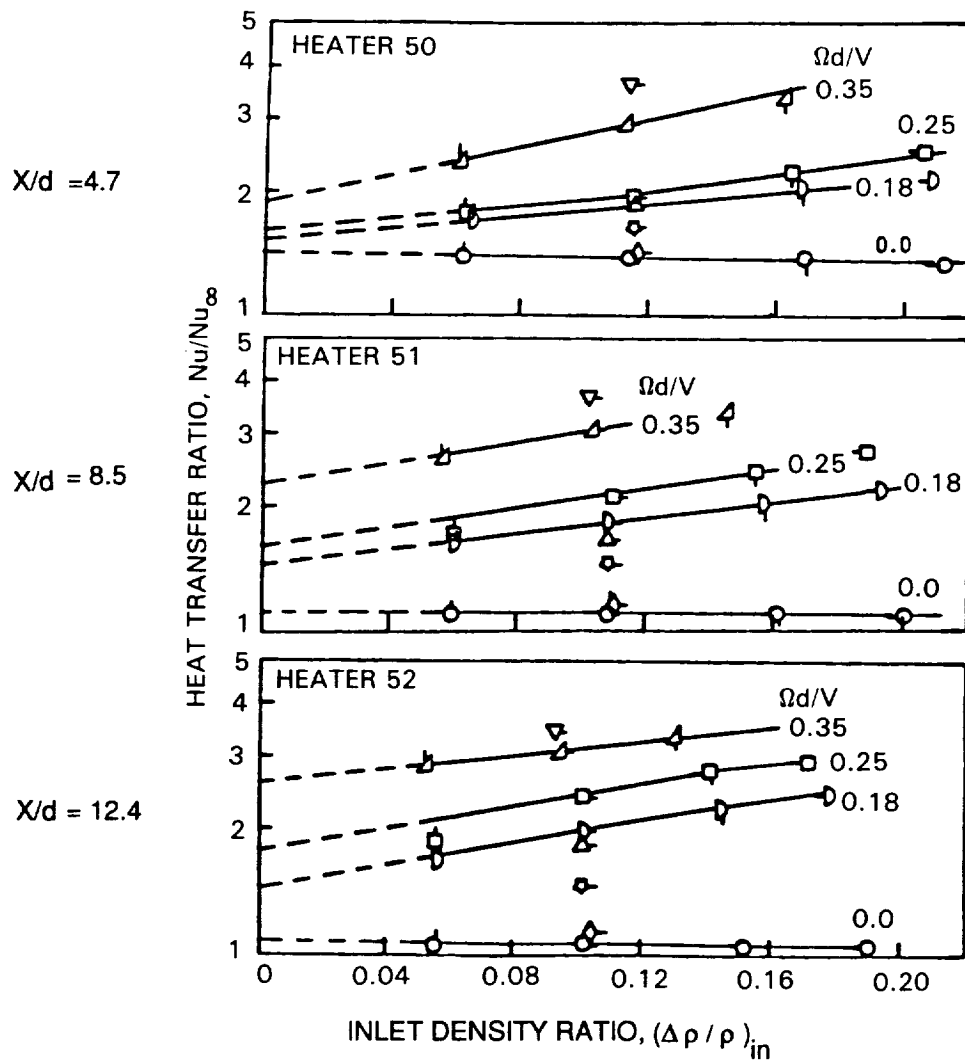


Figure 28.— Variation of Heat Transfer Ratio with Density Ratio for Selected Rotation Numbers.



Determination of the variation of  $Nu/Nu_{\infty}$  with  $(\Delta \rho/\rho)_{in}$  near 0 is more difficult for the data from the leading test surface (Figure 27 - Heaters 34, 35 and 36) in the first leg. Direct extrapolation of the data for  $\Omega d/V > 0.18$  (Symbols  $\square$  and  $\blacktriangle$  - Heater 36) and  $(\Delta \rho/\rho)_{in} < 0.1$  with large negative curvatures would lead to estimated values of  $Nu/Nu_{\infty}$  at  $(\Delta \rho/\rho)_{in} = 0$  which are less than 0.35, the minimum value measured thus far. Therefore, the "dashed" curve leading for the extrapolated values of  $Nu/Nu_{\infty}$  have been "forced" to values greater than, or equal to 0.35 at  $(\Delta \rho/\rho)_{in} = 0$ . It is believed that the secondary flow produced by the Coriolis forces will cause the heat transfer rates to reach a minimum value, i.e.  $Nu/Nu_{\infty} = 0.35$ , and then remain constant or possibly increase.

## 7.2 Effect of Rotation Number

Additional data from parametric variations of density ratio and rotation parameter were necessary to isolate the effects of rotation and buoyancy. The inlet density ratio was varied from 0.07 to 0.22 for selected rotation numbers. Heat transfer results from these experiments were plotted vs. inlet density ratio with rotation number as a secondary variable (section 7.1). The distributions of heat transfer ratio with density ratio were extrapolated for each value of the rotation number to obtain a value of the heat transfer ratio for a density ratio of 0.0 (i.e. limit as  $\Delta T$  approaches 0.0). The heat transfer results obtained from the experiments plus the extrapolated values for a density ratio of 0.0 (dashed lines) are presented in Figures 29 and 30 as the variation of the heat transfer ratio with the rotation number with the inlet density ratio as the secondary variable for three streamwise locations for the first and second passage.

### 7.2.1 High Pressure Surfaces

Heat transfer results from the high pressure side of the first and second passages are shown in Figures 29 and 30 for ranges of rotation number and inlet density ratio. Note that there is no effect of density ratio on the heat transfer ratio for a rotation number of 0 when film properties are used for the dimensionless heat transfer and flow parameters. Increasing the rotation number causes local increases in the heat transfer in the first passages by as much as 3.5 compared to the heat transfer for a rotation number of 0. Whereas the heat transfer ratios for the high pressure surfaces increase sharply with increases in either the density ratio or the rotation number, with one exception, heat transfer in the second passage is relatively unaffected by variations of either parameter. The exception being near the inlet of the second passage, just downstream of the first turn. At this location, the heat transfer increases slightly with increases in the rotation parameter and the density ratio. However, for larger  $X/d$  in the second passage, the effect on the heat transfer for variations in rotation or density ratio diminishes.

LEG 1  $Re \approx 25,000$ ,  $\bar{R}/d = 49$ ,  $\alpha = 0$

SYMBOL	○	◇	☆	△	◐	◻	◔	▽	SYMBOL FLAGS
ROTATION NUMBER	0.0	0.006	0.06	0.12	0.18	0.25	0.35	0.50	
TEST NO. AT $\Delta T = 22.2^\circ\text{C}$ (40°F)	110	—	—	—	115	9	105	—	○
$\Delta T = 44.4^\circ\text{C}$ (80°F)	1	101	117	8	114	4	106	7	○
$\Delta T = 66.7^\circ\text{C}$ (120°F)	111	—	—	—	113	10	107	—	○
$\Delta T = 88.9^\circ\text{C}$ (160°F)	112	—	—	—	116	102	—	—	○

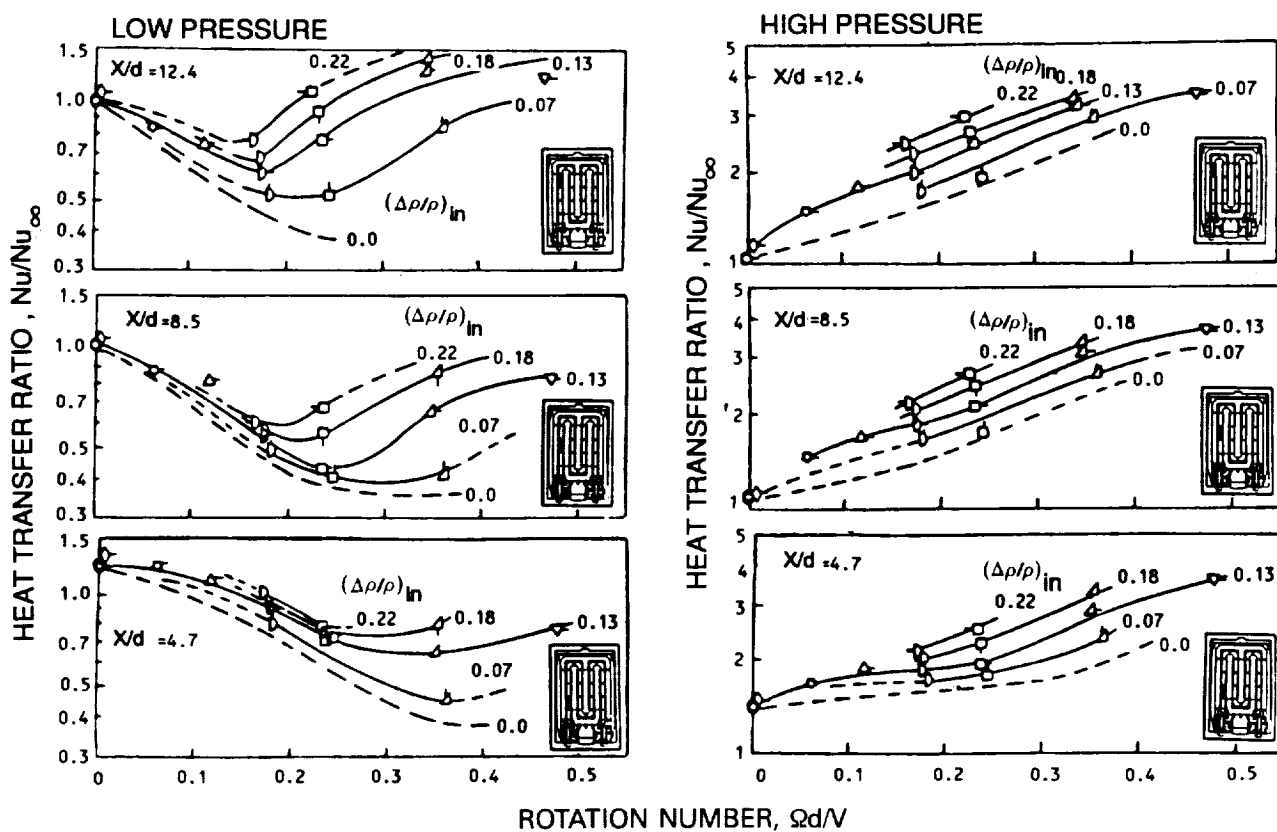


Figure 29.— Variation of Heat Transfer Ratio with Rotation Number for Selected Inlet Density Ratios.

LEG 2  $Re \approx 25,000$  ,  $\bar{R}/d = 49$  ,  $\alpha = 0$

SYMBOL	○	◇	☆	△	D	□	▴	▽	SYMBOL FLAGS
ROTATION NUMBER	0.0	0.006	0.06	0.12	0.18	0.25	0.35	0.50	
TEST NO. AT $\Delta T = 22.2^\circ\text{C}$ ( $40^\circ\text{F}$ )	110	—	—	—	115	9	105	—	○
$\Delta T = 44.4^\circ\text{C}$ ( $80^\circ\text{F}$ )	1	101	117	8	114	4	106	7	○
$\Delta T = 66.7^\circ\text{C}$ ( $120^\circ\text{F}$ )	111	—	—	—	113	10	107	—	○
$\Delta T = 88.9^\circ\text{C}$ ( $160^\circ\text{F}$ )	112	—	—	—	116	102	—	—	○

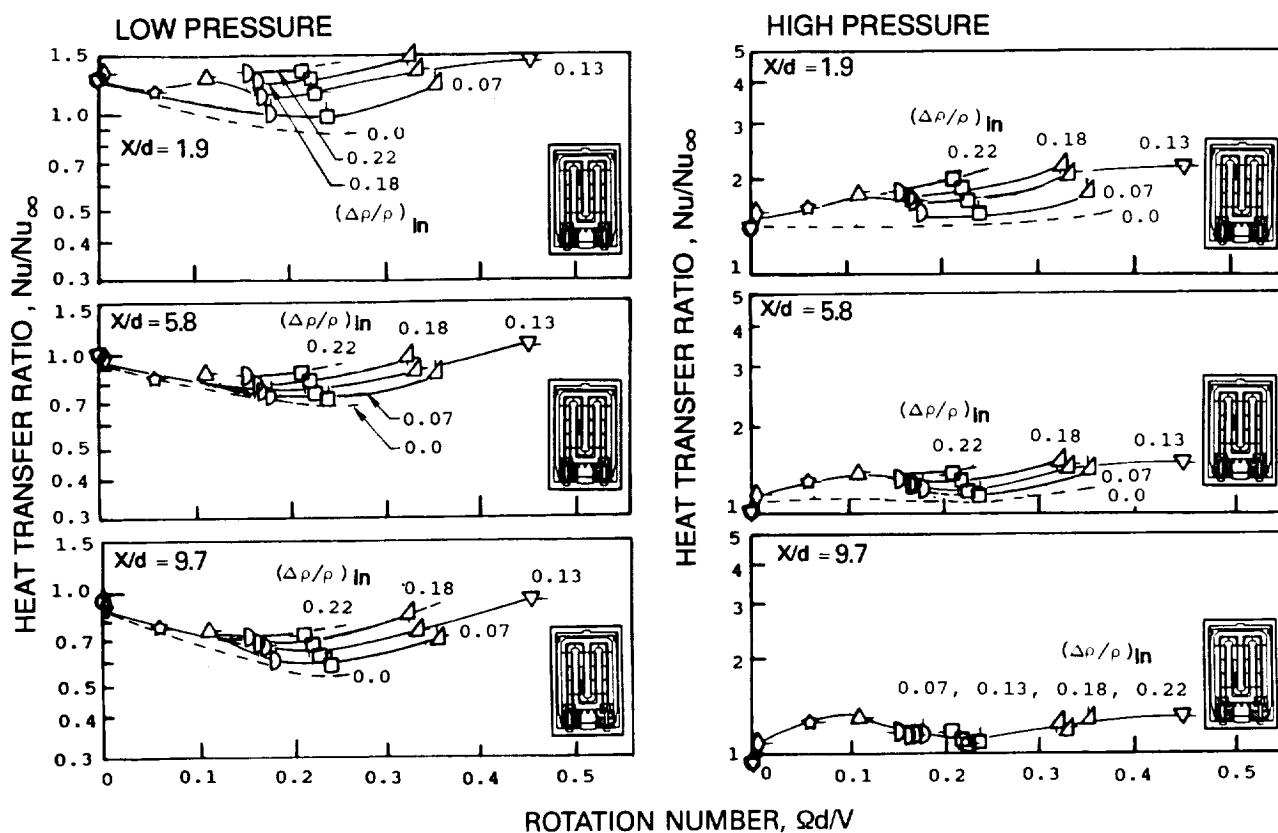


Figure 30.- Variation of Heat Transfer Ratio with Rotation Number for Selected Inlet Density Ratios.

### 7.2.2 Low Pressure Surfaces

The heat transfer from the low pressure surfaces from the first and second passages of Figures 29 and 30 is more complex than that from the high pressure surfaces. Heat transfer in the first passage decreases with increasing rotation number for low values of rotation number (i.e.  $\Omega d/V < 0.2$  at the downstream location) and then subsequently increases again with increases in rotation for larger values of rotation number. Additionally, as with the high pressure surfaces in the first passage, heat transfer increases with increases in the density ratio. A similar characteristic in the heat transfer distributions is observed in the second passage for radially inflow as well. However, with one exception, the large effects of density ratio observed on the low pressure surfaces of the first passage are diminished in the second passage. The exception is that heat transfer is slightly increased with increasing density ratio near the inlet of the second passage.

The extrapolated values of the heat transfer ratios as  $(\Delta \rho/\rho)_{in}$  approaches zero are modified from those previously presented for the same data set in Wagner et al (1989, 1991) and Wagner et al (1990). Based on unpublished (1990) preliminary results from a mass transfer experiment at the University of Darmstadt, Germany and numerical studies of Iacovides and Launder (1990) for flows in rotating radial ducts, the authors now believe that the heat transfer ratio of  $(\Delta \rho/\rho)_{in} = 0$  on the low pressure side of the duct would not increase with increasing rotation number after reaching a minimal value. The conclusion from this position is that the heat transfer coefficients for conditions with  $(\Delta \rho/\rho)_{in} \approx 0.2$  can be as much as 3 to 4 times those obtained when  $(\Delta \rho/\rho)_{in}$  approaches zero.

The more complicated heat transfer distributions on the low pressure surfaces of the coolant passage are attributed to: 1) the combination of buoyancy forces and the stabilization of the near-wall flow for low values of the rotation number and 2) the developing Coriolis driven secondary flow cells for the larger values of the rotation number. It is postulated that the relatively large effects from variations in density ratio near the inlet of the second passage and the small effects near the end of the second passage are due to the development of the near-wall thermal layers. Near the inlet of the second passage, the thermal layers are postulated to be thin because of the strong secondary flows in the first turn region. With increasing  $X/d$ , the turn dominated secondary flows diminish and the counteracting effect of buoyancy and the Coriolis generated secondary flow increases.

### 7.3 Effect of Buoyancy Parameter

The analysis of the equations of motion for flow in a rotating radial passage by Suo (1980) showed that 1) variations in the momentum of the flow in the plane perpendicular to the passage centerline (cross stream flow) will be proportional to the rotation number,  $\Omega d/V$ , and 2) variations in the momentum of the flow parallel to the passage centerline (buoyant flows) will be proportional to the buoyancy parameter  $(\Delta \rho/\rho)(R/d)(\Omega d/V)^2$ . The buoyancy parameter defined is equivalent to the ratio of the Grashof number (with a rotational gravitation term,  $R\Omega^2$ ) to the square of the Reynolds number and has previously been used to characterize the relative importance of free- and

forced-convection in the analysis of stationary and mixed-convection heat transfer. Guidez (1988) used a similar analysis to establish appropriate flow parameters for the presentation of his results. These parameters,  $\Omega d/V$  and  $(\Delta\rho/\rho)(R/d)(\Omega d/V)^2$ , will also be used in the present discussion of the effects of Coriolis and buoyancy forces on the heat transfer.

The data and extrapolated results presented in Figures 29 and 30 show that the effects of Coriolis and buoyancy forces are coupled through the entire operating range investigated. The results from Figure 29 combined with those for  $R/d = 33$ , are presented in Figures 31 and 32 as the variation of the heat transfer ratio with the buoyancy parameter. The local density ratio and radius,  $R$ , are used in the buoyancy parameter. For a constant wall temperature boundary condition, the wall-to-bulk temperature difference (hence the local density ratio) decreases as the flow progresses downstream, therefore, the range of the buoyancy parameter also decreases with increasing values of  $X/d$ . Results for the same value of the rotation number are connected with lines where the results are not well correlated by the buoyancy parameter. The lines at constant rotation number are extrapolated to the value of the heat transfer ratio estimated for a density ratio (and also buoyancy parameter) of 0 as described in section 7.2.

The heat transfer ratios for this trailing side (Figure 32) of the passage increase with the buoyancy parameter. The rate of increase in the heat transfer ratio with increasing buoyancy parameter is greatest at the  $X/d = 12.4$  location for values of buoyancy parameter less than 0.4. For values of buoyancy parameter greater than 0.4, the rate of increase is less. Thus, two ranges of buoyancy parameter appear to exist with different heat transfer characteristics. Generally, the heat transfer variations from the trailing side form a 1:1 correspondence with the buoyancy parameter (i.e., singled value function) and are well correlated by the buoyancy parameter for all values of  $X/d$  shown.

Examination of the heat transfer results from the leading side (Figure 31) suggest that at least three ranges of buoyancy parameter exist where the heat transfer is dominated by different fluid dynamic mechanisms (i.e., Coriolis, buoyancy, etc.). At  $X/d = 12.4$ , there is a range of buoyancy parameter for values less than 0.1 (range A) where the heat transfer ratios decrease sharply (from approximately 1.1 to just over 0.5) with increasing values of the buoyancy parameter. Within the second range from 0.1 to approximately 0.5 (range B), the heat transfer ratios increase sharply with increasing values of the buoyancy parameter. For the third range, with values of the buoyancy parameter greater than 0.5 (range C), the heat transfer ratio increases at a lower rate, with increasing values of buoyancy parameter. For lower values of  $X/d$ , the three ranges are less well defined. However, the minimum value of heat transfer ratio (which defines the end of the first buoyancy parameter range) occurs at increasing magnitudes of buoyancy parameter (0.1 to 0.4) as  $X/d$  decreases from 12.4 to 4.7. The heat transfer on the leading surface at values of  $X/d = 4.7$  and 8.5 is governed by a more complex relationship of streamwise distance, rotation number and buoyancy parameter. However, the results from the leading side for  $X/d = 12.4$  are well correlated by the buoyancy parameter for values of the buoyancy parameter greater than 0.2.

LEG 1 — FLOW OUTWARD  $Re \approx 25,000$ ,  $\alpha = 0$   
LEADING TEST SECTION SURFACES

OPEN SYMBOLS:  $\bar{R}/d = 49$ ; SHADED SYMBOLS:  $\bar{R}/d = 33$

SYMBOL	○	◇	☆	△	D	■ □	▴ ▽	▽	SYMBOL FLAGS
ROTATION NUMBER	0.0	0.006	0.06	0.12	0.18	0.25	0.35	0.50	
TEST NO. AT $\Delta T = 22.2^\circ\text{C}$ (40°F)	110	—	—	—	115	— 9	105 —	—	○
$\Delta T = 44.4^\circ\text{C}$ (80°F)	1	101	117	8	114	11 4	106 125	7	○
$\Delta T = 66.7^\circ\text{C}$ (120°F)	111	—	—	—	113	— 10	107 —	—	○
$\Delta T = 88.9^\circ\text{C}$ (160°F)	112	—	—	—	116	124 102	— 126	—	○

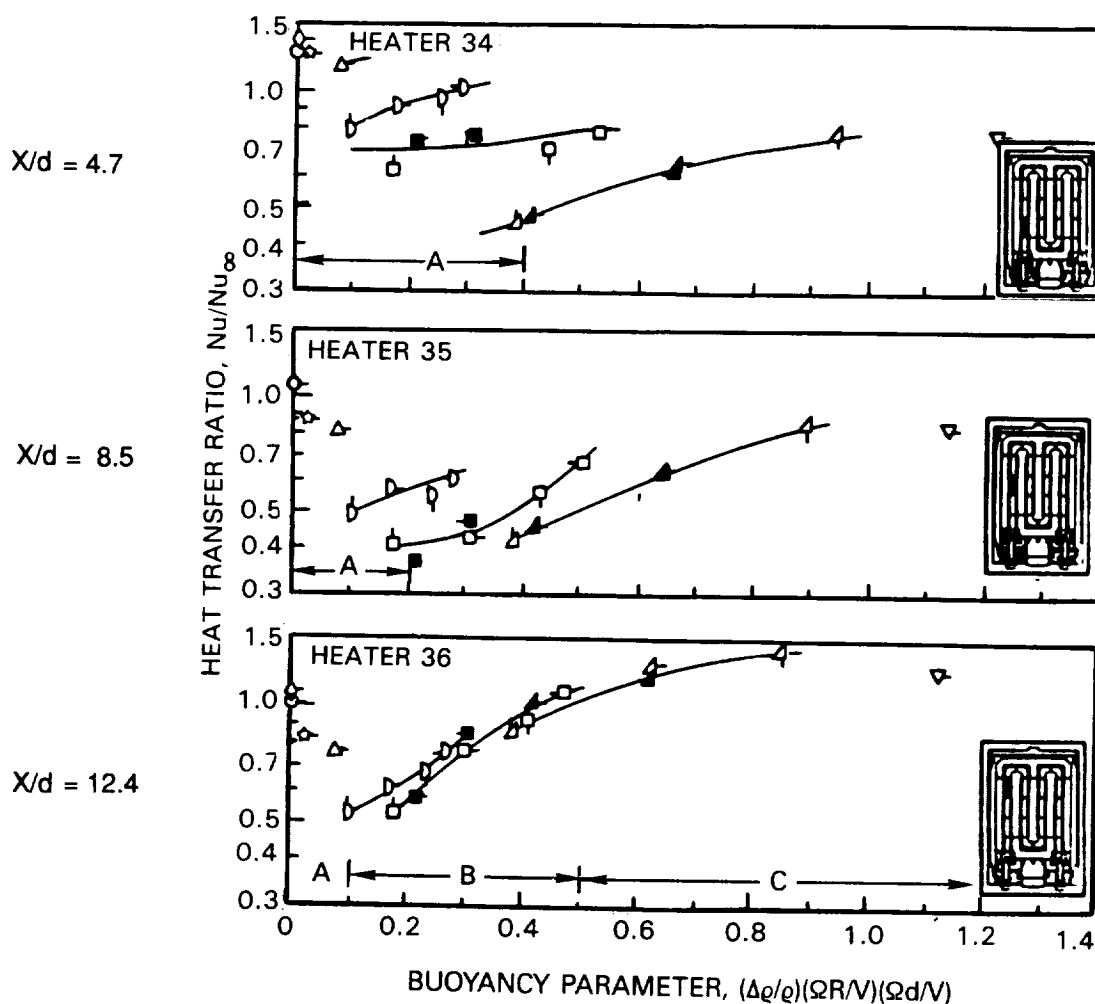


Figure 31.— Variation of Heat Transfer Ratio with Buoyancy Parameter.

LEG 1 — FLOW OUTWARD  $Re \approx 25,000$ ,  $\alpha = 0$   
TRAILING TEST SECTION SURFACES

OPEN SYMBOLS:  $\bar{R}/d = 49$ ; SHADED SYMBOLS:  $\bar{R}/d = 33$

SYMBOL	○	◇	☆	△	◐	■ □	▵ ▴	▽	SYMBOL FLAGS
ROTATION NUMBER	0.0	0.006	0.06	0.12	0.18	0.25	0.35	0.50	
TEST NO. AT $\Delta T = 22.2^\circ\text{C}$ ( $40^\circ\text{F}$ )	110	—	—	—	115	— 9	105 —	—	○
$\Delta T = 44.4^\circ\text{C}$ ( $80^\circ\text{F}$ )	1	101	117	8	114	11 4	106 125	7	○
$\Delta T = 66.7^\circ\text{C}$ ( $120^\circ\text{F}$ )	111	—	—	—	113	— 10	107 —	—	○
$\Delta T = 88.9^\circ\text{C}$ ( $160^\circ\text{F}$ )	112	—	—	—	116	124 102	— 126	—	○

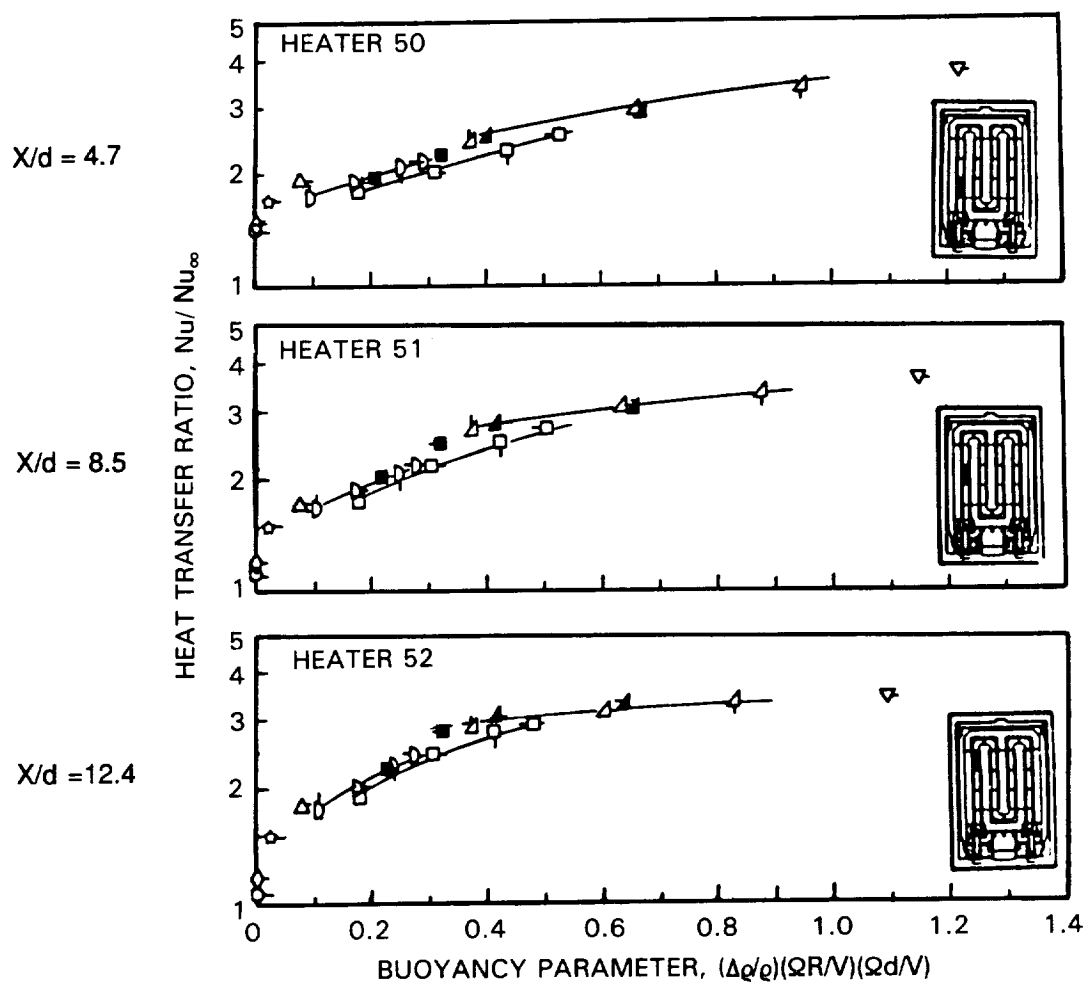


Figure 32.— Variation of Heat Transfer Ratio with Buoyancy Parameter.

The analyses of these heat transfer results show that 1) the buoyancy parameter correlates the heat transfer ratio data from the trailing side of the coolant passage and from the leading side at the downstream location, 2) the data was not correlated by the buoyancy parameter near the inlet on the leading surface due to a complex interaction of stabilization of the near wall flow, buoyancy forces and Coriolis effects, and 3) the heat transfer in rotating, smooth passages is governed by complex interactions of the viscous, Coriolis and buoyancy forces on the fluid.

#### 7.4 Effect of Flow Direction

The data was also analyzed to determine the effects of flow direction (radially inward or radially outward) on the heat transfer characteristics and to determine the differences between the first leg with outward flow downstream of an inlet, the second leg with inward flow downstream of an 180° turn and the third leg with outward flow downstream of an 180° turn. The variations of the heat transfer ratio with buoyancy parameter for the heater test section most downstream of the inlet or turn for each of the three legs are presented in Figures 33 and 34. This is the streamwise location in each leg at which the asymptotic heat transfer characteristics were approached for  $\Delta d/V = 0$ , (see Figure 15).

The data presented in Figures 29 and 30 showed that the effects of Coriolis and buoyancy forces are coupled in the first two passages through the entire operating range investigated. The results from Figures 29 and 30 plus additional results from the third passage are combined with those for  $R/d = 33$  and are presented in Figures 33 and 34 as the variation of the heat transfer ratio with the buoyancy parameter based on the local density ratio and radius,  $R$ . Note that in Figures 33 and 34, the range of the buoyancy parameter data becomes more compressed as the fluid progresses downstream. This is because the wall-to-bulk temperature difference (hence the local density ratio) is decreasing as the fluid progresses downstream and the bulk temperature increases. The ranges of heat transfer ratio for the last location in the first passage is shown as a shaded band with the results from the second and third passages for comparison.

Heat transfer distributions from the low pressure surfaces of each of the three passages (Figure 33) exhibit a decrease with increasing values of buoyancy between 0.0 and 0.15. Heat transfer subsequently increases again with increasing values of buoyancy. Heat transfer on the low pressure surfaces of rotating coolant passages is governed by complex relationships of streamwise location, rotation number, and buoyancy parameter. However, the heat transfer results are reasonably well correlated in the first two passages by the buoyancy parameter for values of buoyancy parameter greater than 0.2.

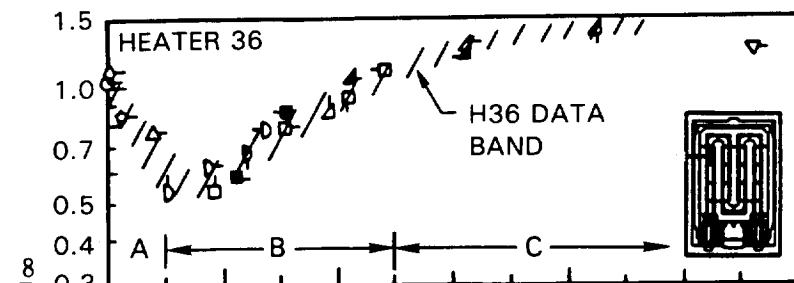
The heat transfer results from the high pressure surfaces in the first passage (Figure 34) are correlated well by the buoyancy parameter. The second passage with radially inward flow had different heat transfer characteristics than the first and third passages with radially outward flow. Whereas the heat transfer ratios for the high pressure surfaces of the first and third passages increased with the buoyancy parameter, the heat transfer in the second passage was lower and relatively independent of buoyancy parameter for values of buoyancy greater than 0.05. These results for co-flowing and counter-flowing



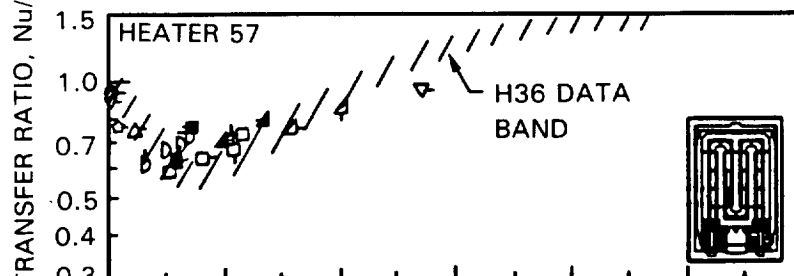
LOW PRESSURE SIDES OF PASSAGE  $Re \approx 25,000$ ,  $\alpha = 0$   
 OPEN SYMBOLS:  $R/d = 49$ ; SHADED SYMBOLS:  $R/d = 33$

SYMBOL	○	◇	☆	△	D	■ □	▴ ▽	▽	SYMBOL FLAGS
ROTATION NUMBER	0.0	0.006	0.06	0.12	0.18	0.25	0.35	0.50	
TEST NO. AT $\Delta T = 22.2^\circ C (40^\circ F)$	110	—	—	—	115	— 9	105 —	—	○
$\Delta T = 44.4^\circ C (80^\circ F)$	1	101	117	8	114	11 4	106 125	7	○
$\Delta T = 66.7^\circ C (120^\circ F)$	111	—	—	—	113	— 10	107 —	—	○
$\Delta T = 88.9^\circ C (160^\circ F)$	112	—	—	—	116	124 102	— 126	—	○

FIRST LEG  
 OUTWARD FLOW  
 DOWNSTREAM OF INLET  
 $X/d = 12.4$   
 LEADING SURFACE



SECOND LEG  
 INWARD FLOW  
 DOWNSTREAM OF TURN  
 $X/d = 9.7$   
 TRAILING SURFACE



THIRD LEG  
 OUTWARD FLOW  
 DOWNSTREAM OF TURN  
 $X/d = 9.7$   
 LEADING SURFACE

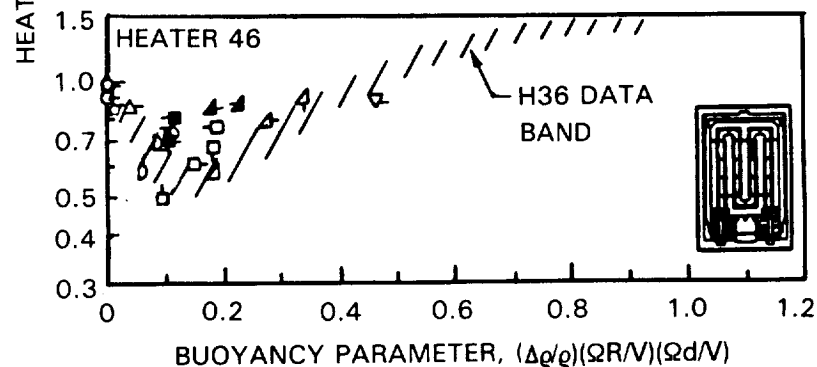
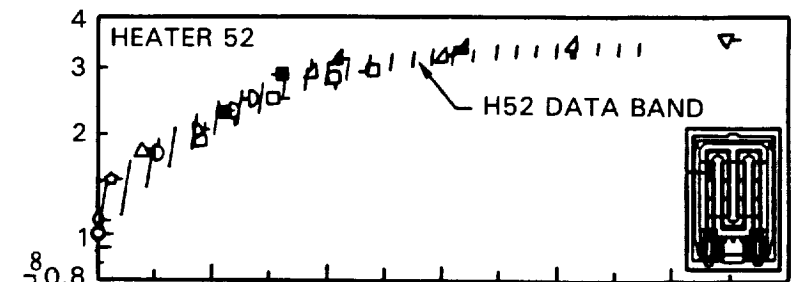


Figure 33.— Comparison of Heat Transfer Ratios from Passages with Inward and Outward Flow.

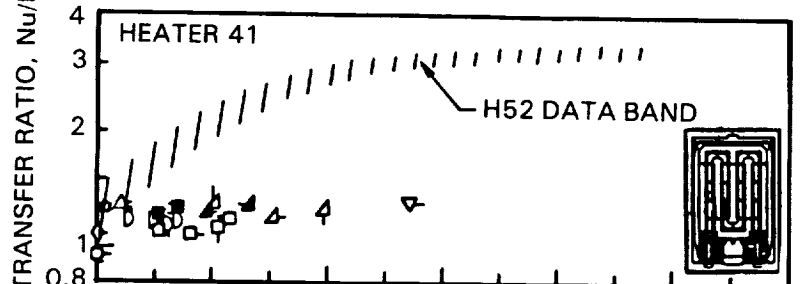
HIGH PRESSURE SIDES OF PASSAGE  $Re \approx 25,000$ ,  $\alpha = 0$   
 OPEN SYMBOLS:  $R/d = 49$ ; SHADED SYMBOLS:  $R/d = 33$

SYMBOL	○	◇	☆	△	◐	■ □	▵ ▴	▽	SYMBOL FLAGS
ROTATION NUMBER	0.0	0.006	0.06	0.12	0.18	0.25	0.35	0.50	
TEST NO. AT $\Delta T = 22.2^\circ\text{C}$ (40°F)	110	—	—	—	115	— 9	105 —	—	○
$\Delta T = 44.4^\circ\text{C}$ (80°F)	1	101	117	8	114	11 4	106 125	7	○
$\Delta T = 66.7^\circ\text{C}$ (120°F)	111	—	—	—	113	— 10	107 —	—	○
$\Delta T = 88.9^\circ\text{C}$ (160°F)	112	—	—	—	116	124 102	— 126	—	○

FIRST LEG  
 OUTWARD FLOW  
 DOWNSTREAM OF INLET  
 $X/d = 12.4$   
 TRAILING SURFACE



SECOND LEG  
 INWARD FLOW  
 DOWNSTREAM OF TURN  
 $X/d = 9.7$   
 LEADING SURFACE



THIRD LEG  
 OUTWARD FLOW  
 DOWNSTREAM OF TURN  
 $X/d = 9.7$   
 TRAILING SURFACE

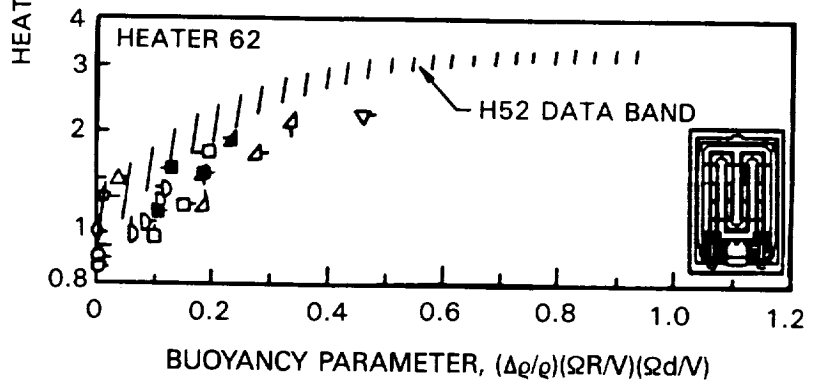


Figure 34.— Comparison of Heat Transfer Ratios from Passages with Inward and Outward Flow.

buoyancy effects on the high pressure surfaces are generally consistent with the stationary combined free-and-forced convection experiments of Eckert et al. (1953). They measured decreased levels of heat transfer for the co-flowing condition( i.e. similar to that of radially inward flow in rotating sytems).

## 7.5 Conclusions

The analysis of the experimental results to determine the combined effects of forced convection, buoyancy and Coriolis forces on heat transfer in smooth rotating radial passages has produced several interesting and remarkable conclusions:

1. Both the density ratio,  $(\Delta\rho/\rho)_{in}$ , and the rotation number,  $\Omega d/V$  were found to cause large changes in the heat transfer ratio, as much as factors of 2.5 and 3.5, respectively.
2. The flow field was never completely dominated by free convection for the test conditions in this study. The conclusion is easily discerned by observing the variation of the heat transfer ratio between the leading and trailing surfaces.
3. The heat transfer ratio was found to be primarily a function of the buoyancy parameter on the low pressure surfaces (i.e., leading surfaces for outward flow and trailing surfaces for inward flow) for values of the buoyancy parameter greater than 0.2 and for  $X/d = 12.4$ .
4. The heat transfer ratio was found to be primarily a function of the buoyancy parameter for the high pressure side of the passage for flow outward only (i.e., trailing side of passage).
5. The variations of heat transfer ratio with buoyancy parameter were approximately the same for the furthest downstream straight section segment on the low pressure side of all three passages. Buoyancy had essentially the same effect on heat transfer on the low pressure side whether the flow is inward or outward.
6. The heat transfer ratio on the high pressure side of the passage is significantly affected by flow direction. The effects of buoyancy and Coriolis forces: (a) combined to increase heat transfer on the flow outward trailing surfaces; and (b) cancelled on the flow inward leading surfaces with the result that the heat transfer ratio is approximately constant. Possible explanations for this phenomena include changes in the turbulence structure due to combinations of flow direction and buoyancy force direction.
7. The heat transfer ratios for  $\bar{R}/d = 49$  and 33 are well correlated by the buoyancy parameter at the downstream test surface of each passage.

## 8.0 CORRELATION OF HEAT TRANSFER RESULTS

### 8.1 Physical Effects of Rotation

It is well documented that secondary flow circulations and shear layer stability variations are the principal manifestations of rotated channel flows. These effects are illustrated in Figure 35 which depicts a rotated square duct with radially outward flowing coolant. The Coriolis force accelerates the low momentum fluid on the sidewalls toward the low pressure (leading) surface where the boundary layer is stabilized, in some cases, becoming laminar. The core fluid shifts toward the high pressure (trailing) surface where boundary layer is highly destabilized, undergoing a turbulent bursting process similar to that found on concave surfaces (Taylor-Goertler roll cells). It is important to understand that the flow on each of the three surface types (leading, trailing, and sidewalls) in the square duct experiences a different set of physical changes during rotation.

Moore (1967) measured the centerline velocity profile in a long rotating square duct shown in Figure 36. Moore's data, shown in Figure 37, validates the shifting of the core fluid from the center of the duct to the high pressure surface. The boundary layer becomes thick on the low pressure surface and thin on the high pressure surface. In a heated duct, this effect would insulate the low pressure wall from the cool core fluid and move this core fluid closer to the high pressure wall, thus increasing the heat pickup there.

Moon (1964) examined the affect of rotation on internal flow in a rectangular duct shown in Figure 38. He measured centerline velocities at five locations in 183 cm (72") long rotating duct. These are plotted along with the boundary layer and displacement thickness in Figure 39. The velocity profiles and boundary layer thickness both show that the low pressure side (suction) boundary layer becomes very thick as the flow moves downstream. At the same time, the boundary layer on the high pressure side of the duct maintains the classical turbulent boundary layer shape, except at the end of the duct, where it becomes thin. This shifting of the boundary layers on both surfaces occurs as the Coriolis acceleration transports fluid from the sidewalls onto the low pressure surface. Note that this thickening on the low pressure side is a strong function of distance from the duct inlet.

Using previously measured skin friction coefficients and the Reynolds analogy, we can generally predict the effects of the Coriolis force on local heat transfer. Moore (1967) shows in Figure 40 that at two rotation number conditions, the skin friction on the high and low pressure surfaces varies significantly and is a strong function of channel aspect ratio. Moore's data at unity aspect ratio (square duct) shows that the low pressure surface skin friction decreases to 65 percent of the stationary value. A straight Reynolds analogy would predict local heat to decrease by 35 percent at these conditions. This magnitude of decrease is realized in the present square duct experiment, but the decrease occurs for higher rotation number conditions; most likely since the duct in this experiment is relatively short and has less length available for Coriolis secondary flow development.

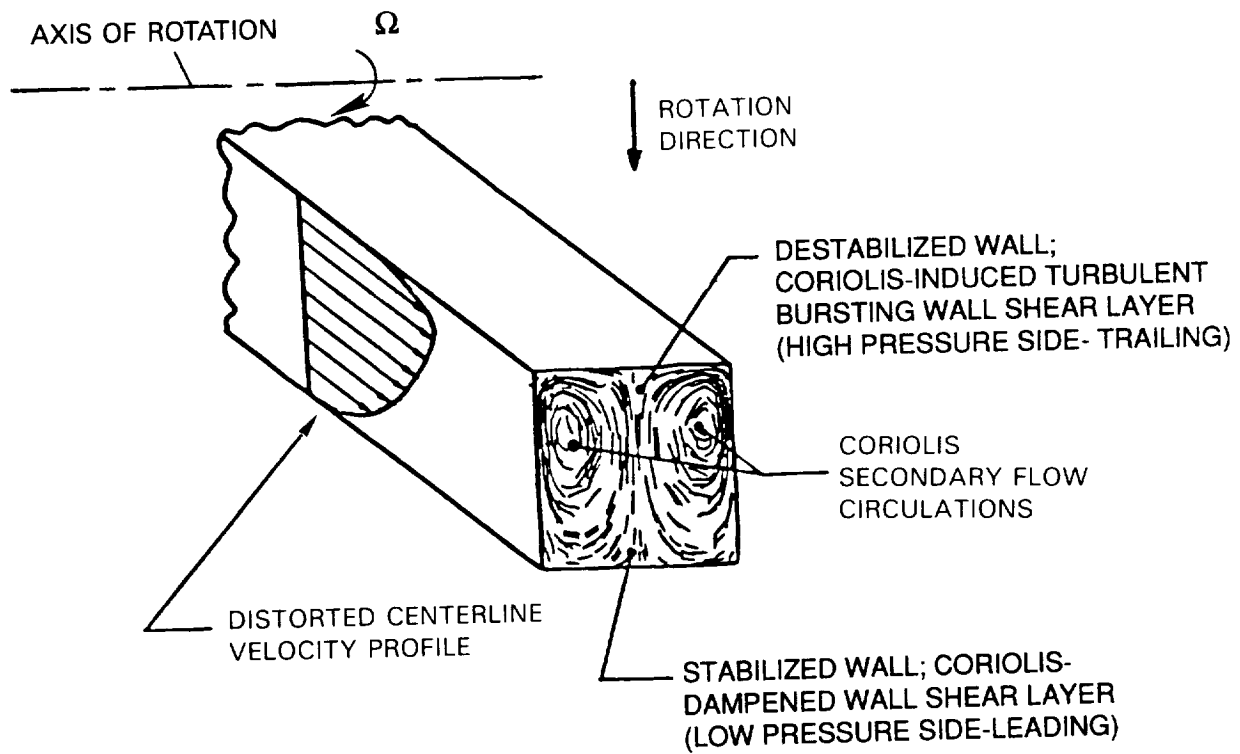


Figure 35.- General Effects of Rotation on Radially Outward Flow in a Square Channel.

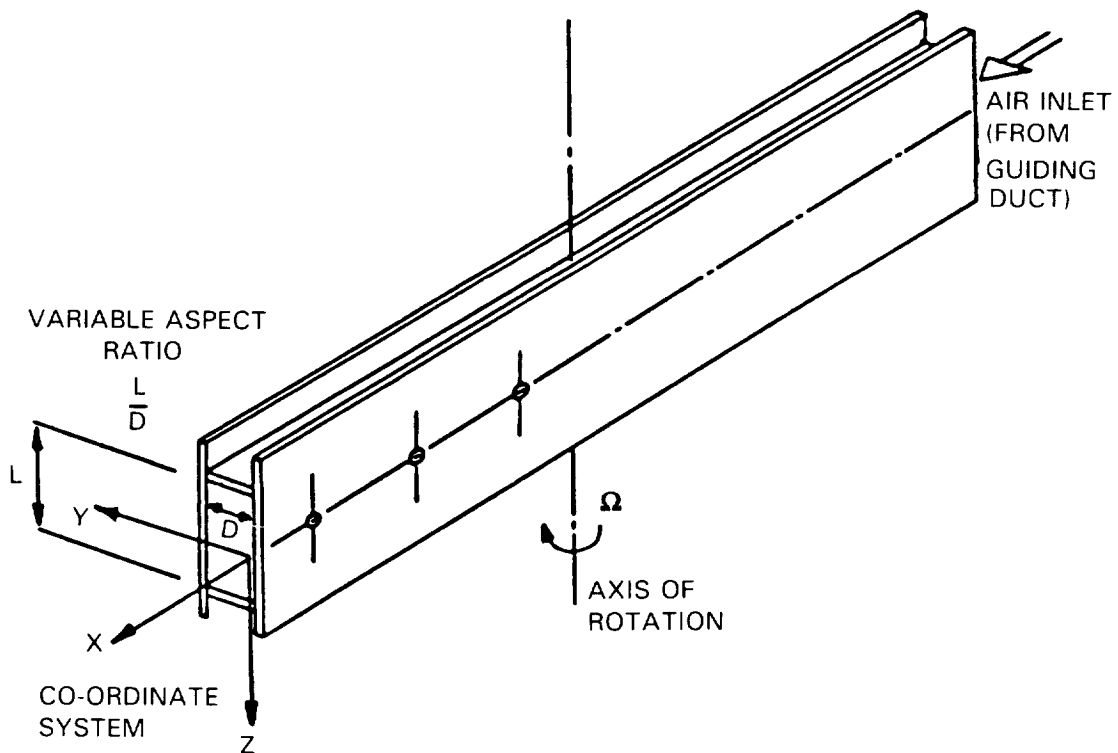


Figure 36.- Schematic of Moore's Test Section (Moore, 1967).

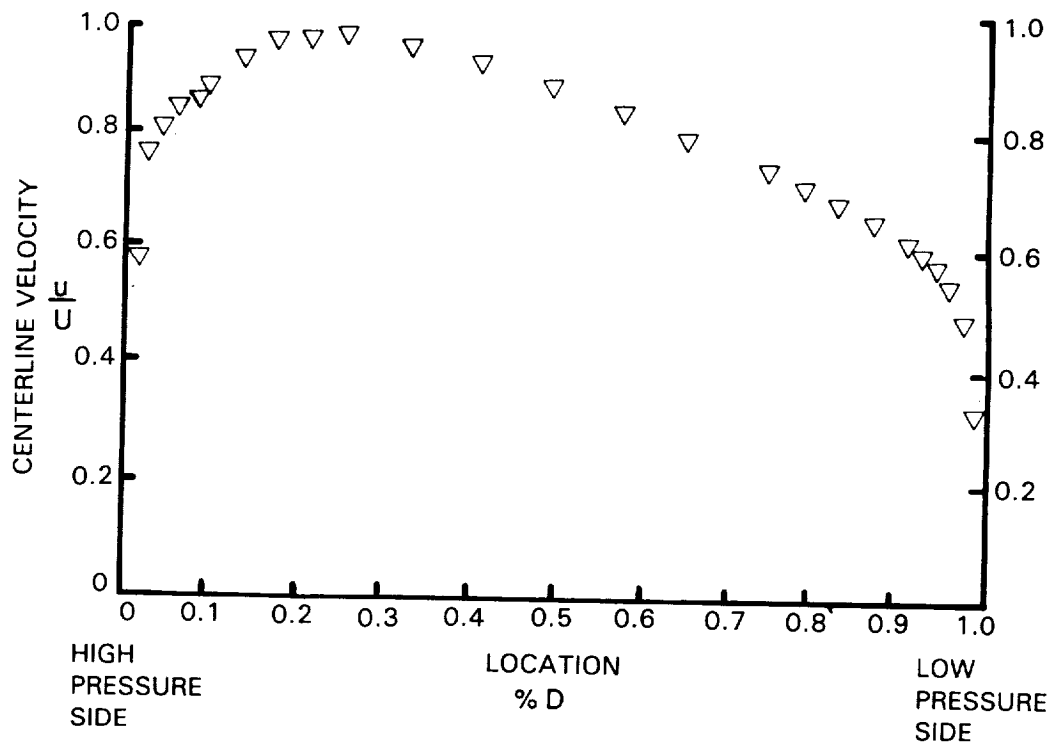


Figure 37.- Moore's Rotating Square Duct Centerline Velocity Profile (Moore, 1967).

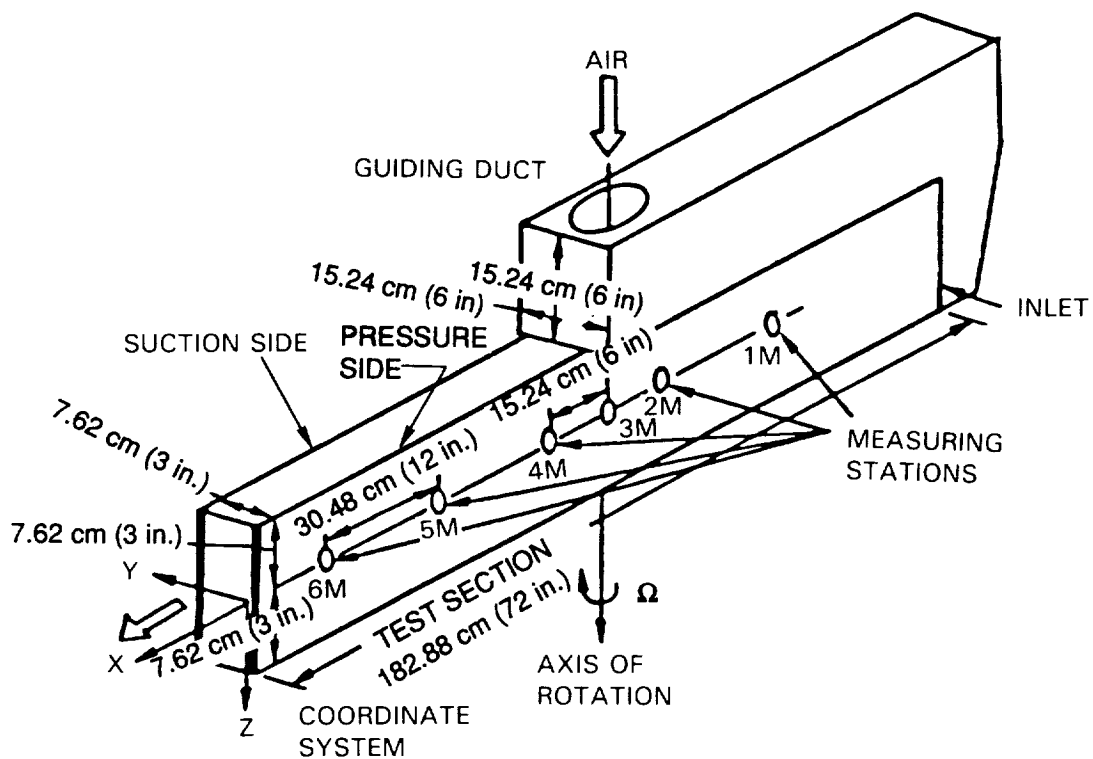


Figure 38.- Rotational Passage of Moon's Experiment (Moon, 1964).

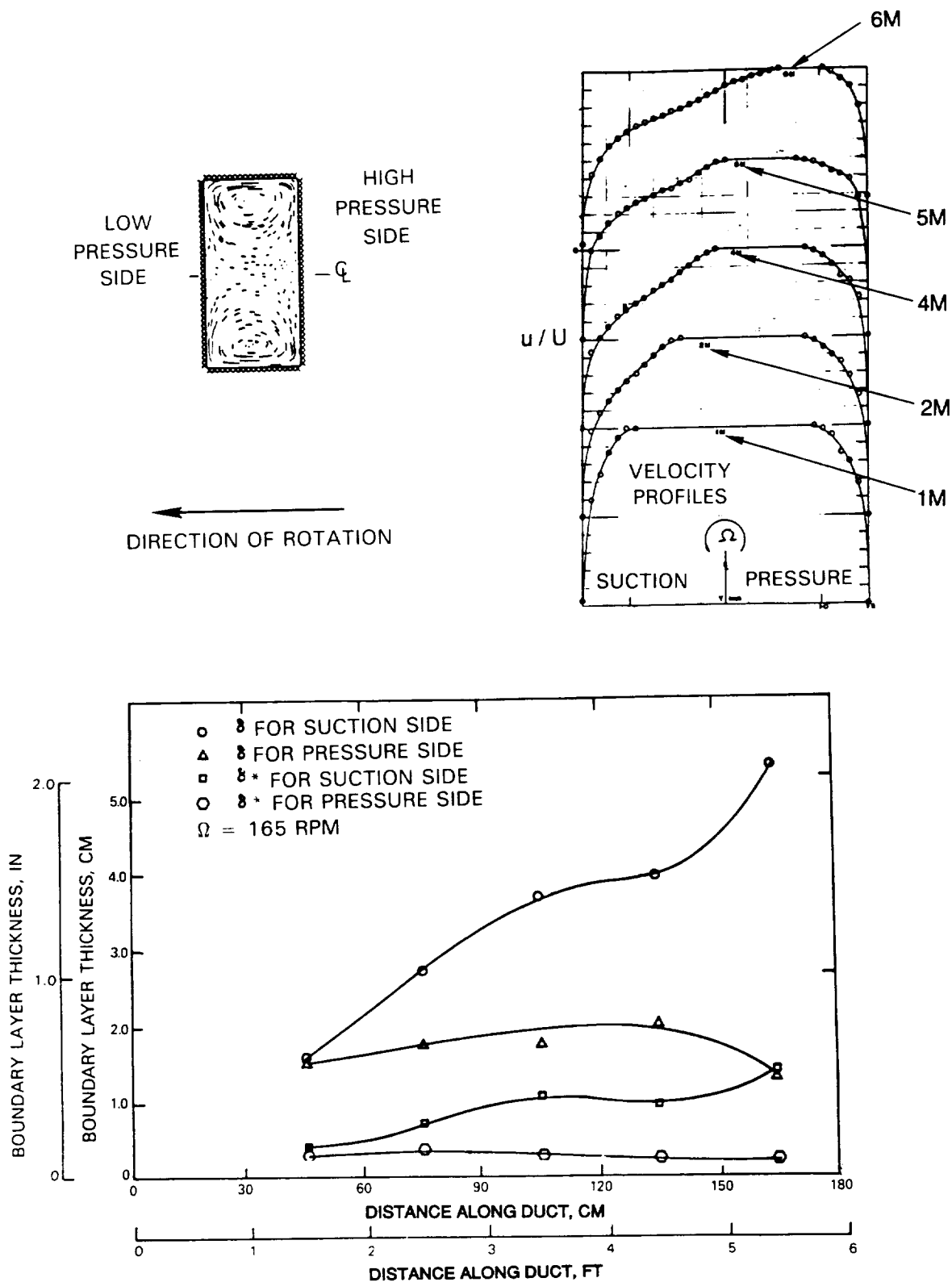


Figure 39.- Moon's Centerline Velocity Profiles with Boundary Layer and Displacement Thicknesses (Moon, 1964).

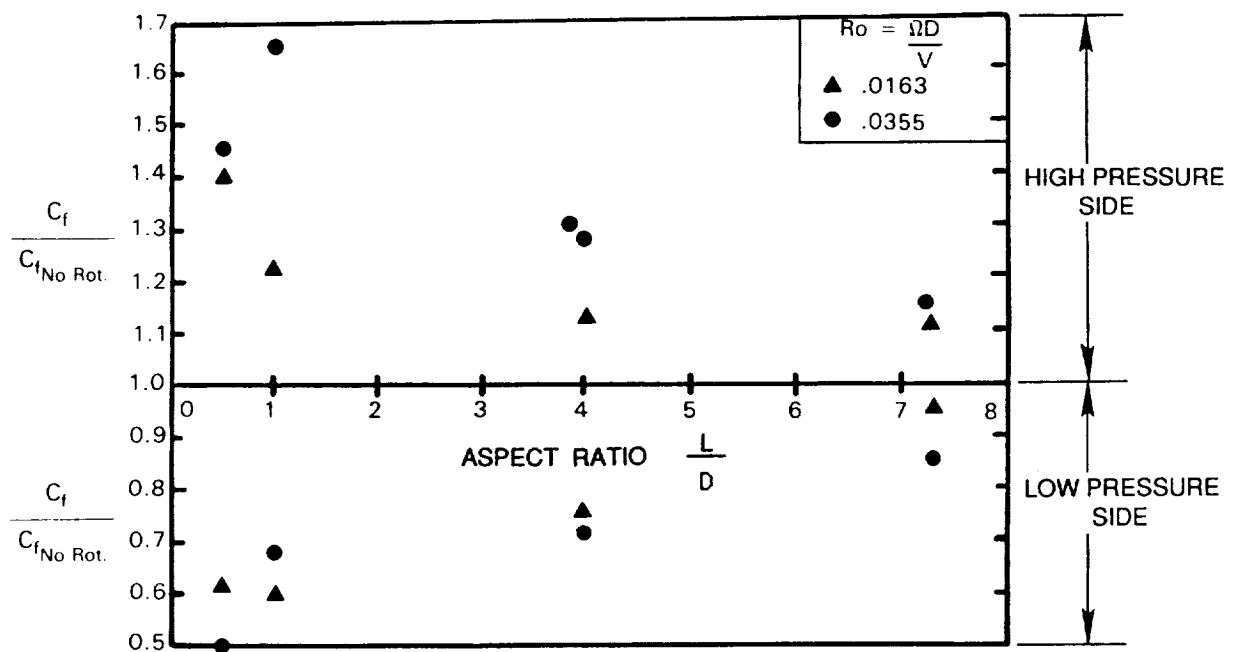


Figure 40.- Moore's Skin Friction Variation with Aspect Ratio (Moore, 1967).

The aforementioned results of Moore and Moon examine the effects of rotation on non-heated channel flows. The principle effect is the generation of secondary flow by the Coriolis acceleration and the resulting wall shear layer modifications. In the case of rotating heated flows, centrifugal buoyancy forces become an important factor.

Figure 41 depicts the directions of the convective and buoyancy forces during rotation. Centrifugal buoyancy forces accelerate the cold, more dense fluid particles away from the center of rotation, while the hot and lighter fluid particles tend toward the axis of rotation. In this experiment the hot fluid along the heated walls tends toward the center of rotation; in the first and third passages of the model, this direction opposes that of the mainstream flow. In the second model passage, where the coolant flows toward the axis of rotation, the mainstream and buoyancy force directions become aligned.

Eckert (1954) defined these two buoyancy conditions as "counterflow" and "parallel flow" and examined them in detail in nonrotating experiments. In Eckert's case, gravity rather than centrifugal forces provides the buoyancy acceleration. In a later section, his results will be compared to the data of this experiment. Eckert's results help explain some of the different trends seen in radially inward versus radially outward flowing coolant passages.

Buoyancy, therefore, complicates the three dimensional flow established by Coriolis secondary flow. The heated wall shear layer always tends toward the axis of rotation and interacts with the cross-stream secondary flows generated by the Coriolis force. In the smooth square duct, the result is a heat transfer distribution strongly dependant on local conditions, both axially and circumferentially. Boundary layers on each of the three surface types (leading, trailing and sidewalls) are influenced differently by the forces of rotation.



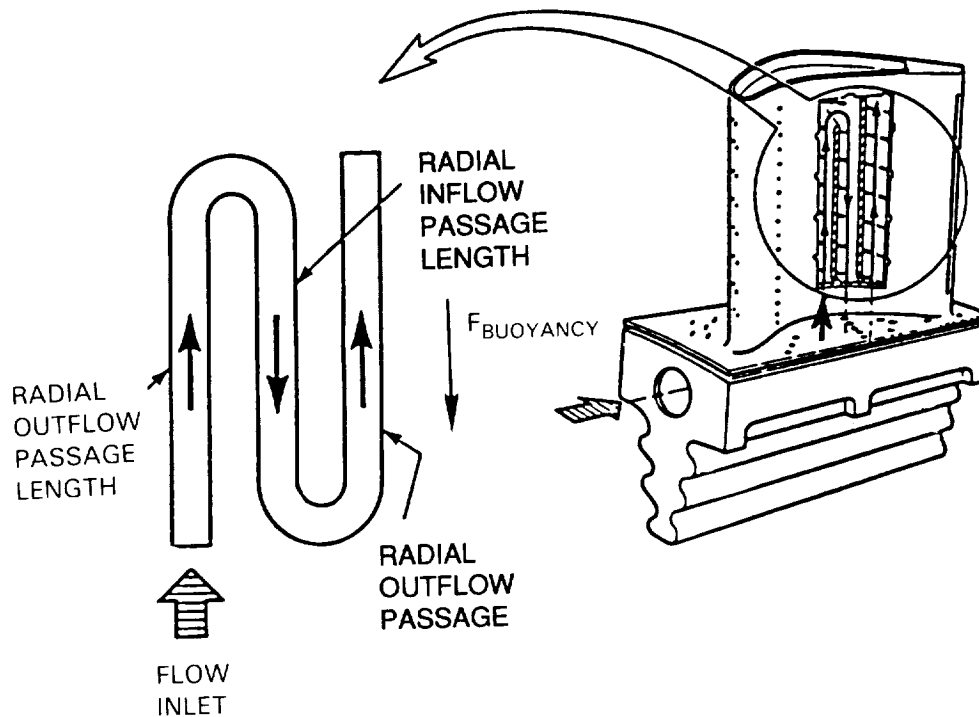


Figure 41.- Mainstream Flow Direction and Buoyancy Force Direction in Radially Inward and Radially Outward Flowing Passages.

## 8.2 Rotation Heat Transfer Correlations

In this section, each passage region (sidewall, high pressure wall, turn, and low pressure wall) will be correlated in a manner that is consistent with the dominate physics for that particular region.



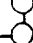

### 8.2.1 Side Wall Heat Transfer

This section covers the correlations of the sidewall heat transfer data in the first radially outward flowing passage. These correlations are presented first because the side wall heat transfer is the best behaved during rotation. On these surfaces, the heat transfer is dominated by the development of Coriolis-induced circulations and influenced less than the leading and trailing surfaces by the stabilizing/destabilizing effects of rotation.

The side wall heat transfer results for  $Re = 25,000$  for the first straight passage are shown in Figure 42. These data correspond with test section surfaces numbered B, C and D shown in Figure 8. The data is plotted as the ratio of rotating to stationary (measured) Nusselt number versus the rotational Grashof number divided by a Reynolds number squared. This ratio breaks down into the following combination of the basic dimensionless parameters:

$$\frac{Gr_x}{Re_x^2} = \left( \frac{\Omega d}{V} \right)^2 \left( \frac{R}{d} \right) \left( \frac{X}{d} \right) \left( \frac{\Delta T}{T} \right) \quad 8.1$$

LEG 1 -- FLOW OUTWARD  $Re \approx 25,000$ ,  $\bar{R}/d = 49$ ,  $\alpha = 0$

SYMBOL	$\diamond$	$\circ$	$\triangle$	$\nabla$	$\square$	$\triangleleft$	$\triangleright$	SYMBOL FLAGS
ROTATION NUMBER	0.006	0.06	0.12	0.18	0.25	0.35	0.50	
TEST NO. AT $\Delta T = 22.2^\circ\text{C}$ ( $40^\circ\text{F}$ )	—	—	—	115	9	105	—	
$\Delta T = 44.4^\circ\text{C}$ ( $80^\circ\text{F}$ )	101	117	8	114	4	106	7	
$\Delta T = 66.7^\circ\text{C}$ ( $120^\circ\text{F}$ )	—	—	—	113	10	107	—	
$\Delta T = 88.9^\circ\text{C}$ ( $160^\circ\text{F}$ )	—	—	—	116	102	—	—	

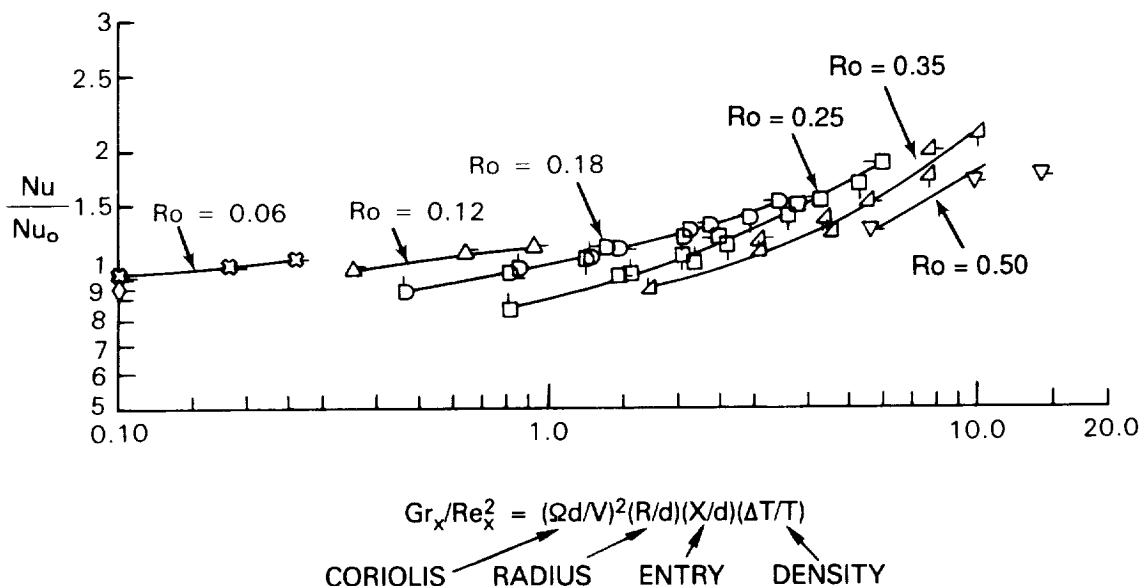


Figure 42.— Sidewall Heat Transfer at  $Re = 25,000$  for the First Straight Passage.

Each of these basic ratios effects the rate of heat transfer in rotating internal flows. The first parameter on the left-hand side of the equation is the rotation number  $Ro = \Omega d/V$ ; it equals the inverse of the Rossby number. The rotation number is a ratio of the Coriolis force to the inertia force. The second term represents the nondimensional radius ratio. The third term is an entry length or development length ratio and the last is a temperature or density ratio.

This method of plotting the data reveals an important trend. The heat transfer behavior changes with increasing rotation number. To facilitate correlating these trends, the data is separate into two groups: Regimes of low and high rotation number. In Figure 42, the steepness in slope of the curves of constant rotation number steadily increases with increases in the buoyancy parameter: Grashoff number divided by Reynolds number squared. At low rotation numbers, the curves remain relatively flat while for the higher rotation numbers the slopes increase. Below and above  $Ro=0.20$ , the rotation and buoyancy forces interact differently and correlate with different parameters. It should be noted that this rotation number level  $Ro = 0.20$ , will also be shown to mark the beginning of important trends on other surfaces in the passage.

a) Side Wall Heat Transfer Low Rotation Regime -- Figure 43 shows the sidewall heat transfer correlated for the low rotation regime  $Ro \leq 0.20$ . The correlating parameter is a product of the rotation number and the buoyancy parameter defined as the rotational Grashof number divided by the Reynolds number squared. The resulting parameter breaks down as follows:

$$\left( \frac{Gr_x}{Re_x^2} \right) Ro^{-1.5} = Ro^{0.5} \left( \frac{R}{d} \frac{X}{d} \frac{\Delta T}{T} \right) \quad (8.2)$$

The low rotation regime sidewall heat transfer data may be correlated as follows:

assuming  $Ro^{0.5}(R/d)(X/d)(\Delta T/T) < 0.9$ ;  $Nu/Nu_0 = 1.0$

and for  $Ro^{0.5}(R/d)(X/d)(\Delta T/T) > 0.9$ ; the following equation holds

$$\frac{Nu}{Nu_0} = 0.635 \left( Ro^{0.5} \frac{R}{d} \frac{X}{d} \frac{\Delta T}{T} \right)^{0.21} \quad (8.3)$$

This equation simplifies into the form

$$\frac{Nu}{Nu_0} = 0.635 Ro^{0.105} \left( \frac{R}{d} \frac{X}{d} \frac{\Delta T}{T} \right)^{0.21} \quad (8.4)$$

b) Side Wall Heat Transfer: High Rotation Regime -- Using  $(Gr_x/Re_x^2)Ro^{-0.8} = Ro^{1.2}(R/d)(X/d)(\Delta T/T)$  as the correlation parameter, Figure 44 presents the side wall heat transfer correlation for the high rotation regime,  $Ro \geq 0.20$ . The data collapses reasonably well for the combination of parameters shown, all but a few points fall within 10% of the equation:

$$\frac{Nu}{Nu_0} = 0.478 Ro^{0.552} \left( \frac{R}{d} \frac{X}{d} \frac{\Delta T}{T} \right)^{0.46} \quad (8.5)$$

The equation reveals the relative strength of each of the individual dimensionless parameters on rotating heat transfer for the side wall.

c) Side Wall Heat Transfer: Reynolds Number Effect -- In Figures 43 and 44, the effects of Reynolds number variations are also evaluated. The tests conducted where the Reynolds number varied from the base condition of  $Re = 25,000$  are indicated on the figures as half open symbols. The open symbols represent  $Re = 25,000$ .

In Figure 43 the test conducted at  $Re = 50,000$  and shown as the only half open symbols on the figure agree very well with this method of correlating the low rotation number regime data.

LEG 1- FLOW OUTWARD  $\bar{R}/d=49, \alpha=0$

SYMBOL	◇	◻	△	D	▲	SYMBOL FLAG
REYNOLDS NO.	25K	25K	25K	25K	50K	
ROTATION NO.	0.006	0.06	0.12	0.18	0.12	
TEST NO. AT $\Delta T = 22.2^\circ\text{C} (40^\circ\text{F})$	—	—	—	115	—	○
$\Delta T = 44.4^\circ\text{C} (80^\circ\text{C})$	101	117	8	114	104	○
$\Delta T = 66.7^\circ\text{C} (120^\circ\text{F})$	—	—	—	113	—	○
$\Delta T = 88.9^\circ\text{C} (160^\circ\text{F})$	—	—	—	116	—	○

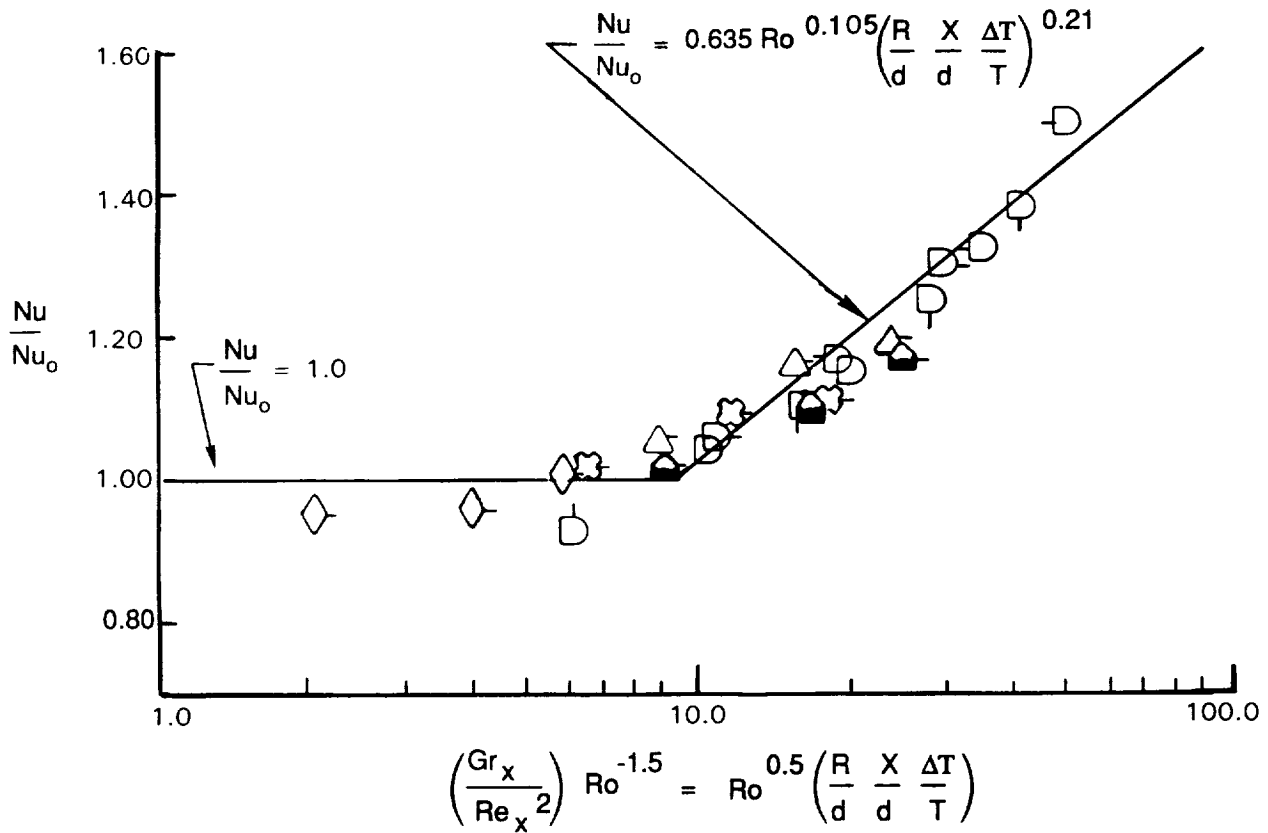


Figure 43.- Effect of Reynolds Number for Low Rotation ( $Ro \leq 0.20$ ) on Sidewall Heat Transfer.

LEG 1 - FLOW OUTWARD,  $\alpha = 0$

SYMBOL	●	◆	◇	◐	□	△	▽	SYMBOL FLAGS
REYNOLDS NO.	25K	25K	12.6K	50K	25K	25K	25K	
ROTATION NO.	0.24	0.35	0.25	0.25	0.25	0.35	0.50	
$\bar{R}/d$	33	33	49	49	49	49	49	
TEST NO. AT $\Delta T = 22.2^\circ\text{C}$ (40°F)	—	—	—	—	9	105	—	○
$\Delta T = 44.4^\circ\text{C}$ (80°F)	11	125	5	6	4	106	7	○
$\Delta T = 66.7^\circ\text{C}$ (120°F)	—	—	—	—	10	107	—	○
$\Delta T = 88.9^\circ\text{C}$ (160°F)	124	126	—	—	102	—	—	○

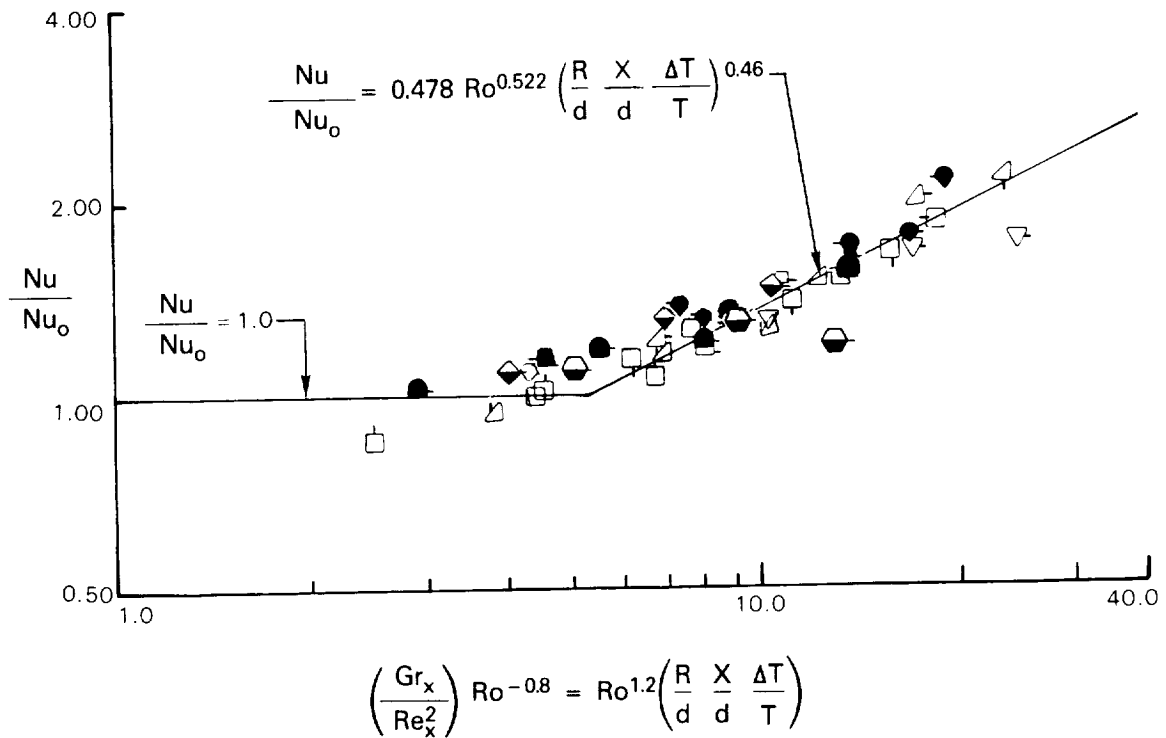


Figure 44.- Effect of Radius Variation on Sidewall Heat Transfer for High Rotation. ( $Ro > 0.20$ ).

Figure 44, correlating the high rotation regime data, compares both high and low Reynolds number cases with the data for  $Re = 25,000$ . Test number 5 at  $Re = 12,600$  and test number 6 at  $50,000$  were both conducted at the same rotation number,  $Ro = 0.25$ . The higher Reynolds number data agrees very well with the previously correlated data except for a single point. The lower Reynolds number data appears slightly higher than the correlation curve, yet still remains less than 15% above this curve. It is believed that low Reynolds number flow is more severely affected by rotation. For the moderate to high Reynolds number flows tested, the buoyancy parameter adequately accounts for the effects of Reynolds number variations.

d) Side Wall Heat Transfer Model Radius Effect -- All the open and half open symbol data correlated to this point has been for the nondimensional model radius ratio  $\bar{R}/d = 49$ . Four tests were conducted at a smaller radius,  $\bar{R}/d = 33$ . Figure 44 presents this data as solid symbols. The behavior is similar to that for the larger model radius. The buoyancy parameter, therefore, accounts for radius ratio effects on heat transfer for the range tested.

### 8.2.2 High Pressure Wall Heat Transfer

This section correlates the heat transfer results for the first passage on the high pressure side of the smooth square channel. This is a radially outward flowing passage, and the high pressure surface wall sections correspond to those numbered 50, 51, and 52 on the trailing side of the model shown in Figure 8.

The heat transfer results are correlated using a combination of the basic nondimensional parameters shown in the previous section.

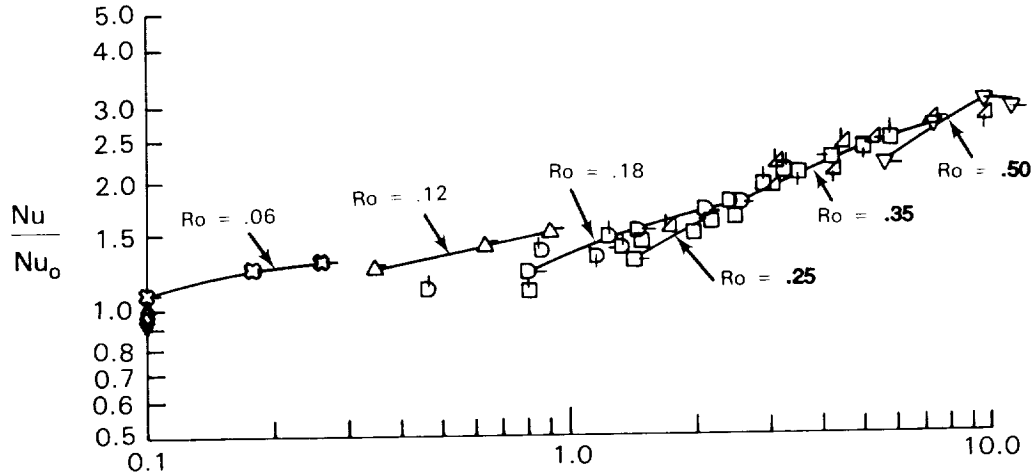
$$\left(\frac{\Omega d}{V}\right)^m \left(\frac{R}{d}\right)^n \left(\frac{X}{d}\right)^p \left(\frac{\Delta T}{T}\right)^q \quad (8.6)$$

In Figure 45 the heat transfer data for  $Re = 25,000$  and radius ratio  $\bar{R}/d = 49$  are shown. The data are plotted as the ratio of rotating to stationary heat transfer versus the nondimensional rotational buoyancy parameter,  $Gr_x/Re_x^2$ . This parameter breaks down into the group of dimensionless parameters listed above, where  $m=2$  and the powers  $n$ ,  $p$  and  $q$  are all equal to one. Lines of constant rotation number,  $Ro$ , connect wall test sections numbered 50, 51, and 52 in Figure 8.

Plotted in this manner, the data reveal an important trend. As the rotational buoyancy parameter increases, and the rotation number surpasses the critical level  $Ro = 0.20$ , the data tend toward falling on a uniform curve. But at lower levels of this parameter, there exist distinct curves of constant rotation number. It is believed that centripetal buoyancy forces become more dominant at higher rotation rates. As would be expected, the temperature or density ratio directly affects the behavior of the heat transfer during rotation. The conclusion reached here is that the complicated interaction between Coriolis and centripetal buoyancy forces greatly changes for low and high rotation number ranges. As a result, the following figures correlate the data according to the two distinct groups mentioned previously; low rotation and high rotation number regimes.

LEG 1- FLOW OUTWARD  $Re \approx 25,000$ ,  $\bar{R}/d = 49$ ,  $\alpha = 0$

SYMBOL	$\diamond$	$\boxtimes$	$\triangle$	$\square$	$\square$	$\triangle$	$\nabla$	SYMBOL FLAGS
ROTATION NUMBER	0.006	0.06	0.12	0.18	0.25	0.35	0.50	
TEST NO. AT $\Delta T = 22.2^\circ\text{C}$ ( $40^\circ\text{F}$ )	—	—	—	115	9	105	—	
$\Delta T = 44.4^\circ\text{C}$ ( $80^\circ\text{F}$ )	101	117	8	114	4	106	7	
$\Delta T = 66.7^\circ\text{C}$ ( $120^\circ\text{F}$ )	—	—	—	113	10	107	—	
$\Delta T = 88.9^\circ\text{C}$ ( $160^\circ\text{F}$ )	—	—	—	116	102	—	—	



$$\frac{Gr_x}{Re_x^2} = \left(\frac{\Omega d}{V}\right) \left(\frac{\Omega R}{V}\right) \left(\frac{X}{d}\right) \left(\frac{\Delta T}{T}\right) = Ro^2 \left(\frac{R}{d}\right) \left(\frac{X}{d}\right) \left(\frac{\Delta T}{T}\right)$$

Figure 45.— High Pressure Surface Heat Transfer for Radially Outward Flow  
 $Re = 25,000$ .

a) High Pressure Side: Low Rotation Number Regime  $Ro < 0.20$  -- Heat transfer on the high pressure side of the outward flowing passage for the low rotation number regime is correlated on Figure 46. The data correlates reasonably well with the parameter

$$Ro^{0.5} \left(\frac{R}{d} \frac{X}{d}\right) \left(\frac{\Delta T}{T}\right)^{0.65} \quad (8.7)$$

For  $Ro^{0.5}(R/d)(X/d)(\Delta T/T)^{0.65} < 12$ , the data can be fit with the constant ratio  $Nu/Nu_0 = 1.0$ , while for  $Ro^{0.5}(R/d)(X/d)(\Delta T/T)^{0.65} \geq 12$

$$\frac{Nu}{Nu_0} = 0.424 Ro^{0.175} \left(\frac{R}{d} \frac{X}{d}\right)^{.35} \left(\frac{\Delta T}{T}\right)^{0.228} \quad (8.8)$$

The open symbols represent data where radius and Reynolds number are held constant and rotation rates and temperature ratios are varied. Also  $X/d$  is varied as data is acquired for 3 locations (Sections 50,51,52 of Fig. 8) in

LEG 1 - FLOW OUTWARD  $\bar{R}/d$ ,  $\alpha = 0$

SYMBOL	◇	◻	△	D	■	●	SYMBOL FLAGS
REYNOLDS NO.	25K	25K	25K	25K	50K	75K	
ROTATION NO.	0.006	0.06	0.12	0.18	0.12	0.12	
TEST NO. AT $\Delta T = 22.2^\circ\text{C}$ (40°F)	—	—	—	115	—	—	
$\Delta T = 44.4^\circ\text{C}$ (80°F)	101	117	8	114	104	103	○
$\Delta T = 66.7^\circ\text{C}$ (120°F)	—	—	—	113	—	—	○
$\Delta T = 88.9^\circ\text{C}$ (160°F)	—	—	—	116	—	—	○

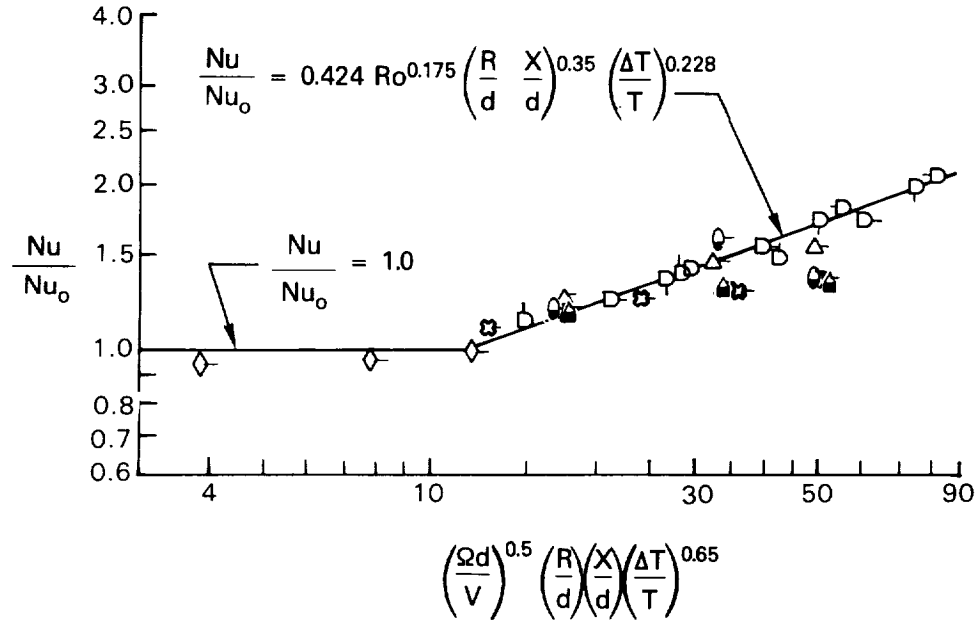


Figure 46.— Effect of Reynolds Number for Low Rotation ( $Ro < 0.20$ ) on High Pressure Surface Heat Transfer.

the straight section. The half open symbols indicate two higher Reynolds number test conditions. The largest discrepancies occur for those test sections located farthest downstream of the entrance or just before the turn. Here the correlation overpredicts the data. It is suspected that the turn effects propagate upstream and affect these few data points. In general the low rotation number regime data are well correlated by the above equation.

b) High Pressure Side: High Rotation Number Regime  $Ro > 0.20$  -- Figure 47 correlates the high pressure surface heat transfer data for rotation number  $Ro \geq 0.20$ . This correlation incorporates singular variations in rotation rate, Reynolds number, radius, density or temperature ratio, and location in the passage. The data best collapses with the parameter

$$\left( \frac{Gr_x}{Re_x^2} \right) = Ro^2 \left( \frac{R}{d} \frac{X}{d} \frac{\Delta T}{T} \right) \quad (8.9)$$



LEG 1 - FLOW OUTWARD,  $\alpha = 0$

SYMBOL	■	●	◆	◐	□	△	▽	SYMBOL FLAGS
REYNOLDS NO.	25K	25K	12.6K	50K	25K	25K	25K	
ROTATION NO.	0.24	0.35	0.25	0.25	0.25	0.35	0.50	
$\bar{R}/d$	33	33	49	49	49	49	49	
TEST NO. AT $\Delta T = 22.2^\circ\text{C}$ (40°F)	—	—	—	—	9	105	—	○
$\Delta T = 44.4^\circ\text{C}$ (80°F)	11	125	5	6	4	106	7	○
$\Delta T = 66.7^\circ\text{C}$ (120°F)	—	—	—	—	10	107	—	○
$\Delta T = 88.9^\circ\text{C}$ (160°F)	124	126	—	—	102	—	—	○

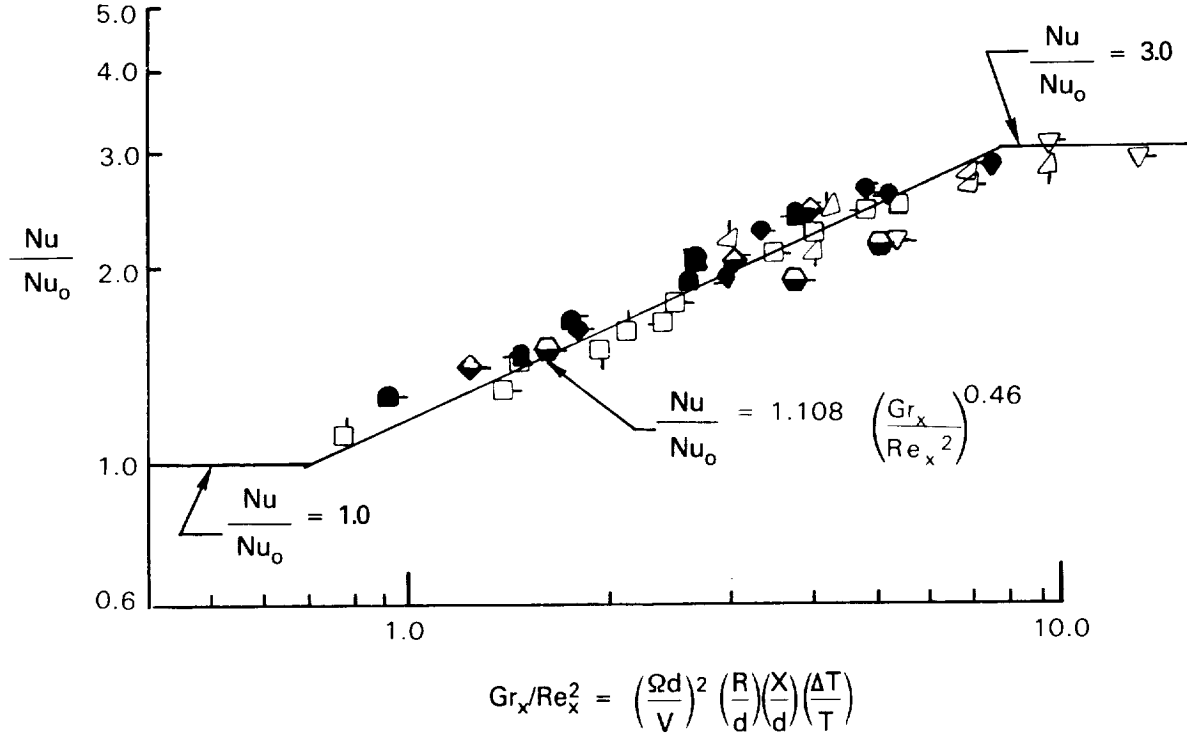


Figure 47.— Effect of Radius Variation on High Pressure Surface Heat Transfer for High Rotation Regime ( $Ro > 0.20$ ).

and can be fit with a three part equation.

$$\frac{Nu}{Nu_0} = 1.0 \text{ for } \frac{Gr_x}{Re_x^2} < 0.8 \quad (8.10)$$

$$\frac{Nu}{Nu_0} = 1.108 \left(\frac{Gr_x}{Re_x^2}\right)^{0.46} \text{ for } 0.8 \leq \frac{Gr_x}{Re_x^2} \leq 8.0 \quad (8.11)$$

$$\frac{Nu}{Nu_0} = 3.0 \text{ for } \frac{Gr_x}{Re_x^2} > 8.0 \quad (8.12)$$

### 8.2.3 Turn Heat Transfer

The experimental model shown in Figure 8 includes three instrumented turns. The first and third turns, referred to as the tip turns, behave very differently from the root turn (second turn) during rotation. Centripetal buoyancy drives the rotating turn heat transfer and the parameter  $(\Omega R/V)(\Delta T/T)$  correlates the data. Each turn contains a total of eight heated wall sections where heat transfer coefficients were obtained. The inside wall of each turn was not instrumented.

a) Tip Turn Heat Transfer -- Figure 48 presents the tip turn outside wall heat transfer results for all values of  $Ro$  and  $\Delta T/T$  tested at  $Re = 25,000$ . Plotted versus the centripetal buoyancy parameter,  $(\Omega R/V)(\Delta T/T)$ , the heat transfer ratio is correlated at each wall section or streamwise location. The largest increases occur at the beginning of the turn and gradually decrease through the turn. Solid symbols correspond to wall sections 5 and 7, and open symbols correspond to sections 6 and 8.

Figure 49(a and b) show the leading (open symbols) and trailing (solid symbols) surface heat transfer results plotted with the centripetal buoyancy parameter. The upper portion of the figure examines the first half of the turn and the lower portion shows the second half. In the first half of the turn, the trailing wall heat transfer is the higher of the two. As the flow turns the corner, reversing from radially outward to radially inward, the leading surface heat transfer becomes the higher of the two sides in the second half of the turn.

Unlike the results of the straight sections, the heat transfer on both the leading and trailing surfaces of the tip turn is generally augmented with rotation. The low pressure surface does not experience a decrease in heat transfer because the centripetal buoyancy forces dominate the Coriolis forces. As the flow negotiates the turn, the cross channel pressure gradient drives the low momentum fluid toward the inside of the turn. Rotation causes the less dense wall fluid to gravitate toward the inside of the turn as the denser mainstream fluid accelerates away from the axis of rotation. In the tip turn the centripetal buoyancy forces enhance the secondary motions already generated by the curvature of the turn; the secondary flows resulting from both curvature and rotation are aligned parallel and complement one another. The result in the tip turn is an intensification in the secondary motions normally generated in a turn and significant increases in the heat transfer during rotation.

b) Root Turn Heat Transfer -- All surfaces in the root turn experience a drop in heat transfer during rotation. Similar to the tip turn, the centripetal forces accelerate the dense mainstream fluid away from the axis of rotation. In the root turn, this direction is toward the inside wall of the turn. The mainstream coolant that normally impinges on the outside wall as the flow turns is acted upon by rotation and inhibited from generating stream secondary flows. As a result, the heat transfer enhancing mechanism of the root turn is hindered.

$$Re \approx 25,000, \bar{R}/d = 49, \alpha = 0$$

SYMBOL	$\diamond$	$\boxtimes$	$\triangle$	$\square$	$\square$	$\triangle$	$\nabla$	SYMBOL
ROTATION NUMBER	0.006	0.06	0.12	0.18	0.25	0.35	0.50	FLAGS
TEST NO. AT $\Delta T = 22.2^\circ\text{C}$ (40°F)	—	—	—	115	9	105	—	$\circ$
$\Delta T = 44.4^\circ\text{C}$ (80°F)	101	117	8	114	4	106	7	$\circ$
$\Delta T = 66.7^\circ\text{C}$ (120°F)	—	—	—	113	10	107	—	$\circ$
$\Delta T = 88.9^\circ\text{C}$ (160°F)	—	—	—	116	102	—	—	$\circ$

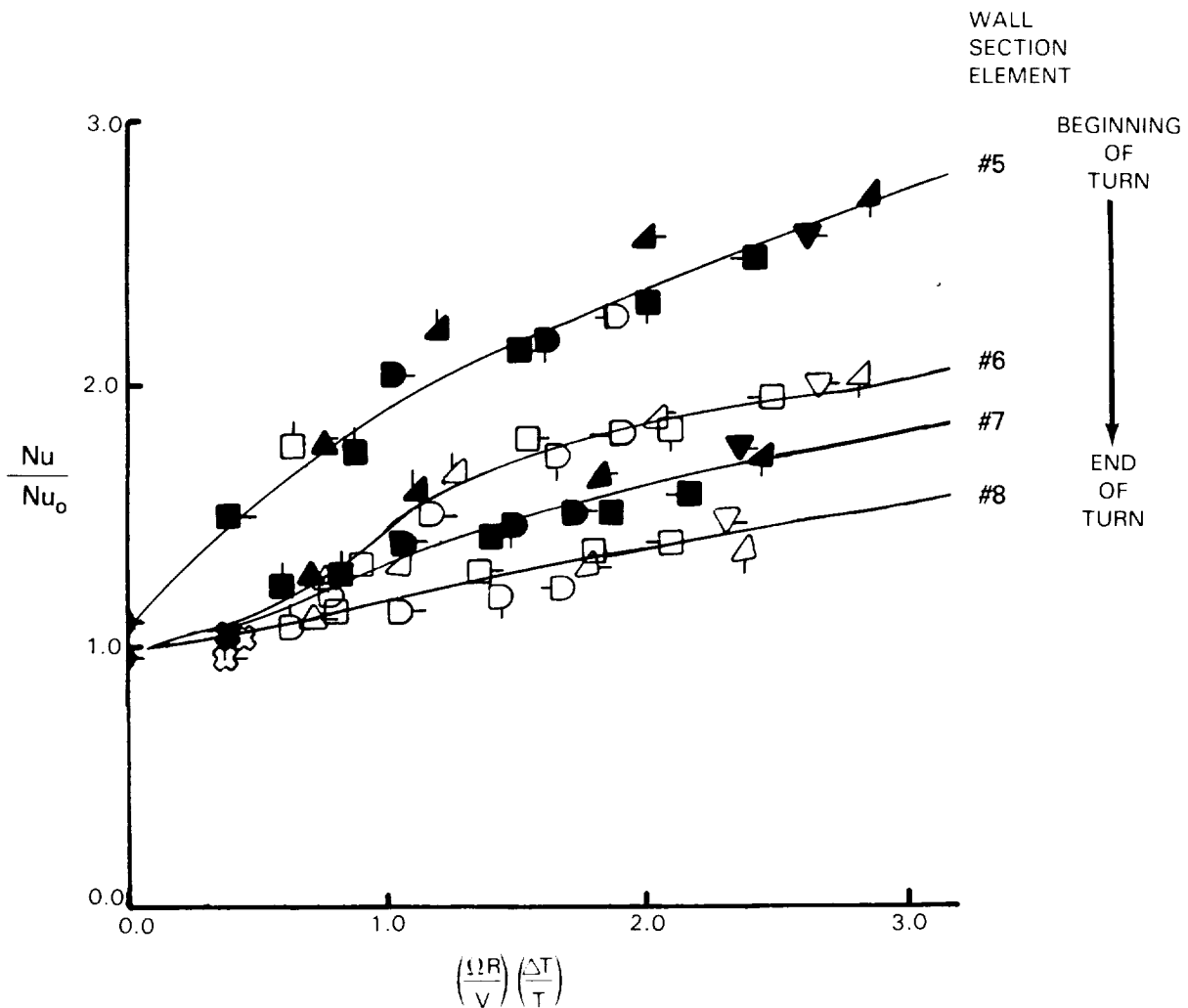


Figure 48.— Tip Turn Heat Transfer: Outer Sidewalls,  $Re = 25,000$ .

$$Re \approx 25,000, \bar{R}/d = 49, \alpha = 0$$

SYMBOL	$\diamond$	$\star$	$\triangle$	$\square$	$\square$	$\triangle$	$\nabla$	SYMBOL FLAGS
ROTATION NUMBER	0.006	0.06	0.12	0.18	0.25	0.35	0.50	
TEST NO. AT $\Delta T = 22.2^\circ\text{C}$ (40°F)	—	—	—	115	9	105	—	$\circ$
$\Delta T = 44.4^\circ\text{C}$ (80°F)	101	117	8	114	4	106	7	$\circ$
$\Delta T = 66.7^\circ\text{C}$ (120°F)	—	—	—	113	10	107	—	$\circ$
$\Delta T = 88.9^\circ\text{C}$ (160°F)	—	—	—	116	102	—	—	$\circ$

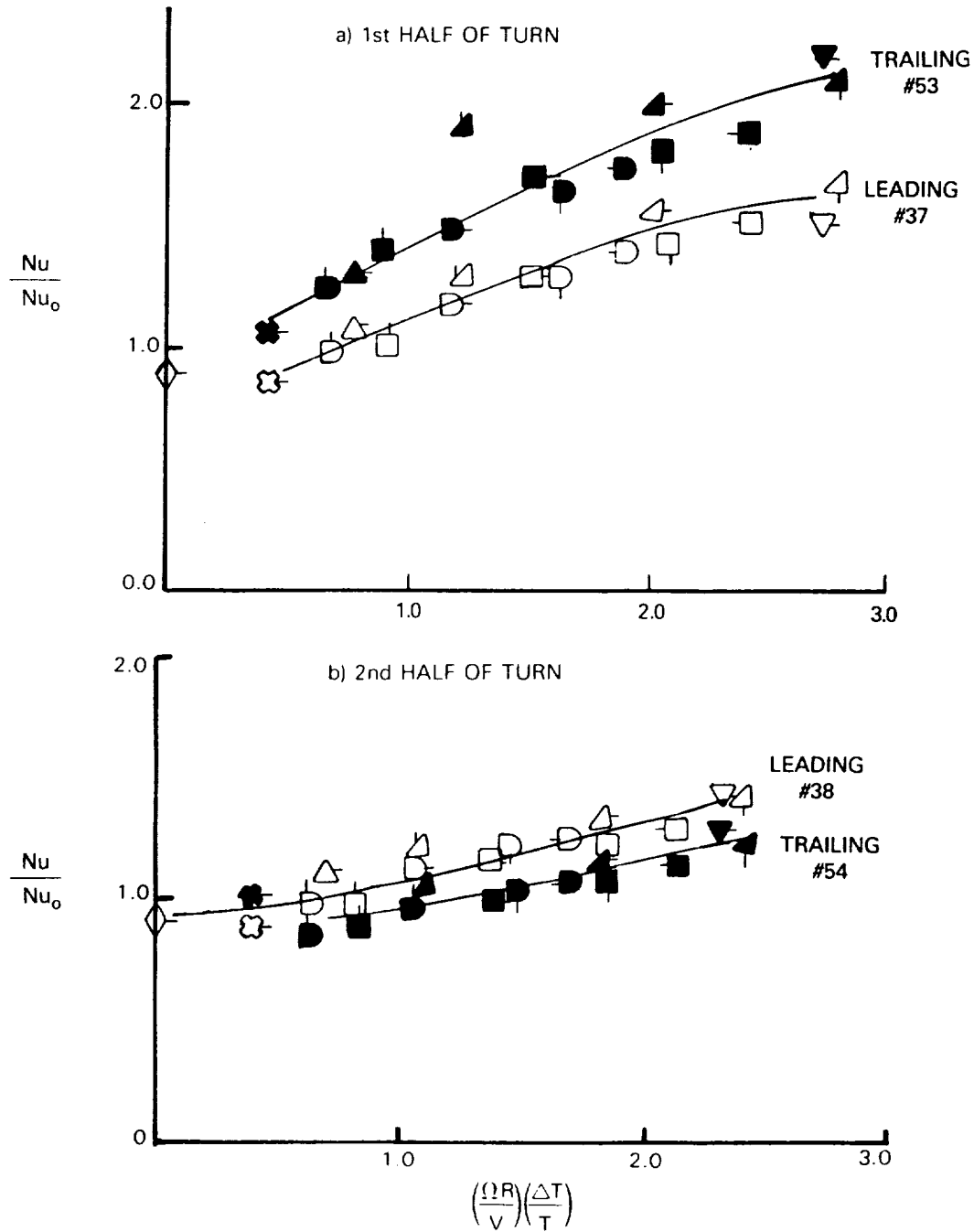


Figure 49.— Leading and Trailing Surface Heat Transfer in Tip Turn  
(Solid Symbols = Trailing Surface).

It is interesting to note that during rotation the root turn heat transfer almost reduces to the level of heat transfer in a straight duct. This suggests that the secondary flows in the root turn can almost be eliminated by centripetal forces. For example, at wall section no. 27 (Figure 50), the heat transfer ( $Nu/Nu_0 = 0.41$ ) decreases from the stationary  $Nu_0 = 165$  to the rotating  $Nu = 68$  at rotation number,  $Ro = 0.24$  (test no. 4). This drop in heat transfer goes from 315% to 130% of stationary fully developed turbulent heat transfer ( $Nu_\infty = 52.3$ ). Essentially, the centripetal buoyancy forces reduce the root turn secondary flows to the magnitude where the flow turns the corner as if it was in a straight duct.

Figure 50 illustrates the root turn results for the outside walls. As noted, rotation decreases heat transfer everywhere in the root turn. The upper portion of Figure 50 presents the wall sections numbered 26 and 29 which are located at the beginning and end of the turn, while those numbered 27 and 28, located in the bucket region of the turn, are shown in the lower portion. They are presented in this manner because of their similar behavior with rotation. The two sections in the bucket region shown the larger decrease in heat transfer, leveling off near 45%. The beginning and end of the turn drop to 60% of the stationary levels.

Figure 51 quantifies the decreases in root turn heat transfer on the leading and trailing surfaces. All four of these surfaces settle around 60% of the stationary measured heat transfer rates.

c) Conclusion: Turns -- The rotation of internally cooled turns significantly changes the heat transfer from the non-rotated levels. Generally, non-rotated turns show a 200-300% increase over fully developed straight duct, turbulent heat transfer. In rotated tip turns, these levels are further increased and in root turns, they are reduced. The dominating mechanism is centripetal buoyancy which sets up forces either opposed to, or in the same direction as, the turn induced secondary flows.

#### 8.2.4 Low Pressure Wall Heat Transfer

This section examines the heat transfer on the leading surface in the first radially outward flowing passage of the model. During rotation this surface becomes the low pressure surface as Coriolis forces accelerate low momentum fluid on the sidewalls toward this surface. The isolated effect of rotation number for Reynolds number of  $Re = 25,000$  is depicted in Figure 52. As the rotation number increases, the heat transfer ratio decreases along the passage near the inlet. For all of the remaining locations on the leading side of the passage, the heat transfer ratio decreases and then increases again with increasing rotation number. Examination of the leading side results shows that the location of the local minimum in the heat transfer ratio for each rotation number moves toward the inlet of the passage as the rotation number is increased.

Figure 53 plots all the leading side data for  $\Delta T = 44.4^\circ C$  ( $80^\circ F$ ) and  $Re = 25,000$ . The data is plotted as  $Nu_x$ ,  $X$  being the distance from the inlet, versus a rotational Rayleigh number. The Rayleigh number was chosen as a correlation parameter in order to determine what flow regime (laminar, transitional or turbulent) the low pressure wall data was in.

$Re \approx 25,000, R/d = 49, \alpha = 0$

SYMBOL	$\diamond$	$\star$	$\triangle$	$\square$	$\square$	$\triangle$	$\nabla$	SYMBOL FLAGS
ROTATION NUMBER	0.006	0.06	0.12	0.18	0.25	0.35	0.50	
TEST NO. AT $\Delta T = 22.2^\circ C (40^\circ F)$	—	—	—	115	9	105	—	$\circ$
$\Delta T = 44.4^\circ C (80^\circ F)$	101	117	8	114	4	106	7	$\circ$
$\Delta T = 66.7^\circ C (120^\circ F)$	—	—	—	113	10	107	—	$\circ$
$\Delta T = 88.9^\circ C (160^\circ F)$	—	—	—	116	102	—	—	$\circ$

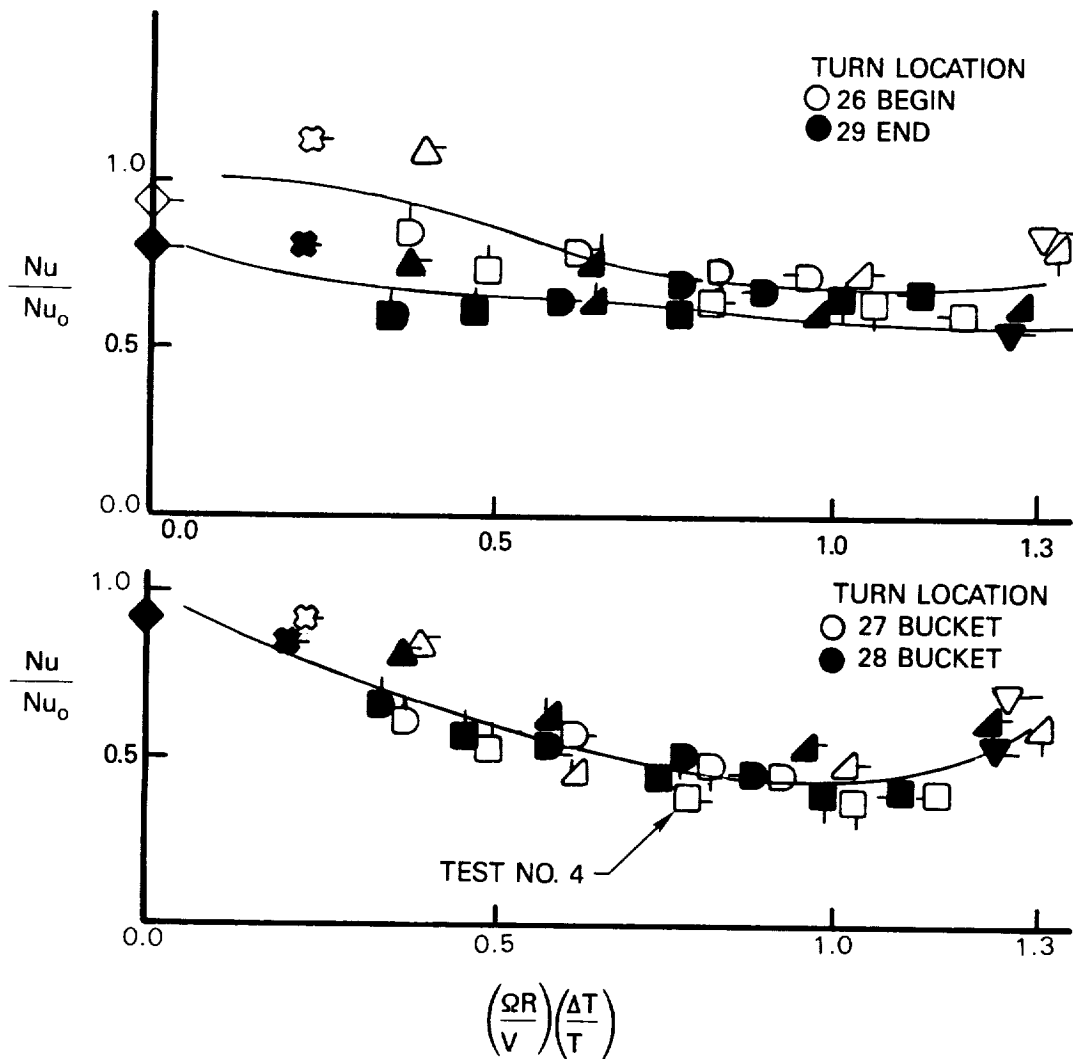


Figure 50.— Root Turn Heat Transfer: Outer Sidewalls,  $Re = 25,000$ .

$Re \approx 25,000, \bar{R}/d = 49, \alpha = 0$

SYMBOL	$\diamond$	$\star$	$\triangle$	$\square$	$\square$	$\triangle$	$\nabla$	SYMBOL FLAGS
ROTATION NUMBER	0.006	0.06	0.12	0.18	0.25	0.35	0.50	
TEST NO. AT $\Delta T = 22.2^\circ\text{C} (40^\circ\text{F})$	—	—	—	115	9	105	—	
$\Delta T = 44.4^\circ\text{C} (80^\circ\text{F})$	101	117	8	114	4	106	7	
$\Delta T = 66.7^\circ\text{C} (120^\circ\text{F})$	—	—	—	113	10	107	—	
$\Delta T = 88.9^\circ\text{C} (160^\circ\text{F})$	—	—	—	116	102	—	—	

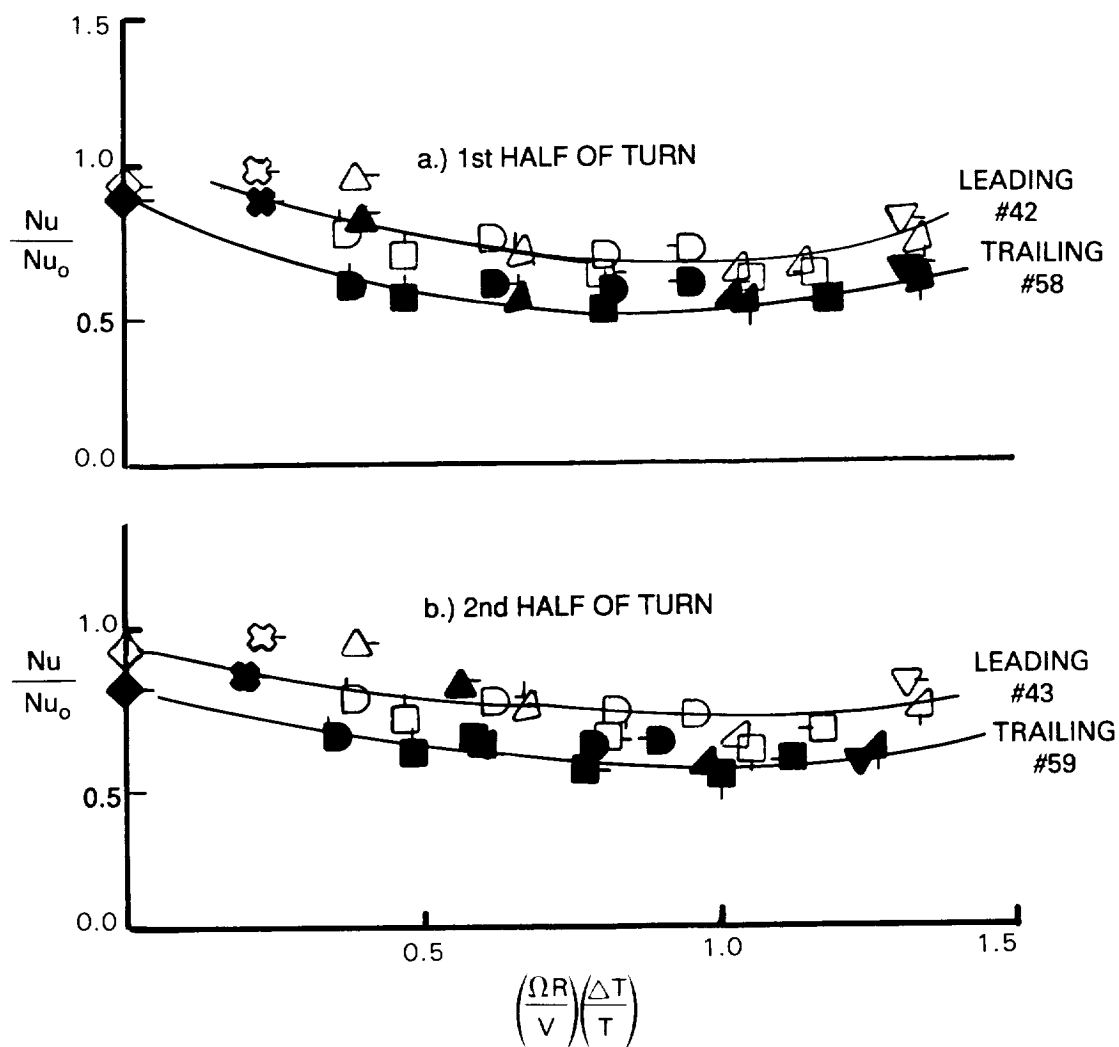


Figure 51.- Leading and Trailing Surface Heat Transfer in Root Turn  
(Solid Symbols = Trailing Surface).

$$Re \approx 25,000$$

$$\left(\frac{\Delta T}{T}\right)_{in} = 0.13$$

$$\Delta T = 44^\circ \text{C} (80^\circ \text{F})$$

$$\bar{R}/d = 49$$

$$\alpha = 0$$

SYMBOL	□	△	○	◇	▽
TEST NO.	1	8	4	106	7
ROTATION NO.	0.0	0.12	0.24	0.35	0.48
RPM	0	275	550	825	1100

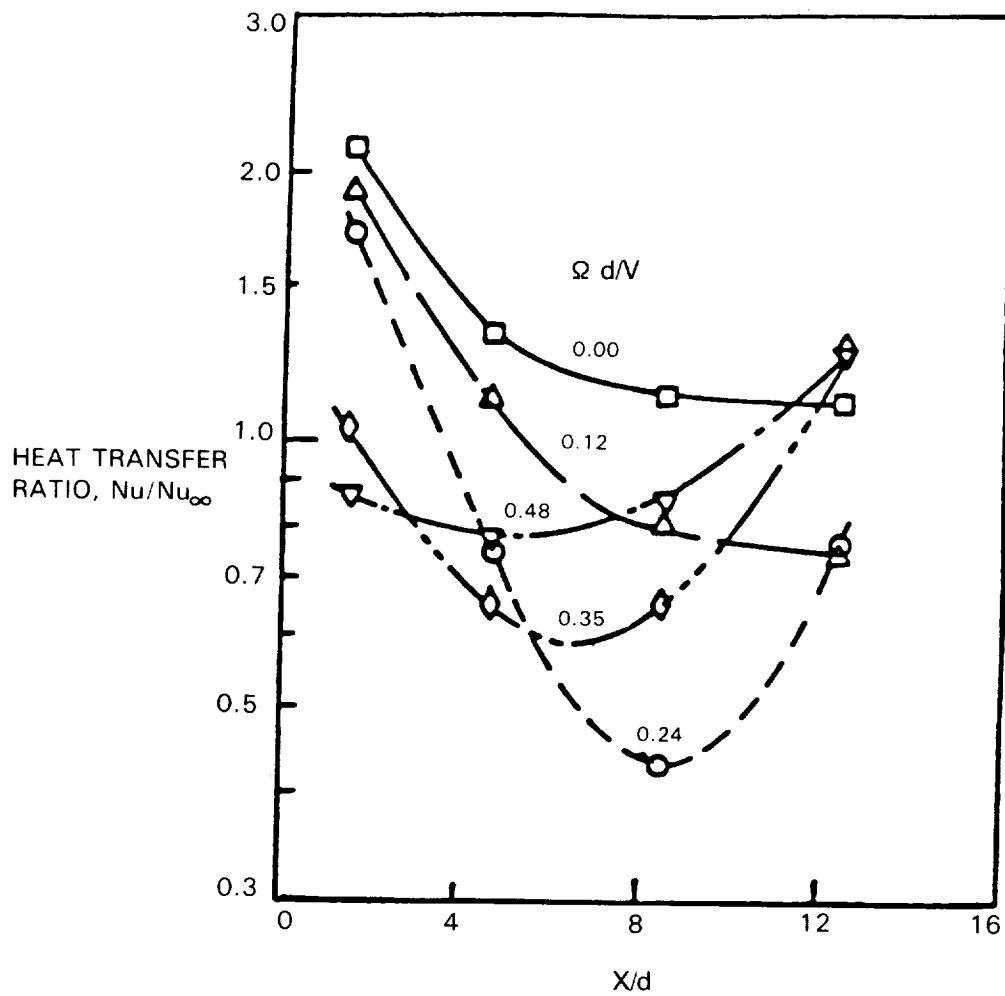


Figure 52.- Effect of Rotation Number on Heat Transfer Ratio for Low Pressure Surface;  $Re = 25,000$   $(\Delta\rho/\rho)_{in} = 0.13$ ,  $\bar{R}/d = 49$ .



$$Re \approx 25,000 \quad \Delta T \approx 44.4^\circ C (80^\circ F)$$

$$\left(\frac{\Delta T}{T}\right)_{in} = 0.13 \quad \bar{R}/d = 49$$

$$\alpha = 0$$

SYMBOL	◇	X	△	◻	◻	◻	▽
TEST NO.	101	117	8	114	4	106	7
ROTATION NO.	0.006	0.06	0.12	0.18	0.25	0.35	0.50
RPM	15	145	275	412	550	825	1100

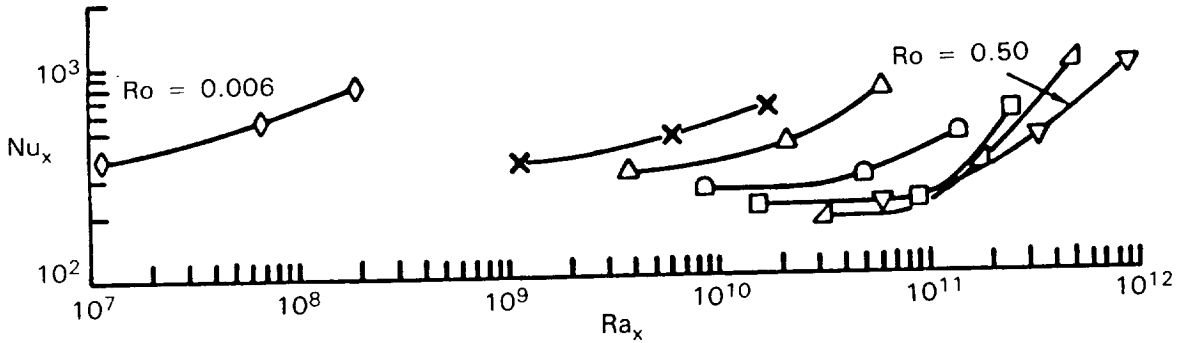


Figure 53.- Leading Side Heat Transfer for First Passage: Radially Outward Flow (Test section elements 34, 35, 36).

$$Ra_x = \left( \frac{\Omega^2 R X^3 \Delta T}{\nu^2 T_b} \right) Pr \quad (8.13)$$

Note for each line of constant  $Ro$  there are three data points. Each of these corresponds to one of the three test section elements downstream of the guard heaters at the inlet: elements 34, 35, and 36 in Figure 8.

For the higher rotation rates,  $Ro \geq 0.25$ , the heat transfer, plotted as  $Nu_x$ , tends to collapse on a single curve. This curve attains a minimum around  $Nu_x = 210$  and begins a sharp upturn at  $Ra_x = 10^{11}$ . Based on the results to date, it is believed that for the lower rotation rates, the data are predominantly governed by Coriolis forces, while at the highest rates centripetal buoyancy dominates. There is a flow regime between these two extremes where the wall shear layer is believed to be laminar.

Figure 54 plots  $Nu_x$  versus  $Ra_x$ , for high rotation,  $Ro \geq 0.25$ , and it includes all four temperature cases (Figure 53 included only  $\Delta T = 44.4^\circ C (80^\circ F)$ ). Two important points should be emphasized. Firstly for  $10^{10} < Ra_x < 10^{11}$  the heat transfer is constant at  $Nu_x = 210$ . This level defines the minimum heat transfer attained for  $Re = 25,000$ . Secondly, for  $Ra_x > 10^{11}$ ,  $Nu_x$  increases significantly. This increase for large  $Ra_x$  is believed to be induced by centripetal buoyancy forces.

SYMBOL	$\square$	$\triangle$	$\nabla$	SYMBOL FLAGS
ROTATION NO.	0.25	0.35	0.50	
TEST NO. AT $\Delta T = 22.2^\circ\text{C}$ ( $40^\circ\text{F}$ )	9	105	—	$\circ$
$\Delta T = 44.4^\circ\text{C}$ ( $80^\circ\text{F}$ )	4	106	7	$\circ$
$\Delta T = 66.7^\circ\text{C}$ ( $120^\circ\text{F}$ )	10	107	—	$\circ$
$\Delta T = 88.9^\circ\text{C}$ ( $160^\circ\text{F}$ )	102	—	—	$\circ$

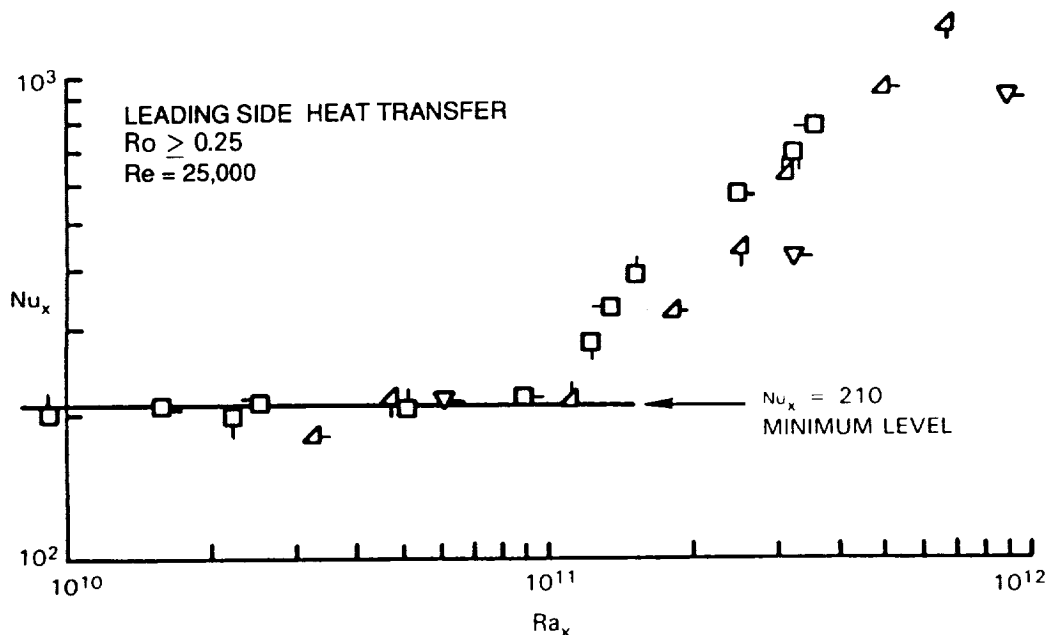


Figure 54.- Leading Side Heat Transfer  $Ro \geq 0.25$ :  $Re = 25,000$   
 (Test section elements 34, 35, 36).

Consider the range of data where the heat transfer is constant at  $Nu_x = 210$  (Figure 54). If this data is compared to both the fully turbulent stationary heat transfer and to Kays (1966), analytical solution for laminar flat plate heat transfer:  $Nu_x = 0.565 Pr^{1/2} Re_x^{1/2}$  (Figure 55), it appears to be nearly identical to the laminar correlation, thus supporting the hypothesis that a flow regime containing laminar shear layer does exist.

These results can be further substantiated by examining the work of J.P. Johnston (1970). In his rotating channel experiment at Stanford University, he discovered regions where the boundary layer on the leading wall was completely laminar for Reynolds numbers as high as  $Re = 15,000$ . Figure 56 schematically depicts the important characteristics of this flowfield.

On the leading side of the 7:1 aspect ratio channel, Johnston saw a nearly parabolic mean velocity profile and an absence of the bursting process normally seen at the wall in turbulent flow. On the trailing side of the channel Taylor-Goertler type vortices developed within the turbulent section of the mean velocity profile. The laminar boundary layer on the leading surface and the highly turbulent boundary layer with longitudinal vortices on the trailing surface help explain the large decreases and increases seen in heat transfer with rotation.

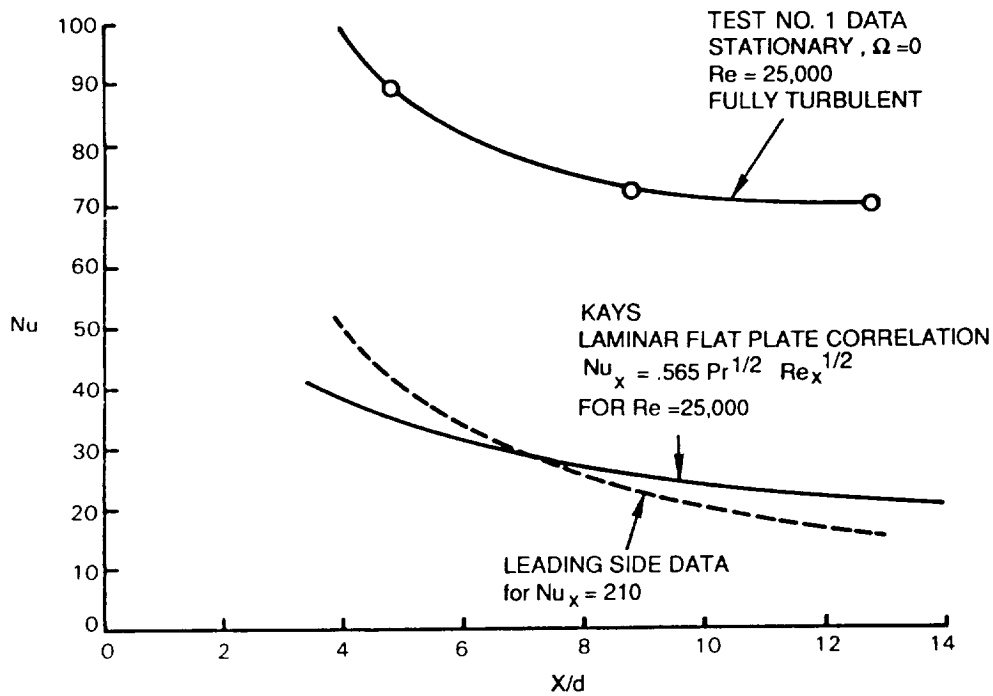


Figure 55.- Leading Side Heat Transfer with Rotation Compared to Kays (1966)  
Laminar Heat Transfer: ( $Re = 25,000$ ,  $R/d = 49$ ,  $\alpha = 0$  ).

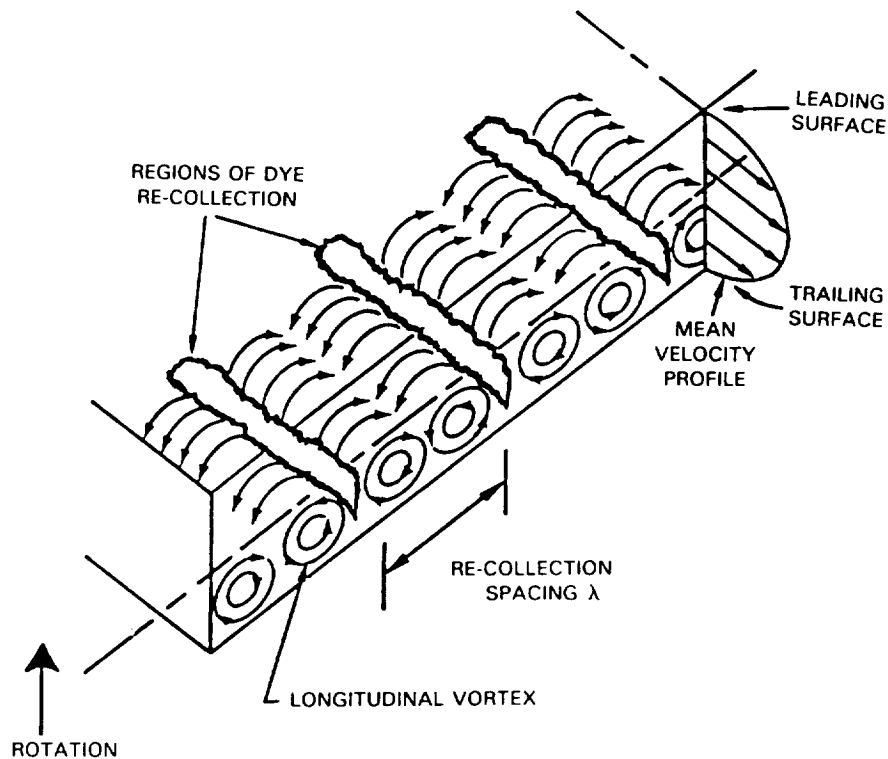


Figure 56.- Flow Visualization of Rotating Channel Flow (Johnston, 1970).

One of Johnston's conclusions was that the rotation induced re-laminarization was highly Reynolds number dependent. To evaluate this dependency, the present data was examined at varying Reynolds numbers.

Figures 57 and 58 compare the heat transfer results for both rotating ( $Ro \approx 0.24$ ) and non-rotating test conditions at  $Re = 12,500$  and  $Re = 50,000$ , respectively, to Kays correlation for laminar flow. The lower Reynolds number flow case, Figure 57, matches the Kays correlation (Kays, 1966) at test sections 34 and 35, while the higher Reynolds number flow case (Figure 58) never reaches the laminar level, although it approaches this minimum. This data indicates that at high rotation rates, the boundary layer on the leading wall is more likely to be laminar at lower Reynolds number. This work compares very well with Johnston's results.

Johnston used flow visualization techniques to establish when the leading wall would laminarize. Figure 59 extends Johnston's mapping of flow regimes with rotation. Data at three different Reynolds numbers (12,600, 25,200 and 49,600 for  $Ro=0.24$ ) is shown to complement Johnston's results. At the low Reynolds number the leading side is laminar. At the high Reynolds number the shear layer is most likely transitional; somewhere close to but not yet laminar. At the middle Reynolds number flow,  $Re = 25,200$ , there exists extensive data to clarify where the flow becomes laminar. Remember this region existed when  $Nu_x = 210$  (Figure 54). This is when  $10^{10} < Ra_x < 10^{11}$ , indicating that buoyancy plays an important role in the laminarization process. Two important results need to be highlighted:

1. For the cases examined, the minimum level of heat transfer attained is predicted by Kays' laminar flat plate correlation.
2. Centripetal buoyancy limits this laminarization process. For  $Re = 25,000$  and  $Ra_x > 10^{11}$  the leading side shear layer becomes transitional and the heat transfer increases.

Thus the low pressure surface wall shear layer becomes either laminar or transitional depending on rotation number and buoyancy forces. In radial outward flow for the cases examined, the heat transfer becomes laminar for  $10^{10} < Ra_x < 10^{11}$  and can be predicted with a flat plate laminar heat transfer correlation. Outside of this range, the boundary layer becomes transitional and is most difficult to accurately correlate.

### 8.3 Comparison of Results with Other Experiments

Many authors have examined the effects of rotation from an isothermal, hydrodynamic point of view. However, few have experimentally analyzed the effects of rotation on internal heat transfer and fewer still have measured the effects of centrifugal buoyancy and Coriolis forces on turbulent heat transfer for conditions similar to those found in today's advanced gas turbine blades. The following sections compare the heat transfer data of this program to the results of several published experiments.

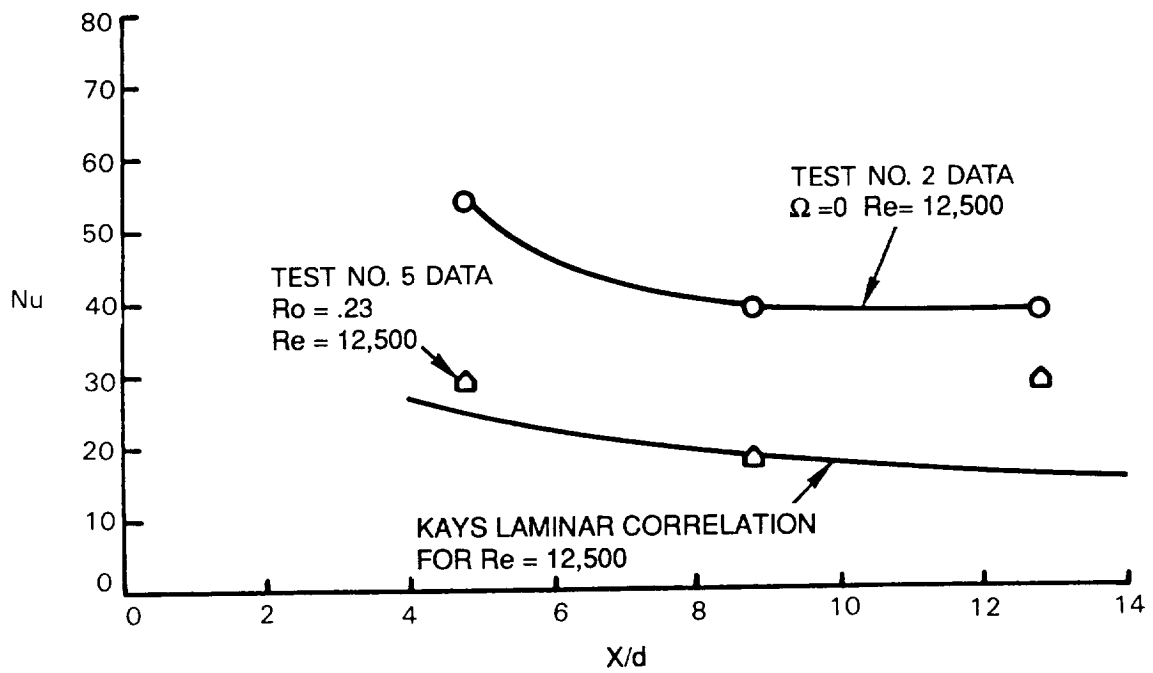


Figure 57.- Leading Side Heat Transfer with Rotation Compared to Kays (1966)  
Laminar Heat Transfer: ( $Re = 12,500$ ,  $\bar{R}/d = 49$ ,  $\alpha = 0$ ).

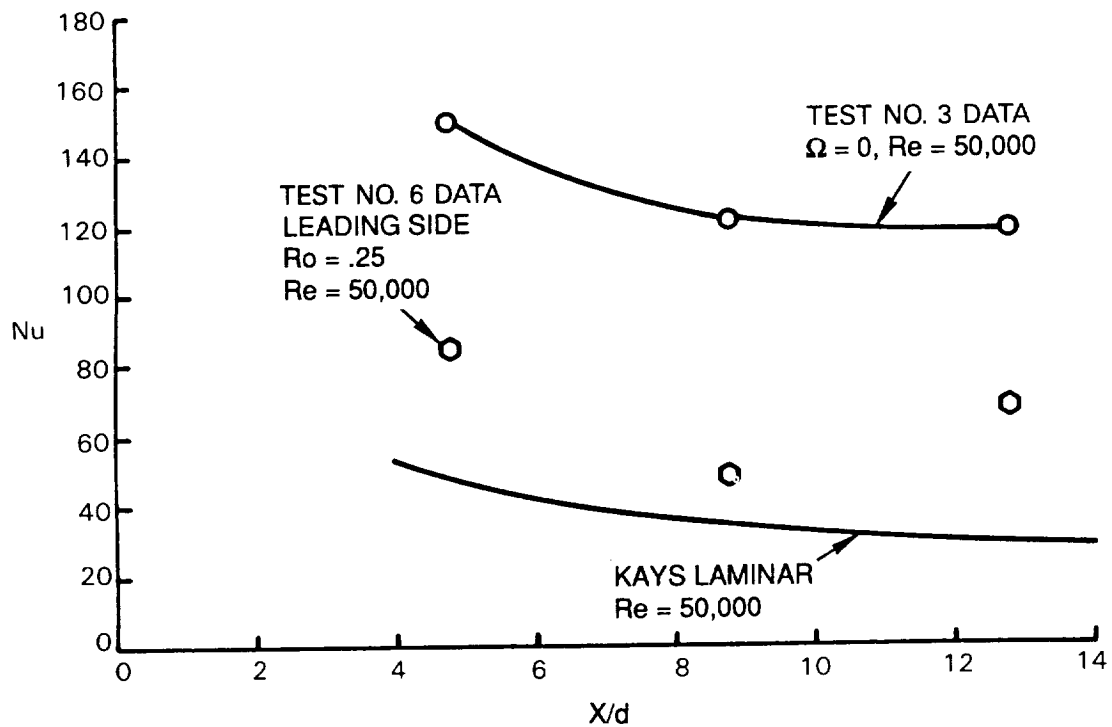


Figure 58.- Leading Side Heat Transfer with Rotation Compared to Kays (1966)  
Laminar Heat Transfer: ( $Re = 50,000$ ,  $R/d = 49$ ,  $\alpha = 0$ ).

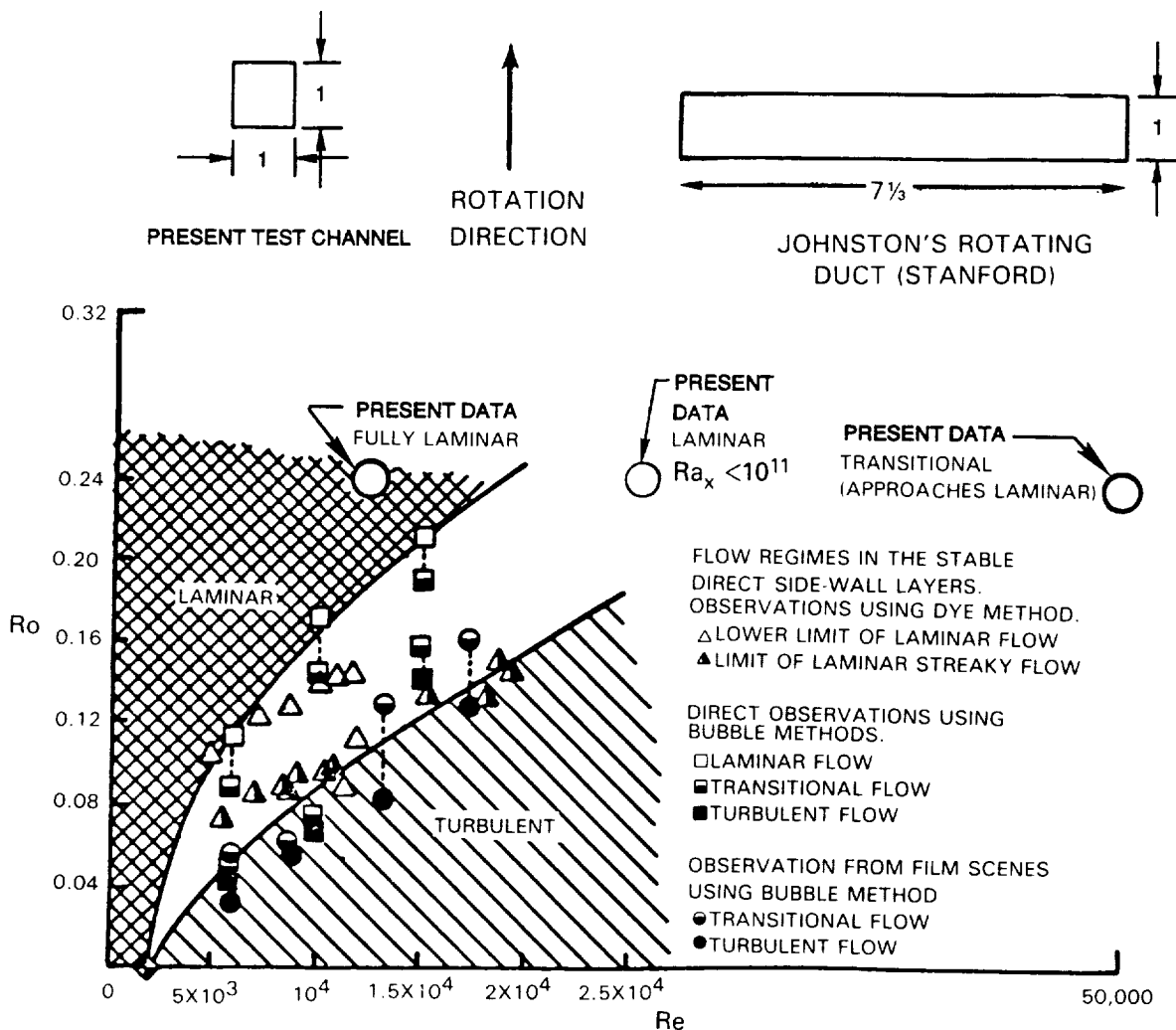


Figure 59.- Present Data and Johnston's Flow Map (Johnston, 1970) Showing Laminarization on the Low Pressure Surface.

### 8.3.1 Comparison with Results of Iskakov (1985)

The upturn in heat transfer rates measured on the low pressure surface with increasing rotation is a phenomena not reported until recently. Only Iskakov (1985) is known to have documented this trend. In a rotating circular duct experiment, he acquired local heat transfer coefficients on both the leading and trailing surfaces for radially outward flow for several Reynolds numbers. At Reynolds number  $Re=32000$ , Iskakov reported both a decrease in the low pressure surface heat transfer to about 85% of the stationary level and a significant upturn as rotation increased. He showed this trend is strongly Reynolds number dependent. As expected, on the other side of the circular duct, the high pressure side, Iskakov measured increasing heat transfer rates. These results are presented in Figure 60. Iskakov's result are compared to data of this program in Figure 61. His correlations are plotted with data for  $Re=25000$  at six rotation rates. The heat transfer coefficients have been averaged over the passage length for the high and low pressure sides of the model for radially outward flow. Recall that Iskakov's duct is circular and the present duct is square.

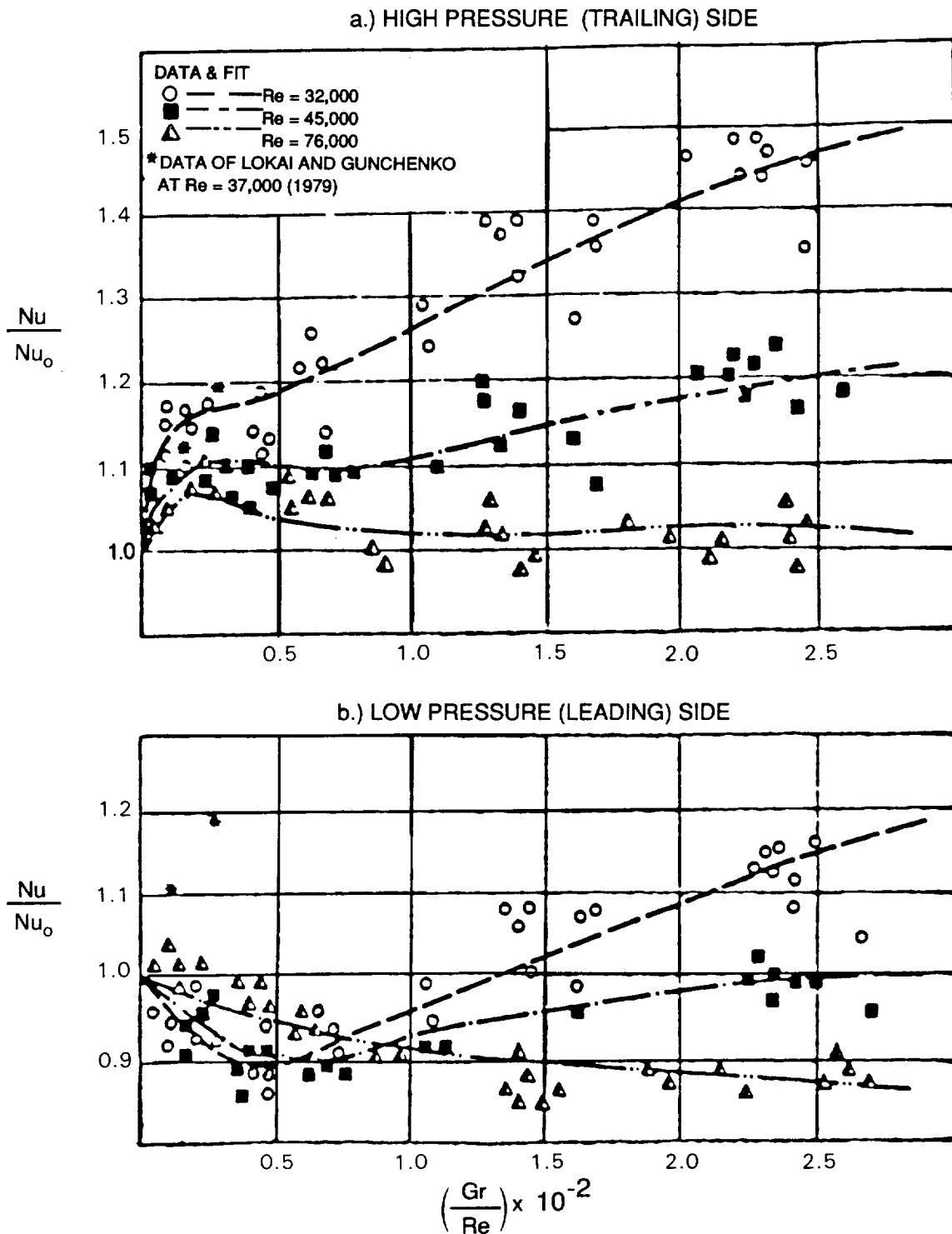


Figure 60.- Effects of Rotation on the Coefficient of Change in Heat Transfer with Centrifugal Flow of Air on the (a) Trailing Side and (b) on the Leading Side (Iskakov and Trushin, 1985).

$$Re \approx 25,000 \quad \Delta T \approx 44.4^\circ\text{C} (80^\circ\text{F})$$

$$\left(\frac{\Delta T}{T}\right)_{in} = 0.13 \quad \bar{R}/d = 49$$

$$\alpha = 0$$

SYMBOL	□					
TEST NO.	117	8	114	4	106	7
ROTATION NO.	0.06	0.12	0.18	0.25	0.35	0.47
RPM	145	275	412	550	825	1100

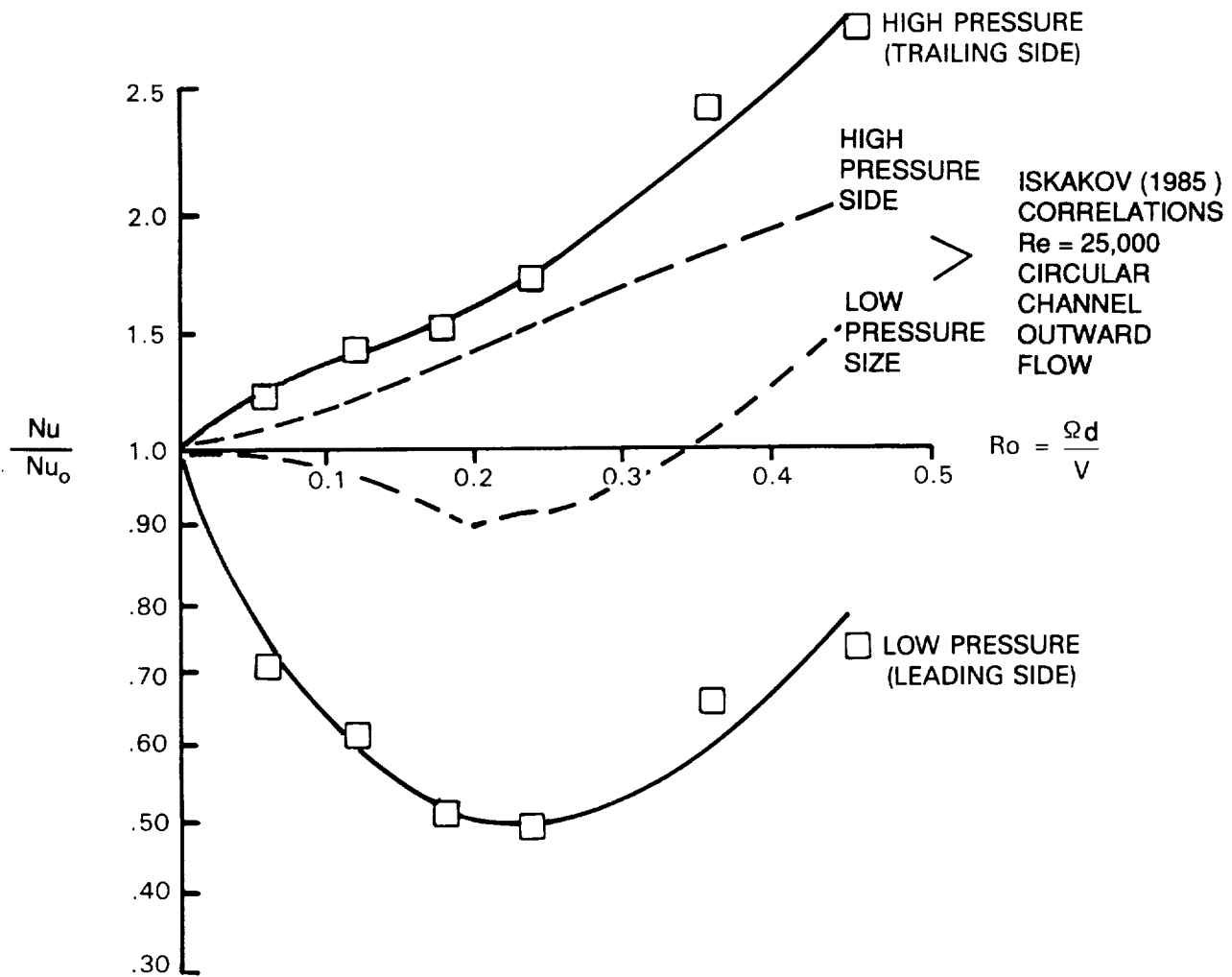


Figure 61.- Comparison of Iskakov's Correlation with Averaged Heat Transfer Data of this Experiment:  $Re = 25,000$  (Iskakov and Trushin, 1985).



On the high pressure side of both models, the enhancement in heat transfer with increasing rotation agrees up to a rotation number of  $Ro=0.30$ . On the low pressure surface both exhibit a drop and then an increase in heat transfer, but the levels remain very different.

This suggests that a square duct may be more susceptible than a circular tube to decreases in heat transfer on the low pressure side. This is believed to result from the Coriolis-induced stabilization of the wall shear layer. Because there are corners in the square duct, the secondary flows are less likely to wash-off this stabilized fluid layer. It is suspected that the secondary circulations migrate toward the high pressure surface leaving a thickened and dampened boundary layer on the low pressure surface. This would explain why the square duct experiences such a large drop in heat transfer on this surface; the level approaching that of laminar flat plate heat transfer.

It is interesting to point out that both experiments report an upturn in low pressure surface heat transfer at a rotation number near  $Ro = 0.20$ . This upturn in heat transfer on the low pressure side of the rotating duct may be a flow separation phenomena (see Isakov and Trushin, 1983 and 1985).

### 8.3.2 Comparison with Results of Morris (1981)

Comparisons with the data and correlation of Morris illustrate one of the most important realizations of the program: Extrapolation of correlations outside the test range of the significant nondimensional parameters is very risky.




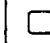
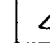
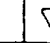

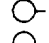
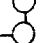
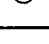
Figure 62 compares Morris' correlation to data from the first straight passage in the present model. Morris' experiment consisted of a rotating circular tube with radially outward flow. This was a constant heat flux experiment where a circular duct was instrumented with thermocouples along the leading surface. These results are then compared to those from the first passage at  $X/d = 12.4$  (radially outward flow) on the leading surface of the NASA model.

The solid lines of Figure 62 indicate Morris' correlation based on data, while the dashed line represent this correlation extrapolated. The heat transfer results obtained on the leading surface at the low rotation number of 0.06 are within 20% of Morris' correlation. This agreement occurs within Morris' experimental range which is indicated in the figure. For values of the buoyancy parameter and rotation number that fall outside the Morris data range, the present data show increases with rotation number which are in general agreement with the Morris correlation. However, the present data show increases in heat transfer with increasing density ratio or buoyancy centripetal parameter, whereas, the Morris correlation would predict a decrease in heat transfer with increasing density ratio.

### 8.3.3 Comparison with Results of Eckert (1954)

This program has shown rotational buoyancy forces strongly influence turbulent heat transfer in rotating smooth passages for conditions found in gas turbine blades. Variations in heat transfer caused by rotation have been shown to be less for radial inward flowing passages than for radial outward flowing passages. This influence of radial flow direction is clarified when the results of Eckert and Diaguilla's (1954) work on buoyancy effects in forced, free and mixed convection are examined.

$$Re \approx 25,000, \bar{R}/d = 49, \alpha = 0$$

SYMBOL							SYMBOL FLAGS
ROTATION NUMBER	0.06	0.12	0.18	0.25	0.35	0.48	
TEST NO. AT $\Delta T = 22.2^\circ\text{C} (40^\circ\text{F})$	—	—	115	9	105	—	
$\Delta T = 44.4^\circ\text{C} (80^\circ\text{F})$	117	8	114	4	106	7	
$\Delta T = 66.7^\circ\text{C} (120^\circ\text{F})$	—	—	113	10	107	—	
$\Delta T = 88.9^\circ\text{C} (160^\circ\text{F})$	—	—	116	102	—	—	

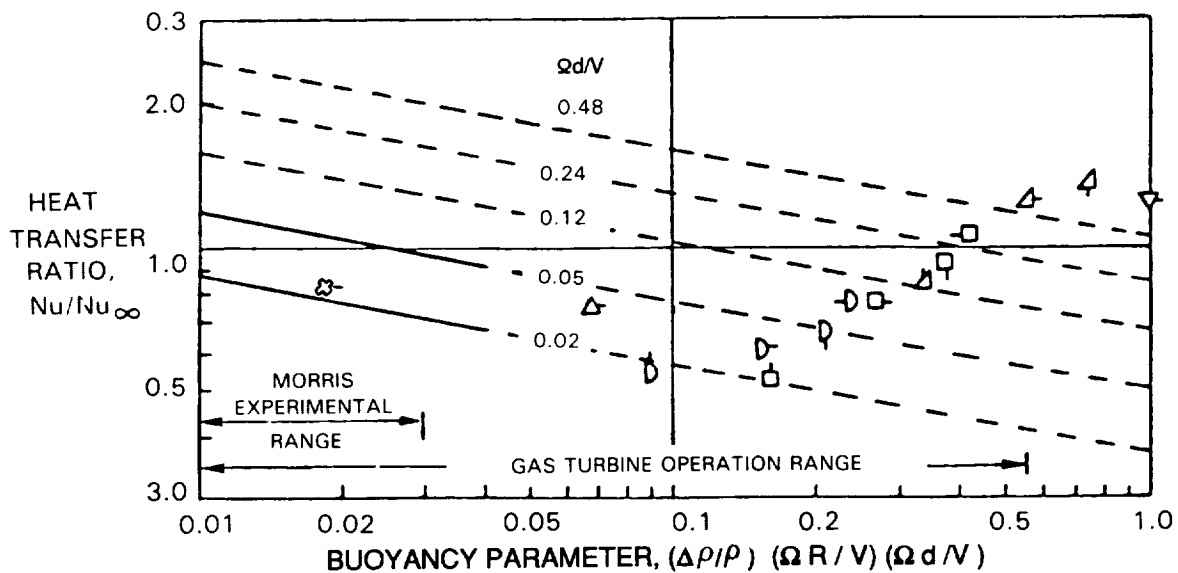


Figure 62.- Comparisons of Leading Surface Rotating Heat Transfer Results for  $X/d = 12.4$  with Morris (1981) Correlation:  
 $Nu = 0.022 (Ra/Re^2) - 0.186 Ro^{0.33} Re^{0.8}$  or  
 $Nu/Nu_\infty = 1.35 [(\Delta \rho/\rho) * (R/d) * (\Omega/d/V)^2] - 0.186 (\Omega d/V)^{0.33}$

Eckert conducted three different experiments in a large (stationary) vertical circular tube where he examined mixed, free and forced-convection heat transfer. A diagram of the test apparatus is shown with the results of his experiments. These are plotted as  $Nu_x$  versus  $Gr_x Pr$  in Figures 63 and 64. Each of these plots contains a free-convection limit which is a mean data fit through the results of Eckert's free-convection experiment.

Figure 63 compares the present data (symbols) for the outward flowing passage to Eckert's curve-fitted (solid) lines for his counterflow tests. In this case Eckert looked at the condition where the wall thermal boundary layer under gravity-induced buoyancy forces moves in a direction opposite to the mainstream flow. This is analogous to the rotating case of the outward flowing passage with heated walls where the buoyancy force is rotation-induced. Here the more dense colder fluid, away from the wall, accelerates outward from the axis of rotation, while the hotter wall fluid tends towards the axis of rotation. All heat transfer coefficients presented are averaged circumferentially around the perimeter of the respective passage.

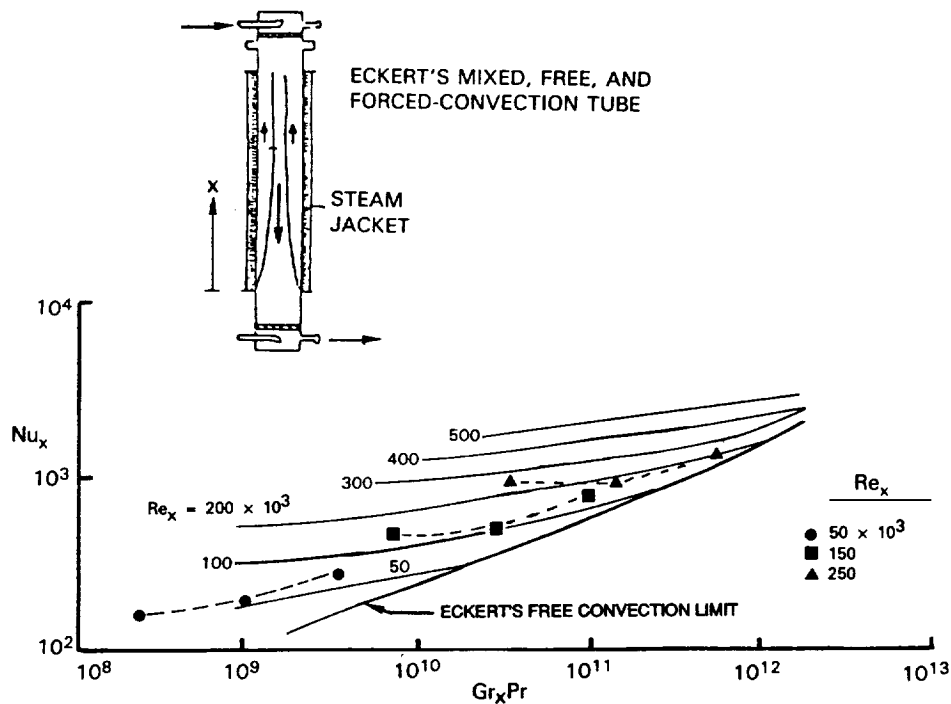


Figure 63.- Circumferentially Averaged Heat Transfer Coefficients for Outflow Passage Compared with Eckert's Counterflow Results (Eckert and Diaguilla, 1954).

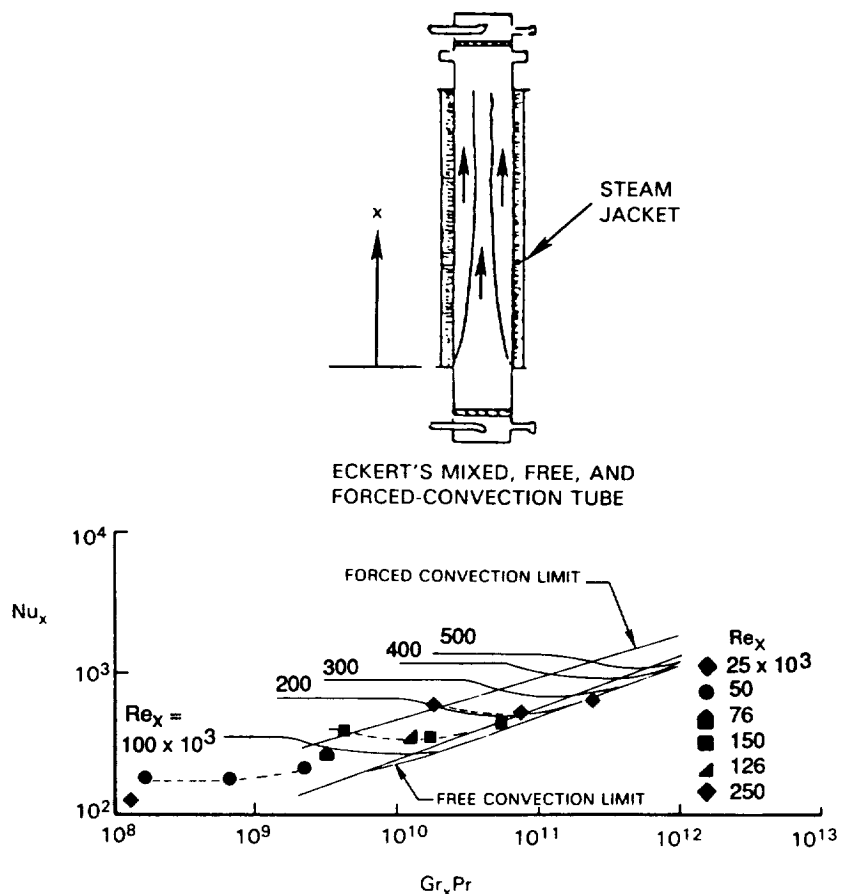


Figure 64.- Circumferentially Averaged Heat Transfer Coefficients for Inflow Passage Compared with Eckert's Parallel Flow Results (Eckert and Diaguilla, 1954).

The present data plotted for various Reynolds numbers based on the distance  $X$ , measured from the beginning of the thermal boundary layer, shows very encouraging trends. Moving to the left most side of Figure 63, the lines of constant  $Re_x$  should eventually become flat as the heat transfer becomes independent of Grashof number and can be correlated by an equation of the form  $Nu_x = CRe_x^a Pr^b$ . Eckert noted for this case that the data did not yet become flat, and therefore, the heat transfer at these lower Grashof number remains dependent on buoyancy. Moving to the right side of the figure, for large Grashof numbers, heat transfer rates approach the free convection limit established by Eckert.

The present data, when averaged circumferentially around the duct perimeter, agrees remarkably well with Eckert's results. The increasing slope through the data indicates the flow is in the mixed flow regime and buoyancy influences the heat transfer process. For large values of  $Gr_x$ , heat transfer rates approach the free convection limit as established by Eckert. The data also indicates a higher free convection limit at the lower values of  $Gr_x$ . Eckert also noticed this trend when comparing the extreme forced-convection data at high Grashof numbers with the free convection data. For low values of  $Gr_x$ , forced convection dominates the heat transfer. As can be seen in the figure, the forced convection limit was not reached with the present set of experiments.

Figure 64 compares the present results for the inward flowing passage with Eckert's parallel flow results. Here, Eckert reversed the mainstream flow direction producing a thermal boundary layer that moved in the same direction as the mainstream. Again, the two experiments compare favorably. The present data falls within the mixed regime defined by Eckert.

This mixed region exists between the forced-convection and free-convection limits indicated on Figure 64. It is important to notice that for this parallel flow case, Eckert's data established the pure forced-convection regime where  $Nu_x$  is independent of  $Gr_x$ . As previously noted, the counterflow experiments did not show this flat region (see Figure 63). This suggests that in the parallel flow case, buoyancy influences heat transfer over a smaller range. Thus, for radially outward flowing passages, heat transfer will more likely be affected over a wider operating range by rotation-induced buoyancy than for radially inward flowing passages.

It has been shown that thermal boundary layer buoyancy acting in the same direction as the turbulent mainstream inhibits heat transfer in the mixed convection region. Both Eckert's experiments in the stationary mode and the rotating results presented here exhibit a local decrease in  $Nu_x$  when  $Gr_x Pr$  falls in the mixed range shown in Figure 64. This local decrease is especially significant when compared with counterflow case. When Nusselt numbers for similar flow conditions for the radially outward and inward flowing case are compared, the counterflow (radially outflow) heat transfer is almost 70% greater than the corresponding parallel flow heat transfer (e.g.  $Nu_x = 875$  compared to 520). Eckert noted that the counterflow situation could result in heat transfer levels as much as twice those in the parallel flow case. This is especially significant when these results are circumferential averages of heat transfer around the perimeter of the coolant passage. As shown in the previous discussion, local heat transfer can be significantly higher and lower than the circumferential averages.

Because of the absence of detailed boundary layer measurements for these experiments, it is not clear what turbulence structure and/or mean flow changes are responsible for the observed heat transfer behavior. Clearly, measurements of this nature will be required to further the physical understanding of this class of shear flows and thereby permit the development of more accurate predictive schemes.

Several conclusion regarding buoyancy can be reached:

1. Rotating coolant passage heat transfer, averaged circumferentially for a square smooth channel, compares favorably with Eckert's work on simultaneously occurring free and forced-convection in a stationary vertical circular tube.
  - A. The radial outward flowing passage with rotation correlates with the stationary counterflow case.
  - B. The radial inward flowing passage with rotation correlates with the stationary parallel flow case.
2. The large average heat transfer variations seen between the outward and inward flowing passages are attributed to buoyancy forces.
3. The mixed convection regime, where free and forced-convection occur simultaneously, is larger for radially outward flowing passages (opposed flow) than for inward flow (parallel flow). As a consequence, heat transfer is more affected by rotation in the outward flowing passage.

## 9.0 CONCLUSIONS

This program has resulted in an extensive body of experimental data from heat transfer experiments in a rotating square passage with smooth walls. It is believed that the large range of test parameters makes this data set unique. The extensive data base aided greatly in the data analysis and correlation and in developing physical models for the complex heat transfer characteristics. A summary of the major program conclusions concerning the separate effects of forced convection, Coriolis, buoyancy and flow direction on heat transfer is presented in this section. A more detailed discussion of these conclusions and the authors' speculations regarding physical models for the cause and effect relationships, can be found in Sections 5.0, 6.0, 7.0 and 8.0 of this report.

For the first passage with radially outward flow:

1. The streamwise distribution of heat transfer in the first passage from the stationary baseline experiment is similar to that for developing flow in the entrance region of a passage and is in good agreement with previous investigators' results.
2. Heat transfer is strongly affected by rotation, causing increases in heat transfer up to 3.5 times fully developed, smooth tube levels on the trailing surfaces and decreases to 40% of fully developed, smooth tube levels on the leading surfaces.
3. The decreases in heat transfer on the leading surfaces with increases in rotation number are attributed to the combined effects of stabilization of the near-wall flow and cross-stream flows which cause heated, near wall fluid from the trailing and sidewall surfaces to accumulate near the leading side of the coolant passage.
4. The increases in heat transfer in the latter half of the coolant passage on the leading side and the increases on the trailing side are attributed to the effects of the large scale development of Coriolis generated secondary flows.
5. Local heat transfer increases (by as much as 200%) with increases in density ratio over most of the passage surface area.
6. Heat transfer decreases (by as much as 20%) with increases in density ratio on the leading side of the passage near the inlet. These decreases are believed to be governed by both the interaction of the near-wall flow stability and the buoyancy effects.
7. Heat transfer results obtained with different combinations of model radius ratio and coolant density were well correlated by the buoyancy parameter  $(\Delta\rho/\rho)(R/d)(Qd/V)^2$  for flow regimes dominated by buoyant forces.

8. Increases in heat transfer ratio on the trailing surfaces were 60% greater than increases on the leading surfaces for the same increase in density ratio for a given rotation number. This difference in heat transfer increase suggests that the interaction of the Coriolis and buoyancy effects is different for the flow near leading and trailing surfaces.
9. The buoyancy parameter correlates the heat transfer ratio results from the trailing side and for the most downstream location of the leading side. The results were not correlated by the buoyancy parameter near the inlet on the leading surface. The lack of correlation was attributed to a complex interaction of stabilization of the near wall flow, buoyancy and Coriolis effects.

The following observations and conclusions were reached concerning flow direction:

1. The effects of varying Reynolds number on heat transfer in the first two passages are reasonably well correlated by the heat transfer ratio  $Nu/Nu_{\infty}$ , where  $Nu_{\infty}$  is the correlation for fully developed, turbulent flow in a stationary rectangular passage.
2. Density ratio and rotation number were found to cause large changes in heat transfer ratio for radially outward flow and relatively small changes for radially inward flow.
3. The heat transfer ratio for the low pressure surfaces of the coolant passages was found to be primarily a function of the buoyancy parameter regardless of flow direction.
4. The heat transfer ratio on the high pressure surfaces was significantly affected by flow direction. The heat transfer was found to be a strong function of a buoyancy parameter for the high pressure surfaces for radially outward flow. Whereas, the heat transfer was relatively unaffected by a buoyancy parameter for the radially inward flowing high pressure surface.
5. Increasing the density ratio generally caused an increase in heat transfer. However, the increase in heat transfer for the inward flowing passage was considerably less than that for outward flow.
6. Circumferentially averaged heat transfer results compared favorably with a previous stationary parallel and counterflow mixed-convection heat transfer experiment by Eckert et al. (1953). Heat transfer from the radially outward flowing passages compared with Eckert's counterflow case while the radially inward flowing results compared with Eckert's parallel flow case.
7. The effect of model orientation angle ( $\alpha = 45^\circ$ ) caused heat transfer to be symmetric about a diagonal in the direction of rotation across the passage.

## 10.0 APPENDIX

### 10.1 ANALYSIS OF EQUATIONS OF MOTION (Suo, 1980)

Consider a fluid flowing in a pipe which is rotating as shown in Figure 65.

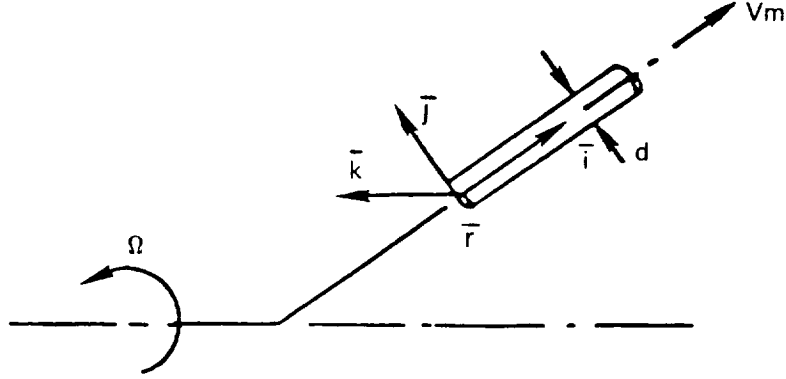


Figure 65.- Rotating Pipe Coordinates.

The equation of motion in a rotating frame of reference is

$$\rho \frac{D\bar{V}}{Dt} = -\nabla p + \mu \nabla(\nabla \cdot \bar{V}) + \mu \nabla^2 \bar{V} - \rho \left[ \underbrace{(2\bar{\Omega} \times \bar{V})}_{\text{Coriolis}} + \underbrace{(\bar{\Omega} \times \bar{\Omega} \times \bar{r})}_{\text{Centrifugal}} \right] \quad (10.1)$$

The last two terms represent the Coriolis and centrifugal acceleration terms, respectively. If Eq. (10.1) is made dimensionless in the normal manner.

$$\begin{aligned} \bar{V}' &= \frac{\bar{V}}{V_m} & \rho' &= \frac{\rho}{\rho_m} & x' &= \frac{x}{d} & z' &= \frac{z}{d} \\ t' &= \frac{tV_m}{d} & \rho' &= \frac{\rho'}{\rho_m V_m^2} & y' &= \frac{y}{d} \end{aligned} \quad (10.2)$$

Then Equation (10.1) becomes

$$\rho' \frac{D\bar{V}'}{Dt'} = -\nabla p' + \left( \frac{1}{Re} \right) [\nabla(\nabla \cdot \bar{V}') + \nabla^2 \bar{V}'] - \rho' \left( \frac{d\Omega}{V_m} \right) \left[ 2\bar{k} \times \bar{V}' - i \left( \frac{r\Omega}{V_m} \right) \right] \quad (10.3)$$

where  $Re$  is  $(V_m d \rho_m / \mu)$  and  $(d\Omega/V_m)$  is the rotation number, (i.e. inverse of Rossby number). In order to determine the important variables in the problem of concern, Eq. (10.3) is further modified by the definition of

$$\rho \equiv \rho_m + \Delta \rho \quad (10.4)$$

$$\rho' \equiv 1 + \frac{\Delta \rho}{\rho_m} \quad (10.5)$$



Equation (10.3) becomes

$$\left(1 + \frac{\Delta \rho}{\rho_m}\right) \frac{D\bar{V}'}{Dt'} = -\nabla p' + \left(\frac{1}{Re}\right) [\nabla(\nabla \cdot \bar{V}') + \nabla^2 \bar{V}'] \quad (10.6)$$

$$- \left(\frac{d\Omega}{V_m}\right) \left[ 2\bar{k} \times \bar{V}' - i \left(\frac{r\Omega}{V_m}\right) + \frac{\Delta \rho}{\rho_m} (2\bar{k} \times \bar{V}') - \frac{\Delta \rho}{\rho_m} \left(\frac{r\Omega}{V_m}\right) i \right]$$

The relative importance of each of the terms on the right can then be examined. First consider the case where  $(\Delta \rho / \rho_m)$  is very large. Then all terms are important and the solution becomes very difficult. An example of such a flow is the flow in a rotating pipe where boiling occurs. In such a flow the liquid has been observed to stratify on the side of the pipe away from the direction of rotation. This flow, while interesting in its own right, is not of interest for the problem of air-cooled turbine blades.

A second extreme is when  $\Delta \rho / \rho_m = 0$ . Then Eq. (10.6) reduces to

$$\frac{D\bar{V}'}{Dt'} = -\nabla p' + \left(\frac{1}{Re}\right) (\nabla^2 \bar{V}') - \left(\frac{d\Omega}{V_m}\right) \left[ 2\bar{k} \times \bar{V}' - \left(\frac{r\Omega}{V_m}\right) i \right] \quad (10.7)$$

If we define a reduced pressure gradient as,

$$\nabla p^* = \nabla p - \rho_m r \Omega^2 i = \nabla \left[ p - 1/2 \rho_m (r\Omega)^2 \right] \quad (10.8)$$

Then Equation (10.7) becomes

$$\frac{D\bar{V}'}{Dt'} = -\nabla p^* + \left(\frac{1}{Re}\right) (\nabla^2 \bar{V}') - \left(\frac{d\Omega}{V_m}\right) (2\bar{k} \times \bar{V}') \quad (10.9)$$

The reduced pressure gradient  $\nabla p^*$  is the pressure gradient minus the pressure gradient caused by centrifugal acceleration. Thus, it represents the pressure gradient driving the flow, because, if only the centrifugal gradient was present, there would be no motion except solid body rotation. The only term to make this equation different from nonrotating flows is the last one, which represents the effect of Coriolis acceleration.

The flows of most interest for the current problem are not at either of the extremes, but lie in between. Consider the case when  $\rho / \rho_m \ll 1$  but is not equal to zero. This allows the Boussinesq approximation to be made where the variation in density is only considered in the driving terms, here the rotational terms

$$\left(1 + \frac{\Delta \rho}{\rho_m}\right) \frac{D\bar{V}'}{Dt'} = -\nabla p' + \left(\frac{1}{Re}\right) [\nabla(\nabla \cdot \bar{V}') + \nabla^2 \bar{V}'] \quad (10.10)$$

$$- \left(\frac{d\Omega}{V_m}\right) \left[ 2\bar{k} \times \bar{V}' \left(1 + \frac{\Delta \rho}{\rho_m}\right) - \left(\frac{r\Omega}{V_m}\right) i - \frac{\Delta \rho}{\rho_m} \left(\frac{r\Omega}{V_m}\right) i \right]$$

Again using the definition of reduced pressure gradient, Eq (10.10) becomes

$$\frac{D\bar{V}'}{Dt'} = -\nabla p' \cdot + \left(\frac{1}{R\theta}\right) \nabla^2 \bar{V}' - \left(\frac{d\Omega}{V_m}\right) \left[ 2\bar{k} \times \bar{V}' + 2\bar{k} \times \bar{V}' \left(\frac{\Delta\rho}{\rho_m}\right) - \frac{\Delta\rho}{\rho_m} \left(\frac{r\Omega}{V_m}\right)_i \right] \quad (10.11)$$

The first two terms within the brackets are the Coriolis acceleration terms. Clearly the second term is always very much smaller than the first term and can be neglected with respect to the first term. The third term is the centrifugal acceleration term; it can approach the value of the first term (with  $r\Omega/V_m \gg 1$ ) and thus cannot be neglected in general. Equation (10.11) then becomes

$$\frac{D\bar{V}'}{Dt'} = -\nabla p' \cdot + \left(\frac{1}{R\theta}\right) \nabla^2 \bar{V}' - \left(\frac{d\Omega}{V_m}\right) \left[ 2\bar{k} \times \bar{V}' - \frac{\Delta\rho}{\rho_m} \left(\frac{r\Omega}{V_m}\right)_i \right] \quad (10.12)$$

The term on the far right represents the effect of centrifugal buoyancy. When  $\Delta\rho/\rho_m (r\Omega/V_m)$  approaches zero, the effect of centrifugal buoyancy should become negligible and Equation (10.12) reduces to Equation (10.9) above. Furthermore, it is clear that in addition to Reynolds number, the terms  $(d\Omega/V_m)$  and  $\Delta\rho/\rho_m (r\Omega/V_m)$  should specify the flow field.

## 10.2 Model Inlet Flow Characterization

Velocity measurements were obtained at the exit of the inlet nozzle system (inlet of the first passage) and at the end of a square channel mounted on the inlet nozzle (Figure 8). The velocity measurements were obtained by traversing a hot wire probe across the passage from the leading to trailing side and from the inside of the passage to the outside. Average and RMS voltage output of the linearized hot wire signal were used to calculate the local mean velocity and local turbulence intensity.

Probe traverse locations and nomenclature are shown in Figure 66. Mean velocity and local turbulence profiles from the measurements are shown in Figures 67 through 70. The mean velocity results for the flow at the nozzle exit (entrance to the first passage) (Figures 67a and 67b top) show the velocity profiles have an approximately parabolic shape. The mean velocity surface and contour plots for the nozzle exit (Figure 68a) show the core flow to be approximately axisymmetric about the passage centerline and slightly skewed toward the outside and toward the trailing side of the passage. Turbulence profiles at the nozzle exit (Figures 67a and 67b bottom and 68b) show increased local turbulence intensity near the edges of the nozzle flow with a centerline turbulence of about 4%.

Mean velocity profiles at the end of the channel (Figures 69a and 69b top) are relatively flat and typical of fully developed turbulent flow. Surface and contour results (Figure 70a) indicate that the mean flow is slightly skewed toward the leading side of the passage. Turbulence profiles at the channel exit (Figures 69a and 69b bottom, and 70b) show a decreased level of centerline turbulence intensity, down from 4% at the nozzle to about 3% at the channel exit.

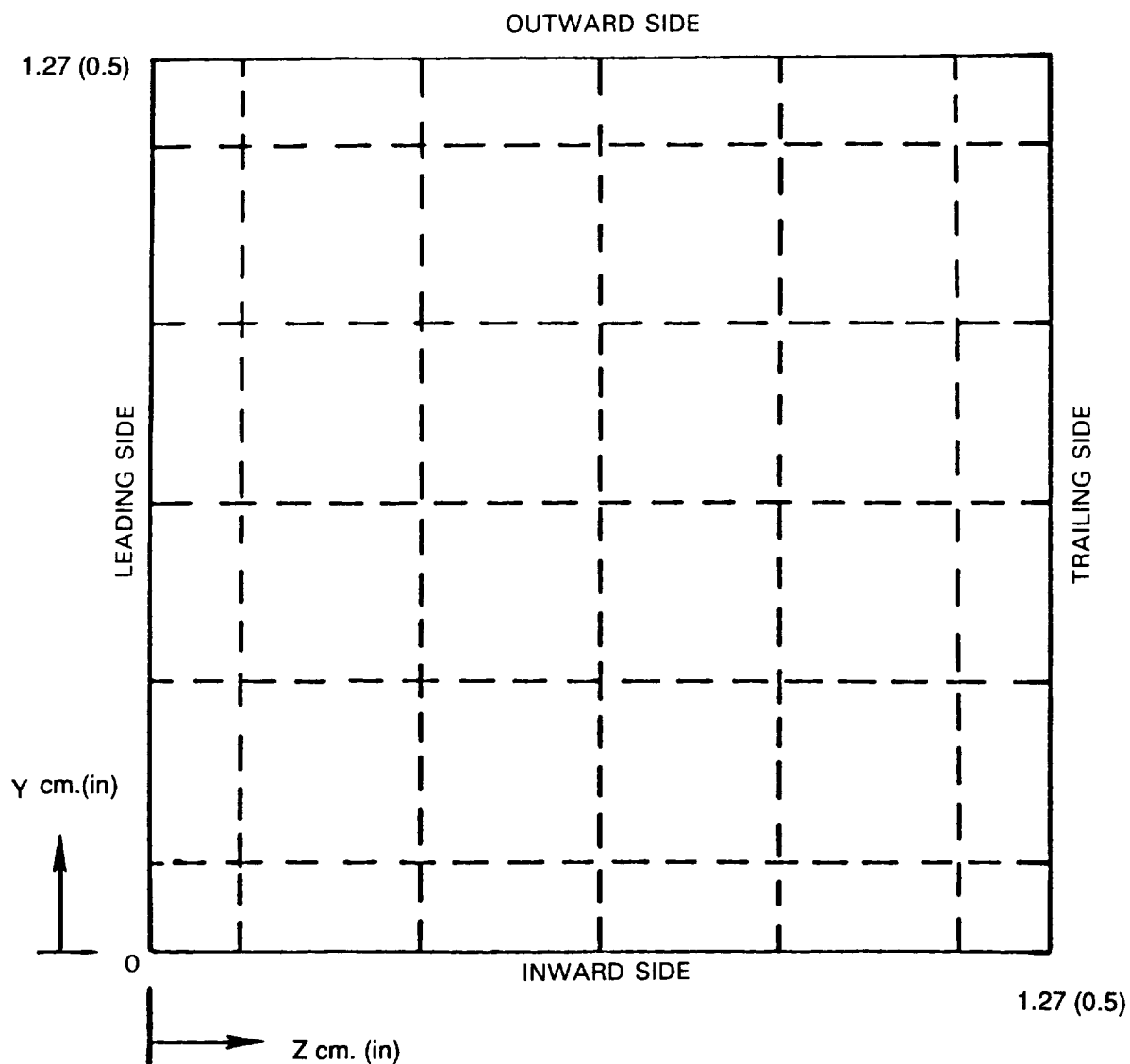


Figure 66.- Nozzle Probe Traverse Locations and Nomenclature.

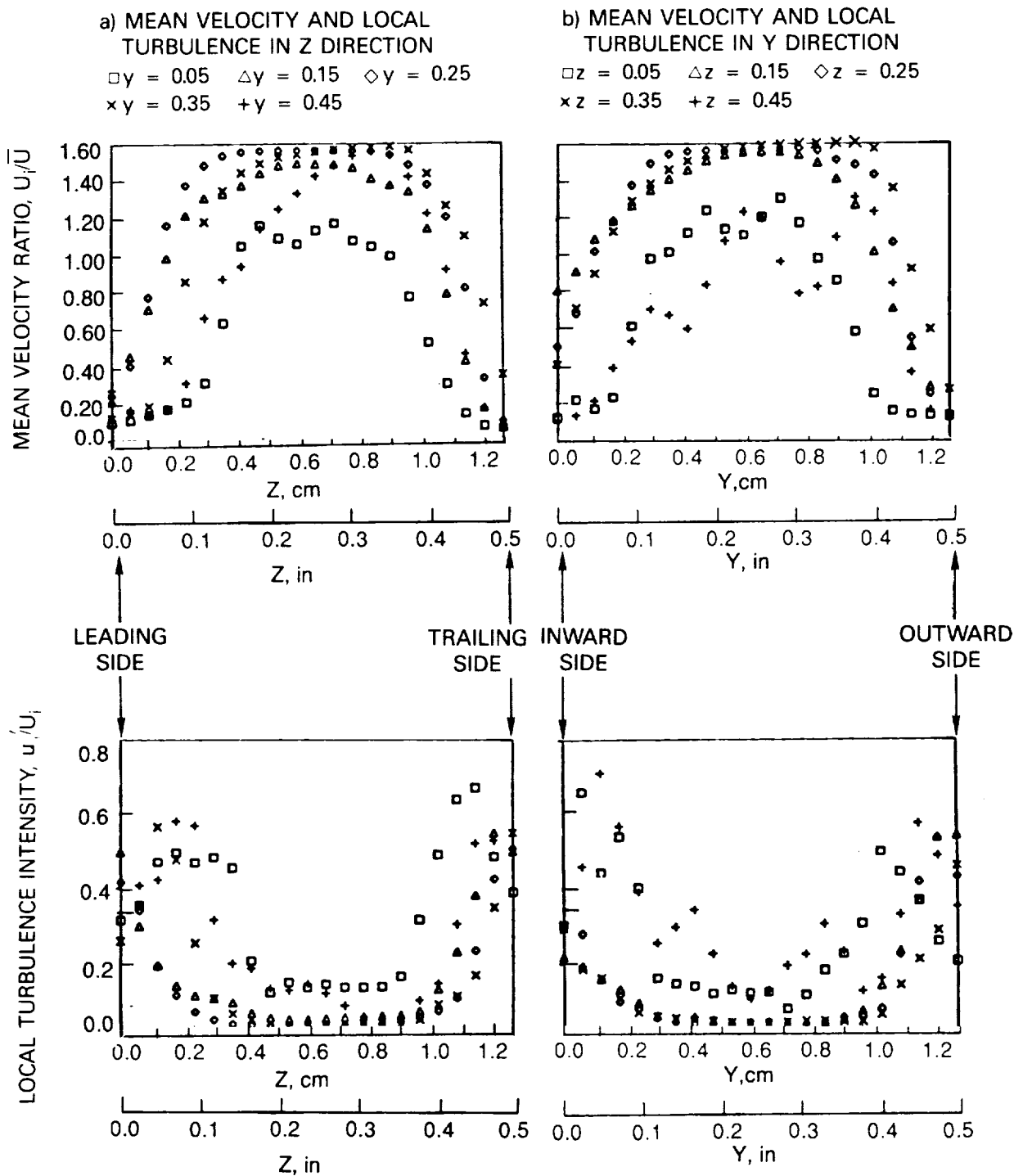
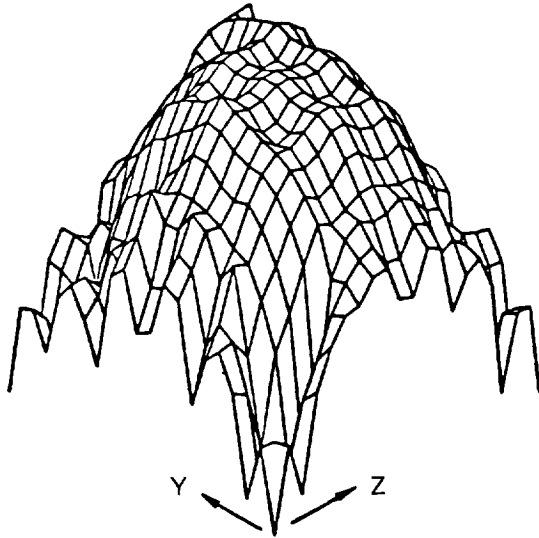


Figure 67.- Nozzle Exit Flow Profiles in Z and Y Directions

a) MEAN VELOCITY SURFACE  
AND CONTOUR,  $U_i/\bar{U}$



b) LOCAL TURBULENCE SURFACE  
AND CONTOUR,  $u_i'/U_i$

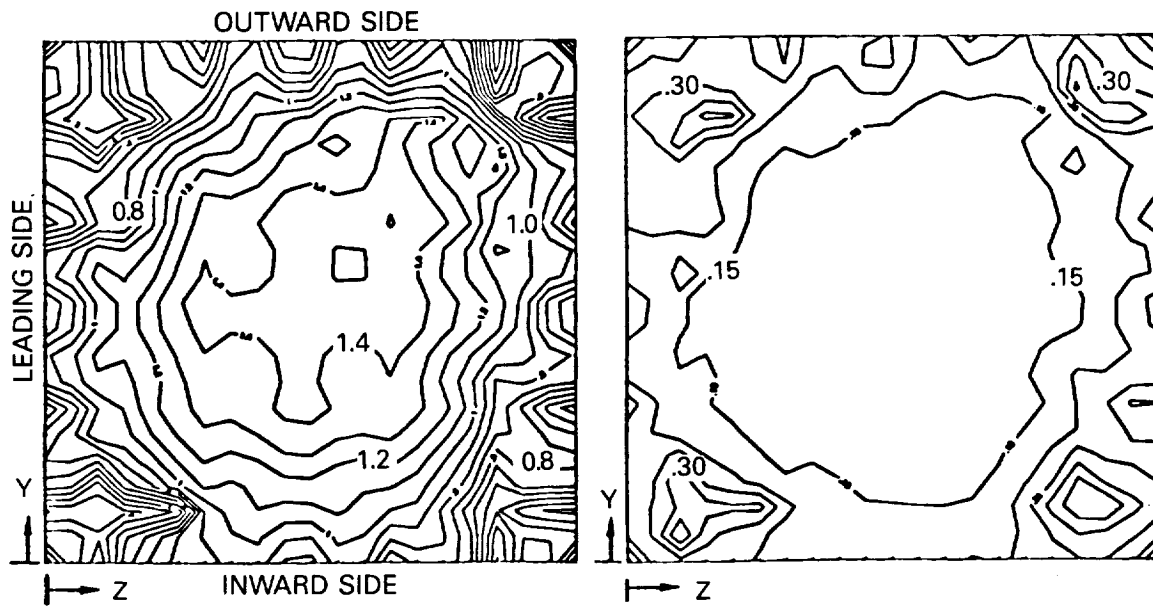
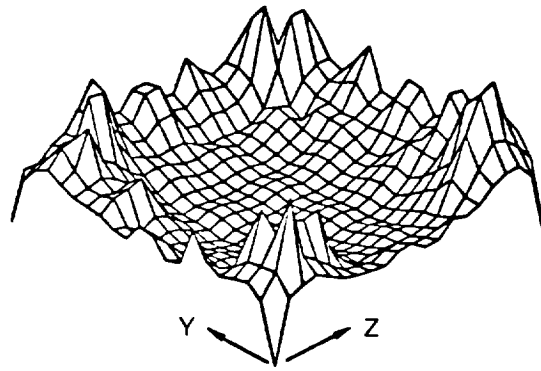


Figure 68.- Variation in Velocity Surfaces and Contours for Nozzle Exit Flow.

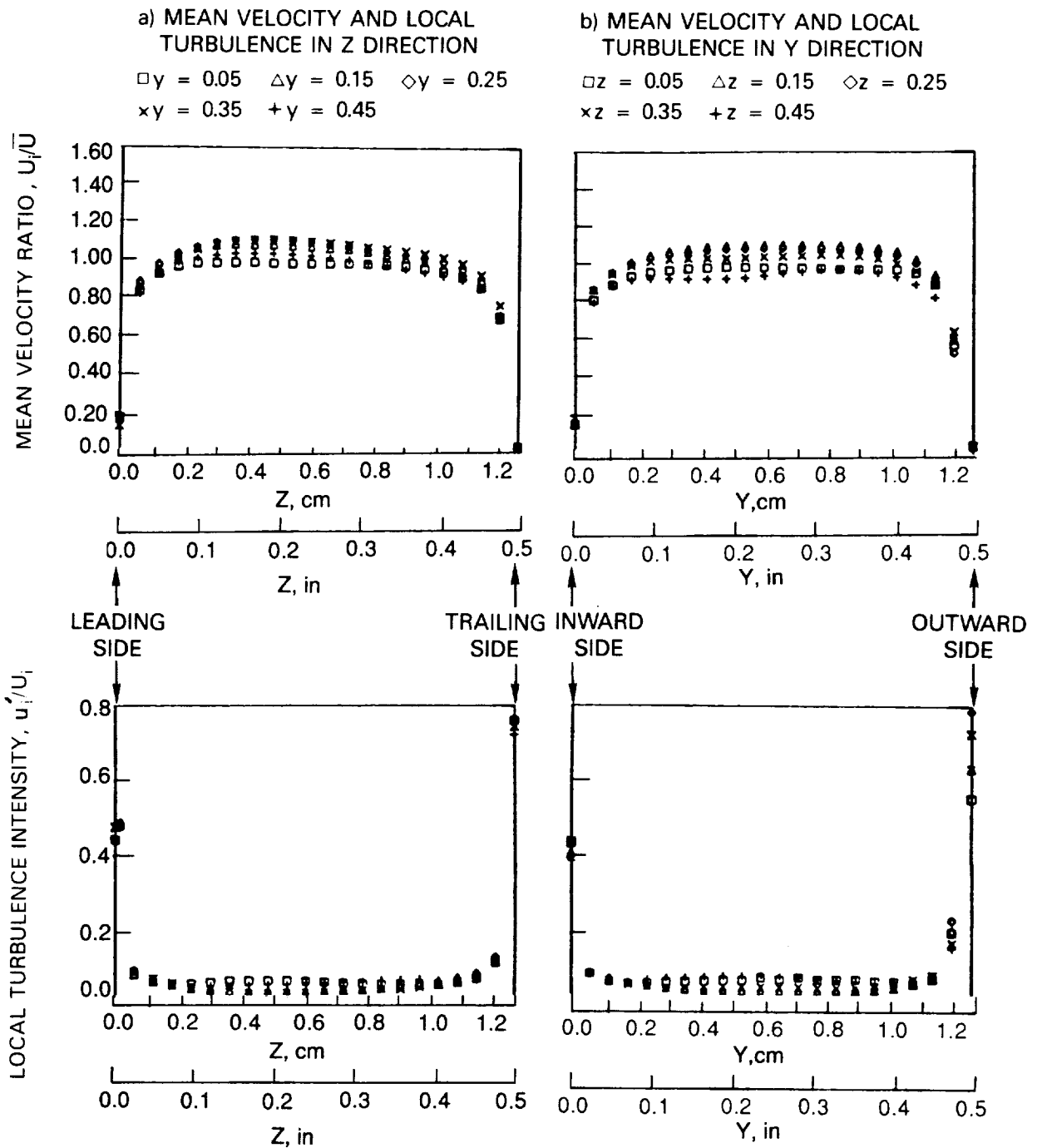
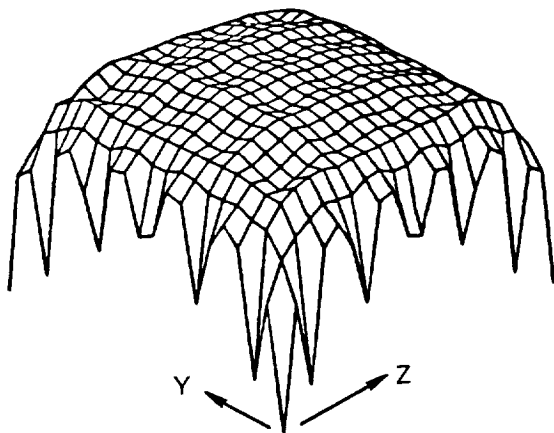


Figure 69.- Channel Exit Flow Profiles in Z and Y Directions

a) MEAN VELOCITY SURFACE  
AND CONTOUR ,  $U_i/\bar{U}$



b) LOCAL TURBULENCE SURFACE  
AND CONTOUR ,  $u_i/U_i$

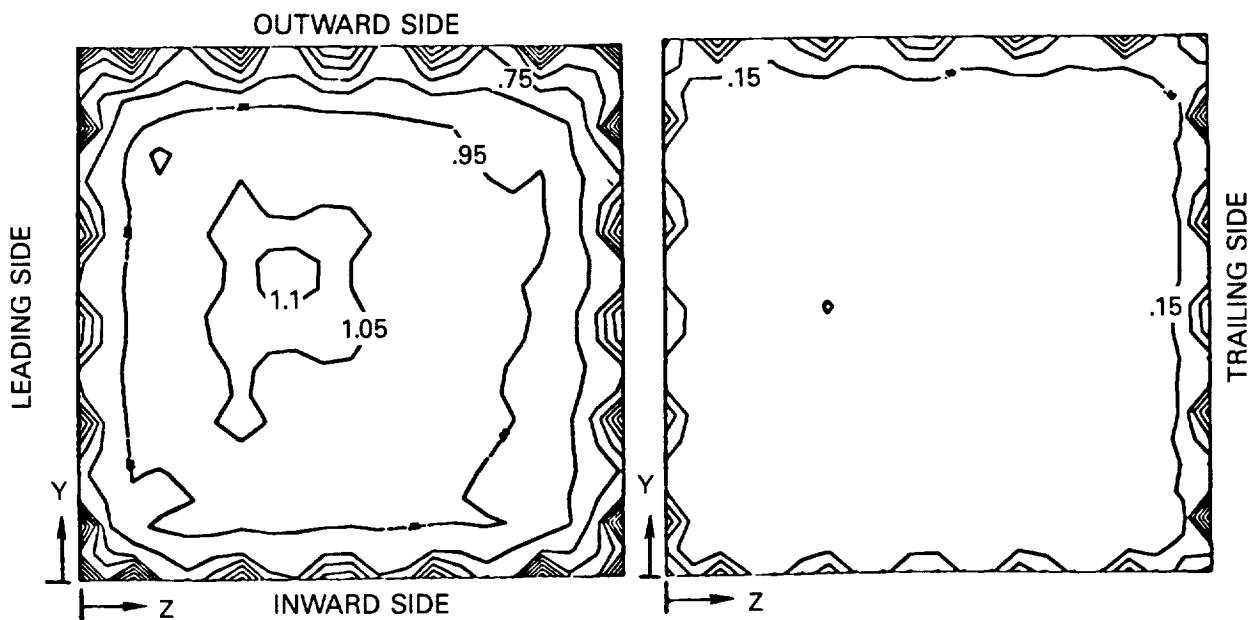
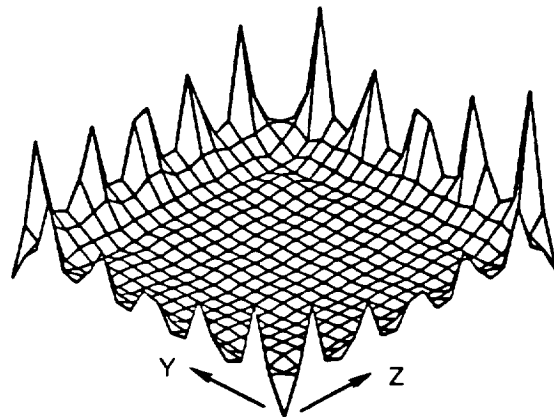


Figure 70.- Variation in Velocity Surfaces and Contours for Channel Exit Flow.

### 10.3 Error Analysis, Repeatability and Symmetry of the Model Heat Transfer Results

An analysis to determine the estimated error in measured heat transfer was conducted using the method described in Abernathy and Thompson (1973). The error analysis was a summation of the estimated inaccuracies in the data used to calculate the heat transfer coefficient and Nusselt number as shown below. When comparative testing is done (as in this program), Abernathy and Thompson suggest that biasing errors may be ignored. Therefore, only the precision errors were determined.

$$(\Delta Nu)^2 = \sum_{i=1}^n [(dNu/df_i)^2 (\Delta f_i)^2] \quad (10.13)$$

where  $f_i$  are the parameters used to determine the Nusselt number

To do the error analysis, assumptions of the estimated inaccuracies had to be made. Generally, where information was read by eye from a device (i.e., flow-meter, pressure guage, etc.), the estimated accuracy was assumed to be 1/4 of the smallest increment. Voltages read by the acquisition system were assumed to be accurate to the least significant digit, except for the thermocouple emfs which were assumed to be accurate to only 25 micro-volts. A summary of the estimated inaccuracies follows:

<u>Parameter</u>	<u>Estimated Error (+)</u>	<u>Method</u>
VD	0.000025 Volt	T.C. wire repeatability
VC	0.000025 Volt	T.C. wire repeatability
VB	0.0001 Volt	least significant measurement
E	0.001 Volt	least significant measurement
I	0.001 Volt	least significant measurement
QALOSS	(0.05) QALOSS	5% accurate estimate
FMA	0.25	1/4 increase on flow meter
CFMA	(0.005)CFMA	0.5% flow meter reading
BFMA	(0.005)BFMA	0.5% flow meter reading
PM <sub>in</sub>	0.25	1/4 increase
TM <sub>in</sub>	0.5	1/2 resolution
h	(0.02)h at the inlet	2%
	(0.06)h at the exit	6%

---

Note: h was only used to estimate the error of determining the effective heat transfer surface area.

This analysis, applied to the case where the stationary test point Reynolds Number is 25,000, showed the error of determining heat transfer at the entrance of the model was  $\pm 2\%$  and the error at the exit was  $\pm 7\%$  of the local heat transfer rate. Of the estimated error, over 90% was due to the error in determining the temperature. Nine percent of the estimated error was due to the error in determining the backloss.

A series of tests were conducted to determine the accuracy, symmetry and repeatability of the rotating heat transfer experiments. The data acquisition procedure, instrumentation, model calibration and heat loss aspects of the accuracy problem were addressed in Section 3. The results from the tests to measure repeatability and model symmetry are reported here.



### 10.3.1 Repeatability

The repeatability of the heat transfer experiments for the baseline rotating flow condition was determined by comparing the heat transfer coefficients obtained from UTRC Run 22.12 (Test No. 4) and UTRC Run 25.08. The "repeat" test was conducted after Test Nos. 9 and 10 which had lower and higher wall temperatures than the baseline flow condition. The ratio of the heat transfer coefficients from the baseline flow condition (Test 4) to that from the repeat test is shown in Table IV for each of the heater elements. The location for each heater element is identified in Figure 71. A comparison of the elements from the first leg of the model, i.e. elements 1-4, 19-22, 33-36 and 49-52, shows that the variation of the "repeat" results from the baseline results are 1 or 2%, except for one element. The variation for the repeat results in the second leg of the model is increased to 4% and the variation in the third leg is up to 9%. The increase in the variation of the results as the distance from the inlet increased was attributed to the uncertainty in the bulk temperature which was calculated as part of the data reduction procedure. The repeatability was considered very good, considering the large decrease in heat transfer due to rotation on the leading surfaces of the first and third passages.

### 10.3.2 Low Rotation

Tests were also conducted at a low rotational rate ( $\pm 15$  rpm). The results from the tests at 15 rpm (Tests 101 and 108) are compared with results from the stationary test (1A) at the baseline operating flow condition as shown in Figure 72. Note that for this flow condition with dimensionless rotation number ( $Ro$ ) equals  $-0.006$ ,  $0$ , and  $+0.006$ , small effects of rotation are noted. However, the results with rotation are either very close (i.e. 5%) or bracket the zero rotation results. The conclusion from this comparison is that acquisition of data through the slipring does not significantly affect the heat transfer results.

### 10.3.3 Effect of Rotation Direction

Data was also acquired with the model rotating in both the positive and negative directions at the baseline operating conditions. These tests were conducted to determine if small asymmetries in the construction of the elements or the assembly of the model were affecting the heat transfer results. The results from Test Nos. 4 ( $+550$  rpm) and 109 ( $-550$  rpm) are presented in Figure 73. The general results from both tests are identical. However, there is as much as a  $\pm 10\%$  variation in the heat transfer coefficient obtained from different elements in the same relative location. For example, element 35 (upper left portion of Figure 73) at the C streamwise location on the leading surface has ratios of  $Nu/Nu_{\infty} = 0.45$  and  $0.53$ , respectively. The conclusions from this comparison of results from the  $\pm 550$  rpm test conditions are (1) that there are no major asymmetries in the model, and (2) that the principal results from the test are not sensitive to model asymmetries.

TABLE IV  
 SYMMETRY OF MODEL AND REPEATABILITY OF HEAT TRANSFER RESULTS  
 ROTATING HEAT TRANSFER EXPERIMENTS WITH SMOOTH WALL MODEL  
 (Run No: 22:12 and 25.08)

Dimensionless Data

<u>Element No.</u>	<u><math>\sim X/d</math></u>	<u>Ro</u>	<u>Nu (22.12)/Nu (25.08)</u>
1	1	0.2410	0.99
2	5	0.2386	0.99
3	9	0.2365	0.98
4	12	0.2345	0.98
5	14	0.3106	0.97
6	15	0.3106	0.99
7	16	0.3079	0.98
8	17	0.3079	0.99
9	2	0.2286	0.99
10	6	0.2274	0.99
11	10	0.2266	0.97
12	2	0.2245	0.98
13	6	0.2237	0.97
14	10	0.2230	0.98
15	11	0.2973	0.95
16	12	0.2973	0.94
17	14	0.2964	1.03
18	15	0.2964	0.95
19	1	0.2410	1.00
20	5	0.2386	0.98
21	9	0.2365	0.98
22	12	0.2345	0.99
23	2	0.2286	0.99
24	6	0.2274	0.98
25	10	0.2266	0.98
26	11	0.3021	0.99
27	12	0.3021	1.00
28	14	0.3012	0.99
29	15	0.3012	0.97
30	2	0.2245	0.98
31	6	0.2237	0.99
32	10	0.2230	0.99
33	1	0.2410	1.00
34	5	0.2386	1.01
35	9	0.2365	1.01
36	12	0.2345	0.95
37	14	0.3106	0.98
38	17	0.3079	0.98
39	2	0.2286	0.96
40	6	0.2274	0.97
41	10	0.2266	0.99

TABLE IV (Cont'd)

Dimensionless Data

<u>Element No.</u>	<u><math>\sim X/d</math></u>	<u>Ro</u>	<u>Nu (22.12)/Nu (25.08)</u>
42	12	0.3021	0.97
43	14	0.3012	0.98
44	2	0.2245	0.96
45	6	0.2237	0.94
46	10	0.2230	0.92
47	12	0.2973	0.91
48	14	0.2964	0.96
49	1	0.2410	1.00
50	5	0.2386	0.98
51	9	0.2365	0.98
52	12	0.2345	0.98
53	14	0.3106	0.99
54	17	0.3079	0.98
55	2	0.2286	0.97
56	6	0.2274	0.96
57	10	0.2266	0.96
58	12	0.3021	0.95
59	14	0.3012	0.97
60	2	0.2245	0.97
61	6	0.2237	0.98
62	10	0.2230	0.97
63	12	0.2973	0.94
64	14	0.2964	0.93

$$Re \approx 25,000$$

$$Ro \approx .24$$

$$RPM = 550$$

$$\left(\frac{\Delta T}{T}\right)_{in} = 0.13$$

$$\Delta T = 44.4 \text{ C}^\circ (80^\circ \text{ F})$$

$$R/d = 49$$

$$\alpha = 0$$

SYMBOL	TEST NO	UTRC RUN NO
○	4	22.12
▲	Repeat	25.8

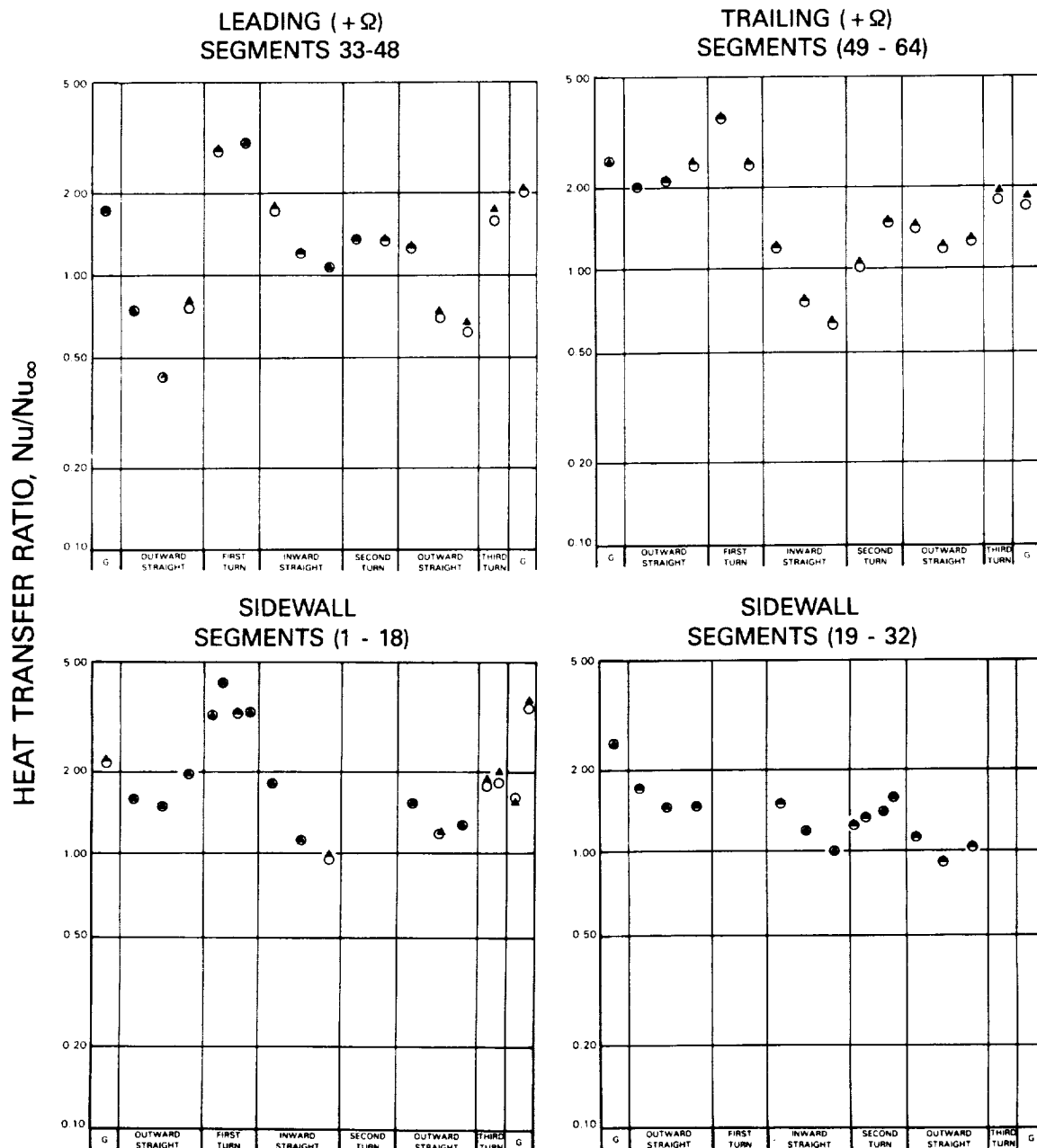


Figure 71.- Repeatability of Heat Transfer Data.

$$Re \approx 25,000$$

$$\left(\frac{\Delta T}{T}\right)_{in} = 0.13$$

$$\Delta T = 44.4^\circ C \text{ (} 80^\circ C \text{)}$$

$$\bar{R}/d = 49$$

$$\alpha = 0$$

SYMBOL	TEST	$\Omega$ RPM	Ro
●	1A	0	0
△	101	+15	+0.006
□	108	-15	-0.006

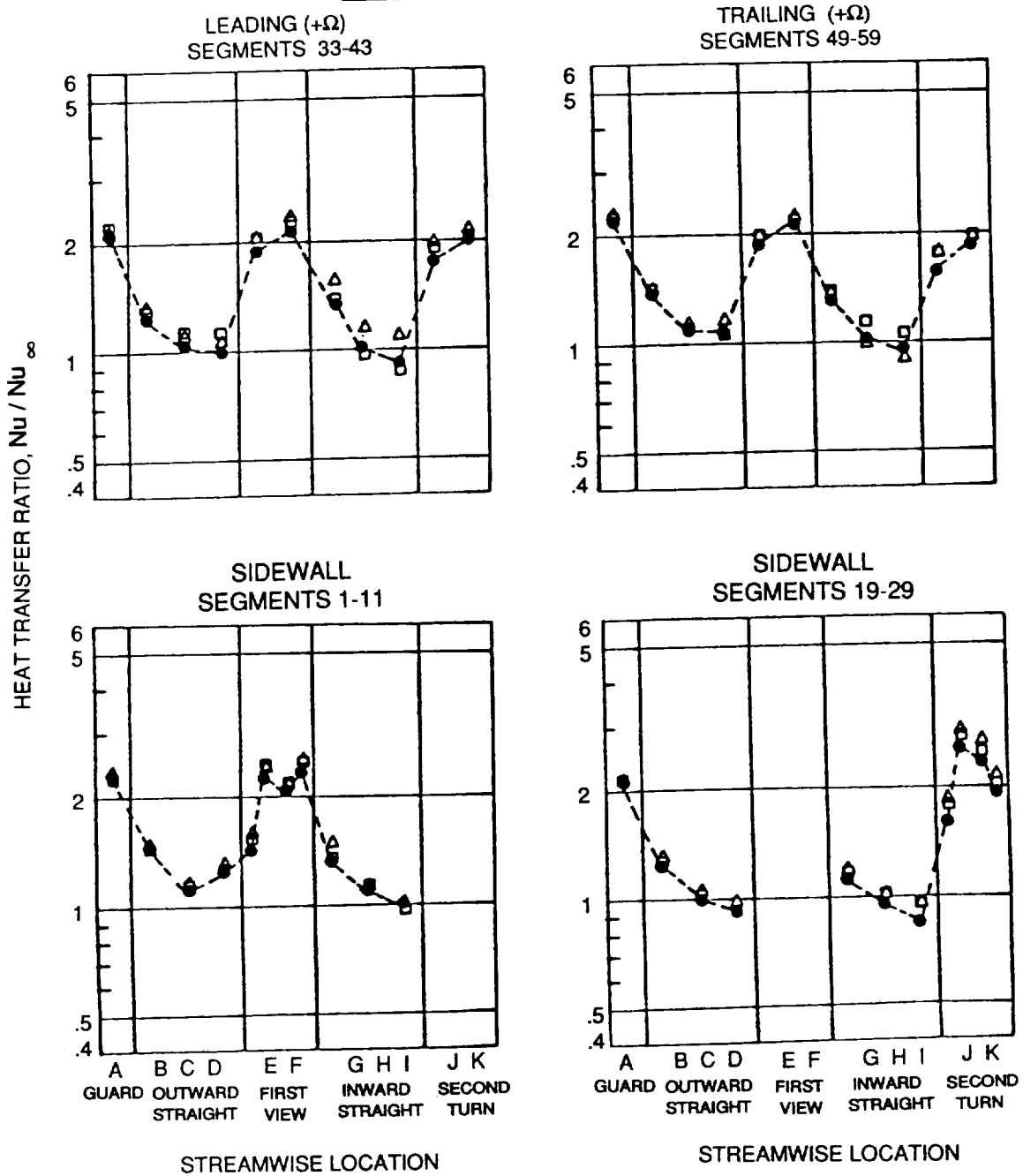


Figure 72.- Effect of Low Rotation on Heat Transfer.

$$Re \approx 25,000$$

$$\left(\frac{\Delta T}{T}\right)_{in} = 0.13$$

$$\Delta T = 44.4 \text{ C}^\circ (80^\circ \text{ F})$$

$$\bar{R}/d = 49$$

$$\alpha = 0$$

SYMBOL	TEST NO.	$\Omega$ RPM	Ro
■	4	550	.238
△	109	-550	-.233

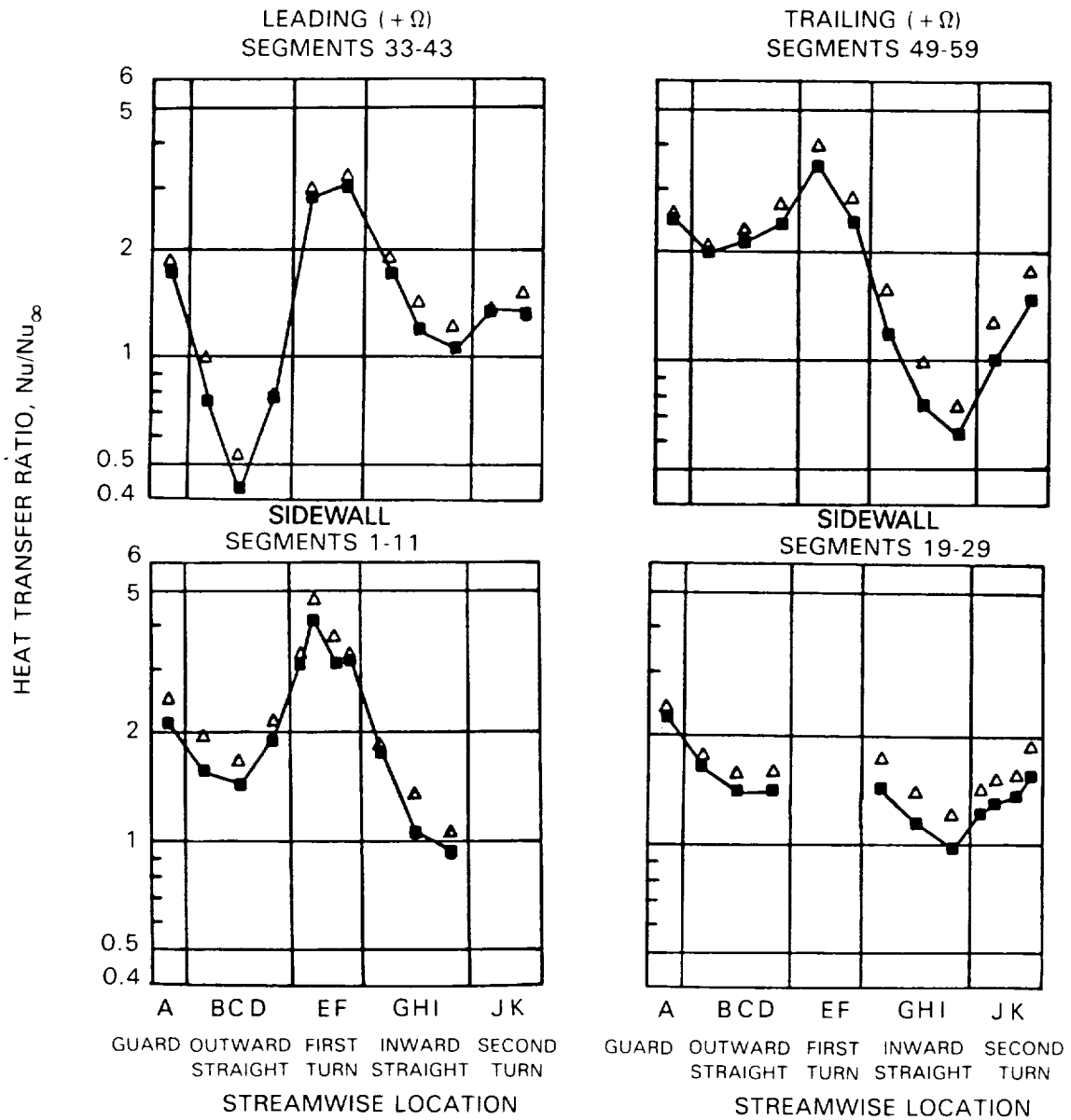


Figure 73 Effect of Rotation Direction on Heat Transfer.

## 10.4 PRESSURE LOSS MEASUREMENTS

Measurements were obtained during all heat transfer tests to determine the pressure drop through the serpentine coolant passage (Figure 8). The measurements for a nonrotating flow condition at a lower-than-standard flow pressure showed that the principal pressure drop occurred in the 180° turns connecting the four straight test section segments. The uncertainty in the pressure measurements and the low dynamic head of the flow at the standard flow pressure  $1.01325 \times 10^6 \text{ N/m}^2$  (10 atm) precluded the acquisition of data which could yield "benchmark quality" results for both the rotating and nonrotating tests. Typical results from these data indicate a variation in the pressure distribution; however, the overall pressure drop from the inlet to the exit of the model indicated small effects of rotation. Following is a discussion of the instrumentation, estimated accuracy, data analysis and typical results from the pressure distribution tests.

### 10.4.1 Instrumentation

The pressure tap locations are located in 16 sidewall test surface elements as shown in Figure 8. The pressure measurements were obtained with a Scanivalve Model ZOC14 (zero, operate, calibrate) differential electronic pressure scanner. The pressure measurement equipment was located on the rotating arm at a radius of approximately 30.5 cm (12"). The pressure scanner was encased in a thermal control unit (Scanivalve Model ZOC TCU). The thermal control unit is specified to maintain a uniform temperature to  $\pm 2^\circ\text{C}$  ( $\pm 3.6^\circ\text{F}$ ) in a stationary environment. The differential pressure transducers were referenced to pressure tap #1 (Figure 8). The power to and the signals from the electronic pressure scanner and thermal control unit were transmitted through sliprings for the rotating tests.

### 10.4.2 Estimate of Pressure Measurement Accuracy

Although the ZOC14 electronic pressure scanner was rated to be accurate within  $\pm 0.08\%$  full scale of the  $6895 \text{ N/m}^2$  (1 psi), full scale value, i.e.,  $5.516 \text{ N/m}^2$  ( $\pm 0.0008$  psi), the uncertainties associated with the transducer temperature variation, the rotating environment and the slipring noise reduced the estimated accuracy and repeatability to approximately 1% full scale or  $68.95 \text{ N/m}^2$  (0.01 psi). This accuracy is compatible with previous UTRC experience for pressure measurements in rotating systems. The value of  $68.95 \text{ N/m}^2$  (0.01 psi) is also approximately  $1.0 Q_{in}$  for the baseline flow condition.

### 10.4.3 Data Analysis

The pressure drops measured in the rotating serpentine coolant passage model were referenced to the pressure drop in the nonrotating model by (1) subtracting the pressure increases due to work from model rotation on the coolant at locations radially outward from pressure tap #1 and (2) adding the pressure drop due to work from model rotation on the coolant at locations radially inward from pressure tap #1. In the four legged model (Figure 8), this pressure rise is of the order  $(Qr^2\Delta\rho)/4$ . The pressure increase due to a nominal  $33.3^\circ\text{C}$  ( $60^\circ\text{F}$ ) temperature increase in the coolant fluid temperature is approximately  $20.685 \text{ N/m}^2$  (0.003 psi or  $0.4 Q_{in}$ ) for the 550 rpm test condition.

#### 10.4.4 Results for $\Omega = 0$ and Low Pressure

Pressure drop measurements were obtained for a unheated, nonrotating test condition at the same Reynolds number as Test No. 1 but at a lower pressure, i.e.  $p = 249.599 \text{ N/m}^2$  (36.2 psia) compared to  $1017013 \text{ N/m}^2$  (147.5 psia). This was done to increase the dynamic head of the flow in the test sections to  $209.6 \text{ N/m}^2$  (0.84 in water or 0.03 psi). This corresponds to about three percent of full scale for the pressure transducers. The pressure drop results are shown in Figure 74 as the ratio of pressure drop from the inlet ( $\Delta P$ ) to the dynamic head of the air in the inlet test section ( $Q_{in}$ ). Note the pressure drop in the straight sections is negligible (as expected) and is about  $0.8 Q_{in}$  in each turn (also as expected). The pressure drop measurements will become more meaningful in the rough wall experiments where the pressure drop in the straight sections will increase by a factor of 10 and become measurable.

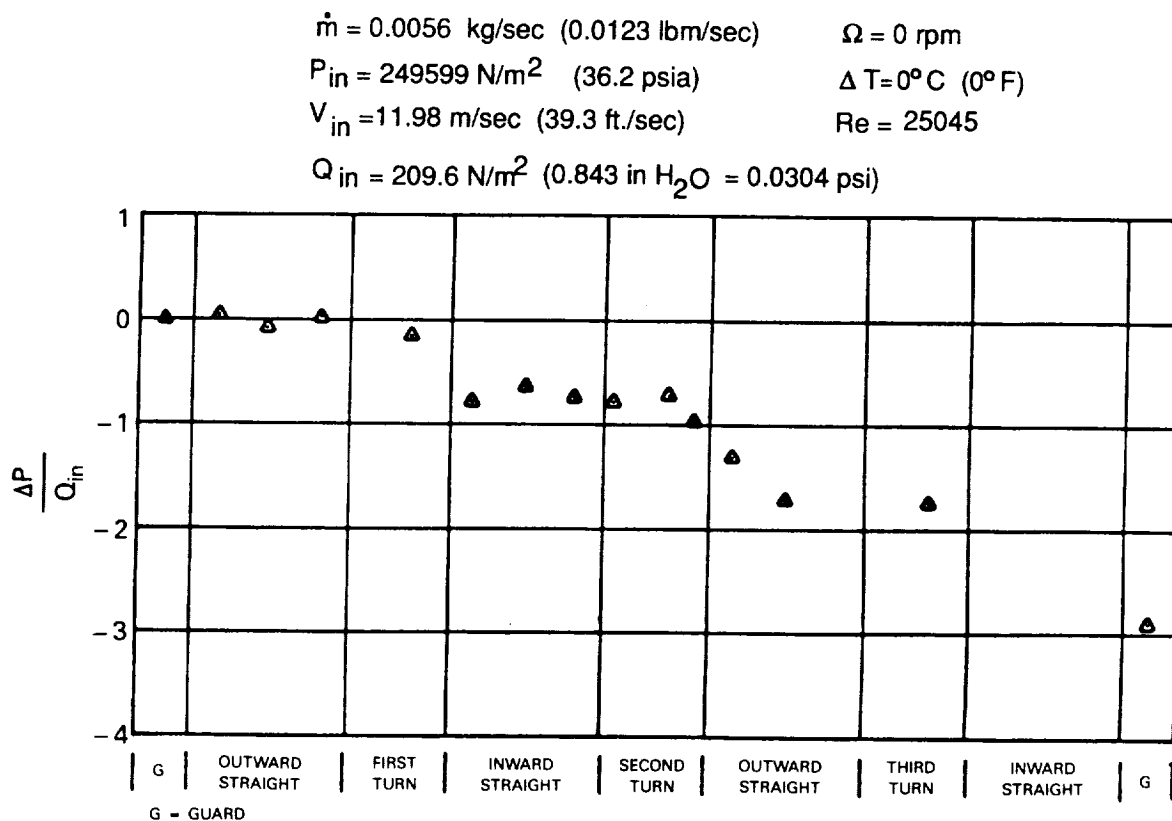


Figure 74.- Pressure Distribution in Nonrotating Model at the Low Model Pressure Condition.

#### 10.4.5 Results for Nonrotating Tests

Pressure drops were measured in the nonrotating model for the operating flow conditions of Tests 1, 2 and 3 (see Table I). The pressure drop in the model with respect to the pressure at Tap No. 1 is shown in Figure 75. The pressure drop distributions measured for the two higher Reynolds numbers were similar to that shown in Figure 74 for a lower pressure flow condition. Note that there is no measurable pressure drop in the straight sections and a pressure drop of approximately  $0.8$  to  $1.0 Q_{in}$  at each of the of the  $180^\circ$



$$\begin{aligned}
 Ro &= 0 & \Delta T &\approx 44.4^\circ\text{C} \ (80^\circ\text{F}) \\
 \text{RPM} &= 0 & \bar{R}/d &= 49 \\
 \left(\frac{\Delta T}{T}\right)_{\text{in}} &= 0.13 & \alpha &= 0
 \end{aligned}$$

SYMBOL	□	△	◇
Re NO.	12.5K	25K	50K
TEST NO.	2	1	3

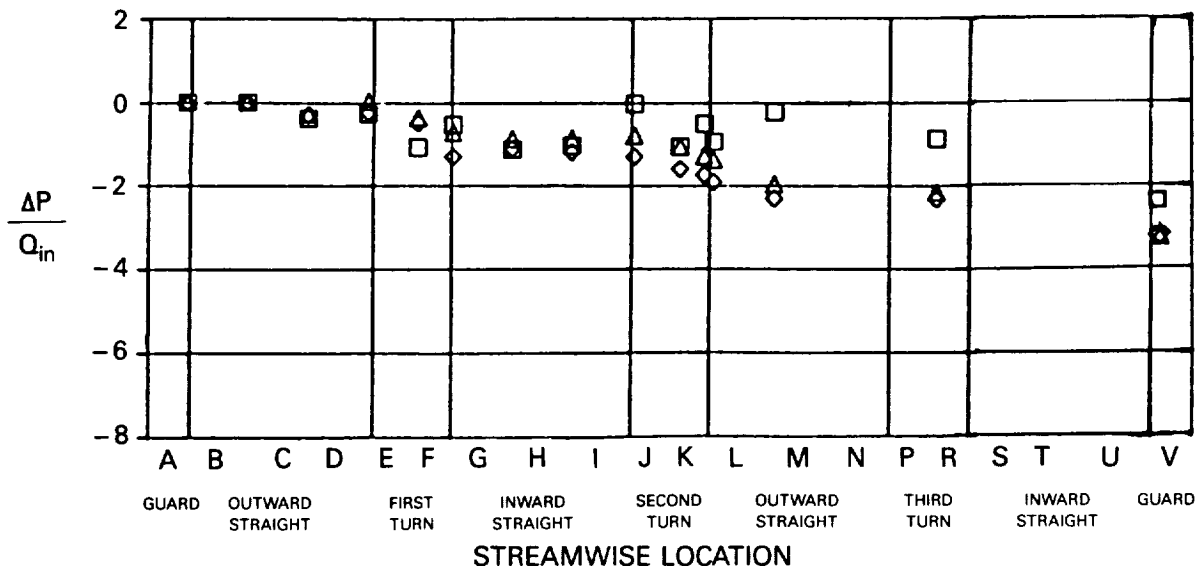


Figure 75.- Effect of Reynolds Number on Pressure Distribution in Nonrotating Model.

turns. As noted previously, the uncertainty for the measurements for Test No. 1 are  $\pm 1.0 Q_{in}$ . This uncertainty decreases to  $0.25 Q_{in}$  for Test No. 3 with Re equal approximately 50,000 and increases to  $4.0 Q_{in}$  for Test No. 2 with Re equal approximately 12,500.

#### 10.4.6 Results for Rotating Tests

Pressure drops were measured for rotating Test Nos. 4, 8 and 114 with Re approximately equal to 25,000. These results for rotating flow conditions are compared with results for Test No. 1. For the first leg of the coolant passage, the pressure drops for all test conditions are approximately equal within the measurement uncertainty. The pressure drop increases with increasing rotation rate for flow in the second and third legs. However, the pressures near the coolant passage exit (pressure measurement location 16) are approximately equal, i.e.  $\pm 0.3 Q_{in}$ . Within the assumptions made for the analysis of the data, there is no explanation for the large (i.e.  $\Delta P/Q_{in} = 3$ ) variations in the pressure distributions shown in Figure 76. However, the translation of the local pressures measured by the ZOC scanner at a radius of approximately 30.5

$$Re \approx 25000 \quad \Delta T \approx 44.4^\circ \text{C} (80^\circ \text{F})$$

$$\left(\frac{\Delta T}{T}\right)_{in} = 0.13 \quad \bar{R}/d = 49$$

$$\alpha = 0$$

SYMBOL	□	△	◇	×
TEST NO.	1	8	114	4
RPM	0	275	412	550
Ro	0	0.118	0.178	0.238

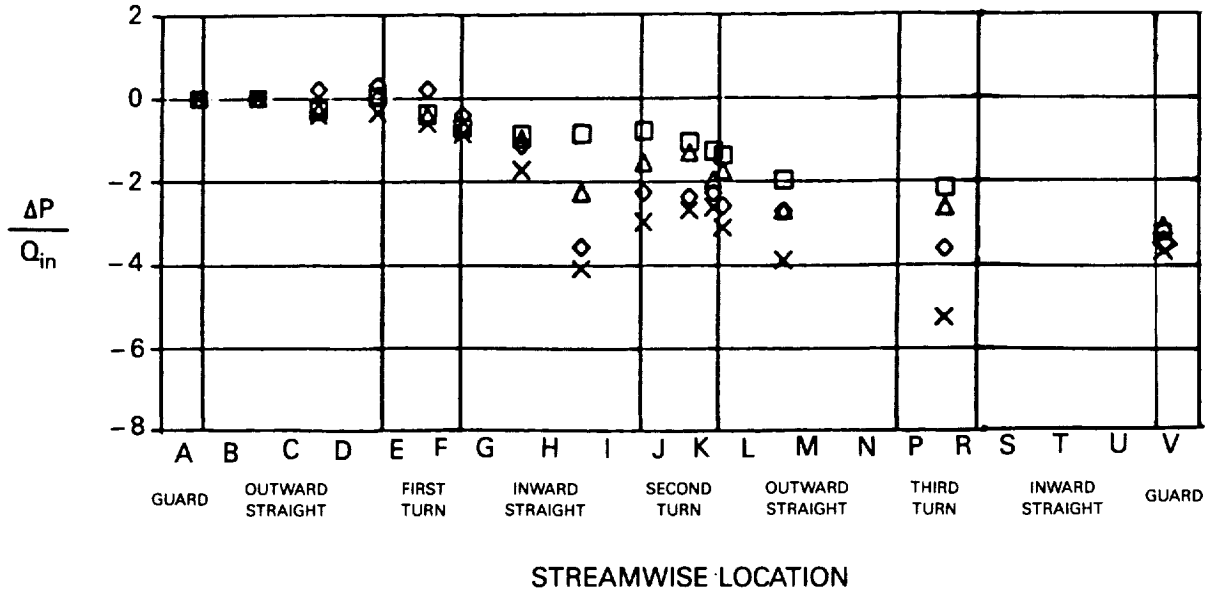


Figure 76.- Effect of Rotation on Pressure Distribution in Model.

cm (12") to the model at radii of 68.6 cm (27") to 81.3 cm (32") requires an assumption of the temperature in the pressure line. A variation of temperature equal to 5.6°C (10°F) in the 16 lines leading from the model to the ZOC electronic pressure scanner could account for the variation of  $\Delta P/Q_{in}$  equal 3.0 measured in the second leg with rotation.

#### 10.5 Model Geometry Information

Table V gives the test model heat transfer geometry information as a function of the local test segment heater location (1-64). Table VI gives the test model pressure tap geometry information as a function of pressure tap location (1-16). The List of Symbols contains the column variable definitions.

TABLE V  
MODEL HEAT TRANSFER GEOMETRY INFORMATION

Heater Segment No.	d		A		CA		RADH		S		X	
	cm	(in)	2 cm	c 2 (in)	2 cm	2 (in)	cm	(in)	cm	(in)	cm	(in)
1	1.3155	0.5179	1.5923	0.2468	3.7258	0.5775	10.190	4.012	1.748	0.688	1.748	0.688
2	1.3155	0.5179	1.5923	0.2468	5.2484	0.8135	14.557	5.731	6.114	2.407	6.114	2.407
3	1.3155	0.5179	1.5923	0.2468	5.2484	0.8135	19.637	7.731	11.194	4.407	11.194	4.407
4	1.3155	0.5179	1.5923	0.2468	5.2484	0.8135	24.717	9.731	16.274	6.407	16.274	6.407
5	1.4323	0.5639	1.9555	0.3031	2.5116	0.3893	28.400	11.181	19.644	7.734	19.644	7.734
6	1.4323	0.5639	1.9555	0.3031	2.4277	0.3763	29.972	11.800	21.303	8.387	21.303	8.387
7	1.4323	0.5639	1.9555	0.3031	2.4277	0.3763	29.972	11.800	22.964	9.041	22.964	9.041
8	1.4323	0.5639	1.9555	0.3031	2.5116	0.3893	28.400	11.181	24.623	9.694	24.623	9.694
9	1.3155	0.5179	1.5923	0.2468	5.2484	0.8135	24.717	9.731	27.993	11.021	2.540	1.000
10	1.3155	0.5179	1.5923	0.2468	5.2484	0.8135	19.637	7.731	33.073	13.021	7.620	3.000
11	1.3155	0.5179	1.5923	0.2468	5.2484	0.8135	14.557	5.731	38.153	15.021	12.700	5.000
12	1.3155	0.5179	1.5923	0.2468	5.2484	0.8135	14.557	5.731	49.873	19.635	2.540	1.000
13	1.3155	0.5179	1.5923	0.2468	5.2484	0.8135	19.637	7.731	54.953	21.635	7.620	3.000
14	1.3155	0.5179	1.5923	0.2468	5.2484	0.8135	24.717	9.731	60.033	23.635	12.700	5.000
15	1.4323	0.5639	1.9555	0.3031	2.5116	0.3893	28.400	11.181	63.403	24.962	16.071	6.327
16	1.4323	0.5639	1.9555	0.3031	2.4277	0.3763	29.972	11.800	65.062	25.615	17.729	6.980
17	1.4323	0.5639	1.9555	0.3031	2.4277	0.3763	29.972	11.800	66.723	26.269	19.390	7.634
18	1.4323	0.5639	1.9555	0.3031	2.5116	0.3893	28.400	11.181	68.382	26.922	21.049	8.287
19	1.3155	0.5179	1.5923	0.2468	3.7258	0.5775	10.190	4.012	1.748	0.688	1.748	0.688
20	1.3155	0.5179	1.5923	0.2468	5.2484	0.8135	14.557	5.731	6.114	2.407	6.114	2.407
21	1.3155	0.5179	1.5923	0.2468	5.2484	0.8135	19.637	7.731	11.194	4.407	11.194	4.407
22	1.3155	0.5179	1.5923	0.2468	5.2484	0.8135	24.717	9.731	16.274	6.407	16.274	6.407
23	1.3155	0.5179	1.5923	0.2468	5.2484	0.8135	24.717	9.731	27.993	11.021	2.540	1.000
24	1.3155	0.5179	1.5923	0.2468	5.2484	0.8135	19.637	7.731	33.073	13.021	7.620	3.000
25	1.3155	0.5179	1.5923	0.2468	5.2484	0.8135	14.557	5.731	38.153	15.021	12.700	5.000
26	1.4323	0.5639	1.9555	0.3031	2.5116	0.3893	10.874	4.281	41.524	16.348	16.071	6.327
27	1.4323	0.5639	1.9555	0.3031	2.4277	0.3763	9.301	3.662	43.185	17.002	17.729	6.980
28	1.4323	0.5639	1.9555	0.3031	2.4277	0.3763	9.301	3.662	44.016	17.329	19.390	7.634
29	1.4323	0.5639	1.9555	0.3031	2.5116	0.3893	10.874	4.281	46.505	18.309	21.049	8.287
30	1.3155	0.5179	1.5923	0.2468	5.2484	0.8135	14.557	5.731	49.873	19.635	2.540	1.000
31	1.3155	0.5179	1.5923	0.2468	5.2484	0.8135	19.637	7.731	54.953	21.635	7.620	3.000
32	1.3155	0.5179	1.5923	0.2468	5.2484	0.8135	24.717	9.731	60.033	23.635	12.700	5.000
33	1.3155	0.5179	1.5923	0.2468	3.7258	0.5775	10.190	4.012	1.748	0.688	1.748	0.688
34	1.3155	0.5179	1.5923	0.2468	5.2484	0.8135	14.557	5.731	6.114	2.407	6.114	2.407
35	1.3155	0.5179	1.5923	0.2468	5.2484	0.8135	19.637	7.731	11.194	4.407	11.194	4.407
36	1.3155	0.5179	1.5923	0.2468	5.2484	0.8135	24.717	9.731	16.274	6.407	16.274	6.407
37	1.4323	0.5639	1.9555	0.3031	5.1877	0.8041	28.819	11.346	20.475	8.061	20.475	8.061
38	1.4323	0.5639	1.9555	0.3031	5.1877	0.8041	28.819	11.346	23.795	9.368	23.795	9.368
39	1.3155	0.5179	1.5923	0.2468	5.2484	0.8135	24.717	9.731	27.993	11.021	2.540	1.000
40	1.3155	0.5179	1.5923	0.2468	5.2484	0.8135	19.637	7.731	33.073	13.021	7.620	3.000
41	1.3155	0.5179	1.5923	0.2468	5.2484	0.8135	14.557	5.731	38.153	15.021	12.700	5.000
42	1.4323	0.5639	1.9555	0.3031	5.1877	0.8041	10.455	4.116	42.354	16.675	16.901	6.654
43	1.4323	0.5639	1.9555	0.3031	5.1877	0.8041	10.455	4.116	45.674	17.982	20.221	7.961
44	1.3155	0.5179	1.5923	0.2468	5.2484	0.8135	14.557	5.731	49.873	19.635	2.540	1.000
45	1.3155	0.5179	1.5923	0.2468	5.2484	0.8135	19.637	7.731	54.953	21.635	7.620	3.000
46	1.3155	0.5179	1.5923	0.2468	5.2484	0.8135	24.717	9.731	60.033	23.635	12.700	5.000
47	1.4323	0.5639	1.9555	0.3031	5.1877	0.8041	28.819	11.346	64.234	25.289	16.901	6.654
48	1.4323	0.5639	1.9555	0.3031	5.1877	0.8041	28.819	11.346	67.554	26.596	20.221	7.961
49	1.3155	0.5179	1.5923	0.2468	3.7258	0.5775	10.190	4.012	1.748	0.688	1.748	0.688
50	1.3155	0.5179	1.5923	0.2468	5.2484	0.8135	14.557	5.731	6.114	2.407	6.114	2.407
51	1.3155	0.5179	1.5923	0.2468	5.2484	0.8135	19.637	7.731	11.194	4.407	11.194	4.407
52	1.3155	0.5179	1.5923	0.2468	5.2484	0.8135	24.717	9.731	16.274	6.407	16.274	6.407
53	1.4323	0.5639	1.9555	0.3031	5.1877	0.8041	28.819	11.346	20.475	8.061	20.475	8.061
54	1.4323	0.5639	1.9555	0.3031	5.1877	0.8041	28.819	11.346	23.795	9.368	23.795	9.368
55	1.3155	0.5179	1.5923	0.2468	5.2484	0.8135	24.717	9.731	27.993	11.021	2.540	1.000
56	1.3155	0.5179	1.5923	0.2468	5.2484	0.8135	19.637	7.731	33.073	13.021	7.620	3.000
57	1.3155	0.5179	1.5923	0.2468	5.2484	0.8135	14.557	5.731	38.153	15.021	12.700	5.000
58	1.4323	0.5639	1.9555	0.3031	5.1877	0.8041	10.455	4.116	42.354	16.675	16.901	6.654
59	1.4323	0.5639	1.9555	0.3031	5.1877	0.8041	10.455	4.116	45.674	17.982	20.221	7.961
60	1.3155	0.5179	1.5923	0.2468	5.2484	0.8135	14.557	5.731	49.873	19.635	2.540	1.000
61	1.3155	0.5179	1.5923	0.2468	5.2484	0.8135	19.637	7.731	54.953	21.635	7.620	3.000
62	1.3155	0.5179	1.5923	0.2468	5.2484	0.8135	24.717	9.731	60.033	23.635	12.700	5.000
63	1.4323	0.5639	1.9555	0.3031	5.1877	0.8041	28.819	11.346	64.234	25.289	16.901	6.654
64	1.4323	0.5639	1.9555	0.3031	5.1877	0.8041	28.819	11.346	67.554	26.596	20.221	7.961

TABLE VI  
MODEL PRESSURE TAP GEOMETRY INFORMATION

Pressure Tap No.	RADP		S		X	
	cm	(in)	cm	(in)	cm	(in)
1	11.582	4.560	3.139	1.236	3.139	1.236
2	16.662	6.560	8.219	3.236	8.219	3.236
3	21.742	8.560	13.299	5.236	13.299	5.236
4	26.822	10.560	18.379	7.236	18.379	7.236
5	30.175	11.880	22.570	8.886	22.570	8.886
6	26.822	10.560	25.491	10.036	0.038	0.015
7	21.742	8.560	30.571	12.036	5.118	2.015
8	16.662	6.560	35.651	14.036	10.198	4.015
9	11.430	4.500	40.909	16.106	15.456	6.085
10	8.890	3.500	44.770	17.626	19.317	7.605
11	11.430	4.500	46.904	18.466	21.450	8.445
12	12.217	4.810	47.691	18.776	0.358	0.141
13	17.297	6.810	52.771	20.776	5.438	2.141
14	22.377	8.810	57.851	22.776	10.518	4.141
15	30.175	11.880	66.487	26.176	19.154	7.541
16	11.582	4.560	84.673	33.336	15.674	6.171

# LIST OF SYMBOLS

$A_c$	Cross sectional area of the passage, $\text{cm}^2$ ( $\text{in}^2$ )
BFMA	Flow meter (B) reading, $\text{kg/sec}$ ( $\text{lbm/sec}$ )
$C_f$	Skin friction coefficient, $\tau_w/(\rho V^2/2)$ , dimensionless
CA	Local heated test surface segment (heater segment) surface area, $\text{cm}^2$ ( $\text{in}^2$ )
CFMA	Flow meter (C) reading, $\text{kg/sec}$ ( $\text{lbm/sec}$ )
$d$	Local hydraulic diameter of the passage, $\text{cm}$ ( $\text{in}$ )
$D$	Channel depth (Moore 1967), $\text{cm}$ ( $\text{in}$ )
$E$	Heater element supply voltage, volts
FMA	Flow meter reading, $\text{kg/sec}$ ( $\text{lbm/sec}$ )
$Gr$	Local rotational Grashof number based on hydraulic diameter, $(\Omega^2 R d^3)(\rho_b - \rho_w)(\rho_b/\mu^2)$ , dimensionless
$Gr_x$	Local rotational Grashof number based on streamwise distance $X$ , $(\Omega^2 R X^3)(\rho_b - \rho_w)(\rho_b/\mu^2)$ , dimensionless
$Gr/Re^2$	Local buoyancy parameter based on hydraulic diameter, $((\rho_b - \rho_w)/\rho_b)(\Omega R/V)(\Omega d/V)$ , dimensionless
$Gr_x/Re^2$	Local buoyancy parameter based on streamwise distance $X$ , $((\rho_b - \rho_w)/\rho_b)(\Omega R/V)(\Omega d/V)(X/d)$ , dimensionless
$h$	Local heat transfer coefficient, $Q_{net}/(CA(T_w - T_b))$ , $W/(m^2C)$ ( $\text{Btu}/(\text{hrft}^2F)$ )
$\bar{i}$	Unit coordinate direction, (Suo 1980, see Section 10.1), dimensionless
$I$	Heater segment current, amps
$\bar{j}$	Unit coordinate direction, (Suo 1980, see Section 10.1), dimensionless
$k$	Thermal conductivity, $W/(mC)$ ( $\text{Btu}/(\text{hrft}F)$ )
$\bar{k}$	Unit coordinate direction, (Suo 1980, see Section 10.1), dimensionless
$L$	Channel width (Moore 1967), $\text{cm}$ ( $\text{in}$ )
$L/d$	Channel aspect ratio (Moore 1967), dimensionless

$\dot{m}$	Mass flow rate, kg/sec (lbm/sec)
$n$	Revolutions per minute (Ito and Nambu 1970), rpm
$Nu$	Local Nusselt number based on hydraulic diameter, $hd/k$ , dimensionless
$Nu_x$	Local Nusselt number based on distance from the channel entrance, $hX/k$ , dimensionless
$Nu_0$	Local Nusselt number based on hydraulic diameter for the stationary (non-rotating) test condition, dimensionless
$Nu_\infty$	Local Nusselt number for fully developed turbulent flow in a square duct $0.0176(Re^{0.8})$ , dimensionless
$P$	Pressure, (local pressure (Suo 1980) see Section 10.1), $N/m^2$ (psi)
$P_{in}$	Model Pressure at tap #1, $N/m^2$ (psi)
$PM_{in}$	Inlet model pressure, $N/m^2$ (psi)
$P_m$	Average channel pressure, (Suo 1980, see Section 10.1), $N/m^2$ (psi)
$P'$	Non-dimensional pressure
$\Delta P$	Pressure difference between the local static pressure tap readings (corrected for pumping effects to the radius of model pressure tap #1) and the model pressure tap #1, $N/m^2$ (psi)
$\Delta P/Q_{in}$	Pressure difference between the local static pressure tap readings (corrected for pumping effects to the radius of model pressure tap #1) and the model pressure tap #1, normalized by the inlet dynamic pressure, dimensionless
$Pr$	Prandtl number, dimensionless
$Q_{in}$	Channel inlet dynamic pressure, $N/m^2$ (psi)
$Q_{net}$	Net heat rate input into the flow field from the heater segment, W (Btu/hr)
$Q_{LOSS}$	Heat flux loss from the heater elements, $W/m^2$ (Btu/(hrft <sup>2</sup> ))
$\vec{r}$	Radius vector (Suo 1980, see Section 10.1), cm (in)
$R$	Radial distance from the axis of rotation, $R_{ADH} + R_{BASE}$ for the heater segments, $R_{ADP} + R_{BASE}$ for the pressure tap locations. cm (in)
$\bar{R}$	Average model radius from the axis of rotation, cm (in)
$R/d$	Non-dimensional radial location

$\bar{R}/d$	Non-dimensional radial location based on the average model radius
$Ra_x$	Rotational Rayleigh number based on distance from the channel entrance, $(\Omega^2 R X^3 \Delta T / (\nu^2 T_b)) Pr$ , dimensionless
RADH	Radial location to the center of a heater segment relative to the base of the model (RBASE). cm (in)
RADP	Radial location of wall pressure tap relative to the base of the model (RBASE). cm (in)
RBASE	Distance from the axis of rotation to the base of the model. The "base of the model" was an arbitrarily defined reference point. RBASE equals 46.673 cm (18.375 in) for $R/d = 49$ , and RBASE equals 24.130 cm (9.50 in) for $R/d = 33$ .
Re	Reynolds number based on hydraulic diameter, $\dot{m}d/(A_c \mu)$ , dimensionless
$Re_x$	Reynolds number based on distance from the channel entrance, $\rho V X / \mu$ , dimensionless
Ro	Rotation number, $\Omega d/V$ , dimensionless
S	Distance measured from the leading edge of the first channel heater segment. cm (in)
STD	Standard rotating baseline flow conditions, $Re = 25000$ , $Ro = 0.24$ , $(\Delta \rho / \rho)_{in} = (\Delta T / T)_{in} = 0.13$ , $\bar{R}/d = 49$ , $\alpha = 0$ , dimensionless
t	Time, (Suo 1980, see section 10.1), sec
$t'$	Non-dimensional time
$T_b$	Local bulk temperature of the fluid, K (R)
$T_w$	Local wall temperature of the channel heater segment, K (R)
$\Delta T$	Temperature difference, $(T_w - T_b)$ , C (F)
$\Delta T/T$	Local temperature ratio, $(T_w - T_b)/T_w$ , dimensionless
$(\Delta T/T)_{in}$	Temperature ratio, $(T_w - T_b)/T_w$ , where $T_b$ is evaluated at the inlet of the model, dimensionless. Note: $(\Delta T/T)_{in} = (\Delta \rho / \rho)_{in}$
$TM_{in}$	Surface temperature at the model inlet, K (R)
$u'_i$	Local fluctuating velocity, m/sec (ft/sec)

$U_i$	Time average local velocity, m/sec (ft/sec)
$\bar{U}$	Average channel velocity, m/sec (ft/sec)
$u/U$	Non-dimensional velocity ratio (Moore 1967), dimensionless
$V$	Local average channel velocity, m/sec (ft/sec)
$\bar{V}$	Local velocity, (Suo 1980, see Section 10.1), m/sec (ft/sec)
$\bar{V}'$	Non-dimensional velocity
$V_{in}$	Inlet channel velocity, m/sec (ft/sec)
$V_m$	Average channel velocity, (Suo 1980, see Section 10.1), m/sec (ft/sec)
VB	Thermocouple voltage, volts
VC	Thermocouple voltage, volts
VD	Thermocouple voltage, volts
$x$	Coordinate direction (Suo 1980, see Section 10.1), cm (in)
$x'$	Non-dimensional coordinate direction
$X$	Distance measured from the leading edge of the first channel heater segment or the end of the last turn region. cm (in)
$X/d$	Non-dimensional distance measured from the leading edge of the first channel heater segment or end of the last turn region.
$y$	Coordinate direction (Suo 1980, see Section 10.1), cm (in)
$y'$	Non-dimensional coordinate direction
$z$	Coordinate direction (Suo 1980, see Section 10.1), cm (in)
$z'$	Non-dimensional coordinate direction
$\alpha$	Model test section orientation angle with respect to the axis of rotation, deg
$\delta$	Boundary layer thickness, cm (in)
$\delta^*$	Displacement thickness, cm (in)
$\mu$	Absolute viscosity, kg/msec (lbm/ftsec)
$\nu$	Kinematic viscosity, $m^2/sec$ ( $ft^2/sec$ )
$\rho$	Local density, (Suo 1980, see Section 10.1), $kg/m^3$ (lbm/ft <sup>3</sup> )



$\rho_b$	Local channel density based on local bulk temperature, kg/m <sup>3</sup> (lbm/ft <sup>3</sup> )
$\rho_m$	Average channel density, (Suo 1980, see Section 10.1), kg/m <sup>3</sup> (lbm/ft <sup>3</sup> )
$\rho_w$	Local channel density based on local wall surface temperature, kg/m <sup>3</sup> (lbm/ft <sup>3</sup> )
$\rho'$	Non-dimensional density
$\Delta \rho/\rho$	Local density ratio, $(\rho_b - \rho_w)/\rho_b$ , dimensionless
$(\Delta \rho/\rho)_{in}$	Density ratio, $(\rho_b - \rho_w)/\rho_b$ , where $\rho_b$ is evaluated at the inlet of the model, dimensionless. Note: $(\Delta \rho/\rho)_{in} = (\Delta T/T)_{in}$
$\tau_w$	Wall shear stress, N/m <sup>2</sup> (psi)
$\Omega$	Rotation rate, radian/sec
$(\Omega R/V)(\Delta T/T)$	Centripetal buoyancy parameter, dimensionless

Subscripts:

b	Bulk property
c	Cross section
f	Skin friction
i	At i'th location
in	Inlet to model
m	Average channel property
net	Net input to the fluid
w	Wall surface property
x	Based on streamwise location X
$\infty$	Fully developed turbulent smooth tube flow
0	Stationary (non-rotating) condition

Superscripts:

-	Vector quantity or average value
'	Non-dimensional parameter or fluctuating parameter
*	Displacement

## REFERENCES

- Abernathy, R.B., et. al., and Thompson, J.W., Jr., Uncertainty in Gas Turbine Measurements, Arnold Engineering Development Center AEDC-TR-73-5, February 1973.
- Aladyev, I. T., Experimental Determination of Local and Mean Coefficients of Heat Transfer for Turbulent Flow in Pipes. NACA TM 1356, 1954. (Translation from Russian).
- Barua, S. N., Secondary Flow in a Rotating Pipe, Proc. R. Society A, Vol. 227, p. 133; 1954-55.
- Bergles, A.E. and Webb R.L., Bibliography of Convective Heat and Mass Transfer List of References. Augmentation of Convective Heat and Mass Transfer, ed. Bergles, A.E. and Webb, R.L., ASME, New York, pp 70-79, 1970.
- Boelter, L. M. K., Young, G. and Iverson, H. W., NACA TN 1451, Washington, July 1948.
- Brundrett, E. and Burroughs P.R., The Temperature Inner-Law and Heat Transfer for Turbulent Air Flow in a Vertical Square Duct. Int. J. Heat Mass Transfer, Vol. 10, pp 1133-1142, 1967.
- Burggraf, F., Experimental Heat Transfer and Pressure Drop with Two-Dimensional Turbulence Promoters Applied to Two Opposite Walls of a Square Tube. In Augmentation of Convective Heat and Mass Transfer., ed. Bergles, A.E. and Webb, R.L. ASME, New York, pp 70-79; 1970.
- Eckert, E.R.G., Diaguila, A.J. and Curren, A.N., Experiments on Mixed - Free and Forced-Convective Heat Transfer Connected with Turbulent Flow Through a Short Tube. NACA Technical Note 2974, 1953.
- Eckert, E.R.G. and Diaguilla, A.J., Convective Heat Transfer for Mixed, Free and Forced Flow Through Tubes, Transactions ASME 76, p. 497-504 (1954).
- Guidez, J., Study of the Convective Heat Transfer in Rotating Coolant Channel. ASME Paper 88-GT-33 presented in Amsterdam, The Netherlands, June, 1988.
- Han, J.C. Glicksman L.R. and Rohsenow, W.M., An Investigation of Heat Transfer and Friction for Rib-Roughened Surfaces. Int. J. Heat Mass Transfer, Vol 21, pp. 1143-1156, 1978.
- Hart, J.E., Instability and Secondary Motion in a Rotating Channel Flow. J. Fluid Mech., Vol. 45, part 2, pp. 341-351; 1971.
- Iacovides, H., Launder, B. E., Parametric and Numerical Study of Fully-Developed Flow and Heat Transfer in Rotating Rectangular Ducts. ASME Paper 90-GT-24.
- Iskakov, K.M. and Trushin, V.A., Influence of Rotation on Heat Transfer in a Turbine-Blade Radial Slot Channel. Izvestiya VUZ. Aviatsionnaya Tekhnika, Vol. 26, No. 1, pp. 97-99, 1983.

- Iskakov, K.M. and Trushin, V.A., The Effect of Rotation on Heat Transfer in the Radial Cooling Channels of Turbine Blades, Thermal Engineering, Vol. 32, p. 93-96, 1985.
- Ito, H., and Nanbu, K., Flow in Rotating Straight Pipes of Circular Cross Section. ASME Paper 70-WA/FE-13, 1970.
- Johnson, B.V., Heat Transfer Experiments in Rotating Radial Passages with Supercritical Water. ASME Heat Transfer 1978 (Bound Publication of Proceedings from 1978 ASME Winter Annual Meetings).
- Johnston, J. P., The Effects of Rotation on Boundary Layers in Turbomachine Rotors, Fluid Mechanics, Acoustics, and Design of Turbomachinery, Part I, NASA SP-304, P. 207-249, 1970.
- Johnston, J.P., Halleen, R.M. and Lezius, D.K., Effects of Spanwise Rotation of the Structure of Two-Dimensional Fully Developed Turbulent Channel Flow. J. Fluid Mech., Vol. 56, part 3, pp. 533-557, 1972.
- Kays, W. M., Convective Heat and Mass Transfer, McGraw-Hill Book Company, 1966.
- Lokai, V.I. and Gunchenko, E.I., Heat Transfer Over the Initial Section of Turbine Blade Cooling Channels Under Conditions of Rotation. Therm. Enging., Vol. 26, pp. 93-95, 1979.
- Metals, B. and Eckert, E.R.G., Forced, Mixed, and Free Convection Regimes. J. Heat Transfer, pp. 295-296, 1964.
- Moon, I-Man, Effects of Coriolis Force on the Turbulent Boundary Layer in Rotating Fluid Machines, MIT Gas Turbine Laboratory Report No. 74, June 1964.
- Moore, J., Effects of Coriolis on Turbulent Flow in Rotating Rectangular Channels. M.I.T. Gas Turbine Laboratory Report No 89; 1967
- Mori, U., Fukada, T. and Nakayama, W., Convective Heat Transfer in a Rotating Radial Circular Pipe (2nd Report). Int. J. Heat Mass Transfer, Vol. 14, pp. 1807-1824, 1971.
- Morris, W.D. and Ayhan, T., Observations on the Influence of Rotation on Heat Transfer in the Coolant Channels of Gas Turbine Rotor Blades. Proc. Instn. Mech. Engrs., Vol. 193, pp 303-311, 1979.
- Morris, W.D., Heat Transfer and Fluid Flow in Rotating Coolant Channels. Research Studies Press, Copyright 1981.
- Rothe, P.H. and Johnston, J.P., Free Shear Layer Behavior in Rotating Systems. J. Fluids Engineering, Vol. 101, pp. 117-120; 1979.
- Sleicher, C. A., and Tribus, M., In Heat Transfer Fluid Mechanics Institute, p. 59, Stanford, California, 1956.

Suo, M., Turbine Cooling in the Aerothermodynamics of Aircraft Gas Turbines, ed. Oates, G., Air Force Aero Propulsion Lab., AFAPL TR 78-52, 1978.

Suo, M., Suggested Program: Heat Transfer to Rotating Tubes. UTRC Proposal P80-377, 1980.

Suo, M., Unpublished Notes, United Technologies Research Center, 1980.

Taylor, J.R., Heat Transfer Phenomena in Gas Turbines. ASME Paper No. 80-GT-172, 1980.

Wagner, J. H., Johnson, B. V., and Hajek, T. J., Heat Transfer in Rotating Passages with Smooth Walls and Radial Outward Flow. ASME Journal of Turbomachinery, Vol 113, pp 42-51, January 1991, (first presented as ASME Paper 89-GT-272, 1989).

Wagner, J. H., Johnson, B. V., and Kopper, F. C., Heat Transfer in Rotating Serpentine Passages with Smooth Walls. ASME Paper 90-GT-331, 1990.

Wagner, R.E. and Velkoff, H.R., Measurements of Secondary Flows in a Rotating Duct. J. Eng. for Power, ASME Paper 72-GT-17, 1972.

Webb R.L., Eckert, E.R.G. and Goldstein R.J., Heat Transfer and Friction in Tubes with Repeated Rib Roughness. Int. J. Heat Mass Transfer, Vol. 14. pp. 601-617. 1971.

Yang, J.W., and Liao, N., An Experimental Study of Turbulent Heat Transfer in Converging Rectangular Ducts. Paper No. 73-WA/HT-27. ASME Journal of Heat Transfer, November 1973.

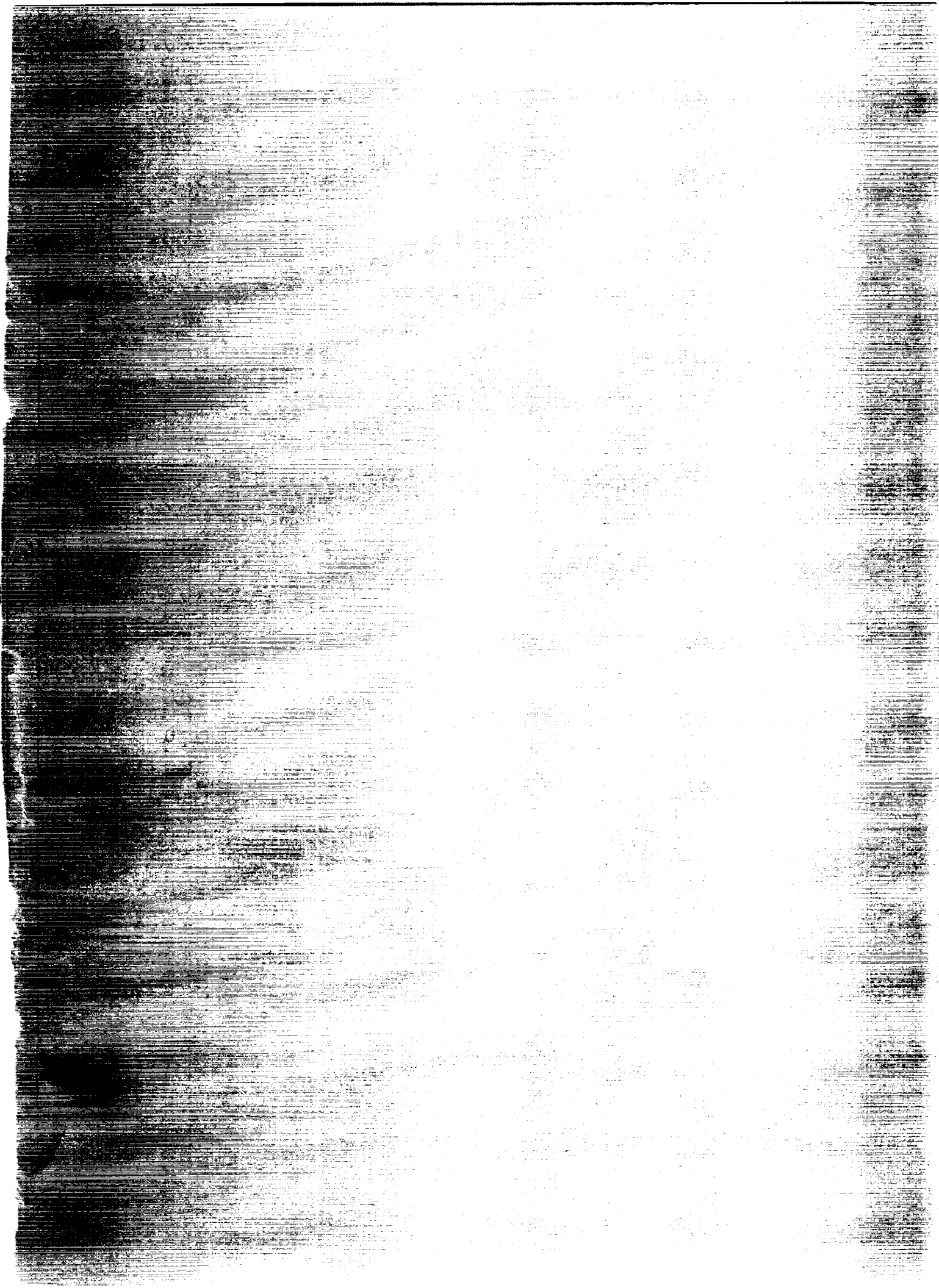
REPORT DOCUMENTATION PAGE			Form Approved OMB No. 0704-0188	
Public reporting burden for this collection of information is estimated to average 1 hour per response, including the time for reviewing instructions, searching existing data sources, gathering and maintaining the data needed, and completing and reviewing the collection of information. Send comments regarding this burden estimate or any other aspect of this collection of information, including suggestions for reducing this burden, to Washington Headquarters Services, Directorate for Information Operations and Reports, 1215 Jefferson Davis Highway, Suite 1204, Arlington, VA 22202-4302, and to the Office of Management and Budget, Paperwork Reduction Project (0704-0188), Washington, DC 20503.				
1. AGENCY USE ONLY (Leave blank)	2. REPORT DATE September 1991	3. REPORT TYPE AND DATES COVERED Final Contractor Report		
4. TITLE AND SUBTITLE Effects of Rotation on Coolant Passage Heat Transfer Volume I—Coolant Passages With Smooth Walls		5. FUNDING NUMBERS  WU 505-62-21 C NAS3-23691		
6. AUTHOR(S) T.J. Hajek, J.H. Wagner, B.V. Johnson, A.W. Higgins, and G.D. Steuber				
7. PERFORMING ORGANIZATION NAME(S) AND ADDRESS(ES)  Pratt & Whitney 400 Main Street East Hartford, Connecticut 06108		8. PERFORMING ORGANIZATION REPORT NUMBER  E-6470		
9. SPONSORING/MONITORING AGENCY NAMES(S) AND ADDRESS(ES)  National Aeronautics and Space Administration Lewis Research Center Cleveland, Ohio 44135-3191		10. SPONSORING/MONITORING AGENCY REPORT NUMBER  NASA CR-4396, Vol. I		
11. SUPPLEMENTARY NOTES Project Manager, Frederick C. Yeh, Internal Fluid Mechanics Division, NASA Lewis Research Center, (216) 433-5872.				
12a. DISTRIBUTION/AVAILABILITY STATEMENT  Unclassified - Unlimited Subject Category 34			12b. DISTRIBUTION CODE	
13. ABSTRACT (Maximum 200 words) An experimental program was conducted to investigate heat transfer and pressure loss characteristics of rotating multipass passages, for configurations and dimensions typical of modern turbine blades. This experimental program is one part of the NASA Hot Section Technology (HOST) Initiative, which has as its overall objective "the development and verification of improved analysis methods that will form the basis for a design system that will produce turbine components with improved durability." The objective of this program was the generation of a data base of heat transfer and pressure loss data required to develop heat transfer correlations and to assess computational fluid dynamic techniques for rotating coolant passages. The experimental work was broken down into two phases. Phase I consists of experiments conducted in a smooth wall large scale heat transfer model and is the subject of this report. In phase II the large scale model was modified to investigate the effects of skewed and normal passage turbulators. The results of phase II along with comparison to phase I will be presented in volume II of a NASA report.				
14. SUBJECT TERMS Heat transfer; Rotation; Turbomachinery			15. NUMBER OF PAGES 140	
			16. PRICE CODE A07	
17. SECURITY CLASSIFICATION OF REPORT Unclassified	18. SECURITY CLASSIFICATION OF THIS PAGE Unclassified	19. SECURITY CLASSIFICATION OF ABSTRACT Unclassified	20. LIMITATION OF ABSTRACT	

NSN 7540-01-280-5500

Standard Form 298 (Rev. 2-89)  
Prescribed by ANSI Std. Z39-18  
298-102

NASA-Langley, 1991





ADDRESS

POSTAL SERVICE

UNIT

WASHINGTON, D.C.

MAIL RATE  
POSTAGE & FEES PAID  
NASA  
Permit No. 937

NASA

POSTMASTER: If Undeliverable (Section 158  
of the Manual) Do Not Return